FIAS Interdisciplinary Science Series Series Editor: Walter Greiner

Walter Greiner Editor

Nuclear Physics: Present and Future





FIAS Interdisciplinary Science Series

Editor-in-Chief

Walter Greiner, Frankfurt am Main, Germany

Editorial Board

Ernst Bamberg, Frankfurt am Main, Germany Marc Thilo Figge, Jena, Germany Thomas Haberer, Heidelberg, Germany Volker Lindenstruth, Frankfurt am Main, Germany Joachim Reinhardt, Frankfurt, Germany Klaus Schulten, Urbana, USA Wolf Singer, Frankfurt am Main, Germany Horst Stöcker, Darmstadt, Germany More information about this series at http://www.springer.com/series/10781

Walter Greiner Editor

Nuclear Physics: Present and Future



Editor
Prof. Dr. h.c. mult. Walter Greiner
Frankfurt Institute for Advanced Studies
Goethe Universität Frankfurt
Frankfurt
Germany

ISBN 978-3-319-10198-9 ISBN 978-3-319-10199-6 (eBook) DOI 10.1007/978-3-319-10199-6

Library of Congress Control Number: 2014949485

Springer Cham Heidelberg New York Dordrecht London

© Springer International Publishing Switzerland 2015

This work is subject to copyright. All rights are reserved by the Publisher, whether the whole or part of the material is concerned, specifically the rights of translation, reprinting, reuse of illustrations, recitation, broadcasting, reproduction on microfilms or in any other physical way, and transmission or information storage and retrieval, electronic adaptation, computer software, or by similar or dissimilar methodology now known or hereafter developed. Exempted from this legal reservation are brief excerpts in connection with reviews or scholarly analysis or material supplied specifically for the purpose of being entered and executed on a computer system, for exclusive use by the purchaser of the work. Duplication of this publication or parts thereof is permitted only under the provisions of the Copyright Law of the Publisher's location, in its current version, and permission for use must always be obtained from Springer. Permissions for use may be obtained through RightsLink at the Copyright Clearance Center. Violations are liable to prosecution under the respective Copyright Law.

The use of general descriptive names, registered names, trademarks, service marks, etc. in this publication does not imply, even in the absence of a specific statement, that such names are exempt from the relevant protective laws and regulations and therefore free for general use.

While the advice and information in this book are believed to be true and accurate at the date of publication, neither the authors nor the editors nor the publisher can accept any legal responsibility for any errors or omissions that may be made. The publisher makes no warranty, express or implied, with respect to the material contained herein.

Printed on acid-free paper

Springer is part of Springer Science+Business Media (www.springer.com)

Preface

This book presents the majority of the talks delivered at the International Symposium *Nuclear Physics: Presence and Future*, which was held from May 29 to June 5, 2013 at Hotel Jakobsberg, Boppard am Rhein, Germany. The symposium was jointly organized by the Frankfurt Institute for Advanced Studies (FIAS), Frankfurt, Germany and Joint Institute for Nuclear Research (JINR), Dubna, Russia.

The symposium was dedicated to Prof. Mikhail Itkis on the occasion of his 70th birthday in recognition of his contributions as a pioneer in the fields of nuclear fission and superheavy nuclei and his commitment as a long-time director of the Flerov Laboratory at JINR, Dubna.

The main objective of the symposium was to present a survey of state-of-the-art topics in nuclear physics by leading practitioners in the field. A major focus was the study of superheavy nuclei and of neutron-rich exotic nuclei. The mechanisms of nuclear fission and nuclear cluster decay also were discussed by several speakers. Further subjects addressed were relativistic heavy ion collisions and the physics of supercritical fields. Transcending the subject of nuclear physics were talks dealing with the astrophysics of compact stars and with theoretical and experimental aspects of general relativity and its possible modification.

The symposium was held in the Jakobsberg resort near Boppard. This hotel is centrally located in one of Germany's most beautiful and picturesque landscapes—the Rhine Valley between Koblenz and Mainz. In fact, this famous wine-growing region has been designated as one of UNESCO's World Heritage sites.

I am grateful to my fellow members of the organizing committee from the Joint Institute for Nuclear Research in Dubna, Sergei Dimitriev and Dmitri Kamanin who helped to shape and organize the symposium. Joachim Reinhardt has edited the proceedings volume and was instrumental in bringing this book into a coherent

vi Preface

shape. Laura Quist has acted as the conference secretary and has helped in a multitude of ways to make the symposium a success. Finally, I am grateful to Dr. Thorsten Schneider and his team at Springer Verlag who expertly handled the production of this book.

Frankfurt, April 2014

Walter Greiner

Contents

Dedication to Prof. Mikhail Itkis	1
Part I Superheavy Elements	
SHE Research at GSI—Historical Remarks and New Ideas Gottfried Münzenberg	9
Opening New Lands on the Nuclear Map Valeriy Zagrebaev and Walter Greiner	21
Superheavy Element Chemistry	33
Nucleon Transfer Reactions in Very Heavy Ion Systems	45
Part II Nuclear Structure	
New Insights into the Structure of Neutron-Rich Nuclei	
$A = 108 - 118$ and $^{160-162}Gd$	57
J.H. Hamilton, Y.X. Luo, A.V. Ramayya, J.K. Hwang, E.H. Wang,	
N.T. Brewer, B. Doll, S.H. Liu, J.O. Rasmussen, I.Y. Lee, S. Frauendorf, G.M. Ter-Akopian, A.V. Daniel, Y.T. Oganessian,	
S.J. Zhu, Y. Shi, F.R. Xu and J.C. Batchelder	

viii Contents

Paradigmatic Lessons from Nuclear Driplines	69
Preliminary Results on Observation of New Shape Isomers Yu.V. Pyatkov, D.V. Kamanin, A.A. Alexandrov, I.A. Alexandrova, N.A. Kondratyev, E.A. Kuznetsova, A.O. Strekalovsky, O.V. Strekalovsky and V.E. Zhuchko	79
Features of Nuclear Reactions with Light Weakly Bound Nuclei at Energies Near the Coulomb Barrier N.K. Skobelev, Y.E. Penionzhkevich, S.M. Lukyanov, V. Kroha, A. Kugler and J. Mrázek	89
Stability Peninsulas in the Neutron-Rich Sector	99
Part III Nuclear Fission	
Dynamics of Collinear Ternary Fission	109
General Laws of Quantum and Statistical Mechanics Governing Fission	121
How Rare Is Cluster Decay of Superheavy Nuclei?	131
New Kind of Nuclear Multi-body Decay (CCT)—Status and Perspectives of Studies	141
Possible Production of Neutron-Rich Heavy Nuclei in Fissile Spallation Targets	151
Igor Mishustin, Yury Malyshkin, Igor Pshenichnov and Walter Greiner	131

Contents ix

Part IV Heavy Ion Physics	
FAIR—Cosmic Matter in the Laboratory	165
Turbulence in Low Viscosity Quark-Gluon Plasma László P. Csernai	175
Parallelization of Kinetic Theory Simulations	183
Part V Supercritical Fields	
Probing Supercritical Fields with Real and with Artificial Nuclei Joachim Reinhardt and Walter Greiner	195
Zepto-Second Atomic Clock for Nuclear Contact Time Measurements. Hartmut Backe	211
Superheavy Nuclear Molecules	223
Part VI Astrophysics and Relativity	
Compact Stars—How Exotic Can They Be?	235
Observational Tests of the Pseudo-complex Theory of GR Using Black Hole Candidates	245
Pseudo-complex General Relativity and Neutron Stars	255
An Introduction to the Mathematics of Pseudo-complex General Relativity	265

x Contents

The Gauge Principle in Covariant Hamiltonian Field Theory Hermine Reichau and Jürgen Struckmeier	275
Combining Quantum Electrodynamics and Electron Correlation Ingvar Lindgren, Sten Salomonson, Daniel Hedendahl and Johan Holmberg	287
Ultra High Energy Neutrons and Other Fermions	297
Photographs	303

Dedication to Prof. Mikhail Itkis

Walter Greiner

This symposium is dedicated to Prof. Mikhail Itkis on the occasion of his 70th birthday. Our personal acquaintance dates back about three decades. I first met Mikhail Itkis at a conference on neutron physics, organized by Prof. Dieter Seeliger (Technische Hochschule at Dresden in East Germany: at that time "Deutsche Demokratische Republik") at a small castle about 40km east of Dresden, near Bautzen. I gave a talk on collective theory of fission. The basic idea was that the essential coordinates of a fissioning nucleus are the distance *R* between the two nuclear centers and the mass asymmetry

$$\eta = \frac{A_1 - A_2}{A_1 + A_2},$$

where A_i are the number of nucleons in the *i*th fission fragments (see Fig. 1).

The potential between the two fragments $V(R, \eta)$ depends for given R on the mass asymmetry η . The collective wave-function $\Psi(R, \eta)$ will show maxima where the potential has minima and vice versa. The probability distribution will show pronounced maxima for symmetric and asymmetric fission. If the potential has several minima, e.g., due to shell structure, *symmetric*, *asymmetric* and *superasymmetric* fission will occur (see Figs. 2 and 3).

I was tremendously pleased when Professor Itkis stood up and showed a figure of his measurements of the fission products of various symmetrically fissioning nuclei, which showed side-maxima—see Fig. 4. Clearly, there was evidence for such superasymmetric fission: in this case it is a symmetrically fissioning nucleus which shows side-maxima in the asymmetry degree of freedom.

Later in time (2010–2012) Prof. Friedrich Gönnenwein (Tübingen) gave beautiful evidence for superasymmetric fission of various heavy nuclei, see Fig. 5. But it was Mikhail Itkis who discovered superasymmetric fission first. I was tremendously happy when these clear and lucid collective ideas found confirmation by Itkis' experiment.

Frankfurt Institute for Advanced Studies, J.W. Goethe-Universität, 60438 Frankfurt, Germany e-mail: greiner@fias.uni-frankfurt.de

1

W. Greiner (⋈)

W. Greiner

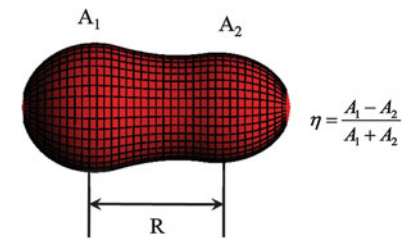


Fig. 1 The deformed nucleus fissioning into two clusters, R is the distance between the two clusters and η is the mass-asymmetry coordinate

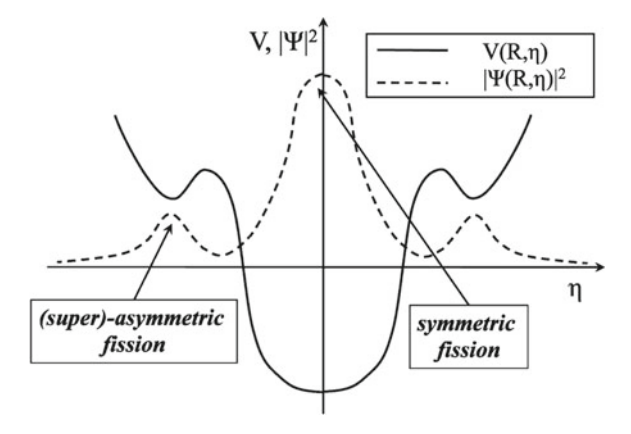


Fig. 2 Potential of a symmetrically fissioning nucleus as a function of the mass-asymmetry η (solid line). The collective wave function squared $|\Psi(R, \eta)|^2$ as a function of η at fixed R (dashed line)

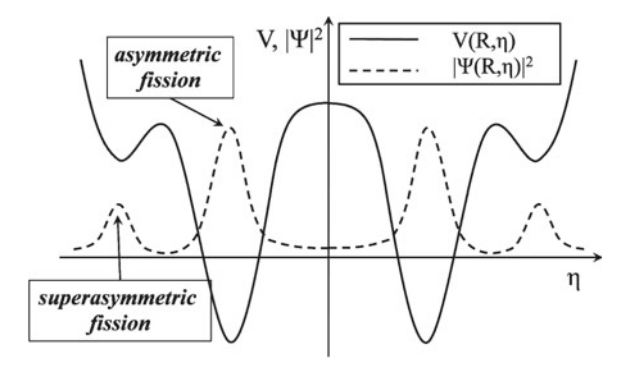


Fig. 3 Potential of an asymmetrically fissioning nucleus as a function of the mass-asymmetry η with additional possibility of superasymmetric fission

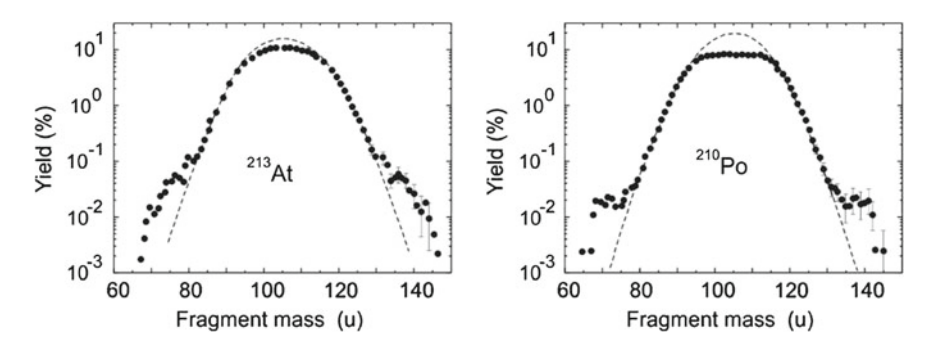


Fig. 4 Symmetrically fissioning nucleus with the contribution from superasymmetric fission

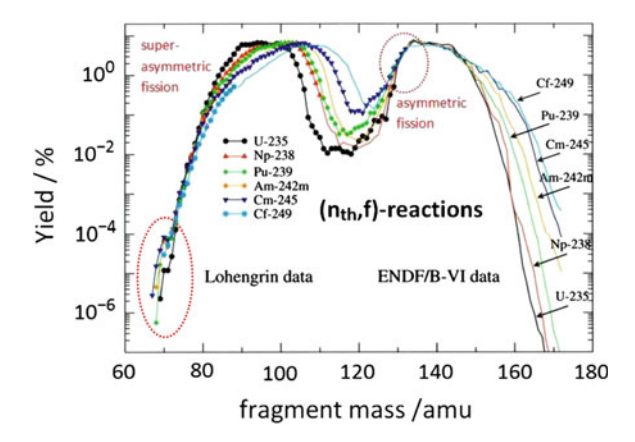


Fig. 5 Fragment distribution of asymmetrically fissioning nuclei with the indication of super-asymmetric fission

This is a master example where a simple theoretical idea was proven by a beautiful measurement—done independently of the theory.

Mikhail is a brilliant nuclear physicist, a dedicated researcher and science organizer, and at the same time a caring and warm person. A full appreciation of his scientific life will now be given. Andrej Popeko helped me in setting this up.

1 Prof. Mikhail Itkis—Pioneer of Nuclear Physics

Professor Mikhail Itkis was born on 7 December 1942 in Kazakhstan, then a socialist republic within the USSR. He graduated from the Moscow State University, where he majored in physics. In 1967 he started his academic career at the Institute of Nuclear Physics (INP) of the Republic of Kazakhstan, one of the scientific divisions of the Kazakhstan Academy of Sciences.

4 W. Greiner



Professor Mikhail Itkis went through many challenges to get to where he is today. Initially the young scientist worked as an engineer in Almaty city (former Alma-Ata). He defended his Ph.D. and habilitation theses in 1974 and 1985, respectively. Professor Itkis became the head of one of the major departments at INP. He has been extensively studying nuclear fission for over 40 years, a topic which occupies one of the central positions in the universal many-body problems of nuclear physics. His work was widely recognized, and he became one of the leading nuclear fission scientists. The group of young Almaty scientists announced first, extremely promising results for nuclear fission, which helped deepen our knowledge of this process and of the properties of nuclear matter. The Almaty team presented experimentally measured fission barriers and moments of inertia of nuclei and studied shell-effect manifestation in mass-energy distributions of low-energy fission fragments.

Subsequently, the Almaty researchers conducted a series of experiments that enabled them to estimate the probability of preactinide nuclei fission. The results also helped the scientists determine the shape of nuclei in the regions of nuclear super-deformations and evaluate the impact of both the shell structure and the effects of the nuclear binding of nucleons on thermodynamic properties of hot nuclei.

These efforts started to bear fruit. The Almaty team observed new features of nuclear fission in the lead region which was crucial for a better understanding of the character of the asymmetric nuclear fission and the impact of both shell effects and the fluctuation-dissipation processes on the formation of mass and energy distributions of fission fragments from cold and hot nuclei.

As Mikhail Itkis was probing deeper into the process of nuclear fission induced by light-charged particles, it was in early 1980s when he discovered another promising field of research, namely, the fission of nuclear systems emerging from heavy-ion induced reactions. His academic interests were so intricately interwoven with the research activities at JINR that in 1992 he was invited to pursue his scientific activities at FLNR.

In 1993 the JINR Scientific Council appointed Professor Itkis a deputy director, and in 1997 he became the director of FLNR, JINR. Professor Itkis started intense research of nuclear fission induced by heavy ions at the U400 cyclotron and founded one of the laboratory experiment divisions intended the study of the reaction dynamics and fission of heavy and superheavy nuclei. Not only did Professor Itkis head the laboratory, but he also initiated and participated in many experiments.

The experiment division staff pioneered unique techniques and constructed a series of setups for evaluating the correlation between the neutron emission, gamma quanta, and fission fragments. The double-arm time-of-flight CORrelation SETup (CORSET) manufactured for this purpose proved to be extremely efficient. Subsequently, the coupling of the spectrometer of fission fragments CORSET with the DETecteur MOdulaire de Neutrons (DEMON), a Belgian-French neutron multi-detector, allowed use of the former as a trigger for multi-detector systems.

Such collaborative work increased the reliability of data on average neutron and gamma-quanta multiplicity in heavy-ion-induced reactions, which allowed for the first time ever separation of reaction channels. One of the key results was the discovery of quasifission processes in the fission of heavy nuclear systems. This breakthrough allowed correct interpretation of experimental constraints to nuclear fusion leading to the formation of superheavy nuclear systems. Over the years, the FLNR JINR staff conducted systematic investigations of fusion-fission and quasifission of heavy and superheavy nuclei at Z=102-122 using the U400 cyclotron. Moreover, the FLNR researchers studied the excitation functions of nuclear reactions, the mass-energy distributions of reaction products, the multiplicities of neutrons and gamma-quanta, and the manifestation of shell effects in cold and hot fusion reactions.

The experiments by JINR FLNR found interesting results on estimates of fission cross sections for superheavy nuclei, which allowed for the study of the formation probability of compound nuclei. The choice of the most promising ion-target combinations and optimal excitation energy for the synthesis of superheavy elements was justified by the core assumptions of the theory.

As director of the Flerov Laboratory (1997–2007), Professor Itkis did his best to develop lab facilities and achieve further progress in the study of nuclear processes. Numerous changes were initiated, i.e., experimental laboratory equipment was expanded, new experimental setups were designed and constructed, superheavy elements 113–118 were synthesized, and their production was investigated. Mikhail Itkis started experiments dedicated to the study of chemical properties of new elements; the research was carried out on fission physics, nuclear reaction mechanisms, nuclear spectroscopy, and the properties of exotic nuclei. In May 2011 the International Union of Pure and Applied Chemistry (IUPAC) officially recognized flerovium and livermorium, elements 114 and 116, added to the Mendeleev periodic table. In May 2012

W. Greiner

IUPAC officially approved the name flerovium for the superheavy element of atomic number 114 and the name livermorium for element 116.

Professor Itkis was awarded numerous JINR awards in recognition of his academic achievements. He won both the G.N. Flerov Prize 2003 and the Alexander von Humboldt Research Prize 2005 (Germany).

In 2009 Professor Itkis was honored to receive the degree of doctor honoris causa of the Goethe University, Frankfurt. In 2011, together with Professor Yuri Oganessian, Professor Itkis was awarded the 2010 State Prize of the Russian Federation for outstanding contributions in science and technology. In March 2006 the Committee of Plenipotentiaries of the JINR Member States appointed Professor Itkis as the JINR deputy director. Numerous presentations at this conference today are in fields to which Professor Itkis made a number of ground-breaking contributions.

Professor Itkis is known for his fundamental work in various fields of physics that played a key role in the establishment and development of many areas of further research. To us, his friends and colleagues, Mikhail is much more than an outstanding scientist. He is a warm and caring friend, a wonderful colleague who gave freely of his time, advice and expertise. From the bottom of our hearts, we would like to congratulate Mikhail on his 70th anniversary. We all wish him good health and new outstanding achievements.



Part I Superheavy Elements

SHE Research at GSI—Historical Remarks and New Ideas

Gottfried Münzenberg

Abstract SHE research at GSI was strongly inspired by the ideas from Dubna: our motivation, the concept of cold fusion, and the continuous exchange of ideas. Experimental highlights on the way to our present understanding of Super Heavy Elements, SHE, and some developments will be discussed. Large progress has been made in the discovery of SHE, even passing the magic proton number 114 and finding first hints for a superheavy shell closure in the region of the heaviest elements. The discovery of the spherical SHE is still waiting. New ideas and methods to access this region are needed. First ideas for SuperSHIP, a next-generation instrument for the separation and identification of SHE, produced in fusion and transfer reactions, will be presented. Some ideas for SHE production will be addressed briefly.

1 Introduction

From the very beginning of the GSI experimental program of superheavy-element research was strongly motivated by Dubna, specifically by the inspiring talks of academician G.N. Flerov (Fig. 1) and the permanent discussions and exchange of ideas with him and Yuri Oganessian (Fig. 2). The results of the experiments with cold heavy ion fusion carried out by Yuri Oganessian, the synthesis of fermium and the transactinide elements with lead targets were convincing so that we started our program on heavy element synthesis at SHIP with cold fusion reactions. The undoubted proof of Yuri Oganessian's concept was the observation of the one neutron channel in the irradiation of ²⁰⁸Pb with ⁵⁰Ti to produce element 104 at SHIP in the year 1981. Examples of the observed decays are displayed in Fig. 3 [7]. This concept

GSI Helmholtzzentrum für Schwerionenforschung, 64291 Darmstadt, Germany e-mail: g.muenzenberg@gsi.de

G. Münzenberg

Manipal University, Manipal 576104, Karnataka, India

G. Münzenberg (⋈)

10 G. Münzenberg



Fig. 1 G.N. Flerov in the GSI barracks 1973 (Foto Zschau, GSI)



Fig. 2 Discussion at Dubna in G.N. Flerov's office, 1983, listening to Yuri Oganessian (*Foto* Dubna)

was continued by us successfully up to the synthesis of element 112, always with exchange of results and ideas, and for the heaviest elements with support of materials and scientists from Dubna.

The way to the heaviest GSI elements was started by the contribution of isotopic 58 Fe to produce element 110 and the support by Sasha Eremin and Andrey Popeko

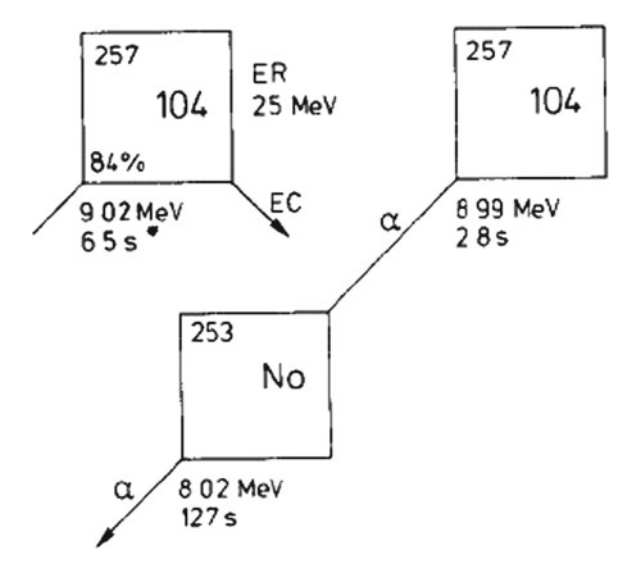


Fig. 3 The synthesis of ²⁵⁷104 in a 1n channel in the irradiaton of ²⁰⁸Pb with ⁵⁰Ti, the experimental proof of cold heavy ion fusion in 1981 at SHIP. *Left* literature, *right* a single-atom decay chain

who joined the SHIP group which was at this time in competition with the experiment at JINR Dubna to produce element 110 in the hot fusion reaction. Certainly a unique situation and an excellent example for science research. This experiment paved the way for elements 111 and 112 at SHIP. Figure 4 shows the discoverers of element 112, among them A. Eremin and A. Popeko from JINR Dubna.

2 The Dubna Situation After the End of the Soviet Union—The New Research Program and Its Realization

In 1992 after the end of the Soviet Union there was great concern in the International Science Community about the future of JINR Dubna. D. Ebert, at that time vice director of JINR, was asked by the German "Physikalische Blätter" to analyze the situation. He pointed out the research potential of the two heavy ion cyclotrons U400 and the new U400M. A corresponding article was written by D. Hartwig from the German Ministry of Research and Technology entitled: "Hat das VIK Dubna eine Zukunft?" (Does JINR Dubna have a future?).

On July 15th 1991 a contract between the German Ministry of Research and Technology and the JINR for "collaboration and use of the technical equipment of JINR" was signed, the "Vereinbarung zwischen dem BMFT und dem VIK über Zusammenarbeit und Nutzung von Anlagen des VIK". In the frame of this agreement Paul Kienle, then director of GSI, Berhard Franzke, and I went to Dubna for discussions. For his research program and upgrade of the cyclotrons Yuri Oganessian needed

12 G. Münzenberg

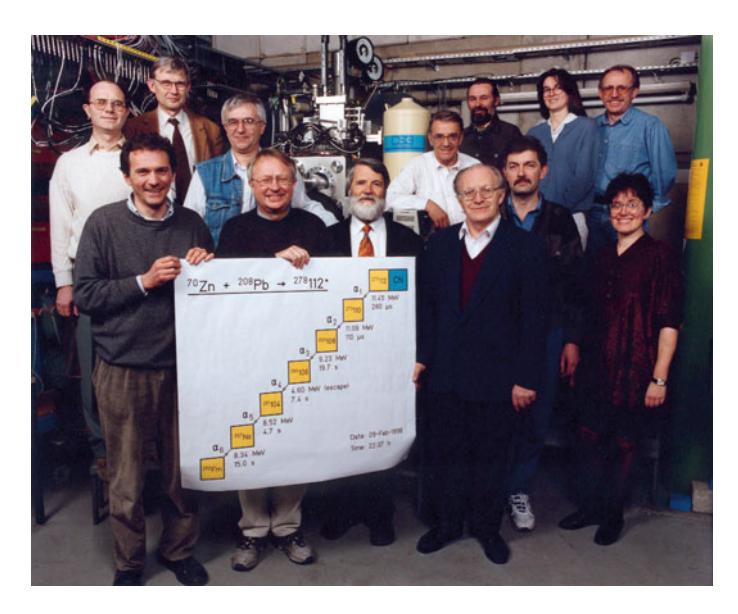


Fig. 4 The discoverers of element 112, leader S. Hofmann with A. Eremin, fourth from *right* and A. Popeko, fourth from *left*



Fig. 5 The Dubna PAC for Nuclear Physics 1998, Chair Chantal Briancon, with Michail Itkis (second from *left*), director of the Flerov Laboratory of Nuclear Physics (*Foto* JINR Dubna)

a powerful ECR ion source. The best at this time was the ECR-4M developed at GANIL. It was bought with money from the BMFT-VIK contract. In our discussions it became clear that Dubna would follow the method of hot fusion for SHE production and GSI continue the complementary way of cold heavy-ion fusion (Fig. 5).

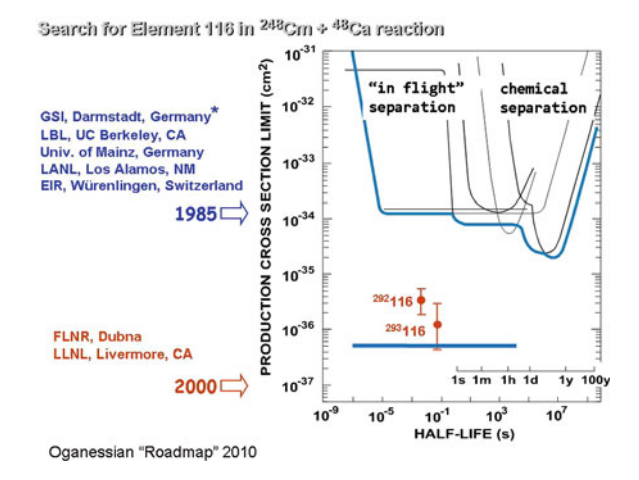


Fig. 6 Yuri Oganessian's vision to increase the sensitivity for the ⁴⁸Ca beam for new SHE [10]

3 Yuri Oganessian's Vision and New Concept: With ⁴⁸Ca to SHE

The new concept of Yuri Ogenessian was the use of ⁴⁸Ca as projectile for SHE synthesis to profit from its double shell closure to enhance the fusion probability in the same way as it was observed with the doubly magic ²⁰⁸Pb in cold fusion [8]. Such an experiment had already been made in the "World collaboration experiment" (Fig. 6) to synthesize element 116 [1], without success. Yuri Oganessian's dream was to increase the sensitivity by three orders of magnitude. His success came in the year 2000, 15 years after the first experiment (Fig. 6). The way to the new superheavy elements beyond 112 had been entered. Preparative investigations to measure the fusion probability were performed in fusion-fission studies by Michail Itkis (Fig. 7). It should be noted here that these studies also saved Dubna much beam time in the Berkeley-118 disaster. Figure 7 shows no symmetric fission in the reaction ⁸⁶Kr + ²⁰⁸Pb. What did we learn and where are we now? Cold fusion reactions led to the discovery of the N=162 subshell already located in the region beyond the liquid drop stability limit [6]. These nuclei exist only by shell stabilization. The Dubna experiments already show indications for the onset of the spherical SHE shell (Fig. 8). Figure 9 shows Walter Henning, Michael Itkis, Yuri Oganessin, and others, discussing results and future experiments at GSI and Dubna.

4 The Future—New Developments

With the discovery of element 118 by Yu.Ts. Oganessian, V.K. Utyonkov, and collaborators including Michail Itkis [9], the natural limit for SHE production involving double magic nuclei, ²⁰⁸Pb and ⁴⁸Ca, has been reached because of the limitation in

14 G. Münzenberg

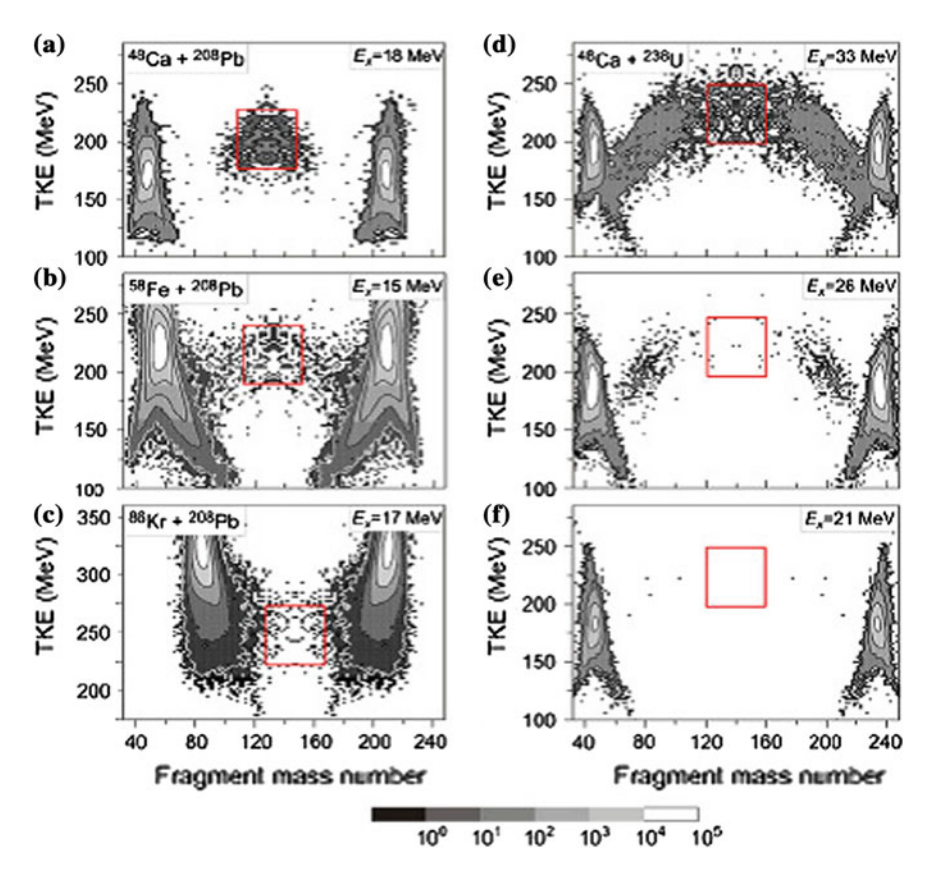


Fig. 7 Examples from the fusion-fission studies performed by Michail Itkis and his group for cold and ⁴⁸Ca fusion [10]

availability of heavy actinide targets [10]. A large field of new elements and isotopes has been discovered. But only their basic properties such as decay mode, half-live, and decay energy have been measured.

The number of known even-even isotopes, needed for determination of the ground state mass, is scarce. A more detailed investigation of nuclear and atomic structure as well as chemistry beyond thermo-chromatography should be made. This requires dedicated high current accelerators, power targets, and new detection systems for complete decay spectroscopy as well as trap systems for direct mass determination, needed, e.g., for direct identification of nuclei which cannot be identified by the α - α parent-daughter correlation method including fissioning and β -decaying nuclides.

The principal goal of SHE research has not been reached yet: the spherical shell of SHE. It still awaits its discovery. The discovery of new elements beyond 118 needs more sensitive experiments. Such research will be possible with the new accelerator

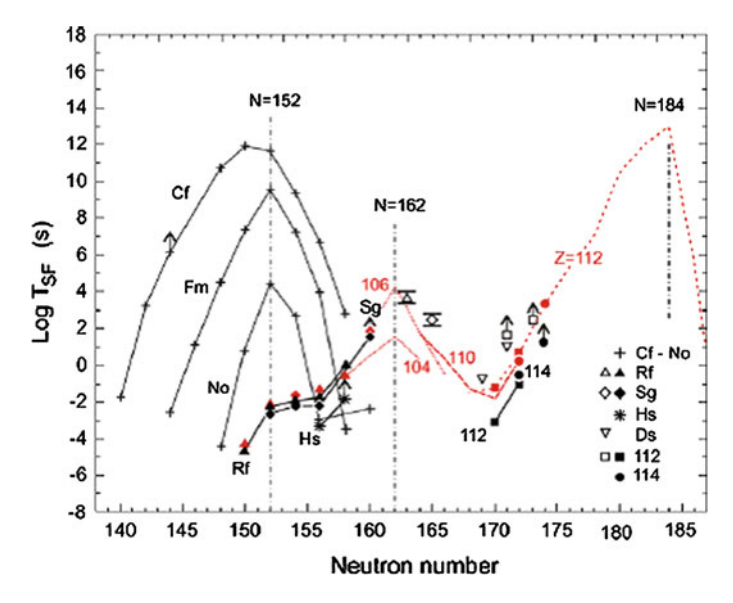


Fig. 8 The logarithmic partial fission half-lives for the heavy and superheavy elements with the peaks at the N=152 subshell in the actinide, the N=162 subshell in the transactinides, and first indications for the spherical shell closure for SHE [10]



Fig. 9 Discussing presence and future with Michail Itkis, Yuri Oganessian, Walter Henning, and collegues (Foto Dubna)

systems at JINR Dubna and the RIKEN accelerator dedicated for SHE research and new separators.

A new generation of separators is under development to mention the S^3 at SPI-RAL and new gasfilled systems at Dubna, Lanzhou, and RIKEN. In a Giessen-GSI-Manipal collaboration, investigations for a next generation separator for fusion and transfer products, SuperSHIP, are under way. What is the best? Requirements are:

16 G. Münzenberg

	Acceptance	Φ_B	Φ_E	$B\rho_{ m max}$	$F\rho_{\max}$	Resolution
	msr	deg	deg	Tm	MV	
Vacuum						
SHIP GSI	3	6, 12, 12, 6	6.6	1.2	20	$v/\Delta v = 50$
VASILISSA mod	15	16, 16, 16	8.8	1	26	$E/\Delta E$
FMA ANL	8	40	20	1	18	$M/\Delta M = 350$
MARA JYFL	9	40	20	1	14	$M/\Delta M = 250$
S ³ GANIL	9	22, 22, 22	25	1.8	12	$M/\Delta M = 350$
Gasfilled						
DGFRS JINR	10	23		3.1		
GARIS RIKEN	22	45		1.9		
TASCA GSI	13	30		2.4		
RITU JYFL	8.5	25		2.2		

Table 1 Examples of in-flight separators used or planned for SHE research

The table displays the angular acceptance in msr, the deflection fields listed with the deflection angles in degrees, F_B refers to magnetic, F_E to electric field, the maximum beam rigidity $B\rho$ and $F\rho$, and the resolving power for velocity or mass

operation with large beam intensities of the order of 10^{14} s⁻¹, high efficiency, fast separation, good projectile beam suppression, and the capability of mass determination. Table 1 shows, that practically all possible types of in-flight separators are used for SHE research.

Let us start with vacuum instruments. The first category covers mass and energy filters. These work as kinematic separators (Fig. 10, right panel) and are made to suppress the projectile beam. They are multistage instruments with three or four magnetic and two electric fields of small deflection angle because they need only small resolution. As shown in the figure, kinematic separation is very sensitive to the type of reaction. Fusion products, transfers, and fission products are well separated by tuning to the respective velocity. At SHIP is was shown that the velocity resolution of about 50 is sufficient to separate xn from α , xn channels [4]. The next category shows recoil mass separators. They follow a completely different philosophy. Their purpose is to separate masses with a resolution of one mass unit. The problem is the multiple ionic charge states of the recoils. In the case of many nuclear masses these lead to overlapping lines, therefore the mass resolution for SHE should be at least 600. These problems are well treated and discussed in the thesis of J. Saren [11]. The higher resolution needs larger deflection angles compared to the filter.

The third category includes magnetic separation. Fig 10, left panel, shows for the example of the reaction 48 Ca + 258 Cm to produce element 116 that magnetic separation cannot separate the fusion products from the projectiles, transfers are separated. This is generally true for all target-projectile combinations. Magnetic separation works well for in separators for projectile fragments which have a completely different kinematics.

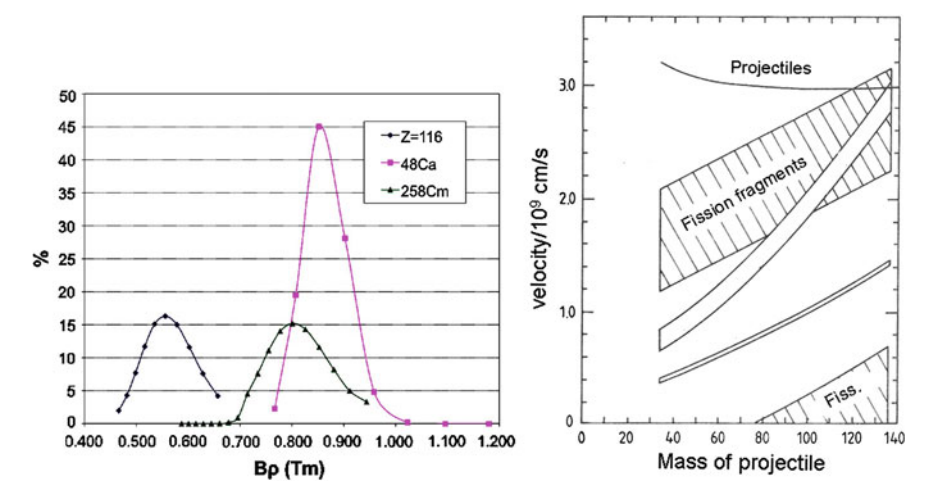


Fig. 10 Separation of SHE. *Left panel* Magnetic deflection of beam, fusion products, and target like transfers (courtesy A. Popeko). *Right panel* the velocities of projectiles, fusion products, target-like transfers, and fission fragments for the hypothetical SHE Z=114 for all possible target-projectile combinations, plotted versus the projectile mass

Presently gas filled separators are widely used with large success for SHE production. The heaviest elements beyond Copernicium were created at the gasfilled separators DGFRS, Dubna, and also at GARIS, RIKEN. Gasfilled separators have large acceptance, and separate heavy nuclei from the light projectiles, irrespective of their production reaction: fusion, transfer, or e.g. incomplete fusion. A detailed investigation has been made at the RITU separator, Jyväskylä [12].

The conservation of beam emittance, a consequence of Liouville's theorem, relates the resolving power and the used area in the dispersive deflection field. As a consequence of the technically limited size of the dispersive elements, separators of high resolving power have a limited acceptance. Sufficient mass resolution at high transmission can only be achieved with a beam cooler and trap or MRTOF systems. First successful experiments have been made with SHIPTRAP at SHIP [3]. Nextgeneration separation systems for SHE will include such a system, however with the capability to separate rare species in the intense background of other reaction products. SHIP is specialized for heavy elements where only *few* reaction channels are open and therefore no isotope separation is needed. Already the investigation of proton emitters, where many channels are open, is difficult with SHIP.

For the investigation of such type reactions a dipole magnet with a quadrupole system was added to SHIP so that the combination worked as recoil mass separator with a resolving power of about 250 [2]. As improvement to the SHIP—SHIPTRAP system the new system will be able to separate rare species from a large background, and include several separation stages.

In our investigations we will study velocity filters and gas filled separators coupled to a cooler, trapping, or MRTOF system to find the optimum instrument in terms of

18 G. Münzenberg

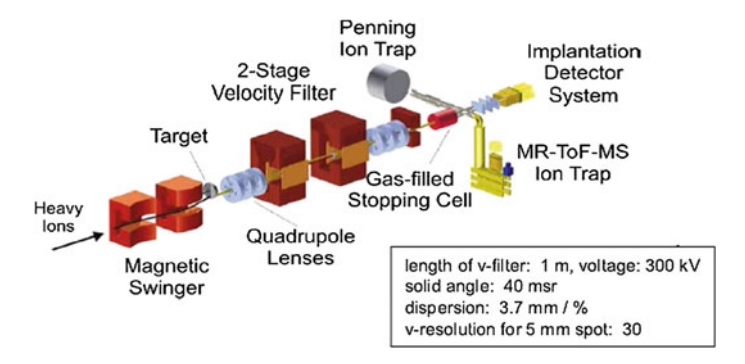


Fig. 11 SuperSHIP

transmission and separation efficiency to be used with intense beams of the order of up to $10^{14}~\rm s^{-1}$. Figure 11 shows a first result, a two-stage crossed-field velocity filter with a small bending magnet, an ion catcher-cooler system, and a MRTOF. The system will separate rare species from large background to have the ability to be used for reactions with light nuclei or transfers where many isotopes are created, and only the most rare and interesting ones are transmitted to the MRTOF [5]. RFQ and IGISOL systems will be discussed in our study. It should be noted that a velocity filter can separate target like transfer products in zero degree direction from projectiles up to mass 90 (Fig. 10). For heavier systems a beam swinger allows investigations of transfers under the grazing angle.

5 Conclusion and outlook

The next generation of SHE experiments beside the extension of the chart of nuclei beyond Z=118 will aim at the spherical SHE shell. It is not clear yet how it can be reached. New ideas and methods are being explored. Not much is known yet about the transactinide elements. The more detailed investigation of the chemical, atomic, and nuclear properties is a most interesting and important task to understand these very special elements with large nucleon and electron shells carrying large angular momenta, and which only exist by shell stabilization. The prerequisite are dedicated accelerator systems with high beam intensity, new instrumentation to work with high beam intensity, including power targets, and separators with the capability of isobar separation. New detectors systems to measure the complete decay of the separated nuclei, laser systems for optical studies and new chemistry beyond gas chromatography are already under development.

The Flerov Laboratory here is clearly on the pole position. Michail Itkis made significant contributions to lay the grounds for the successes of the ongoing programme and its future. All our best wishes to him and the laboratory for a splendid and bright future and continuous success!

References

- 1. P. Armbruster et al., Phys. Rev. Lett. **54**, 406 (1985)
- 2. P. Armbruster, G. Münzenberg, Eur. Phys. J. H 37, 237 (2012)
- 3. M. Block et al., Eur. Phys. J. D 45, 39 (2007)
- 4. W. Faust et al., Nucl. Instr. Meth. **166**, 397 (1979)
- 5. S. Heinz et al., Nucl. Instr. Meth. B 317, 603 (2013)
- 6. S. Hofmann, G. Münzenberg, Rev. Mod. Phys. 72, 733 (2000)
- 7. G. Münzenberg et al., in *Actinides in Perspective*, ed. by N.E. Edelstein (Pergamon, Oxford GB, 1981)
- 8. Y.T. Oganessian et al., Nature **400**, 242 (1999)
- 9. Y.T. Oganessian et al., Phys. Rev. C 74, 044602 (2006)
- 10. Y.T. Oganessian, J. Phys. G 34, 165 (2007)
- 11. J. Saren, Thesis, University of Jyväskylä, Finland, 2012
- 12. J. Saren et al., Nucl. Instr. Meth. A **645**, 508 (2011)

Opening New Lands on the Nuclear Map

Valeriy Zagrebaev and Walter Greiner

Abstract The problem of production and study of heavy neutron-rich nuclei has been intensively discussed during recent years. Many reasons arouse a great interest in this problem. In the upper part of the nuclear map mostly proton-rich nuclei were studied while the unexplored area of heavy neutron-rich nuclides (also those located along the neutron closed shell N = 126 to the right-hand side of the stability line) is extremely important for the understanding of the r process of astrophysical nucleogenesis. For elements with Z > 100 only neutron deficient isotopes (located to the left of the stability line) have been synthesized so far. The "northeast" area of the nuclear map can be reached neither in fusion-fission reactions nor in fragmentation processes. There are only 3 methods for the production of heavy and superheavy (SH) nuclei, namely, a sequence of neutron capture and beta(-) decay, fusion reactions, and multinucleon transfer reactions. Multinucleon transfer processes look most promising for the production and study of neutron-rich heavy nuclei located in the upper part of the nuclear map. Reactions with actinide beams and targets are of special interest for synthesis of new neutron-enriched transfermium nuclei and notyet-known nuclei with closed neutron shell N = 126 having the largest impact on the astrophysical r-process. The estimated cross sections for the production of these nuclei allows one to plan such experiments at currently available accelerators if the problem of separation of heavy transfer reaction products would be solved.

1 Motivation

Due to the "curvature" of the stability line in fusion reactions of stable nuclei we may produce only proton-rich isotopes of heavy elements. For example, in fusion of rather neutron-rich ¹⁸O and ¹⁸⁶W isotopes one may get only the neutron deficient

V. Zagrebaev (⋈)

Joint Institute for Nuclear Research, Dubna, Russia

e-mail: zagrebaev@jinr.ru

W. Greiner

Frankfurt Institute for Advanced Studies, Frankfurt, Germany

e-mail: greiner@fias.uni-frankfurt.de

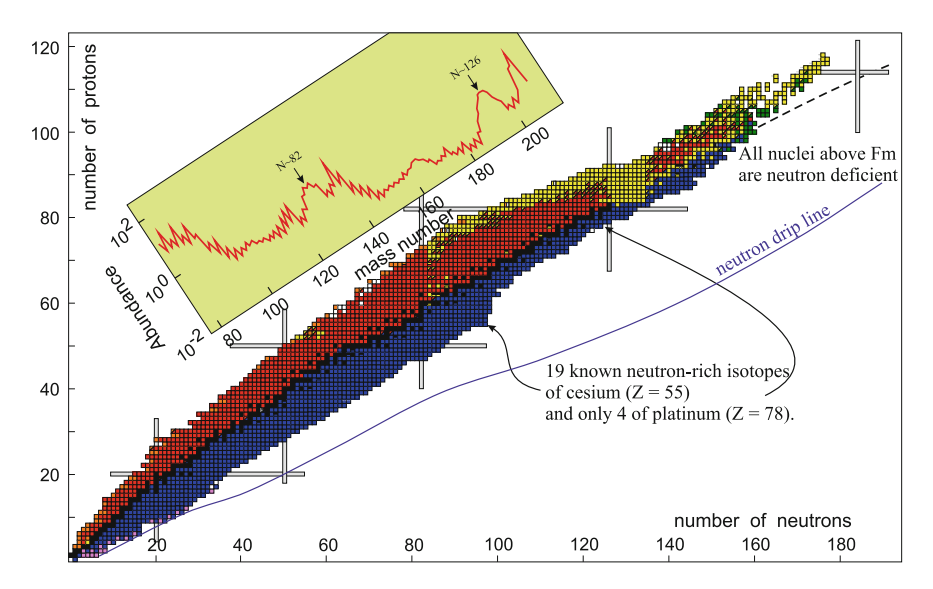


Fig. 1 Nuclear map as it looks today. *Gray* strips indicate positions of proton and neutron closed shells. On the inset relative abundance of the elements in the universe is shown with clear visible maxima in the regions of the "waiting points" along the neutron closed shells N = 82 and N = 126

 204 Pb excited compound nucleus, which after evaporation of several neutrons shifts even more to the proton-rich side. That is the main reason for the impossibility of reaching the center of the "island of stability" ($Z \sim 114$ and $N \sim 184$) in the SH mass region in fusion reactions with stable projectiles. Note that for elements with Z > 100 only neutron-deficient isotopes (located to the left of the stability line) have been synthesized so far. Because of that we also have almost no information about neutron-rich isotopes of heavy elements located in the whole northeast part of the nuclear map: for example, there are 19 known neutron-rich isotopes of cesium and only 4 of platinum (see Fig. 1).

The neutron capture process is an alternative (oldest and natural) method for the production of new heavy elements. The synthesis of heavier nuclei in the multiple neutron capture reactions with subsequent β^- decay is a well studied process. Strong neutron fluxes might be provided by nuclear reactors and nuclear explosions under laboratory conditions and by core–collapse supernova explosions (or mergers of neutron stars) in nature. However, to bypass the two area of fission instability (the so called "fermium gap" and the area of short living nuclei located at $Z=106\div108$ and $A\sim270$) one needs to have neutron fluxes at least 3 orders of magnitude stronger as compared with available nuclear pulsed reactors [1].

The unexplored area of heavy neutron-rich nuclei is extremely important for nuclear astrophysics investigations and, in particular, for the understanding of the r process of astrophysical nucleogenesis (a sequence of neutron capture and β^- decay processes). The origin of heavy elements from iron to uranium remains one of the great unanswered questions of modern physics and it is likely to remain a hot research

topic for years to come. The r-process path is located (and most probably interrupted by fission) just in the region of unknown heavy nuclei with a large neutron excess.

The neutron shell N=126 (and $Z\sim70$) is the last "waiting point" on this path. The half-lives and other characteristics of these nuclei are extremely important for the r-process scenario of the nucleosynthesis. Study of the structural properties of nuclei along the neutron shell N=126 could also contribute to the present discussion of the quenching of shell gaps in nuclei with large neutron excess. The isotopes with extreme neutron–to–proton ratios in the mass region $A=80 \div 140$ (including those around the neutron closed shell N=82) are successfully produced, separated and studied using the fission of actinide nuclei, whereas the neutron-rich nuclei with Z>70 cannot be formed neither in fission nor in fusion reactions. This area of the nuclear map remains blank for many years (see Fig. 1).

The multinucleon transfer processes in near barrier collisions of heavy ions allows one to produce heavy neutron-rich nuclei including those located at the island of stability. These reactions were studied extensively about 30 years ago. Among other topics there had been great interest in the use of heavy-ion transfer reactions to produce new nuclear species in the transactinide region [2–7]. The shell effects (clearly visible in fission and quasi–fission processes [8]) also play a noticeable role in near barrier multinucleon transfer reactions. These effects may significantly enhance the yield of searched for neutron-rich heavy nuclei for appropriate projectile-target combinations. In particular, the predicted process of antisymmetrizing ("inverse") quasi-fission may significantly enhance the yields of long-lived neutron-rich SH isotopes in collisions of actinide nuclei [9].

A possibility for the production of new heavy neutron-rich nuclei in low-energy multinucleon transfer reactions is discussed currently in several laboratories. Unfortunately, hardly any available experimental setups (fragment separators) may be used for this purpose and new equipment has to be designed and installed to discover and examine these nuclei (see below).

2 Multinucleon Transfer Reactions

Several models have been proposed and used for the description of mass transfer in deep inelastic heavy ion collisions, namely, the Focker-Planck [10] and master equations [11] for the corresponding distribution function, the Langevin equations [12], and more sophisticated semiclassical approaches [13–15]. Calculations performed within the microscopic time-dependent Schrödinger equations [16] have clearly demonstrated that at low collision energies of heavy ions nucleons do not "suddenly jump" from one nucleus to another. Instead of that, the wave functions of valence nucleons occupy the two-center molecular states spreading gradually over volumes of both nuclei (see Fig. 2).

The same adiabatic low-energy collision dynamics of heavy ions was found also within the TDHF calculations [17]. This means that the perturbation models based on a calculation of the sudden overlapping of single-particle wave functions of

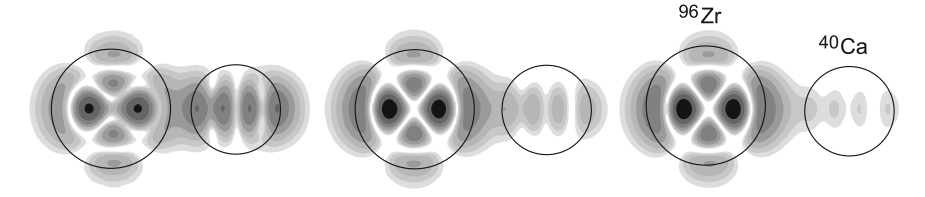


Fig. 2 Change of the wave function of valence neutron initially located in the $2d\frac{5}{2}$ state of 96 Zr nucleus approaching 40 Ca at near barrier collision energy

transferred nucleons (in donor and acceptor nuclei, respectively) cannot be used for description of multinucleon transfer and quasi-fission processes in low-energy heavy-ion damped collisions. Indeed the two center shell model [18] and the adiabatic potential energy look most appropriate for the quantitative description of such processes.

A model based on the Langevin-type dynamical equations of motion was proposed recently [19, 20] for the simultaneous description of strongly coupled multinucleon transfer, quasi-fission and fusion-fission reaction channels (difficult-to-distinguish experimentally in many cases). The distance between the nuclear centers R (corresponding to the elongation of a mono-nucleus when it is formed), dynamic spheroidal-type surface deformations δ_1 and δ_2 , the neutron and proton asymmetries, $\eta_N = (2N-N_{CN})/N_{CN}, \, \eta_Z = (2Z-Z_{CN})/Z_{CN}$ (where N and Z are the neutron and proton numbers in one of the fragments, whereas N_{CN} and Z_{CN} refer to the whole nuclear system) are the most relevant degrees of freedom for the description of mass and charge transfer in deep inelastic scattering jointly with fusion-fission dynamics.

In low-energy damped collisions of heavy ions just the multi-dimensional potential energy surface regulates to a great extent the evolution of the nuclear system. In our approach we use a time-dependent potential energy, which after contact gradually transforms from a diabatic potential energy into an adiabatic one: $V(R, \delta_1, \delta_2, \eta_N, \eta_Z; t) = V_{\text{diab}}[1 - f(t)] + V_{\text{adiab}}f(t)$ [19]. Here t is the time of interaction and f(t) is a smoothing function satisfying the conditions f(t=0)=0 and f(t) = 1, $\tau_{\text{relax}} = 1$, $\tau_{$

For all the variables, with the exception of the neutron and proton transfers, we use the usual Langevin equations of motion with the inertia parameters, μ_R and μ_δ , calculated within the Werner-Wheeler approach

$$\frac{dq_i}{dt} = \frac{p_i}{\mu_i}, \quad \frac{dp_i}{dt} = \frac{\partial V_{\text{eff}}}{\partial q_i} - \gamma_i \frac{p_i}{\mu_i} + \sqrt{\gamma_i T} \Gamma_i(t). \tag{1}$$

Here q_i is one of the collective variables, p_i is the corresponding conjugate momentum, $V_{\rm eff}$ includes the centrifugal potential, $T=\sqrt{E^*/a}$ is the local nuclear temperature, $E^*=E_{\rm c.m.}-V_{\rm eff}(q_i;t)-E_{\rm kin}$ is the excitation energy, γ_i is the appropriate friction coefficient, and $\Gamma_i(t)$ is a normalized random variable with Gaussian distribution. The quantities γ_i , E^* and T depend on the coordinates and, thus, on time (all them evidently are equal to zero at approaching reaction stage).

Nucleon exchange (nucleon rearrangement) can be described by the inertialess Langevin type equations of motion derived from the master equations for the corresponding distribution functions [19]

$$\frac{d\eta_N}{dt} = \frac{2}{N_{CN}} D_N^{(1)} + \frac{2}{N_{CN}} \sqrt{D_N^{(2)}} \Gamma_N(t), \frac{d\eta_Z}{dt} = \frac{2}{Z_{CN}} D_Z^{(1)} + \frac{2}{Z_{CN}} \sqrt{D_Z^{(2)}} \Gamma_Z(t).$$
(2)

Here $D^{(1)}$ and $D^{(2)}$ are the transport coefficients. We assume that sequential nucleon transfers play a main role in mass rearrangement. In this case these coefficients can be easily derived from the neutron and proton transfer rates [19], which are the fundamental quantities of low-energy nuclear dynamics.

The double differential cross-sections of all the binary reaction channels are calculated as follows

$$\frac{d^2\sigma_{N,Z}}{d\Omega dE}(E,\theta) = \int_0^\infty bdb \frac{\Delta N_{N,Z}(b,E,\theta)}{N_{\text{tot}}(b)} \frac{1}{\sin(\theta)\Delta\theta\Delta E}.$$
 (3)

Here $\Delta N_{N,Z}(b,E,\theta)$ is the number of events at a given impact parameter b in which a nucleus (N,Z) is formed in the exit channel with kinetic energy in the region $(E,E+\Delta E)$ and with center-of-mass outgoing angle in the interval $(\theta,\theta+\Delta\theta)$, $N_{\rm tot}(b)$ is the total number of simulated events for a given value of the impact parameter. This number depends strongly on low level of the cross section which one needs to be reached in calculation. For predictions of rare events with the cross sections of $1\,\mu$ b (primary fragments) one needs to test not less than 10^7 collisions (as many as in real experiment).

Expression (3) describes the mass, charge, energy and angular distributions of the *primary* fragments formed in the binary reaction. Subsequent de-excitation cascades of these fragments via emission of light particles and gamma-rays in competition with fission are taken into account explicitly for each event within the statistical model leading to the *final* charge and mass distributions of the reaction products. For the moment this approach is the only one which reproduces quite properly all the regularities of heavy ion deep inelastic scattering and quasi-fission processes. As an example, in Fig. 3 experimental and theoretical energy and mass distributions of reaction fragments are shown formed in collisions of ⁸⁶Kr with ¹⁶⁶Er [22].

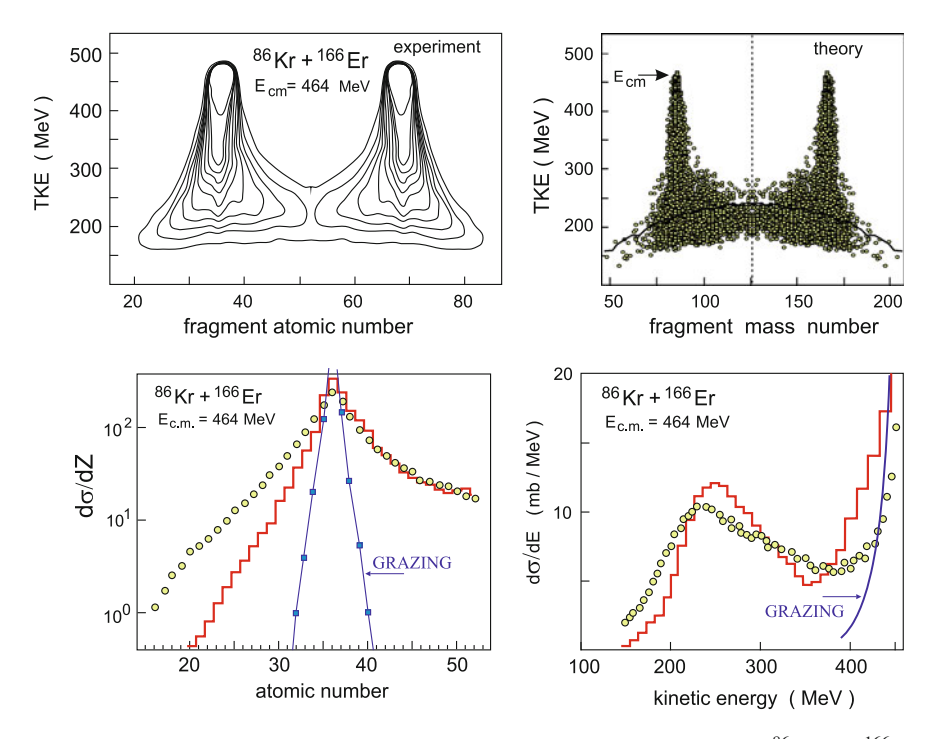


Fig. 3 Charge, mass and energy distributions of reaction fragments in collisions of 86 Kr with 166 Er at $E_{\rm c.m.}=464$ MeV. On the two *bottom panels* the histograms indicate the calculations performed within the model described above whereas the *curves* show the GRAZING calculations [23]

3 Synthesis of Neutron-Rich Transfermium Nuclei

In multinucleon transfer reactions the yields of heavier-than-target (trans-target) nuclei strongly depend on the reaction combination. The cross sections for the production of *neutron-rich* transfermium isotopes in reactions with ²⁴⁸Cm target change sharply if one changes from medium mass projectiles to the uranium beam. Even for rather heavy projectiles (such as ¹³⁶Xe) the nuclear system has a dominating symmetrizing trend of formation of reaction fragments with intermediate (heavier than projectile and lighter than target) masses, see Fig. 4.

We found also that the shell effects (clearly visible in fission and quasi-fission processes [8]) also play a noticeable role in near-barrier multinucleon transfer reactions [9, 24]. These effects may significantly enhance the yield of searched-for neutron-rich heavy nuclei for appropriate projectile–target combinations. In particular, the predicted process of anti-symmetrizing ("inverse") quasi-fission may significantly enhance the yields of long-living neutron-rich SH isotopes in collisions of actinide nuclei (such as U+Cm). In Fig. 5 the calculated cross sections for the production of primary and survived (evaporation residue) SH nuclei in damped

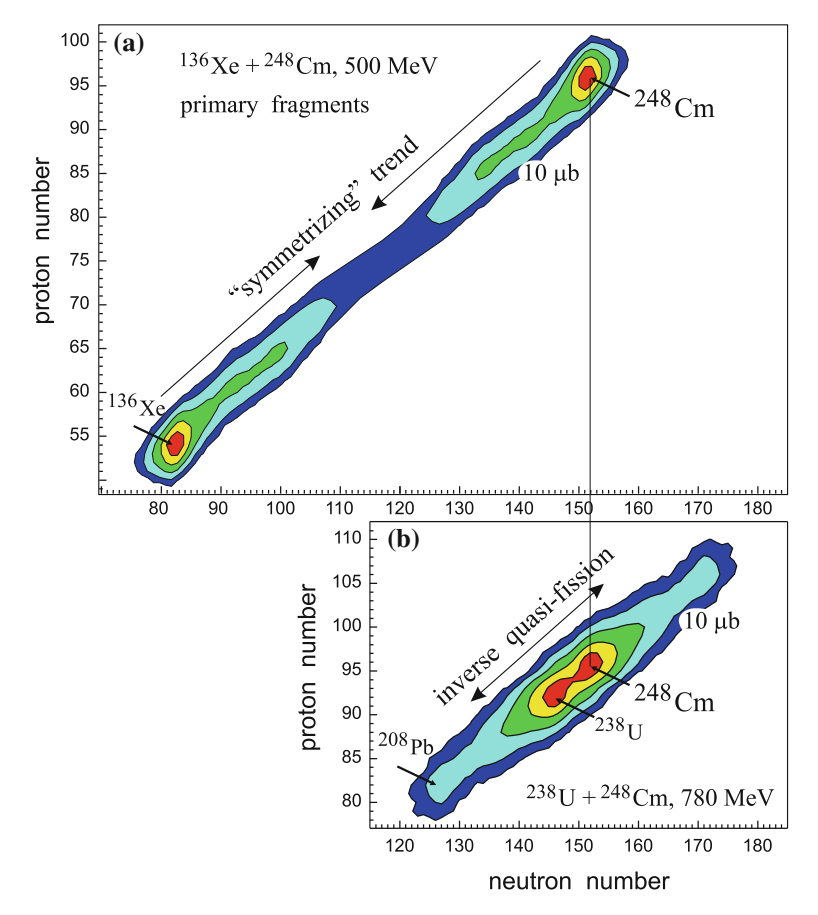


Fig. 4 Landscapes of the calculated cross sections for the production of primary reaction fragments in collisions of 136 Xe (**a**) and 238 U (**b**) with 248 Cm target at $E_{c.m.} = 500$ and $780\,\text{MeV}$, correspondingly (*contour lines* are drawn over one order of magnitude)

collisions of 238 U with 248 Cm at 770MeV center-of-mass energy are shown along with available experimental data. As can be seen, really many new neutron-rich isotopes of SH nuclei with $Z \ge 100$ might be produced in this reaction.

4 Synthesis of Neutron-Rich Nuclei in the Area of N = 126

Actinide beams (as well as actinide targets) might be successfully used also for the production of new neutron-rich heavy nuclei around the closed neutron shell N=126, the region having the largest impact on the astrophysical r-process. Nearbarrier collisions of 136 Xe and 192 Os with a 208 Pb target were predicted to be quite

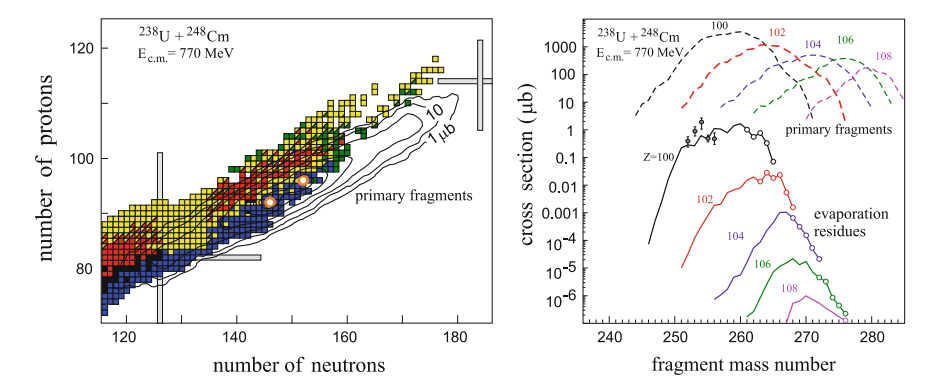


Fig. 5 Cross sections for the production of primary (*left panel*) and survived (*right panel*) transfermium nuclei in collisions of 238 U with 248 Cm target at $E_{c.m.} = 770$ MeV. *Open circles* indicate new isotopes of transfermium elements. Experimental data are taken from [5] for the production of fermium isotopes in this reaction

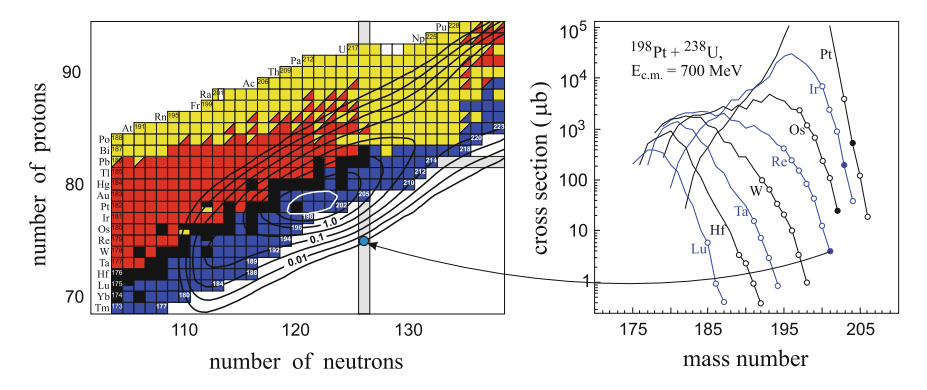


Fig. 6 (*Left panel*) Contour plot of the cross sections (in logarithmic scale) for the formation of primary reaction fragments in collisions of 198 Pt with 238 U at $E_{c.m.}=700\,\text{MeV}$ (millibarns, numbers on the curves). (*Right panel*) Isotopic yields of elements below lead in these collisions. *Circles* denote not-yet-known isotopes (the solid ones show isotopes with closed neutron shell N=126)

promising for the production of new neutron-rich nuclei with $N \sim 126$ [24, 25]. However low-energy collisions of stable neutron-rich isotopes of elements located below lead (such as ¹⁹²Os or ¹⁹⁸Pt) with available actinide targets look even more favorable.

Distribution of primary fragments formed in transfer reactions are concentrated around the line connecting projectile and target (just due to conservation of proton and neutron numbers, see, for example, Fig. 4). If one reaction partner has a neutron excess (such as 238 U), then this line will be inclined to the neutron axis. Distribution of primary fragments in the (Z, N) plane is shown on the left panel of Fig. 6 for the case of transfer reaction products formed in low energy collisions of 198 Pt with 238 U

at $E_{\text{c.m.}} = 700 \,\text{MeV}$. As can be seen a lot of new isotopes in the region of the closed neutron shell N = 126 can be synthesized in this reaction.

Estimated cross sections for the production of the final (survived) isotopes of heavy elements with $Z=71\div78$ in low energy collisions of 198 Pt with 238 U are shown on the right panel of Fig. 6. On average, the cross sections for the production of new neutron-rich heavy nuclei (including those located along the closed neutron shell N=126) in this reaction are higher than in collisions of 136 Xe or 192 Os with 208 Pb target [25].

5 Laser Separation of Heavy Reaction Products

In contrast with fusion reactions (when the compound nucleus moves with well defined velocity in forward direction) it is more difficult to separate a given nucleus from all the transfer reaction products having broad angular, mass and energy distributions. Unfortunately, the neutron-rich heavy nuclei with Z > 70 formed in the multinucleon transfer reactions cannot be separated and studied at available setups created quite recently just for studying the products of deep inelastic scattering (such

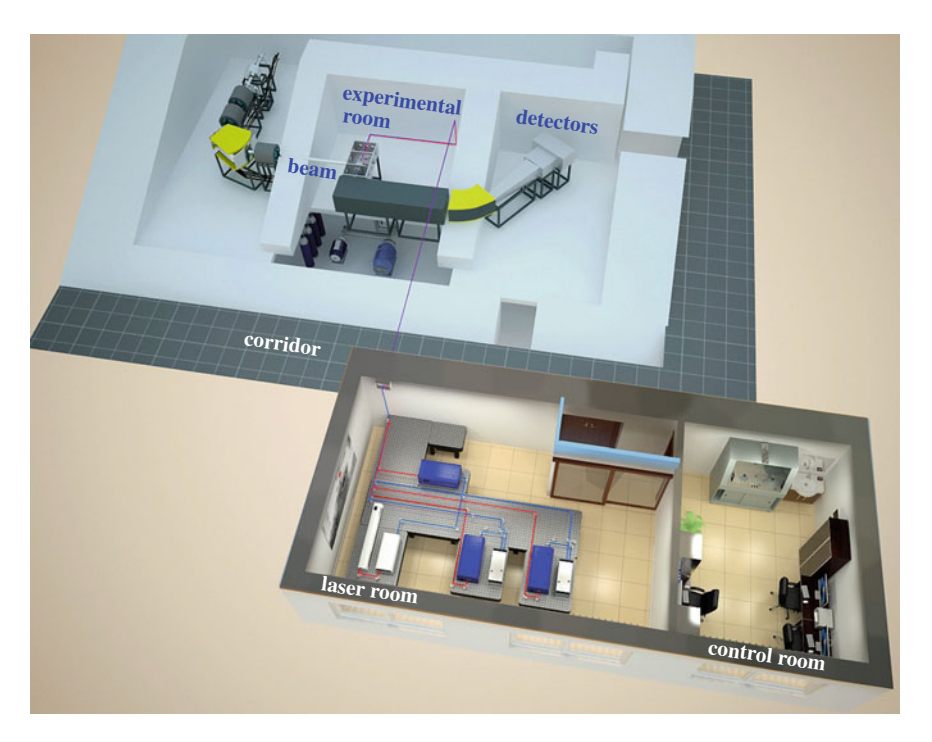


Fig. 7 3d view of the setup GaLS (Dubna) for selective laser ionization and separation of heavy transfer reaction products

as VAMOS, PRISMA and others). These fragment separators (as well as other setups) cannot distinguish heavy nuclei with Z > 70 by their atomic numbers.

However during the last several years a combined method of separation has been intensively studied based on stopping nuclei in gas and subsequent resonance laser ionization of them (see, for example, [26, 27]). The idea of such separation is very simple. All the reaction products stopping in a gas cell (at low collision energies this cell is rather small, about $10\,\mathrm{cm}$ at length) are neutralized and ejected into vacuum through a narrow nozzle. Using 3 tunable lasers, one may adjust their wavelengths in such a way that only atoms of a given element will be ionized (each element has its own electron structure and excitation energies) whereas all others remain neutral and will be pumped out from the vacuum chamber. Ionized atoms (with charge state +1) are conveyed by electric field to a small magnet where additional mass separation takes place, and the sought-for isotopes are delivered to detectors.

Setups of such kind are currently designed and installed in several nuclear laboratories. One of these setups (named GaLS: in gas cell laser ionization and separation) is created at Flerov Laboratory (JINR, Dubna) [28]. Experiments at this setup aimed on production and studying properties of new neutron-rich heavy nuclei are planned to start in 2015 (see Fig. 7). These experiments should spur intensive studies of not-yet-explored lands on the nuclear map and will have significant impact on further progress of low-energy nuclear physics.

References

- 1. V.I. Zagrebaev, A.V. Karpov, I.N. Mishustin, W. Greiner, Phys. Rev. C 84, 044617 (2011)
- E.K. Hulet, R.W. Lougheed, J.F. Wild, J.H. Landrum, P.C. Stevenson, A. Ghiorso, J.M. Nitschke, R.J. Otto, D.J. Morrissey, P.A. Baisden, B.F. Gavin, D. Lee, R.J. Silva, M.M. Fowler, G.T. Seaborg, Phys. Rev. Lett. 39, 385 (1977)
- 3. H. Essel, K. Hartel, W. Henning, P. Kienle, H.J. Körner, K.E. Rehm, P. Sperr, W. Wagner, H. Spieler, Z. Physik A 289, 265 (1979)
- 4. H. Freiesleben, K.D. Hildenbrand, F. Pühlhofer, W.F.W. Scneider, R. Bock, D.V. Harrach, H.J. Specht, Z. Phys. A **292**, 171 (1979)
- M. Schädel, W. Brüchle, H. Gäggeler, J.V. Kratz, K. Sümmerer, G. Wirth, G. Herrmann, R. Stakemann, G. Tittel, N. Trautmann, J.M. Nitschke, E.K. Hulet, R.W. Lougheed, R.L. Hahn, R.L. Ferguson, Phys. Rev. Lett. 48, 852 (1982)
- K.J. Moody, D. Lee, R.B. Welch, K.E. Gregorich, G.T. Seaborg, R.W. Lougheed, E.K. Hulet, Phys. Rev. C 33, 1315 (1986)
- R.B. Welch, K.J. Moody, K.E. Gregorich, D. Lee, G.T. Seaborg, R.W. Lougheed, E.K. Hulet, Phys. Rev. C 35, 204 (1987)
- 8. M.G. Itkis, J. Äystö, S. Beghini et al., Nucl. Phys. A **734**, 136 (2004)
- 9. V. Zagrebaev, W. Greiner, J. Phys. G 34, 2265 (2007)
- 10. W. Nörenberg, Phys. Lett. B 52, 289 (1974)
- 11. L.G. Moretto, J.S. Sventek, Phys. Lett. B 58, 26 (1975)
- 12. P. Fröbrich, S.Y. Xu, Nucl. Phys. A **477**, 143 (1988)
- 13. E. Vigezzi, A. Winther, Ann. Phys. (N.Y.) 192, 432 (1989)
- 14. V.I. Zagrebaev, Ann. Phys. (N.Y.) 197, 33 (1990)
- 15. A. Winther, Nucl. Phys. A 594, 203 (1995)
- 16. V.I. Zagrebaev, V.V. Samarin, W. Greiner, Phys. Rev. C 75, 035809 (2007)

- 17. C. Simenel, A. Wakhle, B. Avez, J. Phys.: Conf. Ser. 20, 012118 (2013)
- 18. J. Maruhn, W. Greiner, Z. Phys. 251, 431 (1972)
- 19. V. Zagrebaev, W. Greiner, J. Phys. G 31, 825 (2005)
- 20. V. Zagrebaev, W. Greiner, J. Phys. G 34, 1 (2007)
- V. Zagrebaev, A. Karpov, Y. Aritomo, M. Naumenko, W. Greiner, Phys. Part. Nucl. 38, 469 (2007)
- A. Gobbi, U. Lynen, A. Olmi, G. Rudolf, H. Sann, in *Proceedings of International School of Physics "Enrico Fermi"*, Course LXXVII, Varenna, 1979 (North-Holland. Amsterdam, 1981)
- 23. http://personalpages.to.infn.it/nanni/grazing/, http://nrv.jinr.ru/nrv/webnrv/grazing/
- 24. V. Zagrebaev, W. Greiner, Phys. Rev. Lett. 101, 122701 (2008)
- 25. V.I. Zagrebaev, W. Greiner, Phys. Rev. C 83, 044618 (2011)
- Yu. Kudryavtsev, T.E. Cocolios, J. Gentens, M. Huyse, O. Ivanov, D. Pauwels, T. Sonoda,
 P. Van den Bergh, P. Van Duppen, Nucl. Instr. Meth. Phys. Res. B267, 2908 (2009)
- S. Rothe, B.A. Marsh, C. Mattolat, V.N. Fedosseev, K. Wendt, J. Phys.: Conf. Ser. 312, 052020 (2011)
- V.I. Zagrebaev, S.G. Zemlyanoy, E.M. Kozulin, Yu. Kudryavtsev, V. Fedosseev, R. Bark, H.A. Othman, Hyperfine Interact. 216, 109 (2013)

Superheavy Element Chemistry

Robert Eichler

Abstract In this chapter dedicated to the 70th anniversary of Professor Mikhail Grigorievich Itkis the achievements and prospective in the field of the chemistry of superheavy elements are covered with emphasis on the results obtained by the collaboration of the Paul Scherrer Institute, Villigen, Switzerland with the Flerov Laboratory for Nuclear Reactions, Dubna, Russia. The status of chemical research with elements Cn and Fl is presented. From the obtained first results interesting scientific questions are deduced and discussed together with some crucial technical developments required to experimentally address these questions in the future.

1 Introduction

The chemical investigation of superheavy elements (SHE) is still a challenging task at the forefronts of nuclear and physical chemistry (for extensive review see [1]). The fundamental interest in this task is mainly formulated by theoretical chemists trying to predict chemical properties at the edges of the periodic table of elements as a benchmark region for the current theoretical understanding of atomic properties and chemical bonds. These exact descriptive and predictive calculations of thermodynamic quantities are complicated by the increasingly strong influence of the high nuclear charge, i.e. atomic number Z, of the heaviest elements on the electronic structure of the atoms. Einstein's principles of relativity directly and indirectly induce changes in the electronic properties of atoms and molecules [1–4]. Therefore, the strict consideration of these so-called relativistic effects is absolutely fundamental in correctly describing chemical processes already for much lighter elements than the SHE.

Theoretical models describing relativistic effects are under permanent development seeking for experimental benchmark data. Here, nuclear chemistry comes into play. SHE are artificially produced in heavy-ion-induced nuclear fusion reactions. Considering state-of-the-art accelerators and available target technology the maximum production rates allow the production of SHE on a one-atom-at-a-time

scale only. Hence, highly sensitive chemical methods have to be developed for their chemical investigation. The single atomic or molecular state is further complicating the practical requirements to the experimental methods applied. The atom has to be given the chance to change between chemical states as often as possible to observe it with a statistical significance in one preferred chemical state. Thus, the number of possible chemical states should be low (two in the best case) for a sensitive assessment of thermodynamic or thermochemical data from the observation. Furthermore, the chemical states should be at certain experimental conditions stable and known to the experimentalists. Here, the advantages of chromatographic methods are obvious. Especially, gas phase adsorption chromatography has proven to be very successful for the chemical identification of SHE (see for review [1, 5]). The advantage of gas phase chemistry methods is based on the speed of the method and on the fast on-line preparation methods of ideal samples for the unambiguous identification of single atoms of SHE based on the measurement of alpha decay chains mostly connected to a final spontaneous fission decay and correlated in time and energy. The In situ Volatilization and On-line technique (IVO) [6] in combination with Cryo-On-Line Detector (COLD) [7] developed for on-line adsorption thermochromatographic experiments with volatile SHE species is the currently most sensitive experimental approach reaching experimental sensitivities in the sub-pico-barn region.

The observation of significantly increased production rates for isotopes of SHE in the nuclear fusion of ⁴⁸Ca with actinide targets at FLNR Dubna in the last 15 years (1999–2014) [8, 9] was quite surprising for the entire scientific community working in the field of SHE. The determined stunning half-lives of several seconds reported for Cn and Fl isotopes paved the way towards first chemical identification experiments. Copernicium is a member of group 12 of the periodic table, together with the elements zinc, cadmium, and mercury. The electronic structure of these elements and thus, their chemical properties are subject to strong influences by the increasingly high nuclear charge Z. Further, modern relativistic theory suggests strongest relativistic effects for the valence electron shell of Rg and Cn within the seventh row of the periodic table [10, 11]. Even more, the relativistic stabilization of 7 s and $7p_{1/2}$ orbitals was predicted to lead to a chemically inert behavior of Cn and Fl similar to noble gases [12]. Other predictions based on semi-empirical extrapolations summarized in [1] and density functional theory [13] predicted a metallic behavior for both elements. Already in 1980 gas phase investigation possibilities were suggested for Cn and Fl, able to distinguish a rather noble-gas like from a noble-metal like behavior [14]. The measurement of the adsorption interaction of elemental atomic Cn and Fl with noble metal surfaces was proposed. The large difference in the interaction potential between a metal adsorption bond and a physisoption interaction was expected to reveal first chemical properties of both elements. However, these suggestions have been made in support of the so far unsuccessful search for SHE in nature.

The suggested principles were taken up by our group and transformed into most sensitive experimental devices to investigate first chemical properties for Cn and Fl [15–17]. Here, a short description of the experimental technique applying the gas adsorption thermochromatography will be given followed by a discussion of the results.

2 The Chemical Investigation of Elements Cn and Fl

2.1 Element Copernicium (Cn, Element 112)

The most efficient production path of element Cn leads over the heavy ion induced nuclear fusion of ^{48}Ca with Pu targets [8]. Hereby, the most long-lived isotopes $^{283}\text{Cn}(T_{1/2}=4\,\text{s})$ and ^{285}Cn ($T_{1/2}=29\,\text{s})$ are produced using as targets material the quite rare and expensive highly enriched isotopes of ^{242}Pu and ^{244}Pu , respectively, in amounts of several milligrams. The primarily produced flerovium isotopes $^{287}\text{Fl}(T_{1/2}=0.5\,\text{s})$ and $^{289}\text{Fl}(T_{1/2}=2.5\,\text{s})$ are expected to decay during the transport time of the species from the production place to the experimental setup. Figure 1 depicts the working principle of the chemical identification device used.

For the chemistry experiments described here, nuclear reaction products recoil from the target of typically 1–2 mg/cm² thickness with the momentum of the beam particles, pass through the target backing which is typically 2 µm Ti thin foil and are finally thermalized in a gas stream of highly purified noble gases (e.g. mixtures of He and Ar). Subsequently, they are flushed through a quartz wool filter held at 1150 K for removing beam sputtering induced aerosol particles from the gas, and through a 3–4 m long PFA Teflon® capillary. Thus, after these separation steps only volatile products end up in the COLD device consisting of an array of sandwiched silicon detectors covered with thin layers of gold and forming thus a rectangular chromatography column sensitive to the decay of radioactive species deposited in the column or decaying in-flight. The gas phase is looped back to the target area

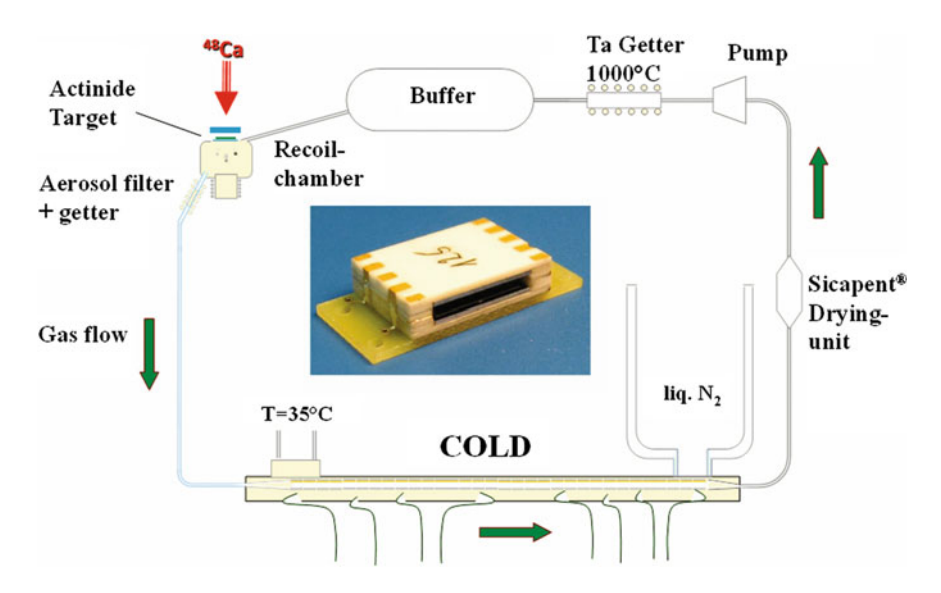


Fig. 1 Principal schematic of the experiments with Cn and Fl adopted from [15]

R. Eichler

through a dedicated helium purification line by a He-tight metal bellows pump. The gas flow is exactly monitored by a mass flow meter.

Along the COLD detector array a temperature gradient of about 5–7 K/cm is applied established by heat conductance between a thermostate-based heating device at the entrance of the chromatography channel and a liquid-nitrogen based cooling device at the exit. This gradient ranges typically from ambient temperatures down to 90 K. The volatile species are retained on the surface at temperatures characteristic for their adsorption interaction with the stationary detector surface. Typically the experiment has to work in a stable and reproducible way for several weeks. The result of the experiment is the thermochromatogram which shows the distribution of identified species along the temperature gradient applied to the stationary chromatography phase. Figure 2 shows the distribution of all observed Cn atoms deposited in COLD in experimental campaigns between 2006 and 2007. They show a reproducible and stable chemical behavior, that can be perfectly reproduced by

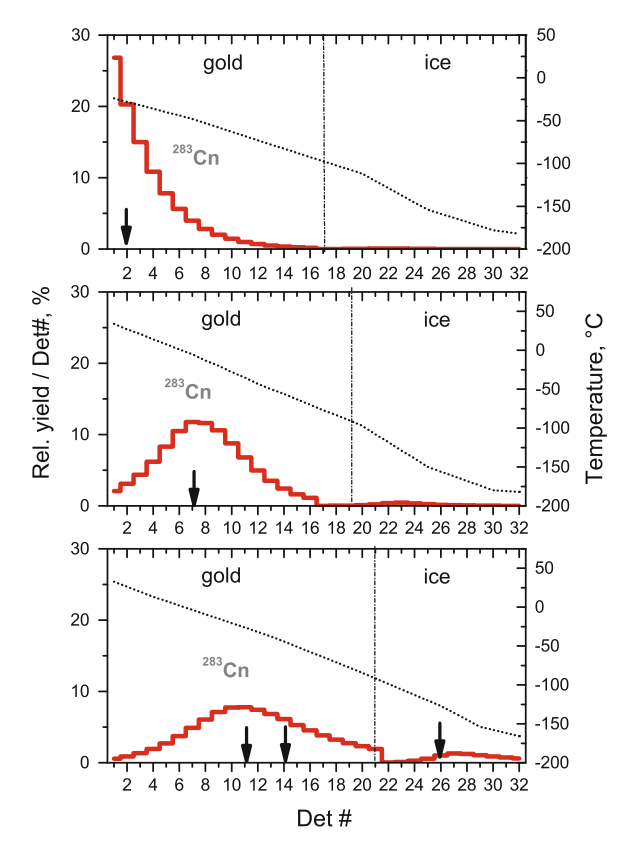


Fig. 2 Observed events of ²⁸³Cn at three different experimental conditions compared to Monte-Carlo simulations considering the given experimental conditions using as $-\Delta H_{\rm ads}^{298}$ _{Au}(Cn) = 52 kJ/mol adopted from [16]

Monte-Carlo simulations (Fig. 2, red lines) of the microscopic adsorption chromatographic process suggested in [18, 19] and further explained in [1]. The observed distribution pattern at the varied experimental conditions allowed to determine the first thermodynamic quantity ever measured for copernicium its standard adsorption enthalpy on gold as $-\Delta H_{\rm ads}^{298}_{\rm Au}(\rm Cn) = 52 \pm 2\,\rm kJ/mol$ [15, 16]. The chemical results were recently confirmed in another experiment with the COLD device using mixed 242,244 Pu targets (see Figs. 3 and 4). Another independent experiment fully confirmed the observation [20].

Hence, this value can be compared directly with the best predictions based on relativistic density functional theory which suggest $-\Delta H_{\rm ads}^{298}_{\rm Au}({\rm Cn})=0.67\,{\rm eV}$ (65 kJ/mol) [13] and $-\Delta H_{\rm ads}^{298}_{\rm Au}({\rm Cn})=0.46\,{\rm eV}$ (44 kJ/mol) [21]. Note here, despite the careful cleaning procedure of the carrier gas the COLD array was covered with ice beginning at temperatures below 95–100 °C. This temperature was assessed by measuring the dew point of the carrier gas. The ice did not influence the deposition behavior of Cn at temperatures below this dew point. However, the depositions on detectors with numbers larger than 20 have to be considered as depositions on ice surfaces.

Properties of macroscopic phases of transactinides cannot be assessed experimentally. Therefore, in [22] an empirical correlation was established between the

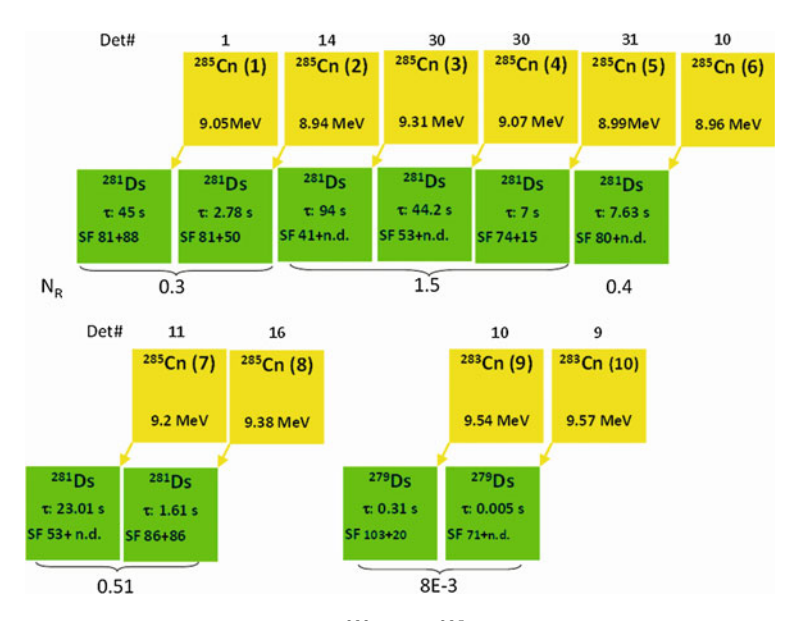


Fig. 3 Decay chains related to the isotopes 283 Cn and 285 Cn observed in the most recent experiment using 242,244 Pu mixed targets and the COLD device. NR are the number of expected random correlations for the observed chain or the group of detected chains, respectively. This transfers into about three of the eight observed 285 Cn being of random origin, whereas the observed 283 Cn (chains 8 and 9) are very safe. *Det* represents the detector number and τ is the lifetime of the decay daughter. The decay energies are given in MeV

R. Eichler

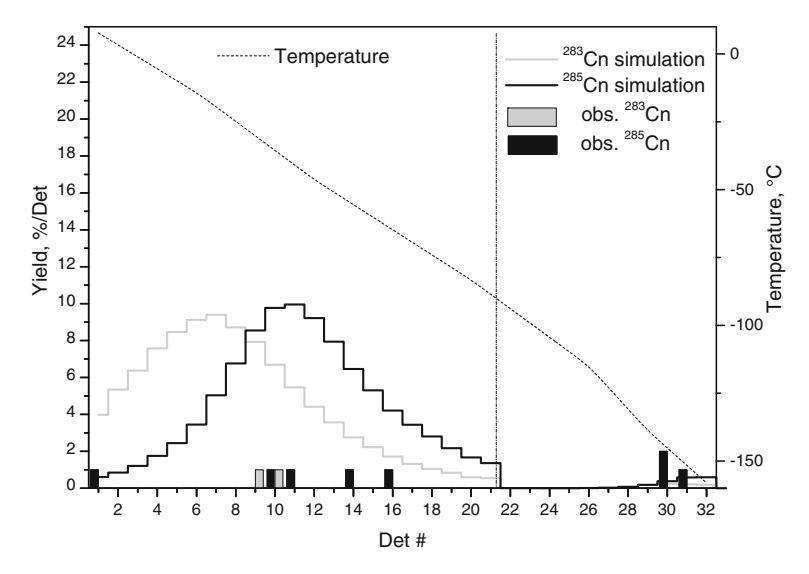


Fig. 4 Thermochromatographic distribution of the recently observed events of 283 Cn and 285 Cn together with Monte-Carlo simulations considering the given experimental conditions using as $-\Delta H_{ads}^{298}_{Au}(Cn) = 52 \, kJ/mol$. Note that 285 Cn has about a factor of seven longer half-life compared to 283 Cn and thus participates longer in the chromatographic transport. Thus its deposition is moved towards lower temperatures as expected by the Monte-Carlo simulation

experimentally assessable microscopic quantity $-\Delta H_{\rm ads}^{298}$ _{Au} and a macroscopic standard thermodynamic value related to the volatility of the solid phase—the stan-

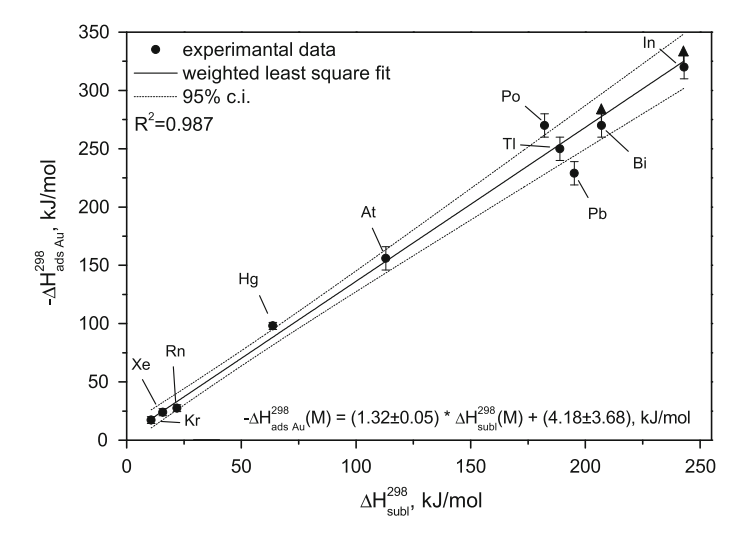


Fig. 5 Empirical correlation between the microscopic property adsorption enthalpy on gold and the macroscopic elemental volatility expressed as the standard sublimation enthalpy updated from [1, 22]

dard sublimation enthalpy $\Delta H_{\rm subl}^{298}$ for a variety of elements. This correlation is updated here with the most recently measured data for the adsorption of single atomic species on gold [23–26] and is shown in Fig. 5.

Thus, the most up-to-date estimation of the macroscopic volatility of a hypothetical solid phase of copernicium is deduced from this correlation as $\Delta H_{\rm subl}^{298}({\rm Cn})=36\pm10\,{\rm kJ/mol}$. A comparison with the most recent predictions shows, that solid state calculations of cohesive energies [27] seem to severely underestimate the volatility and overestimate the solid state binding of copernicium with $E_{\rm coh}=1.13\,{\rm eV}$ (109 kJ/mol) by almost a factor of three. Modern relativistic calculations based on density functional theory calculate atomic properties for copernicium such as radii, ionization potentials, and polarizability [10, 13, 28]. Using these properties empirical physisorption models can be applied to estimate the expected interaction of a hypothetical inert-gas like copernicium with gold as $-\Delta H_{\rm ads}^{298}{}_{\rm Au}({\rm Cn})^{\rm inert}=30\pm5\,{\rm kJ/mol}$ [29]. The straight forward comparison of this value to the experimentally determined adsorption enthalpy allows already for the qualitative statement, that metal bonding must be partially involved in the interaction of Cn with gold, despite of Cn being a very volatile element. The trends established in group 12 of the periodic table are preserved [16] as already suggested in 1976 [30].

2.2 Element Flerovium (Fl, Element 114)

As stated above the production of Cn over the decay of Fl isotopes promised larger production rates compared to its direct production in the nuclear fusion of 48 Ca with 238 U [8, 31, 32]. Hence, this production path was used in the experiments with Cn. As a full surprise the gas phase transport was observed also for the primarily produced isotopes of element flerovium simultaneously with its alpha-decay product Cn [17]. In the first experimental campaign 242 Pu was used as a target. Thus 287 Fl($T_{1/2} = 0.5$ s) was the primary fusion reaction product. Indeed, a decay event identical with the decay characteristics of this isotope reported in [8] was observed in the COLD array. Subsequently, switching to the use of 244 Pu as target material promised the production of even more long-lived flerovium isotopes 288 Fl($T_{1/2} = 0.8$ s) and 289 Fl($T_{1/2} = 2.5$ s). Thus, it was possible to confirm the initial observation [17, 33]. Figure 6 depicts the thermochromatograms obtained for flerovium adsorption on gold surfaces. It can be seen, that the deposition temperature is very close to the starting deposition of ice. However, the flerovium atoms had to pass the gold surface down to temperatures of 180 K, which already points towards a very weak interaction of flerovium with gold.

Using the same statistical approach for the directly observed flerovium atoms as it was used for the Cn data evaluation the adsorption enthalpy of flerovium on gold could be determined as $-\Delta H_{\rm ads}^{298} A_{\rm u}({\rm Fl}) = 38^{+20}_{-3} \,{\rm kJ/mol}$. This compares again to the best predictions based on relativistic density functional theory which suggest $-\Delta H_{\rm ads}^{298} A_{\rm u}({\rm Fl}) = 0.71 \,{\rm eV}$ (69 kJ/mol) [13] and $-\Delta H_{\rm ads}^{298} A_{\rm u}({\rm Fl}) = 0.55 \,{\rm eV}$ (53 kJ/mol) [34]. The further evaluation of the volatility of flerovium using the relation depicted in Fig. 5 leads to a standard sublimation enthalpy of $\Delta H_{\rm subl}^{298}({\rm Fl}) =$

40 R. Eichler

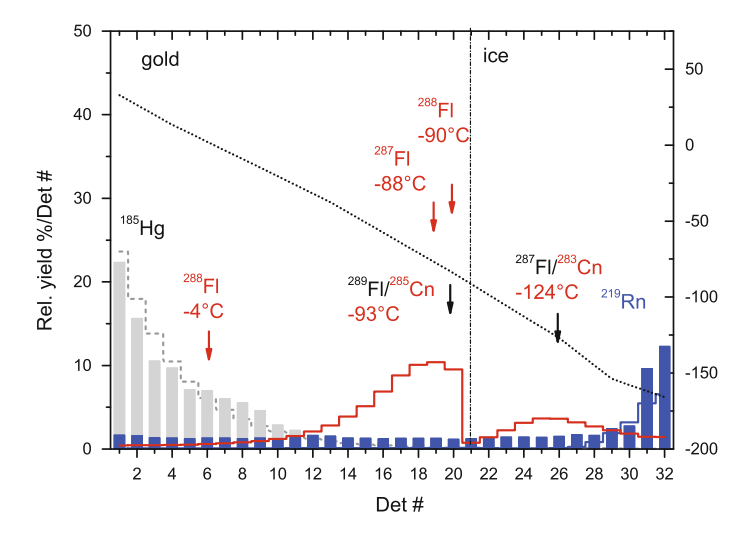


Fig. 6 Thermochromatogram of the events related to 287 Fl and 288 Fl ($red\ arrows$) together with events that support the observations, but where the observation of the first Fl alpha decay was missed ($black\ arrows$). For comparison the deposition of 185 Hg and 219 Rn are shown. The $stepped\ lines$ represent Monte-Carlo simulations for the applied experimental conditions with $-\Delta H_{ads}^{298}_{Au}(Hg) = 98\,kJ/mol\ (grey)$, as $-\Delta H_{ads}^{298}_{Au}(Fl) = 38\,kJ/mol\ (red)$, and as $-\Delta H_{ads}^{298}_{Au}(Rn) = 19\,kJ/mol\ (blue)$

 $25^{+22}_{-10}\,\mathrm{kJ/mol}$. The best available theoretical prediction of the cohesive energy of flerovium is $E_{coh}=0.5\,\mathrm{eV}$ (48 kJ/mol) [35]. Again atomic properties are probably the best estimated properties for the superheavy elements [21, 36, 37]. Thus, using empirical physisorption models $-\Delta H_{ads}^{298}_{Au}(\mathrm{Fl}_{inert})=42\pm5\,\mathrm{kJ/mol}$ was estimated for a noble-gas like flerovium [29]. A direct comparison to the results of the measurements indicates that the suggestion from Pitzer [12] for flerovium behaving as a noble gas was quite adequate. We note here also the recent observation of two decays attributed to flerovium atoms depositing at room temperature in the thermochromatography detector COMPACT [20] that seem to question this interpretation. Hence, we conclude that more data is needed in the future to assess the quite surprising but truly interesting behavior of atomic flerovium.

2.3 Chemical Systems for the Future Investigation of SHE

The chemistry of superheavy elements is full of surprises, as we have learned in the first investigations of copernicium and flerovium. Hence, chemists have to search for chemical systems, where the influence of relativistic effects is expressed in an even more pronounced way. Elements flerovium and copernicium represent an exciting couple since they can be produced simultaneously and their properties can be directly compared with each other. A look into the thermodynamic data available for

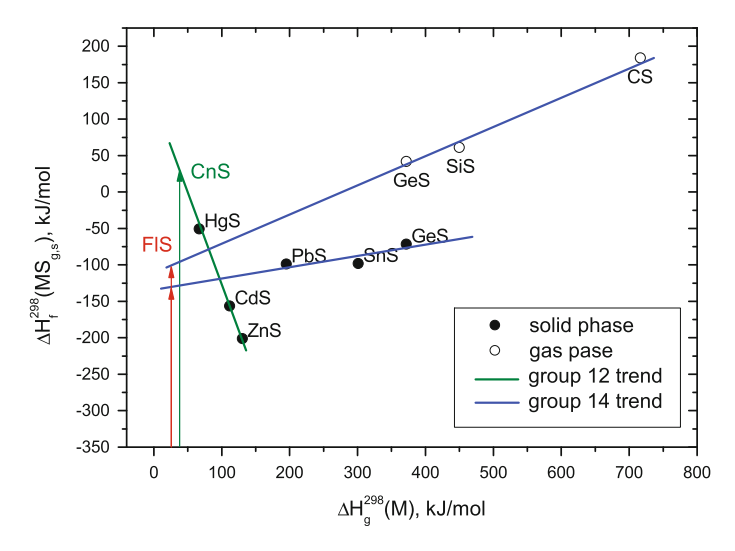


Fig. 7 Mutual correlation of thermodynamic state functions [38] for the monosulphides of the elements of groups 12 and 14 of the periodic table. Correlated are the standard formation enthalpies of the corresponding compounds in the gas phase or solid phase with the standard enthalpy of the formation of monoatomic gaseous elements (i.e. standard sublimation enthalpies)

compounds of group 12 and 14 [38] reveals interesting chemical systems. Mutual correlations of thermodynamic state functions of the elements and their compounds are used to depict chemical trends established by the periodic table [1]. One of the most interesting cases are the compounds with the heavier chalcogenes in group 16, such as sulfur (see, e.g., Fig. 7). Here, a trend reversal is observed leading to more stable sulfides of Fl compared to less stable sulfides suggested for Cn. The hydride case is for group 12 and 14 theoretically well assessed [4]. However, gas phase experiments do not seem possible because of the low thermal stability of these compounds. The recent observation of in-situ hydride formation for Bi and Po as exciting side effects of the superheavy element experiments [39] suggests this compound class for future gas phase chemistry experiments with elements 115 and 116 aside from their elemental state.

2.4 Technical Developments for the Future Investigation of SHE

The main challenge of future chemical investigations of SHE represent their short half-lives and their low production rates. The production rates can be influenced by the intensity of the heavy ion beam and in a limited way by the thicknesses of the target materials. The current developments of heavy ion sources and new accelerators promise a 10-fold increase of beam intensity up to $10-15\,\mathrm{p}\mu\mathrm{A}^{48}\mathrm{Ca}$ in the near future. So far actinide oxide based targets electrochemically deposited onto thin titanium or

42 R. Eichler

beryllium backing foils have been used. These targets stand if used in a stationary way as discussed above beam intensities up to 1 pµA. Rotating targets were recently shown to stand maximum beam pulses of 4 puA [20]. Thus, it becomes obvious that new types of targets have to be developed which are able to stand the promised intense heavy ion beams. Recently, we suggested and successfully experimentally introduced targets based on intermetallic compounds of actinides with palladium [40, 41]. These targets showed clearly a better thermal, chemical, and mechanical stability upon irradiation with intense beams of ⁴⁸Ca. If used as rotating targets further developments on the basis of intermetallic rhodium compounds with actinides may solve the problem for the future production of SHE for chemistry experiments. Regarding the short half-lives of the heavier SHE, gas phase chemical systems based on standard gas-jets have reached their current limits with assessing ²⁸⁸Fl with a half-life of about 0.5 s. Therefore, setups based on vacuum chromatographic techniques are under development [42, 43]. The use of vacuum for adsorption chromatographic studies of elemental states of SHE has some advantages: The rapidity of the transport; the high quality particle spectroscopy; the cleanliness and stability of chromatographic surfaces. This method shall allow assessing the millisecond time domain for future chemical experiments with SHE also performed at the SHE Factory built at the Flerov Laboratory of Nuclear Reactions of the Joint Institute for Nuclear Research (JINR) Dubna.

Acknowledgments We thank the staff of the U-400 cyclotron for providing intense beams of ⁴⁸Ca. The ²⁴²Pu target material was provided by RFNC-VNIIEF, Sarov, Russia. The ²⁴⁴Pu target material was provided by the U.S. DOE through ORNL, Oak Ridge, USA. This work was supported in part by the Russian Foundation for Basic Research and by the Swiss National Science Foundation. The author is grateful to Mikhail G. Itkis for the fruitful discussions and permanent support of the SHE chemistry field.

References

- M. Schädel, D. Shaugnessy (eds.), The Chemistry of Superheavy Elements (Springer, Heidelberg, 2014)
- 2. P. Pyykkä, J.-P. Desclaux, Acc. Chem. Res. 12, 276–281 (1979)
- 3. B. Fricke, Struct. Bond. 21, 90–144 (1975)
- P. Schwerdtfeger (ed.), Theoretical and Computational Chemistry, vol. 14 (Elsevier, Amsterdam, 2004)
- 5. A. Türler, V. Pershina, Chem. Rev. **113**(2), 1237–1312 (2014)
- 6. ChE Düllmann et al., Nucl. Instrum. Meth. A **479**, 631–639 (2002)
- 7. S. Soverna, Radiochim. Acta 93, 1-8 (2005)
- 8. Yu.Ts. Oganessian, J. Phys. G **34**, R165-RR242 (2007)
- 9. Yu.Ts. Oganessian et al., . Phys. Rev. Lett. 104, 142502 (2010)
- 10. E. Eliav, U. Kaldor, Y. Ishikawa, Phys. Rev. A 52, 2765–2769 (1995)
- 11. P. Schwerdtfeger, Heteroatom Chem. **13**(6), 578–584 (2002)
- 12. K.S. Pitzer, J. Chem. Phys. 63(2), 1032 (1975)
- 13. V. Pershina, Radiochim. Acta **99**, 459–476 (2011)
- 14. B. Eichler, T. Reetz, Kernenergie **25**(5), 218–221 (1980)
- 15. R. Eichler et al., Nature **447**, 72–75 (2007)

- 16. R. Eichler et al., Angew. Chem. Int. Ed. 47, 3262-3266 (2008)
- 17. R. Eichler et al., Radiochim. Acta 98, 133-139 (2010)
- 18. I. Zvara, Radiochim. Acta 38, 95–101 (1985)
- 19. I. Zvara, The Inorganic Radiochemistry of Heavy Elements, Methods for Studying Gaseous Compounds (Springer, Heidelberg, 2008)
- 20. A. Yakushev et al., Inorg. Chem. 53, 1624-1629 (2014)
- 21. V. Pershina, at al., J. Chem. Phys. 131, 084713 (2009)
- 22. R. Eichler, Radiochim. Acta 93, 245 (2005)
- 23. A. Serov et al., Radiochim. Acta 99, 593–599 (2011)
- 24. A. Serov et al., Radiochim. Acta 99, 95–100 (2011)
- 25. A. Serov et al., Radiochim. Acta 101, 421-426 (2013)
- 26. E. Maugeri, Radiochim. Acta submitted (2014)
- 27. N. Gaston et al., Angew. Chem. Int. Ed. 46, 1663 (2007)
- 28. V.P. Pershina et al., J. Chem. Phys. 128, 024707 (2008)
- 29. R. Eichler, M. Schädel, J. Phys. Chem. B 106, 5413–5420 (2002)
- 30. B. Eichler, Kernenergie 19, 307 (1976)
- 31. S. Hofmann et al., Eur. Phys. J. A 32, 251–260 (2007)
- 32. K. Gregorich et al., Phys. Rev. C 72, 014605 (2005)
- 33. D. Wittwer et al., Nucl. Instrum. Methods Phys. Res. B 268, 28 (2010)
- 34. A.V. Zaitsevskii et al., Russ. Chem. Rev. **78**, 1173–1181 (2009)
- 35. A. Hermann et al., Phys. Rev. B 82, 155116 (2010)
- 36. A. Landau et al., J. Chem. Phys. **114**, 2977–2980 (2001)
- 37. C.S. Nash, J. Phys. Chem. A **109**, 3493–3500 (2005)
- 38. W.M. Haynes (ed.), CRC Handbook of Chemistry and Physics, 94th edn. (CRC Press, Boca Raton, 2013)
- 39. R. Eichler, J. Phys. Conf. Ser. 420, 012003 (2013)
- 40. I. Usoltsev et al., Nucl. Instrum. Methods Phys. Res. A 691, 5–9 (2012)
- 41. I. Usoltsev et al., Nucl. Instrum. Methods Phys. Res. B 318, 297–305 (2014)
- 42. D. Wittwer et al., Radiochim. Acta 101, 211–219 (2013)
- 43. D. Wittwer et al., Nucl. Instrum. Methods Phys. Res. B 297, 86–93 (2013)

Nucleon Transfer Reactions in Very Heavy Ion Systems

H.W. Gäggeler

Abstract Nucleon transfer reactions in the 238 U + 238 U system were studied at the energies $E_{\rm eff}=6.3\,{\rm MeV/u}$, $E_{\rm eff}=6.9\,{\rm MeV/u}$, and $E_{\rm eff}=8.0\,{\rm MeV/u}$, respectively. Production of above-target nuclides point to formation of transfer products with excitation energies between 30 and 40 MeV and angular momenta of about $18\,\hbar$, independent of bombarding energy. Predictions of heavy element production rates up to lawrencium (Z=103) in the system 238 U + 248 Cm showed that yields drop sharply with increasing number of transferred protons leaving little perspective for possible future production of new neutron-rich isotopes in this reaction. However, a recent theoretical prediction claimed much higher cross sections for elements lawrencium (Z=103) and higher due to assumed increased longer sticking times of the dinuclear system.

1 Introduction

Nucleon transfer in so-called deep-inelastic reactions between very heavy ions were considered suitable for production of new heavy elements since long ago. The universal linear accelerator UNILAC at GSI started operation in the mid-1970th as first device worldwide able to accelerate all elements up to uranium to a sufficiently high energy in order to enable nuclear contact—hence enabling nuclear reactions—with all elements of the periodic table. Of highest priority were extensive search experiments for superheavy elements using the systems ²³⁸U + ²³⁸U [1] and ²³⁸U + ²⁴⁸Cm [2]. Unfortunately, all these attempts failed. However, the reached sensitivities were rather low, mostly around 1 nb to 100 pb only, depending on the assumed half-life of the superheavy nuclei. These values are about three to four orders of magnitude higher compared to actual production cross sections for heaviest elements in fusion reactions with e.g. 22 fb for the formation of element 113 in the reaction between

H.W. Gäggeler (⊠)

Paul Scherrer Institute, 5232 Villigen, Switzerland

e-mail: heinz.gaeggeler@psi.ch

H.W. Gäggeler

Department of Chemistry and Biochemistry, University of Bern, 3000 Bern, Switzerland

46 H.W. Gäggeler

⁷⁰Zn particles particles and a ²⁰⁹Bi target [3]. It was therefore recently speculated [4–7] that deep-inelastic reactions should be reconsidered as a possible tool for heaviest element synthesis applying up-to-date online separators that enable to reach sensitivities at the sub-pb level. This renewed interest was much corroborated by predicted long contact times of heavy dinuclear systems that should result in an increased probability for nucleon transfer [4–7].

One reason for renewed interest in such reactions is the well known fact that proton exchange reactions are always followed by fast charge equilibration processes. Charge equilibration proceeds along the β -stability line. As pointed out in Ref. [4] this would enable access to very neutron-rich isotopes of heaviest elements not accessible by any fusion reaction with currently available beam projectiles and target nuclei (see Fig. 1). An exception might be future use of radioactive ion beams (RIB) with very neutron-rich isotopes but prospects for such options are very limited given the still very low beam intensities accessible at RIB facilities.

In this contribution early studies of nucleon exchange reactions in the system $^{238}\text{U} + ^{238}\text{U}$ are described. Part of these experimental studies have been published recently [8] but have also been presented at a conference in the series "Nuclei far from stability" and in an internal report, both being only documented in unpublished manuscripts [9, 10].

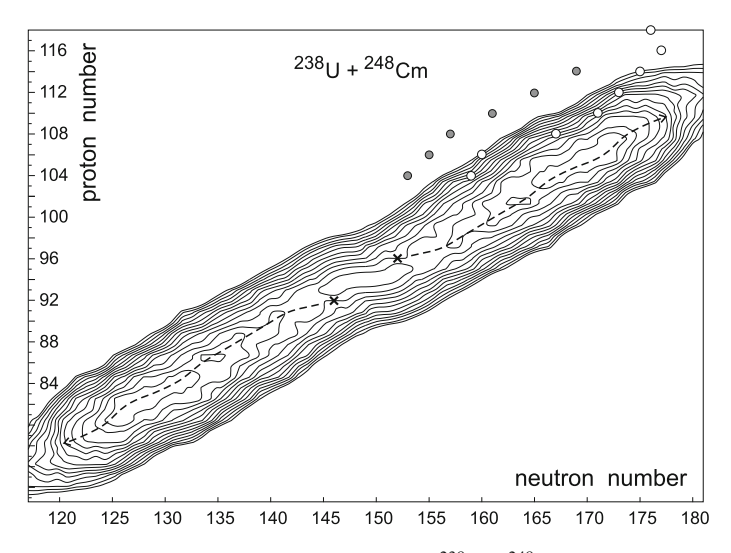
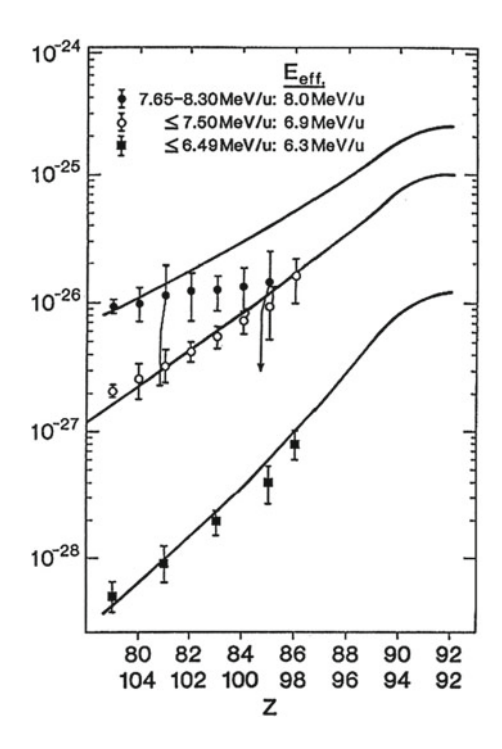


Fig. 1 Potential energy surface of the dinuclear system ²³⁸U + ²⁴⁸Cm. The *dashed line* indicates the minimum of the potential energy surface along which primary products from deep inelastic reactions are formed. The *black dots* represent nuclides formed in cold fusion reactions with Pb and Bi targets and *open circles* represent nuclides formed in ⁴⁸Ca induced fusion reactions with actinide targets (reproduced from [7])

Fig. 2 Charge distribution from the reaction ²³⁸U + ²³⁸U at three different bombarding energies (from [10]). The *solid lines* depict predicted values from [12]



2 Charge Distribution in the $^{238}\text{U} + ^{238}\text{U}$ Reaction

Yields were determined for below-target elements for the effective energies 6.3, 6.9 and 8.0 MeV/u, respectively (Fig. 2). They were deduced after chemical separation of the corresponding elements after bombardment and measurement of isotopes using radiometric techniques (see e.g. [8] and references therein). Missing isotope yields (e.g. for nuclides with too short half-lives or missing suitable decay lines for detection) were extrapolated assuming Gaussian yield distributions for isotope yields of a given element. The solid lines depicted in Fig. 2 represent calculated values based on a model from Wollersheim [11, 12]. Obviously, at the highest bombarding energy for elements with $Z \geq 82$ an increasing deviation between experimental and estimated cross section is observed. This points to an increasing loss of heavy elements caused by prompt fission due to high excitation energies.

If the yield curves depicted in Fig. 2 are extrapolated to higher values of proton transfer the extrapolated yield curve for production of the superheavy element flerovium (Fl, Z = 114) may be deduced as a function of beam energy (Fig. 3). At a first glance, the cross section values for production of Fl look promisingly high.

48 H.W. Gäggeler

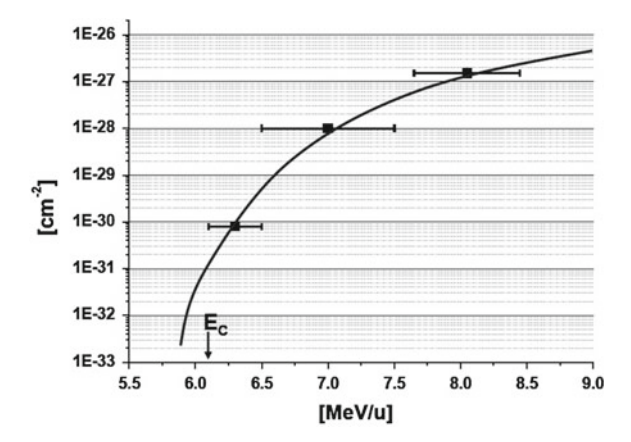


Fig. 3 Excitation function for charge split Z = 70/114 in the reaction $^{238}\text{U} + ^{238}\text{U}$. The interaction barrier is 6.13 MeV/u

3 Excitation Energies and Survival Probability

From measured isotope distributions the average number of evaporated neutrons can be deduced assuming the primary products to be centered at the minimum of the potential energy surface of the dinuclear system (see Fig. 1). An example is shown in Fig. 4 for Au (Z=79). The deviation of the maxima of the yield curves from the most probably primary mass (A'=205) increases from 7 neutrons at $E_{\rm eff}=6.3\,{\rm MeV/u}$ to 10 neutrons at $E_{\rm eff}=6.9\,{\rm MeV/u}$ and finally to 12 neutrons at $E_{\rm eff}=8.0\,{\rm MeV/u}$, respectively.

If we assume that both fragments in the binary reactions have equal temperature then the total excitation energy of a given charge split is proportional to the masses of both primary products. This allows to deduce the total kinetic energy loss (TKEL) for different charge splits. As example the resulting TKEL values for the study at $E_{\rm eff}=6.9\,{\rm MeV/u}$ are shown in Fig. 5. The solid line depicts predicted values using the above mentioned model of Wollersheim. From Figs. 4 and 5 it follows that the high values of excitation energy must heavily influence the survival probability of highly fissile products such as those of actinides and even more of transactinides.

Indeed, as an example Fig. 6 depicts cross sections of various isotopes of radon and californium from the 6p transfer in the system $^{238}\text{U} + ^{238}\text{U}$ at a bombarding energy of $E_{\text{eff}} = 8.0\,\text{MeV}$. The cross section of surviving isotopes of californium are many orders of magnitude lower compared to those of its partner, radon.

Moreover, if the data are depicted on a common x-axis which is normalized to the primary products of both elements at the minimum of the potential energy surface (see Fig. 1), it becomes evident that the average number of neutrons emitted to form surviving isotopes of californium is much lower compared to the situation for radon. We interpret this observation as evidence that surviving californium isotopes are preferentially formed in transfer reactions with excitation energies of about 30 to

Fig. 4 Cross sections (in mb) for isotopes of gold at three different bombarding energies. The *x*-axis lists the mass number of the isotopes and the *dashed vertical line* the minimum of the potential energy surface which is taken as most probable mass number for primary products. The *arrows* indicate the average number of evaporated neutrons to form surviving residues (figure taken from [10])

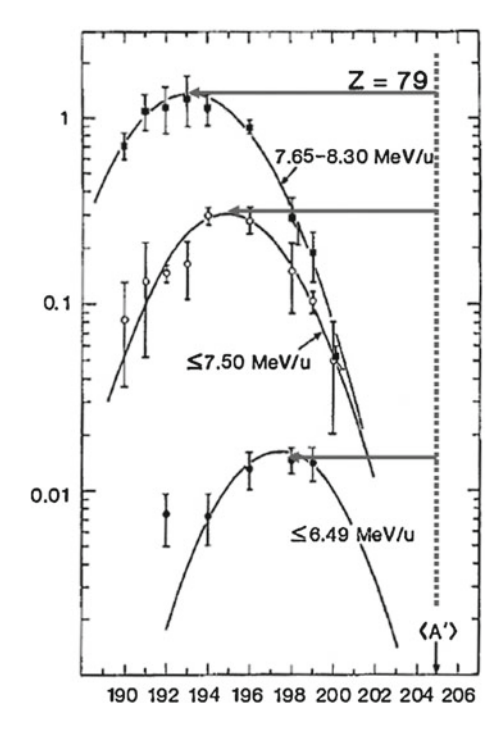
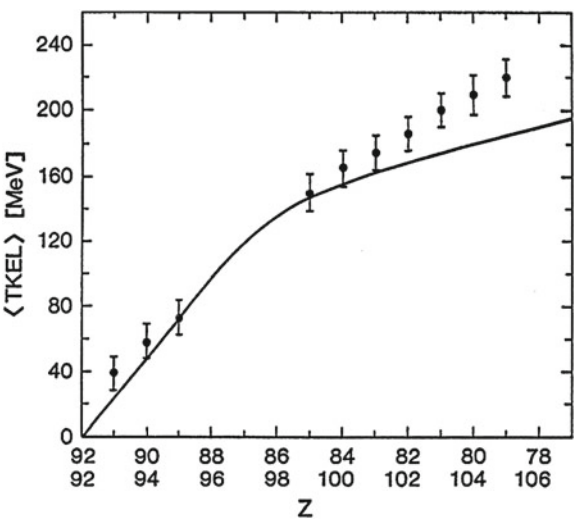


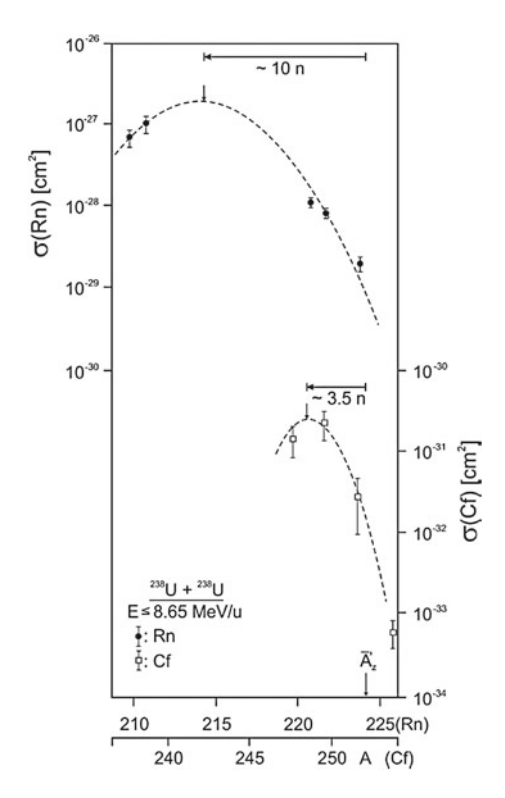
Fig. 5 Total kinetic energy loss (TKEL) values for different charge splits in the reaction 238 U + 238 U at a bombarding energy Eeff = 6.9 MeV/u. The *solid lines* depict a prediction from [12] (figure taken from [10])



40 MeV while radon isotopes are formed in reactions with much higher excitation energies. There seems to exist an energy-cut off at values below about 30 MeV that prevents transfer of 6 protons. On the other hand, californium isotopes formed with much higher excitation energies than 40 MeV obviously do not survive.

50 H.W. Gäggeler

Fig. 6 Cross sections of isotopes of radon (Z=86) and of californium (Z=98) from the transfer of six protons in the reaction 238 U + 238 U at a bombarding energy of $E_{\rm eff}=8.0\,{\rm MeV/u}$. Reproduced from [8]



The difference of cross sections between the maximum of the curve for californium (about $2 \times 10^{-31} \, \mathrm{cm}^2$) and the corresponding value at this mass split (about $10^{-28} \, \mathrm{cm}^2$) reflects an average survival probability for emission of 3.5 neutrons. This results in an average value for Γ_n/Γ_f of about 0.17, which agrees reasonable well with prediction based on the empirical Sikkeland systematics [13] with, e.g., $\Gamma_n/\Gamma_f = 0.36$ for $^{249}\mathrm{Cf}$.

In contrast to the situation for Au (see Fig. 4), the isotope distributions for actinides remain approximately identical for different beam energies. Fig. 7 underlines this observation with the experimental data for californium at four different bombarding energies. Obviously the position of the most probable mass numbers (maximum of Gaussian distribution), the width of the distributions as well as the average cross sections are only slightly influenced by the beam energy. This observation, again, is in support of the assumption that in this reaction highly fissile products such as actinides are formed with approximately 30 to 40 MeV excitation energy.

One additional aspect is angular momenta involved in deep inelastic reactions To study this aspect the ratio between the fission shape isomer $^{242\text{mf}}$ Am and its ground state 242 Am was measured in the 238 U + 238 U reaction at energies between the interaction barrier (6.13 MeV/u) and 8.6 MeV/u. This ratio turned out to be 4 × 10^{-5} , independent of bombarding energy. This surprising result is in support of the

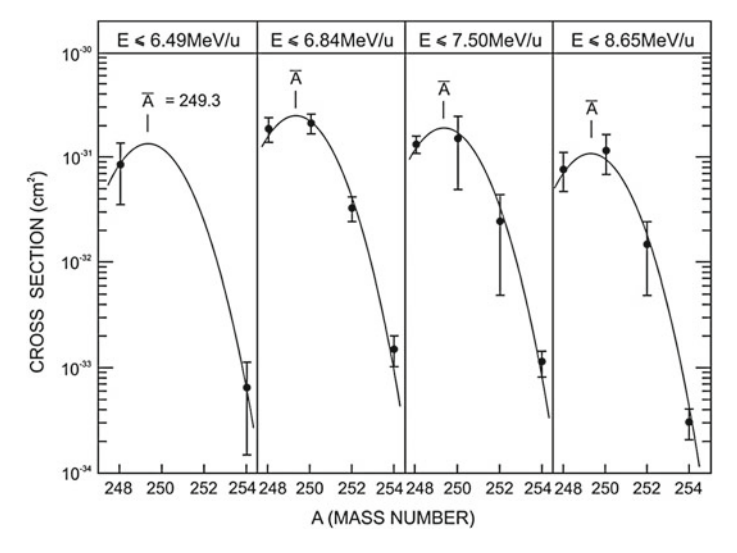


Fig. 7 Yields of isotopes of Cf from the reaction $^{238}\text{U} + ^{238}\text{U}$ at four different energies (reproduced from [8])

assumption that surviving products are formed with identical excitation energy but also angular momentum, independent of bombarding energy. The value 4×10^{-5} , however, is about one order of magnitude lower compared to measured ratios in γ -induced reactions with zero angular momenta of the products [14]. The measured value of shape isomer to ground state results in an average angular momentum of $18\,\hbar\,[9]$ and can be well explained with the cranking model [15]. The cranking model is based on single-particle energies and wave functions at a given deformation. The value of $18\,\hbar$ is in good agreement with prediction (Riedel and Nörenberg [16]) for production of actinides in the $^{238}\mathrm{U}$ + $^{238}\mathrm{U}$ reaction with excitation energies of $35\,\mathrm{MeV}$.

4 Prospects for Formation of Heavy Elements in the ²³⁸U + ²⁴⁸Cm Reaction

Measured charge distribution from the $^{238}\text{U} + ^{238}\text{U}$ reaction (Fig. 2) moved by four protons to scale to the $^{238}\text{U} + ^{248}\text{Cm}$ reaction, isotope yield distribution as shown in Fig. 4, and assuming the surviving products to be mainly formed in the 4n evaporation channel allowed to calculate production cross sections for heaviest elements (Fig. 8a). Γ_n/Γ_f values were taken from [13]. Fig. 8b shows the result of a calculation performed more recently [7].

Indeed, both predictions agree rather well up to atomic number 102 (nobelium). For the atomic number 103 (lawrencium) and above the values predicted in [7] are

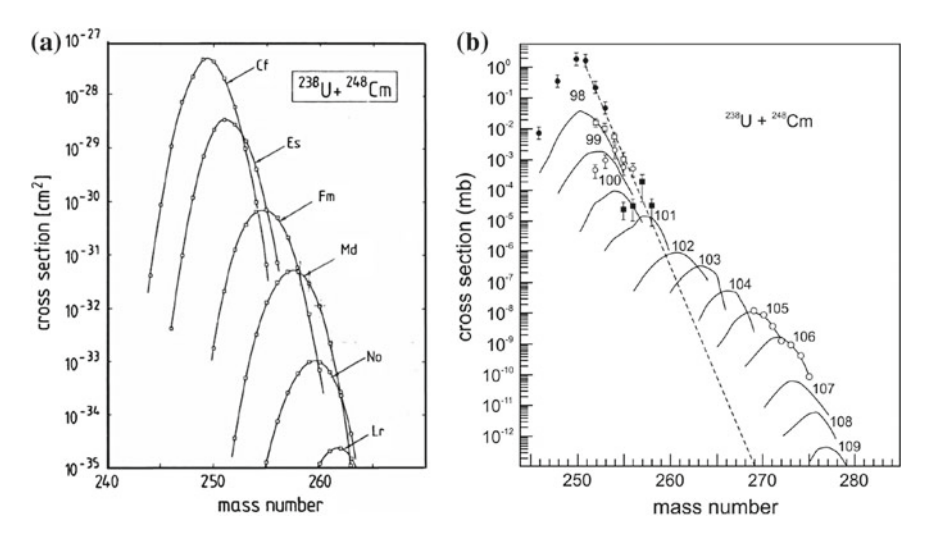


Fig. 8 a (*left*) Predicted cross sections from this work for the reaction 238 U + 248 Cm at $E_{\rm eff} = 6.9$ MeV/u (see text, from [10]). **b** (*right*) Prediction for the same system from [7]. The relative increase in cross sections compared to the general trend (*dashed line*) comes from predicted long sticking times of the dinuclear system

significantly higher compared to those depicted in Fig. 8a. This may be explained by increased sticking times of the interacting system caused by a pronounced local minimum in the potential energy surface due to shell effects of the dinuclear system at about Z=102 and the complementary product Pb [7]. Such increased sticking times were not taken into account in the predictions shown in Fig. 8a.

5 Conclusion

Analysis of formation cross sections in the reaction 238 U + 238 U allowed to conclude that very heavy elements are formed in this system with about 30 to 40 MeV excitation energy favouring the 4n evaporation channel and with 18 \hbar angular momentum. These findings were applied to the system 238 U + 248 Cm to extrapolate cross sections for isotopes of elements up to the heaviest actinide, lawrencium. Predicted cross sections drop sharply with increasing atomic number leaving little perspective for production of new nuclides in the system 238 U + 248 Cm with current accelerator technology. However, in a more recent calculation, due to predicted significantly increased sticking times caused by shell effects, the situation might be much more favourable. In the framework of this calculation it seems possible to produce some new neutron rich isotopes of elements up to about atomic number 105 (dubnium) in deep inelastic reactions in the system 238 U + 248 Cm. However, still much technological effort is needed to reach similar sensitivities (e.g. about 100 fb) with online separators dedicated to deep-inelastic reactions as has been reached with separators designed to isolate products from fusion reactions.

References

- H. Gäggeler, N. Trautmann, W. Brüchle, G. Herrmann, J.V. Kratz, P. Peuser, M. Schädel, G. Tittel, G. Wirth, H. Ahrens, H. Folger, G. Franz, K. Sümmerer, M. Zendel, Phys. Rev. Lett. 45, 1824 (1980)
- J.V. Kratz, W. Brüchle, H. Folger, H. Gäggeler, M. Schädel, K. Sümmerer, G. Wirth, N. Greulich, G. Herrmann, U. Hickmann, P. Peuser, N. Trautmann, E.K. Hulet, R.W. Lougheed, J.M. Nitschke, R.L. Ferguson, R.L. Hahn, Phys. Rev. C 33, 504 (1986)
- 3. K. Morita et al., J. Phys. Soc. Jpn. 81, 103201 (2012)
- 4. V.I. Zagrebaev, Y.T. Oganessian, M.G. Itkis, W. Greiner, Phys. Rev. C 73, 031602 (2006)
- 5. V. Zagrebaev, W. Greiner, J. Phys. G: Nucl. Part. Phys. 34, 2265 (2007)
- 6. V. Zagrebaev, W. Greiner, Nucl. Phys. A 787, 363c (2007)
- 7. V. Zagrebaev, W. Greiner, Phys. Rev. C 78, 034610 (2008)
- 8. J.V. Kratz, M. Schädel, H.W. Gäggeler, Phys. Rev. C 88, 054615 (2013)
- 9. H. Gäggeler, M. Schädel, W. Brüchle, J.V. Kratz, K. Sümmerer, G. Wirth, N. Trautmann, P. Peuser, G. Tittel, R. Stakemann, G. Herrmann, E.K. Hulet, R.W. Lougheed, J.M. Nitschke, R.L. Hahn, R.L. Ferguson, in *Proceedings of 4th International Conference on Nuclei far from Stability*, L.O. Skolen, Helsingor (Denmark), Report CERN-81-09, pp. 763–771 (unpublished). 7–13 June 1981
- H.W. Gäggeler, Reaktionsmechanismen zur Synthese schwerster Elemente aus Schwerionenreaktionen, Habilitation Thesis, ETH Zürich, PSI-Bericht Nr. unpublished (in German) 14 Oct 1988
- 11. H.J. Wollersheim, W.W. Wilcke, J.R. Birkelund, J.R. Huizenga, Phys. Rev. C 25, 338 (1982)
- 12. H.J. Wollersheim, Report GSI-84-34 (1984) (unpublished)
- 13. T. Sikkeland, A. Ghiorso, M.J. Nurmia, Phys. Rev. 172, 1232 (1968)
- V.L. Kuznetsov, E.L. Lazareva, V.G. Nezorezov, N.V. Nikitina, N.M. Parovic, Nucl. Phys. A 324, 29 (1979)
- 15. M. Brack, T. Ledergerber, H.C. Pauli, A.S. Jensen, Nucl. Phys. A 234, 185 (1974)
- 16. C. Riedel, W. Nörenberg, Z. Physik A **290**, 385 (1979)

Part II Nuclear Structure

New Insights into the Structure of Neutron-Rich Nuclei A = 108 - 118 and $^{160-162}Gd$

J.H. Hamilton, Y.X. Luo, A.V. Ramayya, J.K. Hwang, E.H. Wang, N.T. Brewer, B. Doll, S.H. Liu, J.O. Rasmussen, I.Y. Lee, S. Frauendorf, G.M. Ter-Akopian, A.V. Daniel, Y.T. Oganessian, S.J. Zhu, Y. Shi, F.R. Xu and J.C. Batchelder

Abstract The level structures of 108,110,112 Ru (Z=44) and 112,114,115,116,117,118 Pd (Z=46) have been significantly expanded through studies of prompt $\gamma-\gamma-\gamma$ and $\gamma-\gamma-\gamma-\gamma$ coincidences observed with Gammasphere following the spontaneous fission of 252 Cf. Chiral doublet bands were observed in 110,112 Ru. Softness to triaxiality perturbs the bands of 108 Ru and even-N Pd isotopes. In 112 Ru, evidence for wobbling motion is found in the behavior of the γ vibrational band. Similar evidence for wobbling motion is found in 114 Pd, the N=68 isotone of 112 Ru. A transition from triaxial prolate to triaxial oblate was found in $^{112-116}$ Pd with shape coexistent bands in 115 Pd. New levels were observed in 162,163 Gd.

1 Introduction

There is surprising richness of different collective modes in neutron-rich, A = 100 - 124 nuclei. These include:

J.H. Hamilton (\boxtimes) · Y.X. Luo · A.V. Ramayya · J.K. Hwang · E.H. Wang · N.T. Brewer ·

B. Doll · S.H. Liu

Department of Physics, Vanderbilt University, Nashville, TN 37235, USA e-mail: j.h.hamilton@vanderbilt.edu

J.O. Rasmussen · I.Y. Lee

Lawrence Berkeley National Laboratory Berkeley, Berkeley, CA 94720, USA

S. Frauendorf

Department of Physics, University of Notre Dame, Notre Dame, IN 46556, USA

G.M. Ter-Akopian · A.V. Daniel · Y.T. Oganessian

Joint Institute for Nuclear Research, 141980 Dubna, Russia

S.J. Zhu

Physics Department, Tsinghua University, Beijing 10084, China

Y. Shi · F.R. Xu

Physics Department, Peking University, Beijing 100871, China

I.C. Batchelder

Oak Ridge Associated University, Oak Ridge, TN 37830, USA

© Springer International Publishing Switzerland 2015

W. Greiner (ed.), Nuclear Physics: Present and Future,

FIAS Interdisciplinary Science Series, DOI 10.1007/978-3-319-10199-6_6

58 J.H. Hamilton et al.

(A) Super-deformed ground states from $Z=38,40\ N=60,62$ for re-enforcing shell gaps at same super-deformation

- (B) Shape coexistence, near spherical-super-deformed ¹⁰⁰Zr, ¹⁰⁰Nb; prolate-oblate ¹¹⁵Pd
- (C) Prolate-to-oblate transition $^{114}\text{Pd} \rightarrow ^{116}\text{Pd}$
- (D) One and two phonon γ vibrational bands the first in odd A and odd Z nuclei, ^{105}Mo , $^{103,105}\text{Nb}$, $^{107,109}\text{Tc}$
- (E) Transition from super-deformed axial symmetric ⁹⁹Y to triaxial ¹¹³Rh
- (F) Chiral doublet bands in triaxial nuclei, ^{110,112}Ru, ¹¹⁴Pd, ¹⁰⁶Mo
- (G) Wobbling motion of triaxial shapes, ¹¹²Ru, ¹¹⁴Pd

In this paper, we will concentrate on Ru and Pd nuclei as noted in B, C, F and G along with new data on ^{162,163}Gd.

New region centered around 108 Ru, Z=44, N=64 was predicted by Möller et al. [1] to have the largest lowering of the nuclear ground state energy when axial symmetry is broken. In our studies of 99,101 Y to 111,113 Rh we found a smooth transition from axial symmetry, essentially superdeformed 99,101 Y to well deformed β_2 approximately 0.27, maximum triaxial $\gamma=-30^0$ in 111,113 Rh. In triaxial nuclei two new types of motion were predicted. Frauendorf and co-workers [2–4] proposed that rotating triaxial nuclei can exhibit chiral behavior with a superposition of left- and right-handed symmetry. The signature of such behavior would be two sets of $\Delta I=1$ rotational bands with the same parity and degenerate in energy for the same spin. A second new behavior not seen in symmetric nuclei but triaxial nuclei is wobbling motion of their angular momentum, where there is a deviation of the axial collective motion away from the axis with the largest moment of inertia. Wobbling motion produces a series of wobbling bands with quantum numbers $n_w=0,1,2,\ldots$

We have studied the energy levels in $^{108-114}$ Ru and $^{112-118}$ Pd populated in the spontaneous fission of 252 Cf. We have found evidence for chiral bands in 112 Ru and perturbed chiral bands in 108 Ru and $^{112-116}$ Pd. In addition, we found clear evidence for wobbling bands in N = 68 112 Ru and 114 Pd. A transition from triaxial prolate to triaxial oblate shapes was found in $^{112-117}$ Pd and coexistence bands built on these two shapes were found in 115 Pd. The data revealed that it is not 108 Ru as predicted [1], but 112 Ru that is the center of a stable region of triaxial deformation [5].

Finally examples of studies of ^{162,163}Gd in both ²⁵²Cf spontaneous fission and ²³⁸U proton induced fission are presented.

2 Experimental Procedures

A 62 μ Ci source of 252 Cf was placed in Gammasphere with 101 high purity germanium detectors. A large data set with 5.7×10^{11} triple and higher-fold coincidences was obtained (see Ref. [7] for details on the experiment). The 101 detectors were subdivided into 64 angular bins for angular correlation studies [8]. Gamma-gamma angular correlation measurements were carried out to determine spins of the highest

level and transition multipolarities of transitions out of the highest levels by using as the lower transition a known E2 transition between two yrast levels, like $6^+ \rightarrow 4^+$. By determining branching ratios to the yrast levels and the multipolarities of the upper transitions, unique spins and parities were assigned to at least one level in each of the two sets of doublet bands found in 108,110,112 Ru [5, 9, 10] and 112,114,116 Pd [6]. And recently, the data were sorted into 1.1×10^{11} four and higher-fold coincidences. These data are most helpful in searching for weak transitions and weakly populated bands.

The 162,163 Eu isotopes were produced in proton-induced fission of 238 U at the Holifield Heavy Ion Research Facility and then transferred to a moving tape collector. The beams were separated with a high resolution ($\Delta m/m = 10,000$) magnet and delivered to the Low energy Radio-active Ion Beam Spectroscopy Station, LeRIBSS with four segmented clover Ge detectors and two plastic scintilators. The Gd nuclei were studied from decays of Eu activities.

3 Chiral Band Results

The finger prints of chiral doublets are (a) $\Delta I = 1$, doublet bands with the same parity and states with the same spins have very close energies; (b) nearly constant moments of inertia, (c) nearly constant signature splittings with spin and equal value for partner levels. Examples of double levels are shown for 108,112 Ru and 112,114 Pd. The details of other isotopes are found elsewhere [6, 9, 10].

From the analysis of multiple gates in each nucleus and $\gamma - \gamma(\theta)$ measurements of at least one level in each of the bands observed, the level schemes of $^{108-112}$ Ru and $^{112-118}$ Pd were established. Details are found elsewhere [6, 9, 10]. The doublet bands seen in 108,112 Ru are shown in Fig. 1 while the doublet bands in 110 Ru are found in [5, 9, 10]. As seen in Fig. 1, there is an energy staggering in bands 4, 5 in 108 Ru that is not present in 112 Ru. The doublet bands in 112 Ru have all the properties expected for chiral doublets in a rigid triaxial nucleus while 108 Ru is best described as a γ -soft nucleus with perturbed chiral bands [5]. These data indicate that 112 Ru is the center of the region with broken axial symmetry not 108 Ru as proposed by Möller et al. [1].

In our new study, $\Delta I=1$ doublet bands are now seen in 112,114,116 Pd. New level schemes for $^{112-118}$ Pd were obtained with those of 112,114 Pd shown in Fig. 2. From γ - $\gamma(\theta)$ and branching ratios, the spins and parities is at least one member of each of the four bands in each nucleus were determined. At first glance these doublet bands in 112,114 Pd look similar to those in 110,112 Ru that one would consider them as chiral doublets built on a rigid triaxial shape. However, as one examines the details of their energy level staggering, the absence of many crossing E1 transitions, and their signature splitting compared to 110,112 Ru, one sees that 112,114,116 Pd are more soft triaxial nuclei rather than rigid triaxial. This can be seen, for example, in Fig. 3 where the signature splitting for bands 4 and 5 in 110,112 Ru and $^{112-116}$ Pd are compared. As expected for rigid triaxial nuclei, the splitting is essentially zero and constant

50 J.H. Hamilton et al.

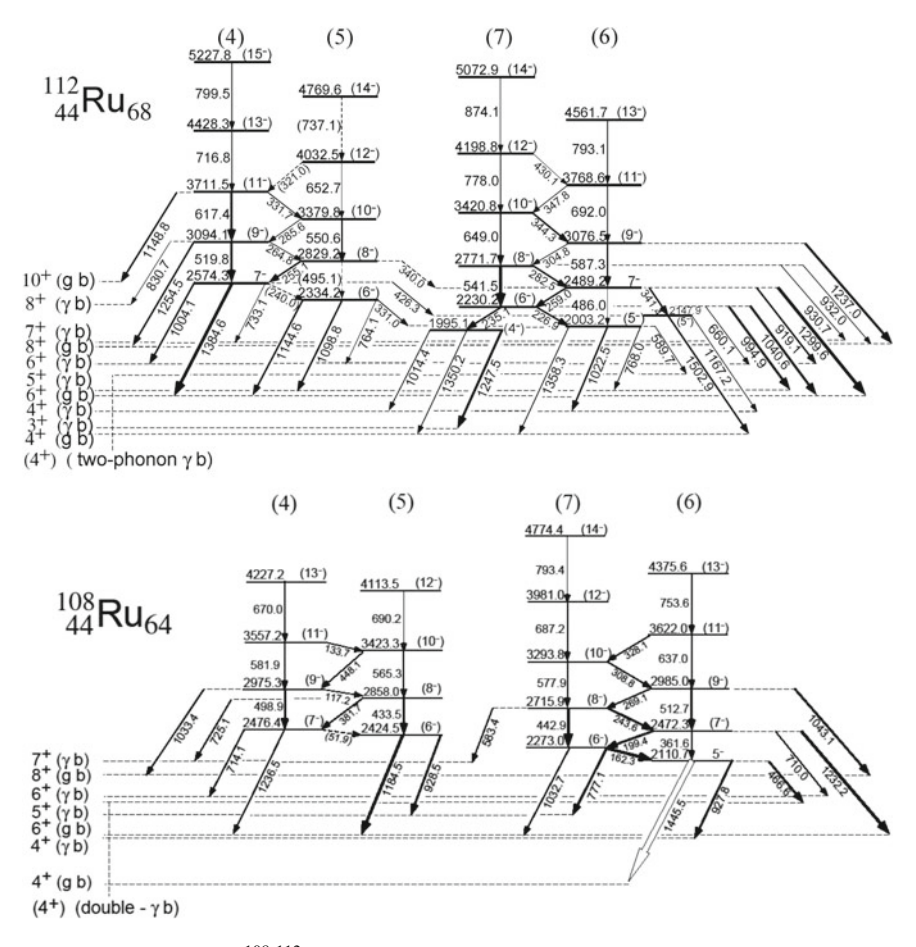


Fig. 1 Doublet bands in ^{108,112}Ru

with spin for 110,112 Ru, while there is considerable staggering in 112,114,116 Pd. Note 112,114 Pd are the N=66 and 68 isotones of 110,112 Ru, respectively. The differences between 110,112 Ru and 112,114,116 Pd can be understood by the latter having a less pronounced triaxial minimum than 110,112 Ru as predicted by Möller et al. [1]. This rigid triaxiality seen centered in 112 Ru is softened as Z increases from 44 to 46 in Pd. The soft triaxiality disturbs the structure of the chiral doublets.

4 Wobbling Motions in ¹¹²Ru and ¹¹⁴Pd

The wobbling excitations in a triaxial nucleus constitute a revolving motion of J about an axis of the triaxial nucleus. Such wobbling motions were first identified in 161,163,165,167 Lu [11–14] and 167 Ta [15, 16] at high spin. Wobbling excitations in

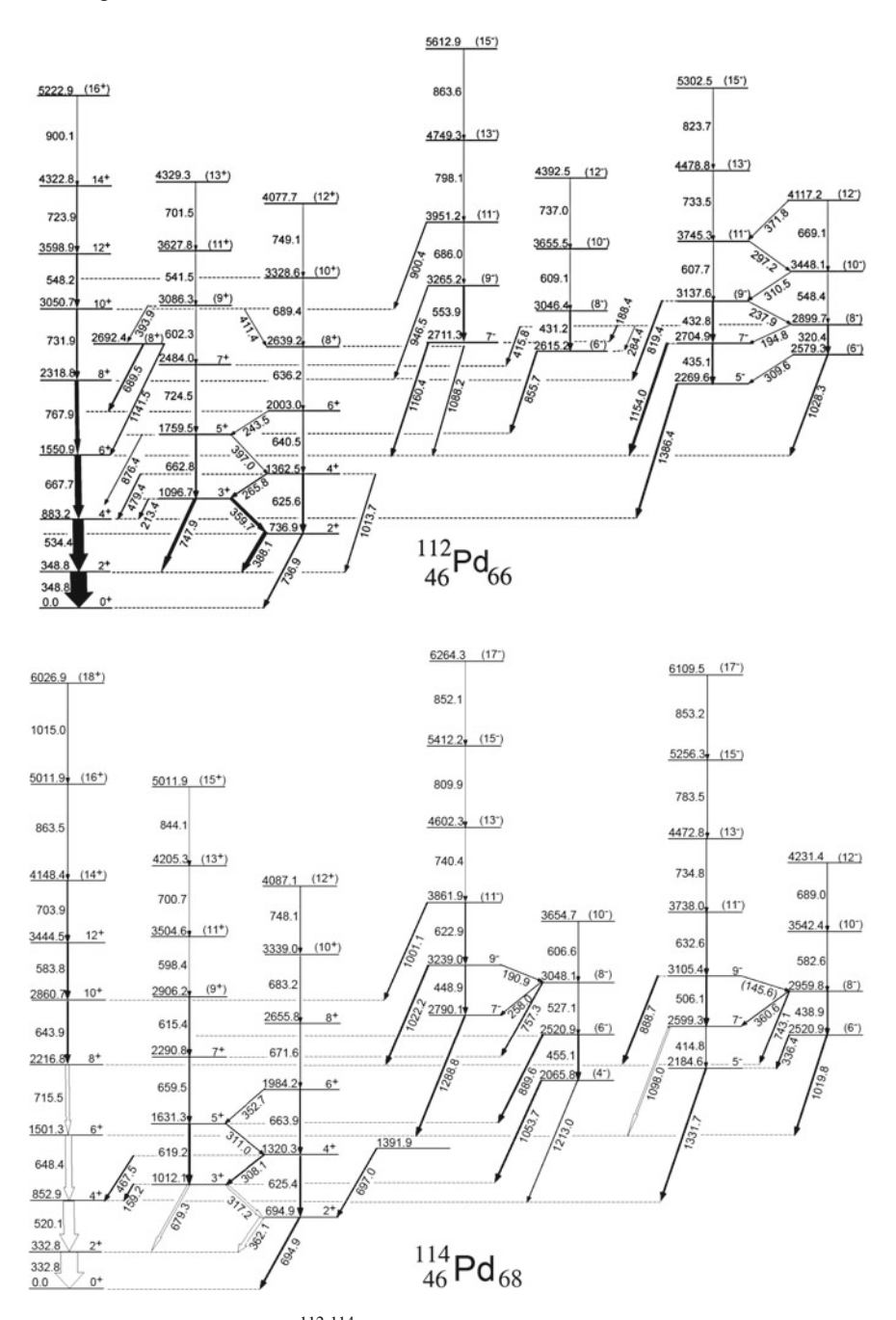


Fig. 2 Partial level schemes of ^{112,114}Pd with yrast, gamma and doublet bands

62 J.H. Hamilton et al.

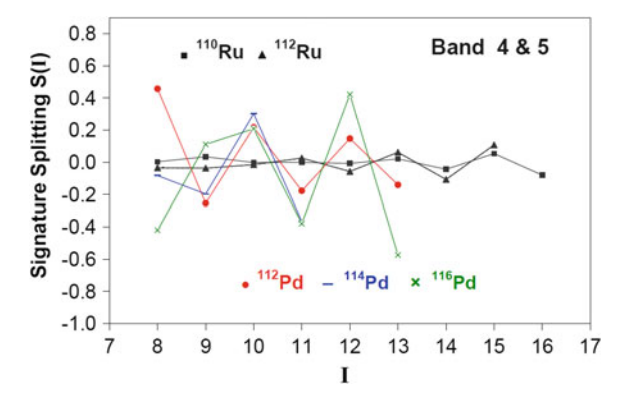


Fig. 3 Signature splitting in bands 4 and 5 in ^{110,112}Ru and ^{112,114,116}Pd

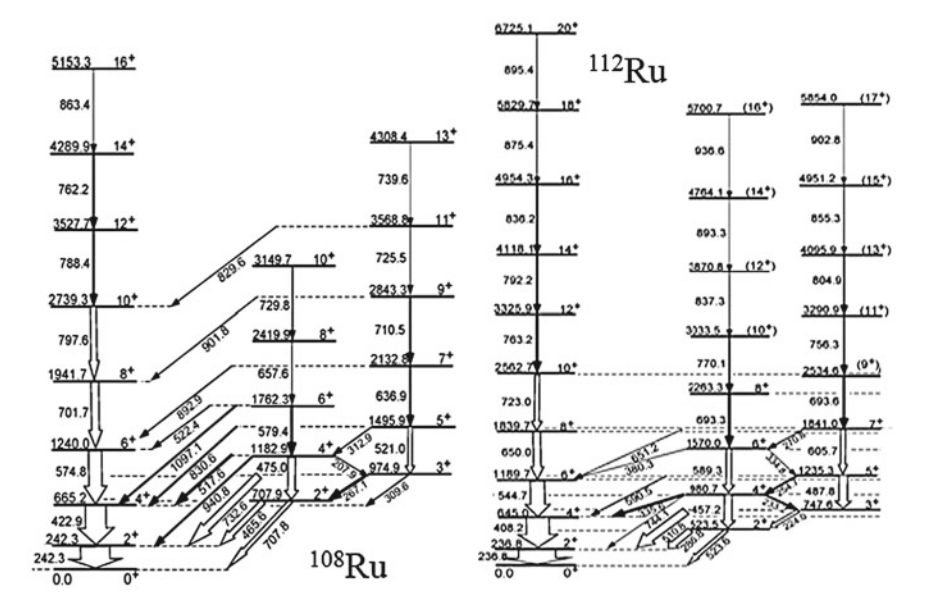


Fig. 4 Yrast and gamma bands in ^{108,112}Ru

a triaxial nucleus are expected to occur at moderate spins if the predicted triaxial shapes lead to different moments of inertia for the three principal axes [17, 18]. Note 112 Ru with substantial triaxiality [5] was found to be the first even-even wobbler [17–19]. The wobbling motions in 112 Ru were identified by analyzing the signature splitting in the quasi- γ band.

The yrast and γ -band structures in 108,112 Ru are shown in Fig. 4. Note the energy staggerings in the quasi- γ band of 108 Ru are opposite to those in 112 Ru [5]. Now very

similar behavior is found in ^{112,114}Pd. In our study of ^{112–118}Pd, the data indicate an evolution of their shapes from triaxial prolate via triaxial oblate to oblate shape.

Caprio [20] made new theoretical calculations of the consequences of this evolution of shapes toward increasing triaxiality for the collective excitation spectrum. A particularly clear signal is the even-odd staggering in the quasi- γ band. For soft axial nuclei, the energies of the even spin members are lower than the odd spin members. For a well-developed triaxial minimum the odd-spin members are below the even-spin ones. In fact, for the well-developed triaxiality, the odd-spin members represent the one-phonon wobbling excitation, and the even-spin ones the two-phonon wobbling excitations.

The search for wobbling motions in 114 Pd, the N=68 isotone of 112 Ru, and in the neighboring Pd isotopes yielded promising results. In Fig. 5, the excitation energies of the quasi- γ band levels were plotted against spins for N=68 isotones 112 Ru and 114 Pd (a), and N=64 isotones 108 Ru and 110 Pd (b), respectively. Note for the lighter N=64 isotones 108 Ru and 110 Pd, the $\alpha=1$ odd-spin curve always lies above the $\alpha=0$ even-spin curve which is normal behavior, to indicate that no wobbling motion is identified. While not shown in Fig. 5, the $\alpha=1$ odd-spin curve

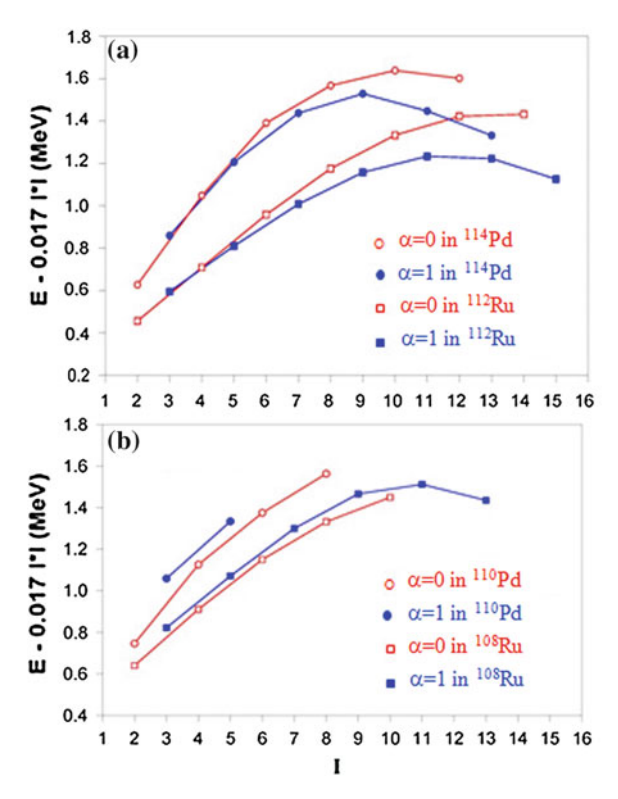


Fig. 5 Excitation energies versus spins in gamma bands in ^{108,112}Ru and ^{110,114}Pd

J.H. Hamilton et al.

of ^{112}Pd is higher than that of the $\alpha=0$ even-spin curve until a crossing takes place at a spin as high as I=10, and in ^{110}Ru the two curves follow a similar trend, but they are very close to each other, and the crossing takes place at spin I=7. However, one can see in Fig. 5 that for the γ bands of both ^{112}Ru and ^{114}Pd the $\alpha=1$ odd-spin curve ($n=1_{\text{wobble}}$) crosses the $\alpha=0$ even-spin curve ($n=2_{\text{wobble}}$) at a spin as low as I=3.5, and then the latter becomes considerably higher than the former, as expected for wobbling motions. Thus, both ^{112}Ru and ^{114}Pd are identified as even-even wobblers. These are the first evidence for wobbling motion at low to medium spin and in an even-even nucleus.

5 Prolate-Oblate Transition

Plots of spin vs $\hbar\omega$ in Figs. 6 and 7 show clear evidences for first band crossings in the ground state bands in $^{112,114,116}\text{Pd}$ around $\hbar\omega$ of 0.36 MeV which is associated with $\nu(h_{11/2})^2$ band crossing. This crossing is blocked in the $h_{11/2}$ bands in $^{115,117}\text{Pd}$. In ^{116}Pd , there is a second crossing at 0.41 MeV and in band 1 in ^{117}Pd a crossing at the same $\hbar\omega$. Total Routhian calculation shows the band crossing around $\hbar\omega=0.41$ MeV is a $\pi(g_{9/2})^2$ oblate band. In Fig. 7, one sees there is no crossing in band 1 of ^{115}Pd around 0.41 MeV like in ^{117}Pd but there is in band 2 of ^{115}Pd . The low-spin crossings in ^{115}Pd are associated with an oblate $\nu(g_{7/2})^2$ band crossing from the theoretical calculations. The differences of bands 1 and 2 in ^{115}Pd are related to triaxial prolate—triaxial oblate shape coexistence in ^{115}Pd . The new data and TRS calculations allowed a systematic study of the band crossings in the even-N $^{112,114,116}\text{Pd}$ and odd-N $^{115,117}\text{Pd}$ isotopes. Now we find a new overall, more complex shape evolution than previously proposed from triaxial prolate in ^{110}Pd via triaxial oblate in ^{112}Pd to nearly

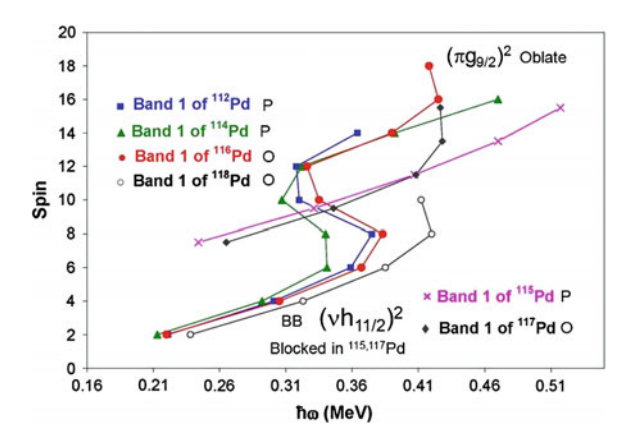


Fig. 6 Band crossings in ^{112–118}Pd

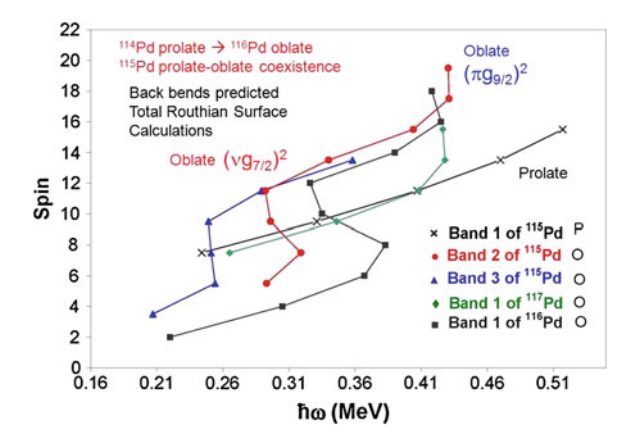


Fig. 7 Band crossings in 115,116,117 Pd

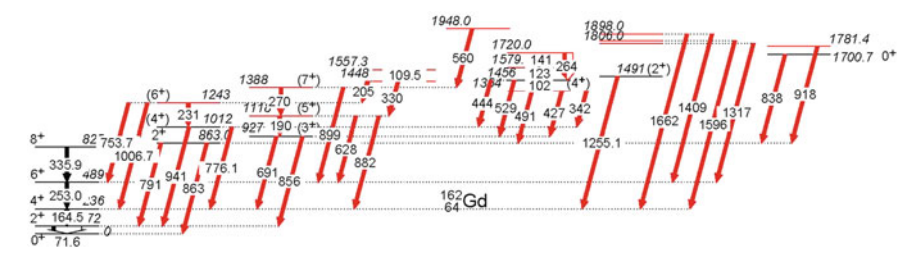


Fig. 8 Level scheme of 162 Gd from the beta decay of 152 Eu produced from the proton induced fission of 238 U

oblate in 114,116 Pd with the large change of the deformation parameter toward nearly oblate in the $\pi(g_{9/2})^2$ alignment in $^{114-118}$ Pd and triaxial-prolate—triaxial-oblate shape coexistence bands in 115 Pd.

6 New Levels in ^{162,163}Gd

The levels in ^{162,163}Gd were studied from the beta decays of ^{162,163}Eu produced from the proton induced fission of ²³⁸U and ¹⁶²Gd from spontaneous fission of ²⁵²Cf. The results of these data are illustrated in Figs. 8, 9 and 10. One sees in ¹⁶²Gd of Fig. 8 we found the first evidence of a gamma vibrational band from 2⁺ to 7⁺ as well as numbers of other levels. Illustrated in Fig. 9 are some of levels identified in ¹⁶²Gd from SF. Many excited levels were found in ¹⁶³Gd of Fig. 10, for the first time. Figure 10 is to illustrate the quality of the data obtained for ¹⁶³Gd. These results are still being analysed.

J.H. Hamilton et al.

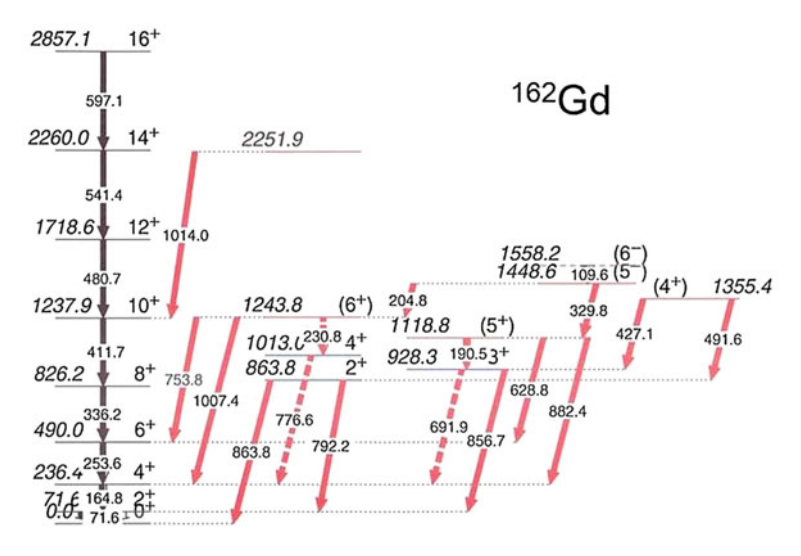


Fig. 9 Level scheme of ¹⁶²Gd from the spontaneous fission of ²⁵²Cf

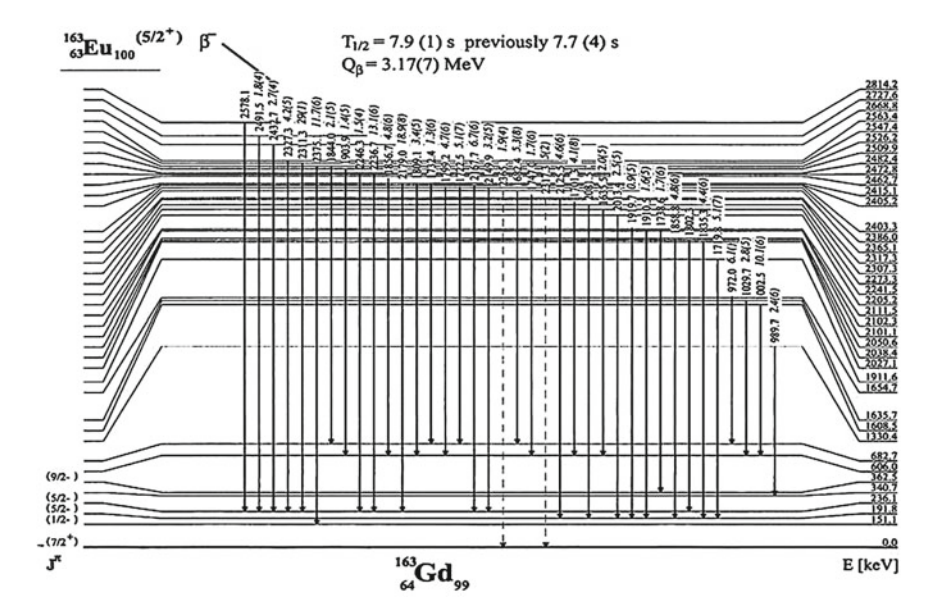


Fig. 10 Level scheme of $^{163}\mathrm{Gd}$ from the beta decay of $^{153}\mathrm{Eu}$ produced from the proton induced fission of $^{238}\mathrm{U}$

Acknowledgments The work at Vanderbilt University, Lawrence Berkeley National Laboratory, was supported by the U.S. DOE Grants DE-FG-05-88ER40407 and DE-AC03-76SF00098. The work at the Joint Institute for Nuclear Research work was supported by the Russian Foundation for Basic Research grant RFBR 11-02-00657-a and Russian Ministry of Education and Science

grant NSh-7235.2010.2. The work at Tsinghua University in Beijing was supported by the Major State Basic Research Development Program Contract 2007CB815005, the NNSF of China Grant 10975082, Grant No. 11175095, and the Special Program of HESF Grant 20100002110077. Two of the authors, GMT and AVD, were supported by the Joint Institute for Heavy Ion Research where it is supported by its member institutions.

References

- 1. P. Möller et al., Phys. Rev. Lett. 93, 162502 (2006)
- 2. S. Frauendorf, J. Meng, Nucl. Phys. A 617, 131 (1997)
- 3. S. Frauendorf, Rev. Mod. Phys. 73, 463 (2001)
- V.I. Dimitrov, S. Frauendorf, in *Proceedings of Third International Conference on Fission and Properties of Neutron-rich Nuclei*, ed. by J.H. Hamilton, et al. (World Scientific, Singapore, 2003), p. 93
- 5. Y.X. Luo et al., Phys. Lett. B 670, 307 (2009)
- 6. Y.X. Luo et al., Phys. Rev. C (submitted)
- 7. Y.X. Luo et al., Nucl. Phys. A **874**, 32 (2012)
- 8. A. Daniel et al., Nucl. Inst. Meth. B 262, 399 (2007)
- 9. Y.X. Luo et al., J. Mod. Phys. E 18, 1697 (2009)
- 10. S.J. Zhu et al., J. Mod. Phys. E 18, 1717 (2009)
- 11. S.W. Ødegård et al., Phys. Rev. Lett. 86, 5866 (2001)
- 12. G. Schönwaßer et al., Phys. Lett. **B552**, 9 (2003)
- 13. P. Bringel et al., Eur. Phys. J. A 24, 167 (2005)
- 14. H. Armo et al., Phys. Lett. B **553**, 197 (2003)
- 15. D.J. Hartley et al., Phys. Rev. C 80, 041304(R) (2009)
- 16. D.J. Hartley et al., Phys. Rev. C 83, 0641307 (20011)
- 17. S. Frauendorf et al., to be published, See also A. Bohr and B.R. Mottelson, Nuclear Structure, vol. 2 (World Scientific, Singapore, 1975) cf. p. 197
- 18. A.S. Davydov, G.F. Filippov, Nucl. Phys. 8, 237 (1958)
- 19. J.H. Hamilton et al., Nucl. Phys. A 834, 28c (2010)
- 20. M. Caprio, Phys. Rev. C 83, 064309 (2011)

Paradigmatic Lessons from Nuclear Driplines

J.S. Vaagen, S.N. Ershov and M.V. Zhukov

Abstract Science is—as emphasized 50 years ago by Thomas Kuhn in his academic bestseller The Structure of Scientific Revolutions—driven by paradigms, rooted in outstanding discoveries and practice. At the centennial for the nuclear atom, it may be appropriate to address the current paradigmatic situation for nuclear physics on background of the large investments made during the last decades. Following Rutherford's paradigm, nuclear physics has developed by colliding nuclei and from studying the fragments that emerge. With restriction to new forms of transient cold nuclear matter, we will address if and how new discoveries have influenced the way we think about nuclear architecture, drawing parallels with comparable development in other branches of science. Recent discoveries in halo nuclei, ¹¹Be and the Borromean ²²C will serve as our cardinal examples. The challenges at driplines may appear less dramatic than what calls for a Kuhnian turnover, still we hope to convey that valuable lessons may be learned. The attention-grabbing dripline lessons we address are rooted in emergent degrees of freedom involving *cluster* constituents. This is a great challenge for the ruling paradigm, a shell-model inspired ab initio nucleon-based theory, developed and tested for stable nuclei, and currently being tuned to encompass

J.S. Vaagen (⊠)

Department of Physics and Technology, University of Bergen, 5007 Bergen, Norway e-mail: Jan. Vaagen@ift.uib.no

S.N. Ershov

Joint Institute for Nuclear Research, 141980 Dubna, Russia e-mail: ershov@theor.jinr.ru

M.V. Zhukov

Fundamental Physics, Chalmers University of Technology, 41296 Göteborg, Sweden

e-mail: f2bmz@chalmers.se

J.S. Vaagen et al.

dripline lessons. Our mental pictures and dynamic understanding of many of the outstanding dripline phenomena will, however, remain linked to cluster degrees of freedom. This duality makes our paradigmatic lessons conceptually less dramatic than what Kuhn's "incommensurability" may imply.

1 Energy Culture

Last summer the newly built Viking ship "Harald Harfagre (Hairfair)" sailed through historic waters in Western Norway. At the starboard of present days' largest Viking ship, a 35 m long dragon, stood a grey haired physicist. Proud, filled with the feeling of being part of a timeless ENERGY CULTURE!

The NUCLEAR PARADIGM is very much about *energy and stability* of matter. Our theoretical understanding made a transition 100 years ago with the Bohr-Rutherford atom and Niels Bohr's ad hoc quantum theory, which introduced the concepts of stationary states and quantum jumps. June 11–14 an International History of Science Conference in Copenhagen, organized by the Niels Bohr Archive, addresses young Bohr's 1913 paper Trilogy [1].

Our late colleague Jens Bang contributed to both atomic and nuclear physics. In his book "Raids into Niels Bohr's Thoughts" [2] Bang emphasizes Bohr's focus on designing an energy(state) architecture, with correct stability and radiation properties, involving the known charged constituents (electron(s) and nucleus) in Rutherford's nuclear atom of 1911, tuning the model to reproduce emergent features of radiation data.

Nuclear Physics is an energy driven science. Our field now spans from transient matter under the extreme conditions of the Early Universe, to weakly bound cold matter at nuclear driplines, calling for a better understanding of many-body open quantum systems. In 2011 we contributed paradigmatic dripline lessons to the Rutherford Centennial [3]. We welcome the opportunity to make the picture more complete at this contemplative gathering at Jakobsberg.

2 The Role of Paradigms

Physicists seldom use the words paradigm and paradigm shift, coined in their modern meaning just 50 years ago by MIT professor of philosophy Thomas Kuhn in his bestseller "The Structure of Scientific Revolutions" (1962). This may be a loss. The book was reprinted last year in a 50th Anniversary Edition [4] and is still worth reading, a gateway to bridging the Two Culture gap. A quick look in Google reveals the role of the paradigm concept in "intellectual" discourses.

Historically the word paradigm dates back to the Greek word *paradeigma* which played an important part in Aristotle's theory of argument, especially in the book called Rhetoric (see Ian Hacking in Kuhn's *Structure* [4]). The word paradigm,

in spite of its numerous interpretation variants, also in Kuhn's own writings, has been important in highlighting how scientific puzzle-solving is guided or framed by specific attention-grabbing successes. In an anniversary article [5] on *Structure* in Science last year, Lehoux and Foster point out that: "These 'paradigms' or 'exemplars' structure inquiry by providing a touchstone for the coordination of research, the formulation of experimental routines, and, in many cases, a theory worthy of further articulation".

Thus Rutherford's paradigm is linked to his scientific *practice*, his epistemological way to extract and develop lessons and knowledge—we still measure transverse and longitudinal momentum transfer. Bohr drew inspiration from this, and focused his thinking on emergent degrees of freedom: An atomic "architectural" paradigm, which still is kept in our school books. Kuhn himself had background in physics, a field which provided historic content to his use of the notion paradigm or exemplar. It may be of interest to know that Kuhn was in Copenhagen for a Bohr interview when Bohr suddenly died—in November 1962, the year of Kuhn's book.

The nuclear stuff has rich possibilities for combinations, internal clustering that reveals itself in collision experiments. The binding energy in a nucleus is however very small compared with the total mass of its constituents, less that 1 %, the most extreme cases occuring at driplines where nearly free (Borromean) cluster binding is part in a million of the mass. Comparing this with *models of the nucleon*, the mass of current quarks carries only 1 % of the nucleon mass, here the interplay dominates. Thus it is futile to treat Borromean nuclei within a current quark model.

3 Is the Nuclear Paradigm Still an Eye Opener?

Borromean nuclei represent exemplars of exotic dripline behaviour rooted in emergent three-body cluster degrees of freedom and no binary bound states. Here we address two examples.

Recently 22 C has made headlines as the so far most outstanding exemplar discovered; Three constituents 20 C + n + n, dominated by binary relative *s*-motions and a very small but still not settled three-body separation energy. Last year we published [6] a hyper-harmonic model study of binding energy constraint on matter radius and soft dipole excitations of 22 C. A very low three-body separation energy of some tens of keV was found required to obtain even the lower experimental bound on the matter radius. More details are given in Sect. 5. This conclusion has been supported by a very recent "Search for 21 C and constraints on 22 C", at NSCL, MSU by Mosby et al. [7]. We also found in our hyper-harmonic analysis that the soft dipole mode in 22 C is strongly affected by the loose binding, arguing for a Coulomb fragmentation study.

The next case is rooted in a prediction we made in 1995, in the paper [8] " β decay of ¹¹Li to the deuteron channel and halo analog states in ¹¹Be". More than a decade later, the prediction was confirmed at TRIUMF [9] by Raabe et al., published in

J.S. Vaagen et al.

2008 with the title " β -Delayed Deuteron Emission from ¹¹Li: Decay of the Halo". A decay that proceeds mainly to the ⁹Li + d continuum.

These studies leave little doubt about the real nature of Borromean clustering and the validity of the theoretical three-body paradigm.

Unveiling Borromean exotics seems still to make it to the catwalk of science, not only in nuclear physics, but also in a number of other branches of science where Borromean rings (loops) are literally formed. See also the FIAS logo. Google has a list of beautiful examples. Here we also learn that Borromean links should not be used to make armour. It becomes too stiff!

4 Halo Nuclei

While Bohr in 1913 published his Trilogy on the atom, working in Rutherford's lab in Manchester, the master himself published a textbook on nuclear phenomena "Radioactive Substances and their Radiations" ([10], see Ref. [3]).

"No doubt the positively charged centre of the atom is a complicated system in movement, consisting in part of charged helium and hydrogen atoms" [10]. This sentence is from Rutherford's 1913 textbook. Alphas pop out of nuclei, so why should they not pre-exist within? Clustering, in particular alpha clustering in nuclei has a rich but also controversial history, with the three-alpha Hoyle resonance state as a landmark.

Clustering, a true emergent aspect of nuclear structure, has had a revival with halo physics. Rutherford would have been pleased to learn that much of our present understanding has been derived from Helium, from the beta-unstable but hadronically very loosely bound isotopes ⁶He and ⁸He. While the Helium atom is an alpha with a veil of two electrons, the ⁶He nucleus is an alpha with a veil—a halo—of two neutrons, ⁸He four neutrons. Since neither a *neutron-neutron* nor a *neutron-alpha* pair can form bound states, a new binding mechanism has been discovered, different from one dominated by a mean field, the atom model for the electrons.

The challenge of understanding this and similar consecutive observations, became of interest for the nuclear physics community and among theorists in particular, only after the Scandinavian experimentalists P. Gregers Hansen and Björn Jonson in 1987 put forward an *ad hoc* halo *theory*, conceived according to the legend in a lunchroom conversation at the Niels Bohr Institute with the late Danish theorist Jens Bang, already mentioned in Sect. 1. Hansen and Jonson turned the idea into a Europhysics Letters [11] "The Neutron Halo of Extremely Neutron-Rich Nuclei", with proper reference to discussion with Bang. Thus the name halo nuclei came into being.

A second quote from Rutherford's 1913 textbook shows that he was puzzled by the question of nuclear binding, "It would appear as if the positively charged atoms of matter attract one another at very small distances for otherwise it is difficult to see how the component parts at the centre are held together" [10]. Now we know more after pioneering theory work by Efimov and Migdal, and two decades of few-body modelling of Borromean nuclei.

Hansen and Jonson refer to Migdal in their ground-breaking paper; "This suggests that for a nuclear potential that leaves a single neutron marginally unbound, the additional attractive contribution from the *nn* interaction will frequently be sufficient to bind two neutrons to the nucleus. This special case of three-body problem has been considered by Migdal [12], who finds that several nuclei should exhibit a bound state of this kind, which may be interpreted as a dineutron near the nuclear surface. He also points to the possibility that cluster states more complex than dineutrons may exist".

Hansen and Jonson made a *phenomenological* model with a point-dineutron, useful in the spirit of Rutherford for understanding important aspects of the new halo phenomenon, and challenging for theorists seeking a more complete quantum mechanically correct picture.

5 The Cluster Approach to Nuclear Structure

In a domain of the low-energy nuclear physics the nuclear structure can be described by taking into account only nucleons—protons and neutrons. At small energy and momentum transfers we do not need to account for degrees of freedom that involve the internal nucleon structure. Very often the opposite tendency is observed—we see effects from the cooperative action of nucleon groups (clusters). Recall Rutherford's 1913 observations (Sect. 4), the first nuclear structure paradigm. This does not mean that the respective phenomena cannot in principle be described using nucleons, but by considering explicitly the cluster degrees of freedom we get a simpler and more transparent physical explanation.

Clustering phenomena in nuclear physics have many facets. Three may be mentioned here:

- (i) Clustering is a *widespread* phenomenon and is met across the whole periodic table but particularly frequent among the lighter nuclei below calcium.
- (ii) It is a *real* phenomenon—clusters appear often as decay fragments. The alpha particle is the most remarkable cluster example, being the most tightly bound nucleus which tends to keep its own identity inside nuclei.
- (iii) It is an *elusive* phenomenon. By elusive we mean that clusters appear in bound states within a nuclear environment produced by other nucleons that affects the cluster structure and attempts to dissolve it. But some physical conditions enhance clustering phenomena. They emerge in weakly bound systems and find extreme realization in halo nuclei where only a few percent of the wave functions of halo nucleons overlap with core cluster wave functions.

The importance of cluster degrees of freedom was already emphasized at the dawn of the nuclear structure theory when Wheeler suggested [13] the resonating group method where "The wave function for the composite nucleus is written as a properly antisymmetrized combination of partial wave functions, corresponding to the various possible ways of distributing the neutrons and protons into various groups, such as

74 J.S. Vaagen et al.

alpha-particles, *di*-neutrons, etc". In a relatively simple but physically natural way the clustering phenomena in nuclei can be described within *few-body* cluster models [14] that assume an approximate treatment of the antisymmetrization. Below two selected examples of cluster model applications to descriptions of halo structure are discussed in more detail.

The first example is again the three-body cluster model of the Borromean ²²C with an inert ²⁰C core. Figure 1 shows the calculated dependence of the ²²C matter radius on the value of the two-neutron separation energy [6]. The experimental value 2.98 fm extracted from reaction cross sections was used as the ²⁰C core matter radius. The two curves correspond to calculations with different potentials for the interaction of halo neutron with ²⁰C core (the lower and upper curves are for the narrow and broader geometry, respectively). As expected a broader potential leads to larger radii at the same binding energy. The upper curve starts from ground state energies of about 400 keV. Continuation of this curve to larger binding energies requires larger depths of the core-neutron potential and leads to appearance of twobody bound states. Concerning the general behaviour of the ²²C matter radius with binding energy, we notice that this dependence (see the insert in Fig. 1) is close to linear at larger separation energies, becoming strongly nonlinear at smaller energies and diverging in the vicinity of the breakup threshold. The main frame of Fig. 1 shows the same curves versus a logarithmic scale of energy. The figure compares calculations with the values of the ²²C matter radius tentatively extracted [15] from experimental cross sections. Bars show that even the lower experimental value of

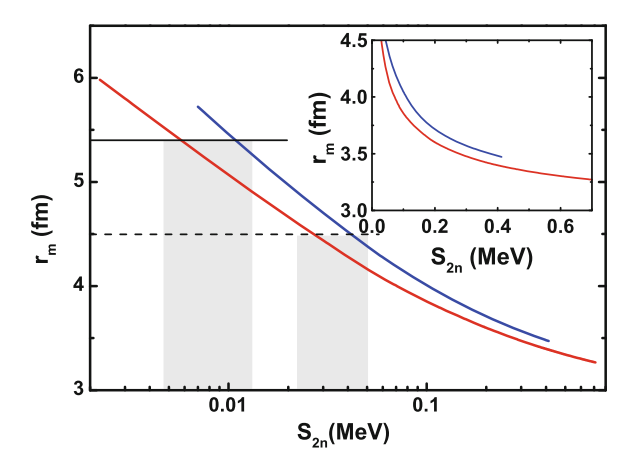


Fig. 1 The dependence of the 22 C r.m.s. matter radius on the two-neutron separation energy (logarithmic scale). The *lower* and *upper* curves correspond to calculations with the radius of the neutron-core potential equal to 3.5 and 4.5 fm, respectively. The *horizontal solid* and *dashed lines* are the mean value and lower boundary of the experimental matter radius [15], respectively. *Bars* show theoretical estimations of the S_{2n} energy at which the experimental mean value and lower boundary of the matter radius can be obtained. The insert shows the same curves, but for a linear energy scale

this radius would require very small binding energy of a few tens keV, diminishing to a very tiny binding for the suggested ²²C experimental value.

The second example is a recent application [16] of a two-body cluster model with core excitations to description of the ¹¹Be nuclear structure. A coupling with excited core states involves additional partial waves. This allows to account for some emergent core degrees of freedom and provides a more comprehensive description of nuclear properties. Such extension is analogous to increasing the number of shells within the framework of shell-model approaches.

The ¹¹Be nucleus is the cardinal example of the one-neutron halo system. The neutron separation energy of ¹¹Be is only 0.5 MeV, significantly smaller then in neighbouring isotopes. There is a parity inversion near the ground state of ¹¹Be, which is not a $1/2^-$, as one would expect from the spherical shell model, but a $1/2^+$ state. That such an inversion should occur in ¹¹Be was already suggested a long time ago [17]. But, the notion of a mean field is not so well established in nuclei of this very light mass region and models starting directly from an effective two-body interaction have failed to reproduce the inversion without an ad hoc renormalization. In calculations shown below the lowest ¹⁰Be core excited 2⁺ state was considered as a quadrupole vibration. Shallow potentials were applied for neutron-core interaction, preventing motion in Pauli forbidden orbits. A good description of available experimental data including dipole excitations of ¹¹Be is obtained. The dipole excitations of the ¹¹Be continuum may play an important role to clear up the structure of negative parity resonances. Dipole transitions excite predominantly the 3/2 continuum states. If the $3/2^-$ resonance has a structure that can be reached by the dipole transition from the ground state then the traces of the resonance may be seen in the dipolestrength distribution dB(E1)/dE obtained from Coulomb dissociation experiments [18]. The experimental data shown in Fig. 2 do not indicate a presence of the first 3/2 resonance at 2.1 MeV but have irregular behaviour in the vicinity of 3 MeV where the second 3/2⁻ resonance has been found. Within the current realization of the two-body cluster model of ¹¹Be only one the 3/2⁻ low-lying resonances is obtained. The other negative parity resonance may have structure which falls outside our model assumptions. Our theoretical calculations of the dB(E1)/dE distributions made under the condition that the resonance has excitation energy 2.8 MeV (the second 3/2⁻ resonance) are shown in Fig. 2 and describe well the experimental data. The theoretical dipole strength has a deep minimum after that energy. If the energy of the 3/2⁻ resonance was fixed at 2.1 MeV (position of the first 3/2⁻ resonance), the deep minimum in the dB(E1)/dE theoretical distribution appeared after this excitation energy which is not compatible with the measured experimental data.

Noteworthy continuum progress has been made very recently [19] for the doubly closed ¹⁶O, in a first principle description of the Giant Dipole Resonance, combining the Lorentz Integral Transform and the Coupled-Cluster ab initio many-body expansion Method. Thus nucleon-based ab initio approaches are making impressive headway away from driplines.

J.S. Vaagen et al.

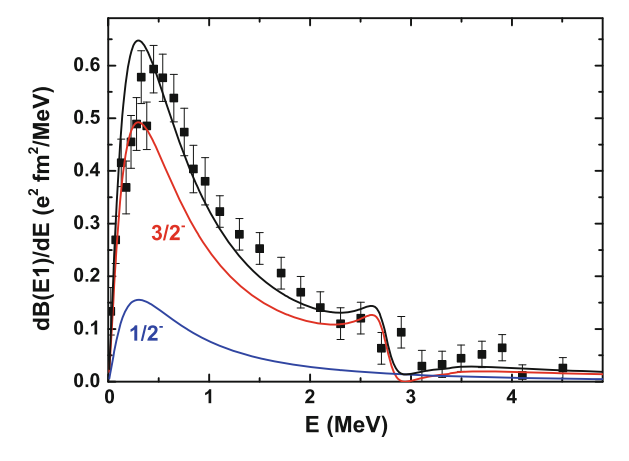


Fig. 2 Dipole-strength distributions of 11 Be. The *lower* and *middle lines* show the dipole transition from the $1/2^+$ ground state to the $1/2^-$ and $3/2^-$ continuum excitations, respectively. The energy E is calculated from the 10 Be + n threshold. The *upper line* is the total distribution. Experimental data are taken from the work [18]

6 A Respected Physicist

Aspirations to become a nuclear physicist ranked high among professions in the post-war years.

In his book [20] on Reminiscences of a White House Science Advisor, "The President's Scientists", D. Allan Bromley gives the key to his country's post war science success (p. 224):

- 1. Find the best people in the country on the basis of peer review.
- 2. Fund them as generously as possible within the overall available resources to do what *they* (our emphasis) think represent the best use of their time.
- 3. Keep the hell out of their hair while they are doing it.

Was this the Garden of Eden?—It had not always been so: "It's rather odd," said G. H. Hardy (the mathematician), one afternoon in the early Thirties, "but when we hear about 'intellectuals' nowadays, it does not include people like me and J.J.Thomson and Rutherford". This quote is taken from Snow [21], novelist and scientist with access to both camps. He watched the new science grow, and also the growing divide between the two cultures, about which he later expressed great concern in his famous essay.

Now there are dark clouds in the horizon. Not only have times changed, also attitudes, and unqualified interference is increasingly "getting into the hair of science".

In his editorial in Science Magazine 3 May this year [22], Prewitt (International and Public Affairs of Columbia University) asks the question: Is Any Science Safe? Is peer review safe from marginalization? He gives examples, very relevant to our field, nuclear physics.

We may ask if conditions for fundamental discoveries and paradigmatic changes are impeded, in spite of large technological investments. Is computational physics within the present theory framework the future of nuclear structure science? With no surprises calling for paradigm shifts?

In recent years Public management has grown, some will say out of proportion. We may doubt that this brings science forward, nor Humanities and Sciences closer.

7 Perspectives

The paradigmatic aspects of the nuclear stuff under extreme conditions mostly belong to the last 25 years, preceded by forty years of shell model (SM) based theory work, normal work for normal matter. The new findings do not challenge the SM as paradigm for *Normal Science* (Kuhn) work in nuclear structure, the question is if and how the SM can address and encompass dripline exotics and the pathway to open quantum systems, reactions.

Here we are in doubt. The SM may for normal science provide a 'Unified view of Nuclear Structure', the name of a recent expert conference (2012) in Strasbourg (see [23]), but not a *satisfactory* exhaustive paradigm. It will however help in showing how and possibly why we fail when driplines are approached. The challenges at driplines may however appear less dramatic than what calls for a full Kuhnian turnover, a paradigm shift, *and to what*?

Nuclear structure, with all its beautiful collective phenomena, has lived well with a *composite paradigm*. We will continue to do so, but new dripline lessons will keep alive the hope for a more complete understanding of the transition to open quantum systems.

Return again to last summer. While the first author was crew member on the Norwegian Viking ship, a Chinese ice-breaker Xue-Long, the Snow-Dragon, was exploring the Arctic. While Harald Hairfair was exploring by a *simulation experiment* how things might have be done in the past, the Chinese explored future sailing routes in Nordic waters and foreign resources.

And not for the first time; in the early 1400s, China had 7 fleets of giant junks under sail to foreign destinations to map the world. In 1429 the Norwegian coastal defence "leidangen" was called out for the last time: To protect Bergen against the Hansa. The dragons were now outdated, Norway no longer a sea power. Europe had learned the value of 'ruling the waves' and taken marine development further, its future strength. In 1452 Leonardo da Vinci was born, an icon for a new Europe where also technology mattered. *Nuclear Science* was born in Europe 500 years later—time scales should be kept in mind. Today it is an essential aspect of our world society and growing rapidly in Asia. We are proud to have been part of this venture, which has transgressed ordinary matter into matter under extreme conditions, extending the range of the nuclear paradigm.

This conference is dedicated to Misha Itkis's 70th birthday. We join in the congratulations. Two of the authors of this paper also congratulate the third, Misha Zhukov

J.S. Vaagen et al.

who turns 70 in July, twenty years after the seminal paper on Borromean nuclei, to which his contribution was essential. Acknowledging the support from our Institutions, we also add that Georgy Flerov (JINR) would have been 100 and that Spartak Belyaev (The Kurchatov institute) celebrates 90 this year.

References

- 1. N. Bohr, The trilogy: on the constitution of atoms and molecules, Phil. Mag. 26, 1, 476, 857 (1913)
- 2. J. Bang, Strejftog i Niels Bohrs tanker (Hernovs Forlag, København, 1999)
- 3. J.S. Vaagen, S.N. Ershov, M.V. Zhukov, J. Phys. Conf. Ser. 381, 012049 (2012)
- T. Kuhn, The Structure of Scientific Revolutions, 1962 (The University of Chicago Press, Chicago, 2012)
- 5. D. Lehoux, J. Foster, Science **338**, 885 (2012)
- 6. S.N. Ershov, J.S. Vaagen, M.V. Zhukov, Phys. Rev. C 86, 034331 (2012)
- 7. S. Mosby et al., arXiv:1304.4507 (2013)
- 8. M.V. Zhukov, B.V. Danilin, L.V. Grigorenko, J.S. Vaagen, Phys. Rev. C 52, 2461 (1995)
- 9. R. Raabe et al., Phys. Rev. Lett. 101, 212501 (2008)
- E. Rutherford, Radioactive Substances and their Radiations (Cambridge University Press, Cambridge, 1913)
- 11. P. Hansen, B. Jonson, Europhys. Lett. 4, 409 (1987)
- 12. A. Migdal, Yad. Fiz. 16, 427 (1972) [Sov. J. Nucl. Phys. 16, 238 (1972)]
- 13. J.A. Wheeler, Phys. Rev. 52, 1107 (1937)
- 14. M.V. Zhukov et al., Phys. Rept. **231**, 151 (1993)
- 15. K. Tanaka et al., Phys. Rev. Lett. **104**, 062701 (2010)
- 16. S.N. Ershov, J.S. Vaagen, M.V. Zhukov, Phys. Atom. Nucl. (accepted for publication)
- 17. I. Talmi, I. Unna, Phys. Rev. Lett. 4, 60 (1969)
- 18. R. Palit et al., Phys. Rev. C 68, 034318 (2003)
- 19. S. Bacca et al., Phys. Rev. Lett. 111, 122502 (2013)
- 20. D.A. Bromley, *The President's Scientists* (Yale University Press, New Haven, 1994)
- C. Snow, The Two Cultures, The New Statesman and Nation (1956), reprinted in *The World Treasury of Physics, Astronomy and Mathematics*, ed. by T. Ferris (Little, Brown & Company, 1991)
- 22. K. Prewitt, Science, 3 May (2013)
- 23. Nuclear Physics News, 23, January–March, 36 (2013)

Preliminary Results on Observation of New Shape Isomers

Yu.V. Pyatkov, D.V. Kamanin, A.A. Alexandrov, I.A. Alexandrova, N.A. Kondratyev, E.A. Kuznetsova, A.O. Strekalovsky, O.V. Strekalovsky and V.E. Zhuchko

1 Introduction

In our previous publications devoted to the collinear cluster tri-partition (CCT) of the low excited nuclei [1, 2] we have discussed the role of scattering medium in the registration of the CCT products. This decay mode has been called by us "collinear cluster tri-partition" (CCT) in view of the observed features of the effect, that the decay partners fly apart almost collinearly and at least one of them has magic nucleon composition. Briefly, even if initially two CCT partners fly in the same direction perfectly collinearly they get some angular divergence after passing the scattering medium on the flight pass due to the multiple scattering. Thanks to such effect they can be registered independently in the "stop" mosaic detector. Actually even thin backing of the radioactive source provides the observable effect.

2 Experiments and Results

In order to increase the effect the additional absorbers (metal foils) were introduced just behind the source at the distance of approximately 1 mm. The layout of the experiments (Ex1 and Ex2) is presented in Fig. 1.

The geometry of the source unit is shown in detail in Fig. 2. Additional absorber foil was placed at 1 mm distance from the Cf source. Typical fission fragment overcomes such distance approximately in 0.1 ns.

Ternary events were analyzed. It means that three fragments were really detected in coincidence in three different silicon detectors. For the sake of convenience, the FFs from such events are labeled as M_1 , M_2 and M_3 in an order of decreasing masses

Yu.V. Pyatkov (⋈)

National Nuclear Research University "MEPHI", 115409 Moscow, Russia e-mail: yvp_nov@mail.ru

Yu.V. Pyatkov · D.V. Kamanin · A.A. Alexandrov · I.A. Alexandrova · N.A. Kondratyev · E.A. Kuznetsova \cdot A.O. Strekalovsky \cdot O.V. Strekalovsky \cdot V.E. Zhuchko Joint Institute for Nuclear Research, 141980 Dubna, Russia e-mail: kamanin@jinr.ru

© Springer International Publishing Switzerland 2015 W. Greiner (ed.), Nuclear Physics: Present and Future, FIAS Interdisciplinary Science Series, DOI 10.1007/978-3-319-10199-6_8 80 Yu.V. Pyatkov et al.

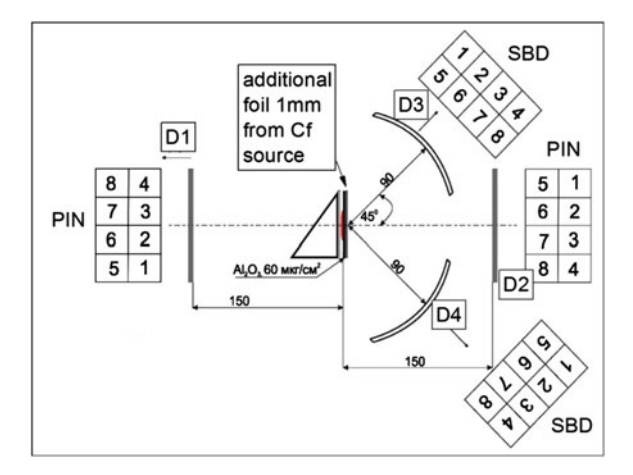
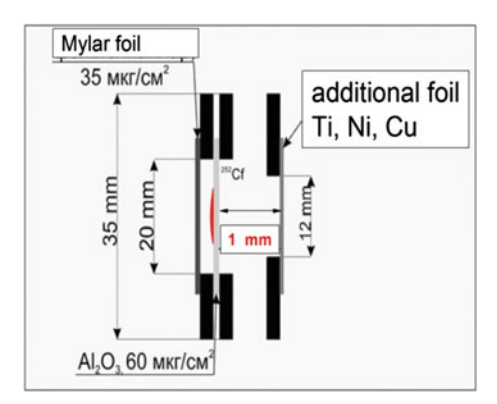


Fig. 1 Layout of the setup used in two first experiments aimed at studying of the influence of the additional absorber on the characteristics of the CCT products. D1 and D2 are the mosaics of PIN diodes. Mosaics D3 and D4 are based on the surface-barrier detectors (SBD). All in all 32 silicon detectors were used. Micro-channel plates based timing detector (*in the center*) gives "start" signal while silicon detectors provide signals for measuring of both time-of-flight (TOF) and energy (E) of the fragments. Thus the mass of each fragment detected can be estimated using these two parameters

Fig. 2 ²⁵²Cf source and additional foils placed around



in the ternary event. Mass distribution for ternary events from mosaics D1 and D2 is shown in Fig. 3. The total mass of the two heavier fragments $M_1 + M_2$ is plotted vs. the mass of the lighter fragment M_3 . As can be inferred from the figure in all the events where the lightest fragment corresponds to the knocked out Ti ions (M_3 is around 48 amu) we observe missing mass of fission fragments. It is a very astonishing fact.

Really, if the elastic Rutherford scattering of one of the fission fragments (FF) took place on the Ti foil the total mass $M_1 + M_2$ should lie in the vicinity of the mass of the mother system namely 252 amu (taking into account emitted neutrons, approximately four on the average and experimental mass resolution).

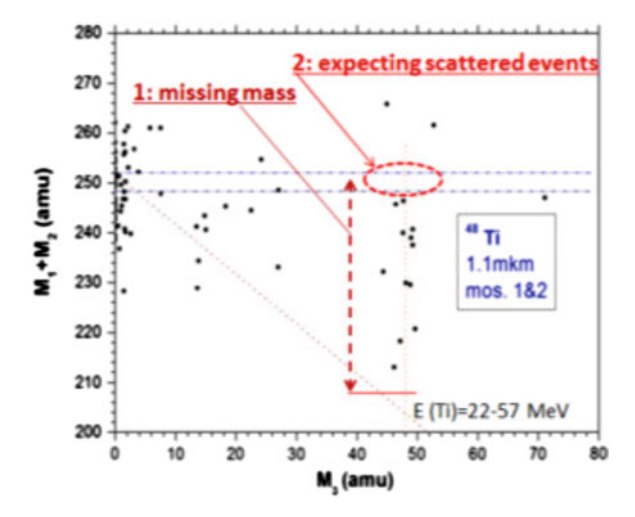


Fig. 3 Mass distribution for the ternary events from Ex1. Ti foil 1.1 mkm thick was used as the additional absorber

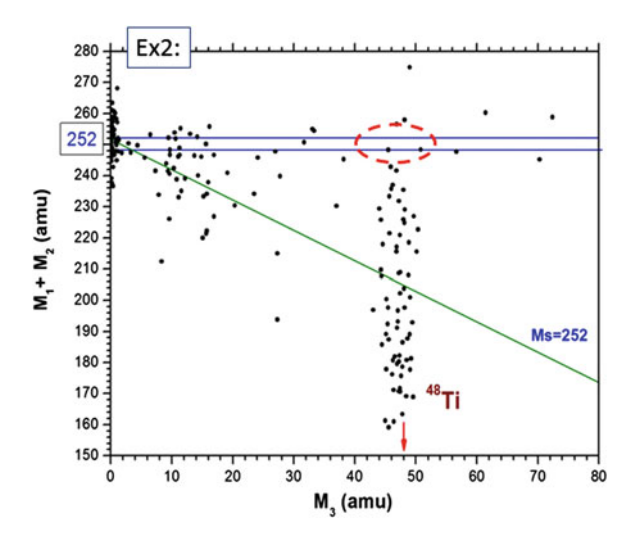


Fig. 4 Mass distribution from Ex2 for ternary events detected in the mosaics D1 and D2. Ti foil 2.2 mkm thick was used as the additional absorber

Similar result was obtained in Ex2 (Fig. 4) where twice thicker Ti absorber was used. Some points in the expected region for the events resulted from the elastic scattering (dashed oval) can be traced back to random coincidences alpha-FF.

Unfortunately, the quality of the SBD detectors, namely essential effective "dead" layer on the surface, did not let us to reconstruct correctly the masses of the FF hitting the mosaics D3 and D4 at large angles in relation to the symmetry axis of the setup.

82 Yu.V. Pyatkov et al.

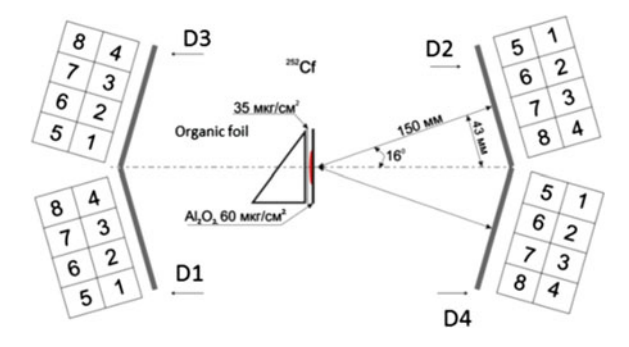


Fig. 5 Layout of the spectrometer used in Ex3 and Ex4

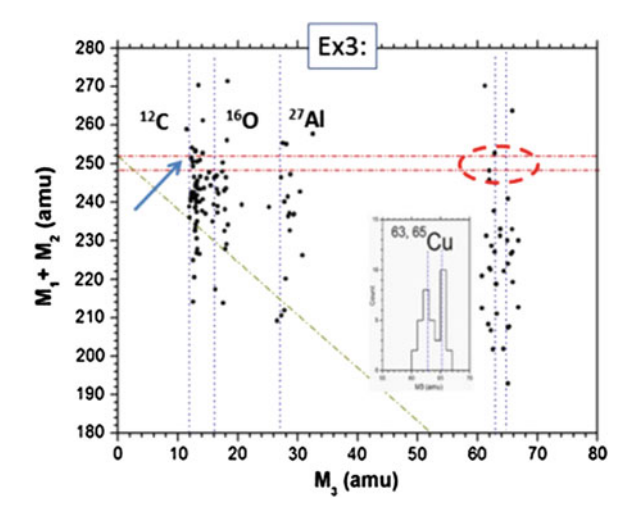


Fig. 6 Mass distribution for ternary events from Ex3. Cu foil 0.83 mkm thick was used as the additional absorber. The events which are caused by the random coincidences alpha-FF were excluded thanks to the selection on energy E3. See text for details

In the revised version of the spectrometer only PIN diodes were used and the position of the mosaics was changed (Fig. 5).

Mass distribution similar to those shown in Figs. 3 and 4 is presented in Fig. 6. The panel in the figure demonstrates the mass resolution achieved. We can resolve two isotopes of Cu in the natural mixture. The peculiarity of the plot emphasized above confirms in this case as well. A better mass resolution let us conclude that the effect of Rutherford scattering being accompanied by the loss of the mass of the scattered fission fragment takes place also in scattering on ¹⁶O and ²⁷Al nuclei from the source backing. At the same time at least some part of the FF scattered on the ¹²C nuclei from the organic foil (Fig. 5) undergo scattering without loss of mass. Corresponding events are marked by the arrow.

The mass distribution $M_1 - M_2$ obtained in Ex4 for the heaviest fragments of ternary events within knocked out Ni ion as a third one is shown in Fig. 7. The points in the vicinity of the line $M_1 + M_2 = 252$ amu are due to the random coincidences of the Ni ions detected in the mosaics D3 and D4 with the FF of binary fission. The counting rate in those mosaics is high enough following the probability of the Rutherford scattering at big angles. The linear structures observed (to guide the eye they are marked in Fig. 7 by the blue lines) are linked with the known magic nuclei. From the methodical point of view it confirms that mass calibration for the masses M_1 and M_2 is unbiased. In principal, negative shift in the mass calibration i.e. incorrect lower values of the sum $M_1 + M_2$ could be the reason of the effect observed.

Linear structures similar to those shown in Fig. 7 were observed in our previous experiments at the COMETA setup where only source backing played a role of scattering medium (Fig. 8). There are some differences caused likely by the geometry of the experiments compared but in all the cases we observe very bright manifestation of clustering linked with magic nuclei.

The experimental findings presented above allow us to assume the following:

- 1. Inelastic impact, at least the frontal one, makes free the constituents of the dinuclear system (fission fragment) formed in the binary fission.
- 2. Bearing in mind the distance between the Cf source and the generating foil $(\sim 1 \text{ mm})$ the lower limit of the life-time of this di-nuclear system (shape isomer) is about 0.1 ns.
- 3. Relative probability of elastic Rutherford scattering of fission fragments i.e. taking place without missing mass seems to be much less in our experiments than those in the inelastic channel. In other words, *the bulk of the fragments from the conventional binary fission are born apparently, as shape-isomers*.

3 Discussion

In the frame of the hypothesis put forward there are at least three main questions to be discussed, namely, population of the isomeric states in the FFs in the fission process, survival probability of these states and mechanism of their break-up.

Preformation of the FF of the conventional binary fission in the form of a dinuclear system (DNS) is very much expected keeping in mind both theoretical and experimental indications known. Vladimirski [3] was may be the first who postulated that the fission probability has a noticeable value only if two cluster structures such as magic cores within the light and heavy fragment corresponding to the N=50 and Z=50, N=82 shells are not destroyed. A dumbbell-like configuration consisting of two magic clusters connected by a flat cylindrical neck was considered as a typical shape of the fissioning system. In this case the fragment at the scission point should look like a di-nuclear system consisting of the magic core and some part of the neck. Preformation of two magic clusters in the body of the mother system at the early stage of the descent from the fission barrier was established in the calculations of

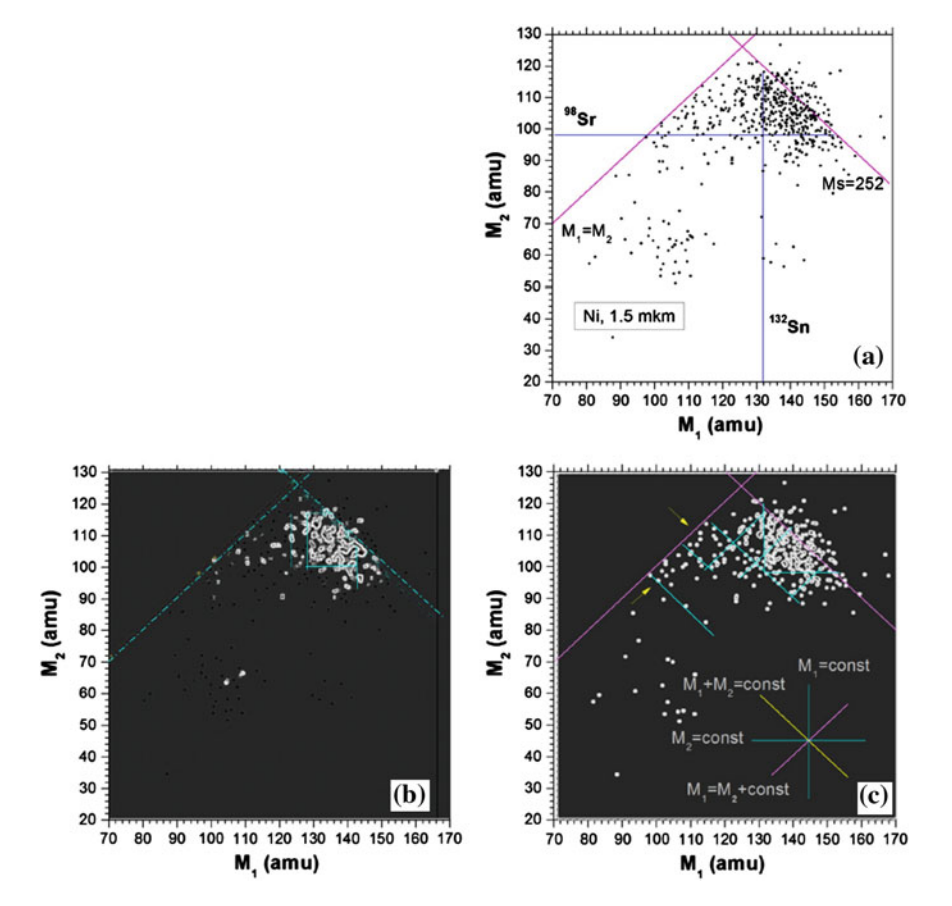


Fig. 7 Mass distribution for ternary events from Ex4 with the lightest fragment to be the ion knocked out from the Ni foil 1.5 mkm thick (a). All the mosaics (see Fig. 1) were taken into account. The same distribution processed by the filter sensitive to the density of the points in the image (b). Rectangular-like structure is vividly seen. By the less "strong" filter more details are revealed (c). Four different directions of the linear structures observed are shown in the *bottom* of the figure

the potential energy surface in ten dimensional deformation space for some actinides [4]. It takes place in the valley both mass-asymmetric (marked by number 3 in Fig. 9) and symmetric (valley 4) shapes of the fissioning system. Similar calculations reveal as well three cluster aligned configurations [5, 6]. After the first rupture of such configuration a di-nuclear system can be also formed. In our work [7] we supposed a fissioning system to be completely clusterised. The fission ways obtained in the frame of the model agree well with those predicted by Brosa et al. [8] and with experimental findings [9].

From the experimental side, for instance, systematic investigations of the farasymmetric fission at the mass separator Lohengrin [10] let conclude that "fission is not only determined by the double shell closure in the heavy sphere of the scission

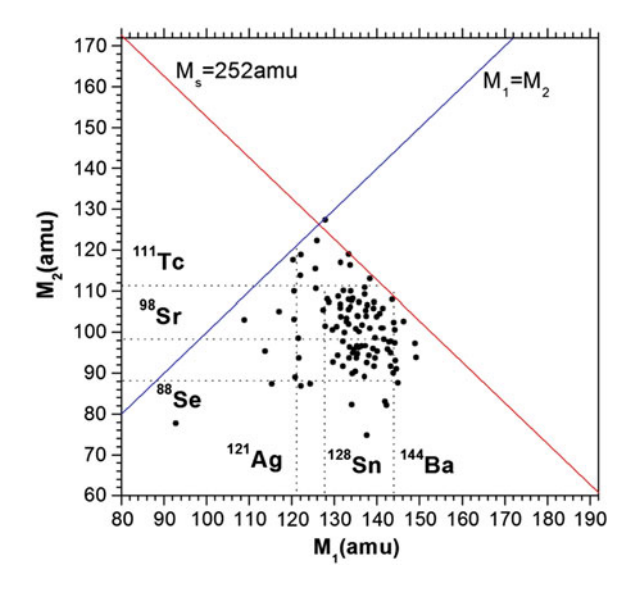


Fig. 8 Mass distribution for ternary events from the experiment at the COMETA setup. The source backing only played a role of scattering medium

point dumbbell configuration around A=132 ($Z=50, N\simeq82$) but also by the effect of the double shell closure of Z=28 and $N\simeq50$ in the corresponding light sphere".

Survival probability of the DNS is determined by the competition between its possible fusion and fission. Both partial probabilities depend from the DNS excitation energy just after scission of the mother nucleus. An idea concerning the possibility of fusion can be obtained from the driving potential for the typical fission fragment (E. A. Cherepanov, private communication) (Fig. 10).

The driving potential $V_{\rm dr}$ is defined as follows:

$$V_{\rm dr} = B_1 + B_2 + V(R) - B_{\rm in}$$
,

where B_1 , B_2 , $B_{\rm in}$ are the nuclear binding energies of the DNS nuclei and the mother system, the nucleus-nucleus potential V(R) incorporates the nuclear and Coulomb potentials. The spin is supposed to be zero for all the nuclei involved. As can be inferred from the figure fusion is preferable at any division of the mother nucleus. At the same time initial DNS representing, for instance, the pair of 82 Ge (magic)/ 25 Ne nuclei should overcome essential barrier (up to six MeV) depending on the excitation energy of the DNS on its way to fusion. Comparable barrier preserves the system from fission. Thus, the heights of the barriers let expect the DNS life time at least in the nanosecond range.

86 Yu.V. Pyatkov et al.

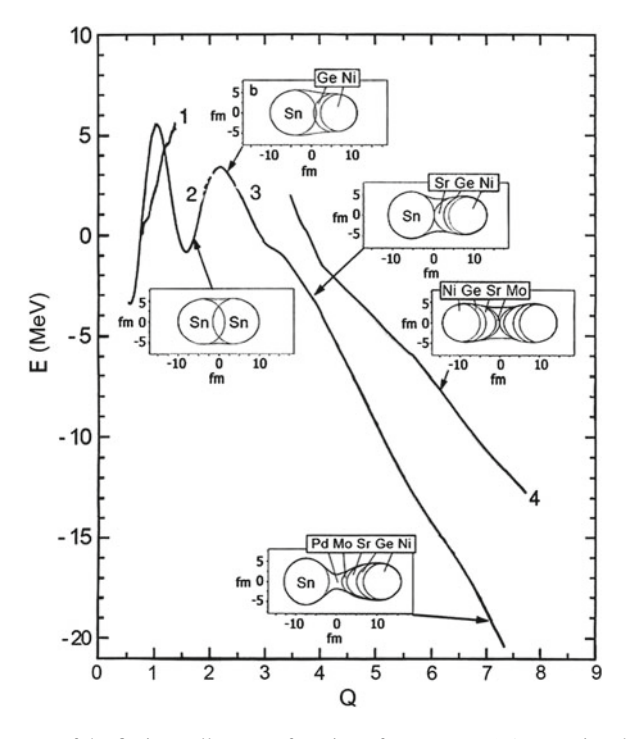


Fig. 9 The bottoms of the fission valleys as a function of parameter Q (proportional to the quadrupole moment) for 246 Cm. The panels depict the shapes of the fissioning system at the points marked by arrows

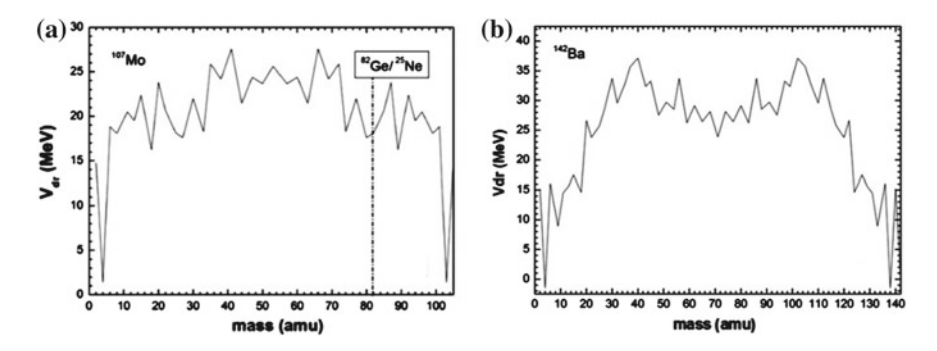


Fig. 10 Driving potential of the DNS as a function of the mass of one of the fragments for the 107 Mo (a) and 142 Ba (b) nuclei

We suppose the break-up of the DNS to be the result of its inelastic scattering in the degrading foil. Decreasing of the inter-center distance between the constituents of the molecule during the front impact leads to increasing of interaction energy sufficient to overcome the barrier (Fig. 11).

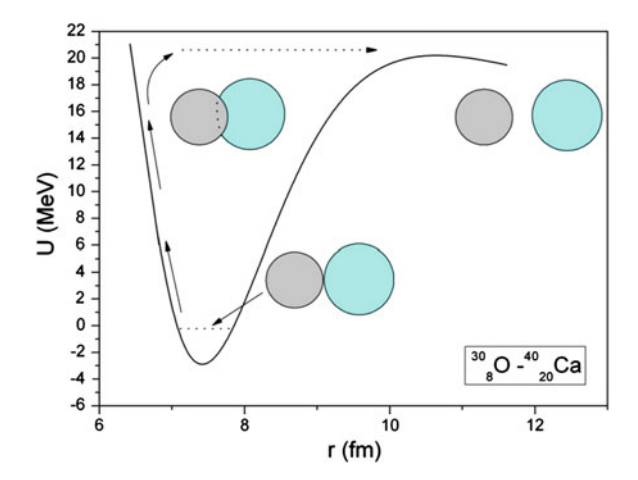


Fig. 11 Interaction energy of two nuclei as a function of the distance between their centers. See text for details

4 Conclusions

- A new mechanism of ternary decay based presumably on the Rutherford break-up of the fragment in the shape-isomeric state is observed.
- 2. Break-up is only one of the different ways leading to the CCT.
- 3. The results obtained let us to suppose that the bulk of the fragments from the conventional binary fission are born in the shape-isomeric states.
- 4. The conclusions above can be regarded as preliminary until further estimation of the life times of the shape isomers under discussion will be obtained.

5 Congratulation

I'd like to join cordially to the congratulations addressed to Prof. Itkis and say many thanks for his role in my own professional trajectory based on the effective formula: help by fruitful criticism.

References

- 1. Yu.V. Pyatkov et al., Eur. Phys. J. A45, 29 (2010)
- 2. Yu.V. Pyatkov et al., Eur. Phys. J. A48, 94 (2012)
- 3. V.V. Vladimirski, JETP (USSR) 5, 673 (1957)
- 4. V.V. Pashkevich et al., Int. J. Mod. Phys. E18, 907 (2009)
- 5. Yu.V. Pyatkov et al., Phys. At. Nuclei **66**, 1631 (2003)

88 Yu.V. Pyatkov et al.

6. V. Pashkevich et al., Int. J. Mod. Phys. **E19**, 718 (2010)

- 7. Yu.V. Pyatkov et al., Nucl. Phys. **A611**, 355 (1996)
- 8. U. Brosa et al., Phys. Rep. **197**, 167 (1990) 9. Yu.V. Pyatkov et al., Phys. At. Nuclei **67**, 1726 (2004)
- 10. I. Tsekhanovich et al., Nucl. Phys. **A688**, 633 (2001)

Features of Nuclear Reactions with Light Weakly Bound Nuclei at Energies Near the Coulomb Barrier

N.K. Skobelev, Y.E. Penionzhkevich, S.M. Lukyanov, V. Kroha, A. Kugler and J. Mrázek

Abstract Experiments for studying the cross sections of fusion and transfer reactions involving beams of halo (⁶He), cluster (⁶Li and ⁷Li), and loosely bound (³He) nuclei and nuclei of light and heavy elements are presented. The analysis of the experimental cross sections for these reactions was undertaken. The specific features of the behavior of the cross sections of evaporation residual nuclei and transfer reaction products at energies near the Coulomb barrier were observed. In particular, there was an increase in the fusion cross sections with halo nuclei at sub-barrier energies. The neutron and cluster transfer cross sections in the reactions with cluster nuclei reach their maximum values at an energy near the Coulomb barrier.

1 Introduction

Understanding the mechanisms of fusion and transfer reactions with beams of radioactive and weakly bound stable nuclei is essential for the synthesis of superheavy elements and astrophysics. Small binding energies of the valence nucleons in halo nuclei and nuclear clusters in loosely bound nuclei should influence the processes of interacting nuclei at energies close to Coulomb reaction barriers. Moreover, the possibility of the occurrence of the reaction affects the $\mathcal Q$ value, which is typically positive in these cases.

Reactions induced by halo nuclei such as ⁶He have been actively studied by numerous scientific centers. The studies revealed several interesting phenomena, i.e., the sub-barrier fusion enhancement and high probability of direct processes (particle breakup, one- and two-nucleon transfer reactions) which have different reaction mechanisms [1–4].

Similar to radioactive nuclei with a halo structure, loosely bound nuclei, such as ^{6,7}Li, etc., have a low threshold of breakup into clusters, and thus a high probability

N.K. Skobelev (⊠) · Y.E. Penionzhkevich · S.M. Lukyanov Joint Institute for Nuclear Research, Dubna, Moscow Region, Russia e-mail: skobelev@jinr.ru

V. Kroha · A. Kugler · J. Mrázek Nuclear Physics Institute, Řež, Prague, Czech Republic

© Springer International Publishing Switzerland 2015 W. Greiner (ed.), *Nuclear Physics: Present and Future*, FIAS Interdisciplinary Science Series, DOI 10.1007/978-3-319-10199-6_9 90 N.K. Skobelev et al.

of clusterization in an excited state. The 6 Li threshold excitation energy for the formation of the $\alpha+d$ clusters is 1.47 MeV, and 7 Li is observed to decay into the $\alpha+t$ clusters at the excitation energy exceeding 2.47 MeV. These threshold values are of the same magnitude as the two-neutron separation energy for 6 He, which is 0.975 MeV. Transfer reactions may dominate at different bombarding energies below the Coulomb barrier because of both the cluster structure of nuclei and a large positive Q value. Can one expect any specific features to arise in reactions that involve stable projectiles, such as 3 He, and have low binding energy of 7.718 MeV (2.57 MeV/A)? Since 3 He is characterized by a lower proton separation energy ($S_p=5.49\,\mathrm{MeV}$) and a low two-proton separation energy ($S_{2p}=7.71\,\mathrm{MeV}$), reactions with 3 He should result in an increasing contribution from direct reactions, such as pickup and stripping reactions.

This report is aimed at investigating the reaction mechanisms that arise from bombardment of ⁴⁵Sc, ¹⁹⁷Au, and Pt with ⁶He, ⁶Li, and ³He ions at energies in the vicinity of the Coulomb barrier. The goal was accomplished by analyzing excitation functions for the formation of various nuclides as products of the complete fusion, and radioactive nuclei in direct reactions, including those with a positive *Q* value.

2 Experimental Procedure

The experiments were conducted at the JINR accelerator complex DRIBs [4], the U-400M JINR cyclotron with ACCULINNA separator [5] and the U120M cyclotron of the Institute of Nuclear Physics of the Czech Republic in Řež [6] using the activation technique. After the irradiation of thin 45 Sc, 197 Au, and Pt foils by the beams of accelerated 6 He, 6 Li, and 3 He ions, the induced activity in targets was measured. All measurements were carried out using an HPGe detector with 50% efficiency relative to NaJ and the HWHM of 1.3–1.8 keV for a γ -ray energy of 1.3 MeV. To identify the nuclides produced in the reactions, we considered their γ -decay energies and lifetimes and used the nuclear data [7].

3 Experimental Results

3.1 Fusion Reactions

Based on the measured yields of isotopes formed after the evaporation of neutrons from the compound nucleus 203 Tl and taking into account the 6 He beam intensity and the target thickness, we calculated the cross sections for the formation of various isotopes and determined their dependence on the bombarding energy (the excitation functions) [4]. Contrary to the excitation functions for neutron evaporation x = 3 - 7 (Fig. 1), the cross sections for the 2n-evaporation channel (the nucleus 201 Tl is formed) are significantly higher than the values calculated using the statisti-

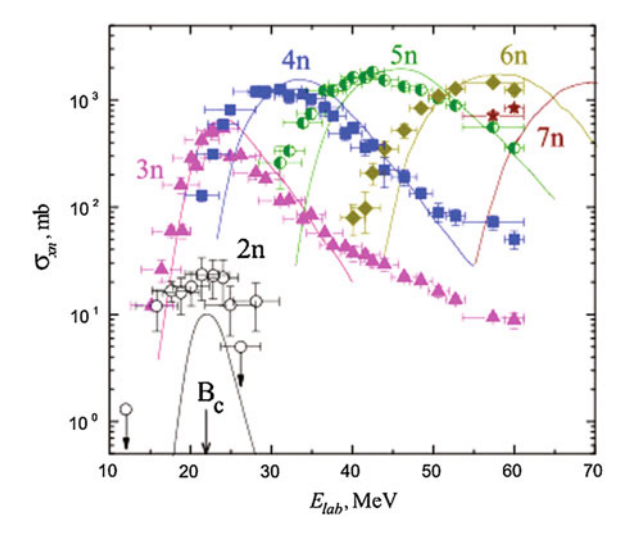


Fig. 1 Excitation functions for the 197 Au + 6 He \rightarrow $^{203-xn}$ Tl reaction, where x=2-7. The symbols are evaporation channels (2n–7n). The curves are the calculations with the "ALICE-MP" code, using the following parameters for the interaction potential: $r_0=1.29$ fm, V=-67 MeV and d=0.4 fm. B_c is the Coulomb barrier

cal model with the one-dimensional barrier between the interacting nuclei. This may be connected with the fact that the reaction with total absorption of 6 He by the 197 Au target nucleus has a large positive Q value equal to +12.2 MeV.

We have observed quite a similar situation in the case of the interaction of 6 He with 206 Pb. The difference between the two reactions lies in the fact that in the 6 He $+^{206}$ Pb case, the Q value is equal to +4.2 MeV. The difference between the experimental and calculated data is particularly well seen in Fig. 2, where the excitation function

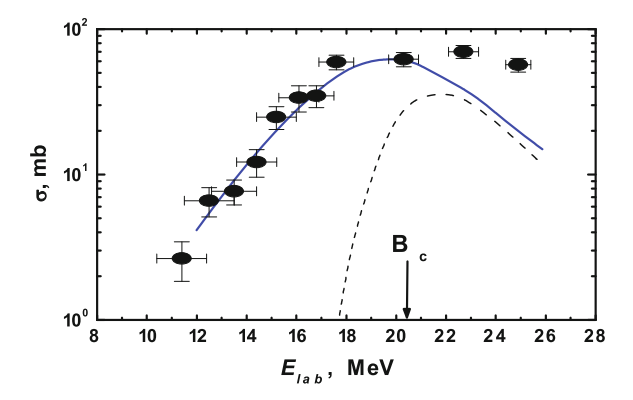


Fig. 2 Excitation function measured for the 206 Pb(6 He, 2 n) 210 Po reaction. The experimental cross sections for the formation of 210 Po(\bullet), dashed line—calculations within the framework of the statistical model, solid line—calculations using the two-step fusion model [9], B_c is the Coulomb barrier

92 N.K. Skobelev et al.

for the $^{206}\text{Pb}(^{6}\text{He}, 2n)^{210}\text{Po}$ reaction is shown. According to the statistical model calculations (see the dashed line), the cross section for this reaction at the peak of the excitation function should be small since its maximum is located at energies below the Coulomb barrier [8]. The agreement between the experimental reaction cross sections for the $^{206}\text{Pb}(^{6}\text{He}, 2n)^{210}\text{Po}$ reaction and the data calculated for the two-step fusion process can be considered as evidence that the sequential fusion process for weakly bound nuclei is the main process which influences the fusion probability of ^{6}He with ^{206}Pb and leads to an increase in the reaction cross section at energies deeply below the barrier. The data on fusion reactions, followed by the evaporation of two neutrons ($^{206}\text{Pb} + ^{6}\text{He}$ and $^{197}\text{Au} + ^{6}\text{He}$) at energies close to the Coulomb barrier differ from predictions within the framework of the statistical model for compound nuclei decay. Strong enhancement is observed for these exit channels, which is in agreement with prediction of the sequential fusion model [9].

The sub-barrier fusion has recently been investigated in detail in the reactions with beams of loosely bound cluster nuclei $^6\mathrm{Li}$ and $^7\mathrm{Li}$ bombarding $^{209}\mathrm{Bi}$ [10, 11] and $^{198}\mathrm{Pt}$ [12]. These fusion reactions have a large positive Q value for $^{198}\mathrm{Pt}$ and a small negative Q value for $^{209}\mathrm{Bi}$. The experimental excitation functions for individual fusion channels and excitation functions for complete fusion obtained by summing up cross sections for all evaporation channels were compared with the calculated excitation functions for evaporation models that take into account coupled channels. Compared with the calculations, no suppression or enhancement of fusion cross sections was found in these studies for the reactions with $^6\mathrm{Li}$ and $^7\mathrm{Li}$.

In studies on the reaction 197 Au + 3 He, the Q value for the compound nucleus reaction is 10.84 MeV, and it is possible to observe appreciable cross sections for fusion products in the sub-barrier energy region. The cross section measurements for the 197 Au(3 He, 2n) 198 Tl and 197 Au(3 He, 3n) 197 Tl reaction channels were performed using the 3 He beam at the U120M cyclotron, Řež. Figure 3 shows a sum of the cross sections for the 2 N and 3n evaporation reaction channels as a function of 3 He energy.

The production cross sections of ¹⁹⁷Tl and ¹⁹⁸Tl calculated with the NRV program [13] and the PACE [14] code are also presented in the Fig. 3. As can be seen from the figure, the results of the calculation done with the PACE4 code agree well with the experimental data on fusion cross sections with ³He. The comparison suggests that channel couplings in fusion reactions induced by ³He can be neglected.

3.2 Transfer Reactions

Large cross sections were observed for the first time for the neutron transfer with 6 He to the nucleus of the target in the 6 He + 197 Au reaction at sub-barrier energies [4]. The measured excitation functions for the formation of the gold isotopes 194 Au, 196 Au and 198 Au for the reaction are shown in Fig. 4.

The contribution of complete fusion with subsequent evaporation of charged particles to the formation of these isotopes is negligibly small. The neutron transfer mainly contributes to the formation of gold isotopes. Thus, the simplest ways in

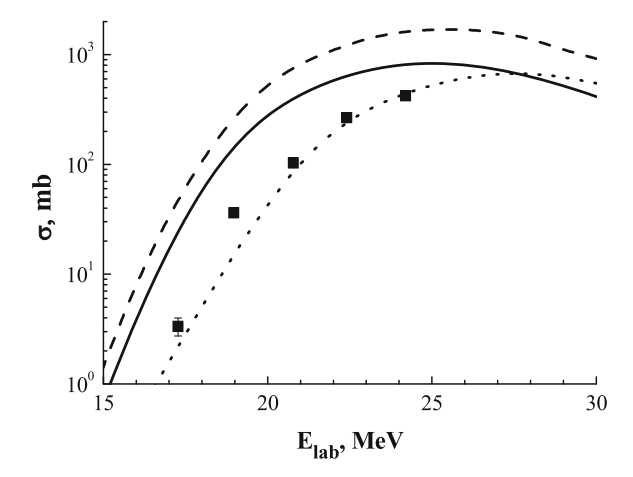


Fig. 3 The dependence of the total cross sections for the 197 Au(3 He, 2n) 198 Tl and 197 Au(3 He, 3n) 197 Tl reactions on 3 He energy (*squares*) and their comparison to the cross sections calculated with the NRV program (channel couplings taken into account, *solid line*; channel couplings not taken into account, *dashed line*) and the PACE4 code (*dotted line*). $B_c = 22.38$ MeV

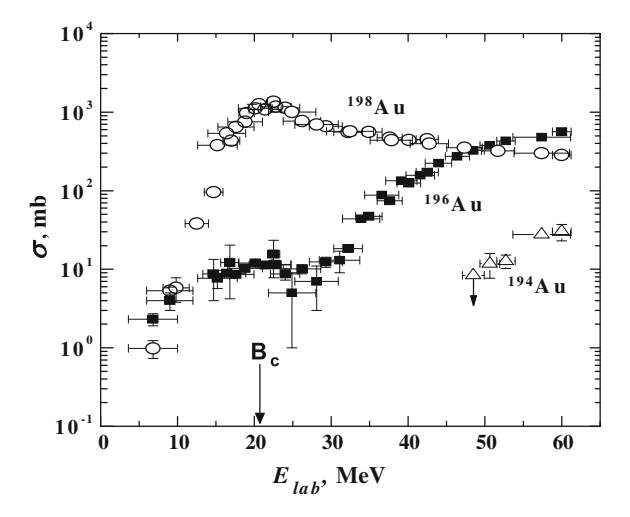


Fig. 4 Experimental excitation functions for the formation of the isotopes *triangle* 194 Au, *black-square* 196 Au and *circle* 198 Au in the 197 Au + 6 He reactions

which target-like isotopes might be formed in the given reaction are the following: the isotopes ¹⁹⁶Au and ¹⁹⁴Au result after the removal of one and three neutrons from ¹⁹⁷Au, respectively, whereas ¹⁹⁸Au is formed after the pickup by ¹⁹⁷Au of one neutron from ⁶He. The one-neutron transfer reaction from ⁶He to the ¹⁹⁷Au target at deep sub-barrier energies takes place with relatively high probability, which might be due to the interaction of quasi-free neutrons.

94 N.K. Skobelev et al.

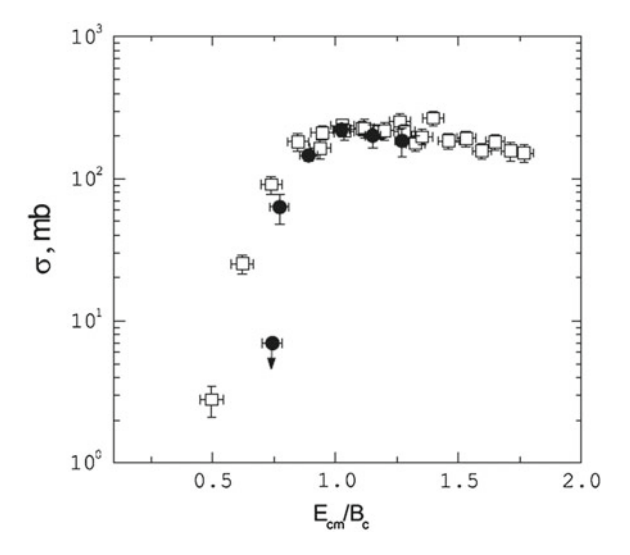


Fig. 5 Excitation function for the isotope 199 Au produced in the interaction of 6 Li with 198 Pt. The symbols represent: *bullet* our data; *square* data for the d $+^{198}$ Pt reaction are presented for comparison

Transfer reactions induced by ⁶He ions have also been studied in light nuclei [15–17]. The most complete data [17] were obtained for the ⁴⁵Sc + ⁶He reaction, in which the neutron transfer to the target nucleus was observed with a relatively large cross-section for the ⁴⁶Sc formation, reaching its maximum value near the Coulomb barrier.

In the study of the reactions with the $^6\mathrm{Li}$ beam, yields of isotopes with nucleon transfer on the target nuclei have been measured [10]. Figure 5 depicts the excitation function with the formation of isotope $^{199}\mathrm{Au}$ in the reaction $^{198}\mathrm{Pt}(^6\mathrm{Li},\alpha n)^{199}\mathrm{Au}$, which has a positive Q value. The large cross sections of reactions with the formation of gold isotopes $^{199}\mathrm{Au}$ and $^{198}\mathrm{Au}$ and the position of the excitation functions indicate that these isotopes can be formed neither in fusion nor in charge-exchange reactions. Comparison of the formation cross section values for $^{199}\mathrm{Au}$ production in reactions involving deuterons and $^6\mathrm{Li}$ nuclei indicate that, apparently, mainly in the bombardment of Pt nuclei by $^6\mathrm{Li}$, the reaction of so-called inelastic sequential breakup of $^6\mathrm{Li}$, leading to the deuteron capture, may proceed. These data were confirmed in work [18]. The one-neutron transfer cross sections for this reaction are much smaller.

It is noteworthy that the comparison of reaction cross sections for ^6Li and d shown in Fig. 5 clearly suggests a conclusion that that the deuteron cluster in ^6Li has exactly the same properties as a free deuteron in the vicinity of the Coulomb barrier. We also observed the deuteron transfer in the $^{209}\text{Bi} + ^6\text{Li}$ reaction with the maxima of the cross sections located at the Coulomb barrier [10].

Thus, in the reactions involving halo nuclei (e.g., ⁶He) and nuclei with cluster structure (such as ⁶Li), the sub-barrier nucleon or cluster transfer is observed.

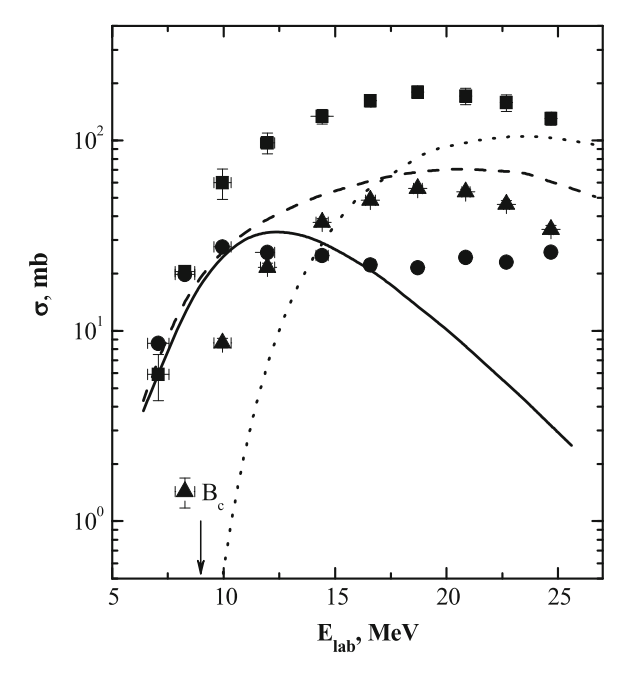


Fig. 6 The excitation functions of the reaction products $^{45}\text{Sc} + ^3\text{He}$. The cross sections are presented with symbols: *square*-cross section of the ^{45}Sc (^3He , 2p) ^{46}Sc , *triangles*— ^{45}Sc (^3He , α n) ^{43}Sc and *circles*— ^{45}Sc (^3He , α) ^{44}Sc . Curves are calculated cross sections for these reactions using the code ALICE-MP (*dashed-and-dotted, dashed and solid curves*, respectively)

It reaches its maximum in the vicinity of the Coulomb barrier, which clearly points to the peripheral nature of these reactions.

Figure $\overset{6}{6}$ shows the dependence of the Sc formation cross sections on the 3 He projectile energy. The 44 Sc and 46 Sc isotopes are formed in one-nucleon transfer reactions, which in the case of light projectiles are referred [6] to as stripping (46 Sc) and pickup (44 Sc) reactions.

Due to the positive Q value, both reactions are well manifested in ${}^3\text{He}$ energy below the Coulomb barrier. In the case of transfer to the ${}^{45}\text{Sc}$ target nucleus, one neutron from the ${}^3\text{He}$ excitation function (${}^{46}\text{Sc}$) has behavior typical of one-neutron transfer reactions. The excitation function resulting in formation of ${}^{44}\text{Sc}$ shows slightly unusual behavior. Despite the large positive Q value (+9,254 MeV) for the (${}^3\text{He}$, α) reaction, a distinct peak is observed in the excitation function near the Coulomb barrier. Competition with the (${}^3\text{He}$, α n) channel reaction manifests itself at energies above the Coulomb barrier, but the neutron pickup channel ${}^3\text{He}$ still exists and has a noticeable cross section, even with an increase in the cross section for this reaction, for example, in response to ${}^{59}\text{Co} + {}^3\text{He}$ [6].

The cross sections for the formation of 196 Au and 198 Au nuclei in the 197 Au $+^{3}$ He reaction were measured [18] (Fig. 7). It is noteworthy that in this case both reactions, 197 Au (3 He, 2p) 198 Au and 197 Au (3 He, α) 196 Au, occur at sub-barrier energies.

96 N.K. Skobelev et al.

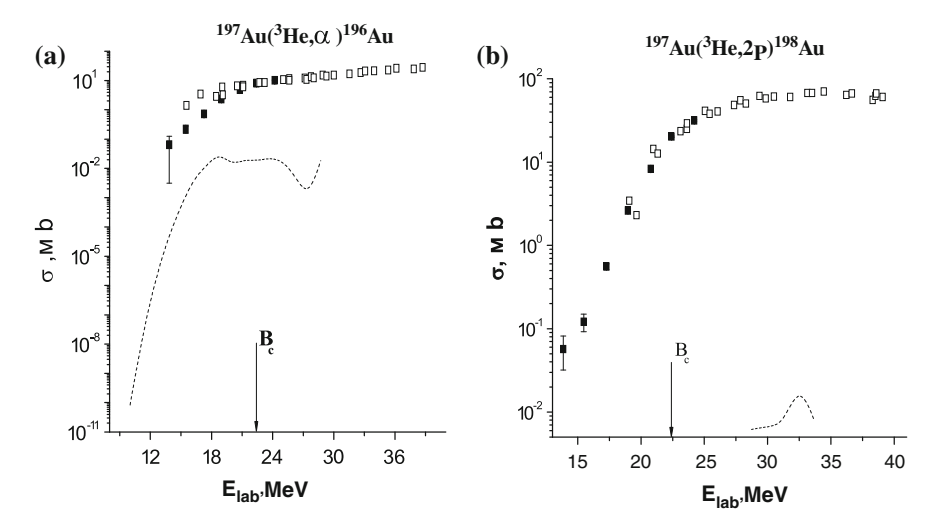


Fig. 7 The excitation functions for formation of \mathbf{a}^{196} Au and \mathbf{b}^{198} Au in the interaction of 197 Au with 3 He ($B_c = 22.38\,\text{MeV}$)

The excitation function for 196 Au, which formed the α particle just like in reactions with 45 Sc (Fig. 6), reaches its maximum near the Coulomb barrier.

4 Conclusions

We have considerably extended the experiments to study fusion and transfer reactions at higher energy of accelerated ⁶He ions (up to 20MeV/A) [5]. The comparison of calculations with the experimental data did not reveal significant suppression of complete fusion as ⁶He energy increases.

The following conclusions can be drawn from the above results:

- The data on fusion reactions, followed by the evaporation of two neutrons ($^{206}\text{Pb} + ^{6}\text{He}$ and $^{197}\text{Au} + ^{6}\text{He}$) at energies close to the Coulomb barrier, differ from predictions in the framework of the statistical model for the compound nuclei decay. For these exit channels, a strong enhancement is observed, which is consistent with calculations within the sequential fusion model.
- The data on reaction cross sections and their comparison with experiments conducted at lower energies suggest that the specific features of the nuclear structure of ⁶He are more pronounced at energies near the Coulomb barrier. As the ⁶He energy increases, the nature of the interaction in similar reaction channels does not qualitatively differ from the interaction with other light particles (α and d).
- The reaction channels with a positive Q value are well profound in the case of the interaction of weakly bound nuclei.

- In particular, in reactions with a positive Q value, neutron transfer to the target nucleus and projectile nucleus most likely occur.
- Neutron transfer reaction cross sections or cluster capture cross sections reach their maximum values in the vicinity of the Coulomb barrier in the case of the formation of a reaction product of a densely packed core or a cluster (in this case, α particles).

The authors thank Prof. M.G. Itkis for the support of international cooperation conducive to the implementation of these works, and constant interest in the obtained results.

References

- 1. L.A. Canto et al., Fusion and breakup of weakly bound nuclei. Phys. Rep. 424, 1–112 (2006)
- J.F. Liang, C. Signorini, Fusion induced by radioactive ion beams. Int. J. Mod. Phys. E 14, 1121–1150 (2005)
- J.J. Kolata et al., Breakup of ⁶He incident on ²⁰⁹Bi near the Coulomb barrier. Phys. Rev. C 75, 031302R (2007)
- Yu.E. Penionzhkevich, R.A. Astabatyan, N.A. Demekhina et al., Excitation functions of fusion reactions and neutron transfer in the interaction of ⁶He with ¹⁹⁷Au and ²⁰⁶Pb. Eur. Phys. J. A 31, 185–194 (2007)
- N.K. Skobelev, Yu.E. Penionzhkevich, A.A. Kulko, Study of fusion and nucleon transfer channels for the reaction ¹⁹⁷Au + ⁶He at ⁶He energies up to 20 MeV/A. Izv. RAN. Ser. Fiz. 77, 396–402 (2013) (Bull. Russ. Acad. Sci. Ser. Phys. 77, 360–365 (2013))
- N.K. Skobelev, A.A. Kulko, Y.E. Penionzhkevich et al., Cross sections for isotopes ⁴³Sc and ⁴⁶Sc in the ⁴⁵Sc + ³He reaction. Izv. RAN. Ser. Fiz. 77, 878–882 (2013) (Bull. Russ. Acad. Sci. Ser. Phys. 77, 795–799 (2013))
- S.Y.F. Chu, L.P. Ekström, R.B. Firestone, The Lund/LBL Nuclear Data (1999), http:// nucleardata.nuclear.lu.se/nucleardata/toi/
- 8. Yu.E. Penionzhevich at al., Deep sub-barrier fusion enhancement in the 6 He + 206 Pb reaction. Phys. Rev. Lett. **96**, 162701 (2006)
- V.I. Zagrebaev, Sub-barrier fusion enhancement due to neutron transfer. Phys. Rev. C 67, 061601 (2003)
- Yu.E. Penionzhkevich et al., Complete and incomplete fusion of ⁶Li ions with Bi and Pt. J. Phys. G. Nucl. Part. Phys. 3, 025104 (2009)
- 11. A.A. Hassan, S.M. Lukyanov, R. Kalpakchieva, Yu.E. Penionzhkevich et al., Bull. Russ. Acad. Sci. Ser. Phys. **70**, 1785 (2006)
- 12. A. Shrivastava, A. Navin et al., Phys. Rev. Lett. **103**, 23702 (2009)
- 13. Fusion code of the NRV, http://nrv.jinr.ru/
- O.B. Tarasov, D. Bazin, LISE++: radioactive beam production with in-flight separators. Nucl. Instr. Meth. B 266, 4657–4664 (2008), http://groups.nscl.msu.edu/lise/
- A. Di Pietro et al., Reactions induced by the halo nucleus ⁶He at energies around the Coulomb barrier. Phys. Rev. C 69, 044613 (2004)

98 N.K. Skobelev et al.

 A. Navin et al., Direct and compound reactions induced by unstable helium beams near the Coulomb barrier. Phys. Rev. C 70, 044601 (2004)

- 17. N.K. Skobelev, A.A. Kulko, V. Kroha et al., Excitation functions for the radionuclides ⁴⁶Sc produced in the irradiation of ⁴⁶Sc with deuterons and ⁶He. J. Phys. G. Nucl. Part. Phys. **38**, 03510 (2011)
- 18. N.K. Skobelev, Y.E. Penionzhkevich, E.I. Voskoboynik et al., Fusion and transfer cross sections of ³He induced reaction on Pt and Au in energy range 10–24.5 MeV. Phys. Part. Nucl. Lett. **11**, 114 (2014)

Stability Peninsulas in the Neutron-Rich Sector

K.A. Gridnev, V.N. Tarasov, D.K. Gridnev, X. Viñas and Walter Greiner

Abstract Using HF + BCS method with Skyrme forces we analyze the neutron drip line. It is shown that around magic and new magic numbers the drip line may form stability peninsulas. It is shown that the location of these peninsulas does not depend on the choice of Skyrme forces. It is found that the size of the peninsulas is sensitive to the choice of Skyrme forces and the most extended peninsulas appear with the SkI2 set.

1 Introduction

One of the fundamental questions in nuclear physics is what combinations of neutrons and protons can build up a stable nucleus. The nuclear landscape called nuclear chart is shown in Fig. 1. A large number of stable isotopes are still nuclear "terra incognita". Moving away from stable nuclei by adding either protons or neutrons, one finally reaches the particle drip lines where the nuclear binding ends. Stable nuclei are confined between proton and neutron drip lines, beyond which it is impossible to add any to the nucleus protons or neutrons. The nuclei beyond the drip lines are unbound to nucleon emission.

The yet unexplored parts of the nuclear chart may help answering many questions of fundamental importance: What are the limits of nuclear existence? What are the properties of nuclei with an extreme N/Z ratio? There are also related important questions in the field of nuclear astrophysics. Nuclei far from stability valley are different from that around the stability line: here one finds the distortion of the

K.A. Gridnev (⋈)

Saint Petersburg State University, Uljanovskaja 1,198504 St. Petersburg, Russia e-mail: kgridnev@yahoo.com

V.N. Tarasov

NSC, Kharkov Institute of Physics and Technology, Akademicheskaya 1, Kharkov 61108, Ukraine

D.K. Gridnev · W.Greiner

Frankfurt Institute of Advanced Studies, Routh-Moufang-Strasse 1, 61348 Frankfurt, Germany

X.Viñas

University of Barcelona, Diagonal 645, E-08028 Barcelona, Spain

© Springer International Publishing Switzerland 2015 W. Greiner (ed.), *Nuclear Physics: Present and Future*, FIAS Interdisciplinary Science Series, DOI 10.1007/978-3-319-10199-6_10 100 K.A. Gridnev et al.

known "magic" numbers, large spatial extensions of such nuclei and other interesting structural phenomena [1].

The standard theoretical approach in locating the neutron drip line is to take a stable nucleus with a fixed proton charge Z and increase the number of neutrons N until the resulting nucleus would be "overloaded" in the sense that it gets rid of extra neutrons through decay. This method, however, implies a simple structure of the drip line, namely, that every line corresponding to a fixed number of protons on the nuclear chart crosses the neutron drip line only once. Yet, it might happen that the drip line has a more complicated structure [2–11]. In the vicinity of "magic" numbers or "quenched magic" numbers the following scenario can take place. At some point being filled with neutrons the nucleus looses its stability but then after adding more neutrons the stability is restored. This leads to a new phenomenon in nuclear physics: formation of stability peninsulas on the nuclear chart, see Fig. 1. The analysis of the phenomenon of stability restoration through adding neutrons has been undertaken in [2–11], where long isotope rows of the elements Pb, Zr, Ar, Kr, Rn, Gd, Ba, S, U were considered. Thereby, the phenomenon of stability restoration through adding neutrons was in focus. Having found such new isotopes we also investigated their properties like masses, deformation, root mean square radii etc. The stability peninsulas appear for almost all variants of the Skyrme forces: they are all elongated

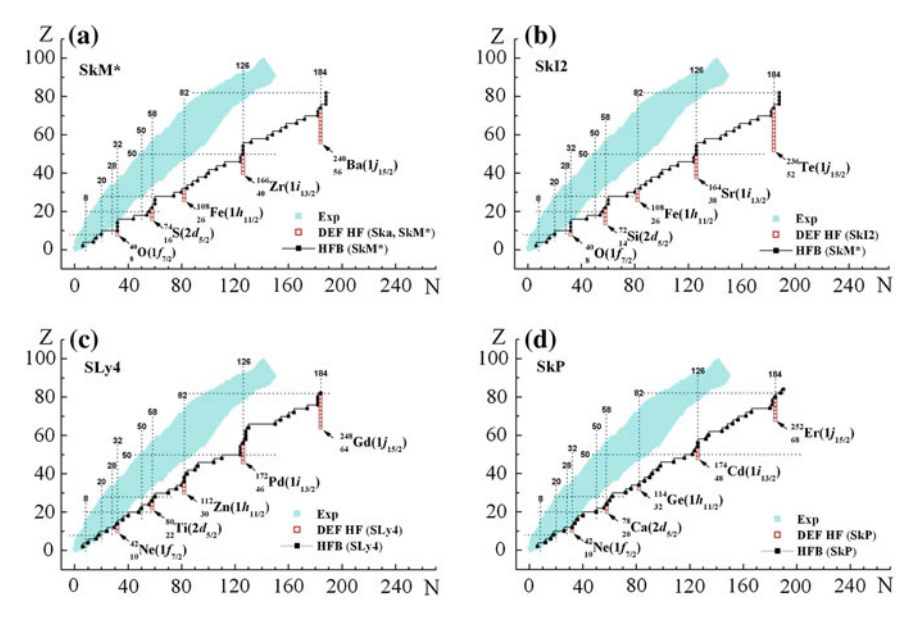


Fig. 1 The nuclear chart and the 1n *drip line*. Filled blue area shows experimentally known nulei. The *solid line* going through the *dark squares* is the 1n *drip line* in HFB calculations [1]. Red empty squares a nuclei stable against one–neutron emission according to DEF HF calculations with SkM* (a), SkI2 (b), SLy4 (c) and SkP (d) forces. The dotted line goes corresponds to magic numbers N = 8, 20, 28, 50, 82, 126, 184 and to the new magic numbers N = 32, 58

along magic numbers but the degree of elongation depends on the particular type of force.

2 Results

The aforementioned scenario of formation of stability peninsulas has been analyzed by us in [2–11] for the isotopes of O, Ar, Ni, Zr, Kr, Pb, Rn and other elements. The calculations were performed using the HF+BCS approach with Skyrme forces accounting for deformations (DEF HF approach). In [4–8] it was shown that nuclei lying close to such peninsulas possess low–lying quasistable one–particle states. By adding neutrons one makes these levels dive into the discrete spectrum, thus stabilizing the isotope.

The discussion of the DEF HF method one finds, for example in [3]. The DEF HF calculations are performed using the deformed harmonic oscillator basis, where the basis parameters are optimized on each iteration, for details see [3]. The optimization procedure consists in choosing optimal oscillator frequencies, which minimize the total energy within a given basis. Let us mention that the optimization procedure facilitates the calculation and, more important, corrects the basis functions for the spatially extended density distributions near the drip line [3]. The pairing constant is set to $G = (19.5/A)[1 \pm 0.51(N-Z)/A]$, where the plus and minus signs refer to protons and neutrons respectively. In DEF HF calculations we include only bound one particle states. In spite of ignoring the continuum states this method still provides a good agreement with the HFB, see [4–8]. Since all nuclei, which lie on the stability peninsulas are spherical we also use a spherical code (SPH HF) , which solves the HF equations directly rather than using a particular basis. In the BCS scheme of the spherical code we implement the inclusion of localized quasibound continuum states.

We used the following sets of Skyrme forces Ska, SkM*, SLy4, SkI2 and SkP (below under Skyrme forces we shall mean only these sets of forces). Stability peninsulas originate for all Skyrme forces, which produce low–lying quasibound one–particle states with high angular momentum (which are responsible for a high centrifugal barrier confining the particles).

The observed stability peninsulas with respect to one neutron emission are shown in Fig. 1 for different Skyrme forces. It is easy to see from Fig. 1 that the formation of peninsulas on the neutron drip line happens at the same N values for all forces but peninsula edges have different Z values.

It should be stressed that nuclei forming stability peninsulas are spectrally bound in the sense that there exists a well-defined ground state wave function, which minimizes the energy functional for such nuclei. At this point they become well-defined compact objects and the question about their lifetime becomes correctly formulated. And though for some nuclei it may be energetically favorable to get rid of two or more neutrons, a large centrifugal barrier of the last filled levels may serve as an indication that this lifetime would be large.

102 K.A. Gridnev et al.

We found that Ska and SkM* forces occupy an intermediate position between SkI2 and SkP, in the sense that more elements are stable with SkI2 and less with SkP. The forces SkI2 are the most optimistic, at the same time the formation of stability peninsulas for SkP is rather rare. The difference between two of these forces is depicted in Fig. 1.

In Fig. 1 one finds the comparison with benchmark HFB calculations [1]. We denote one–neutron separation energy by S_n . By definition, 1n drip line separates on nuclear chart the regions, where $S_n > 0$ (nuclei stable against one neutron emission) and $S_n \le 0$ (nuclei unstable against one neutron emission). In our method we use the Koopmans theorem to approximate one neutron separation energy S_n through the energy of the last occupied level and determine the drip line from the condition $S_n = 0$, where even small positive S_n indicates the stability against one–neutron emission.

In drip line in Fig. 1 for various Skyrme forces has typical bend points around known magic numbers N=82 (SLy4), 126 (SkM*, SkI2, SLy4, SkP), 184 (SkM*, SkI2, SLy4, SkP) and also for N=32 (SkM*, SkI2, SkP) and 58 (SkM*, SkI2, SLy4, SkP). The bend points indicate the stability enhancement around these N-values. It is worth noting that the stability peninsulas are formed for various Skyrme forces around the same neutron numbers. As we have already mentioned the stability restoration results from low–lying quasibound states, which immerse into the bound spectrum for higher N, see [4–8].

Below we list the stable isotopes that form stability peninsulas and the responsible subshells for the Skyrme forces SkM* and Ska. $1f_{7/2} - ^{40}$ O; $2d_{5/2} - ^{76}$ Ar, 74 S; $1h_{11/2} - ^{110}$ Ni, 108 Fe; $1i_{13/2} - ^{174}$ Cd, 172 Pd, 170 Ru, 168 Mo, 166 Zr; $1j_{15/2} - ^{256}$ Hf, 254 Yb, 252 Er, 250 Dy, 248 Gd, 246 Sm, 244 Nd, 242 Ce, 240 Ba. From Fig. 1 it can be seen that the stability peninsulas with SkI2 forces are by one or two Z longer than those formed with SkM*. For N=184 the last stable isotope with SkI2 forces is 236 Te having Z=52, which is close to the magic Z=50. The neutron to proton ratio in 236 Te reaches N/Z=3.54. In the case of 40 O one has N/Z=4! For SLy4 and SkP forces the whole nuetron drip line becomes shifted in the positive Z direction. The edges of stability peninsulas for SLy4 are formed by the isotopes 42 Ne, 80 Ti, 112 Zn, 172 Pd, 248 Gd. And for SkP forces the edges of stability peninsulas correspond to the isotopes 42 Ne, 78 Ca, 114 Ge, 174 Cd, 252 Er.

For all Skyrme forces the nuclei forming stability peninsulas are spherical in DEF HF calculations, which is characteristic of magic numbers. The spherical form allows to run additional check with SPH HF method, where pairing is treated more precisely. Such additional calculations were done for 40 O, 74 S, 108 Fe, 166 Zr and 240 Ba using SkM*, and taking into account localized states with $n \le 10$ and $l \le 14$. The pairing contribution for these nuclei was equal to zero, which testifies for the magicity of corresponding neutron numbers. Let us add that 74 S (SkM*, Ska), 72 Si (SkI2), 80 Ti (SLy4) and 78 Ca (SkP) have N = 58.

The most impressively extended stability peninsula occurs at N = 184. Figure 2 shows the fragment of the neutron drip line around N = 126 and 184 for SkM* forces (Fig. 2a) and SLy4 forces (Fig. 2b). The edge of stability peninsula, which is formed at N = 126 (SLy4 forces) corresponds to 172 Pd (Fig. 2b). The quasistable 170 Ru is

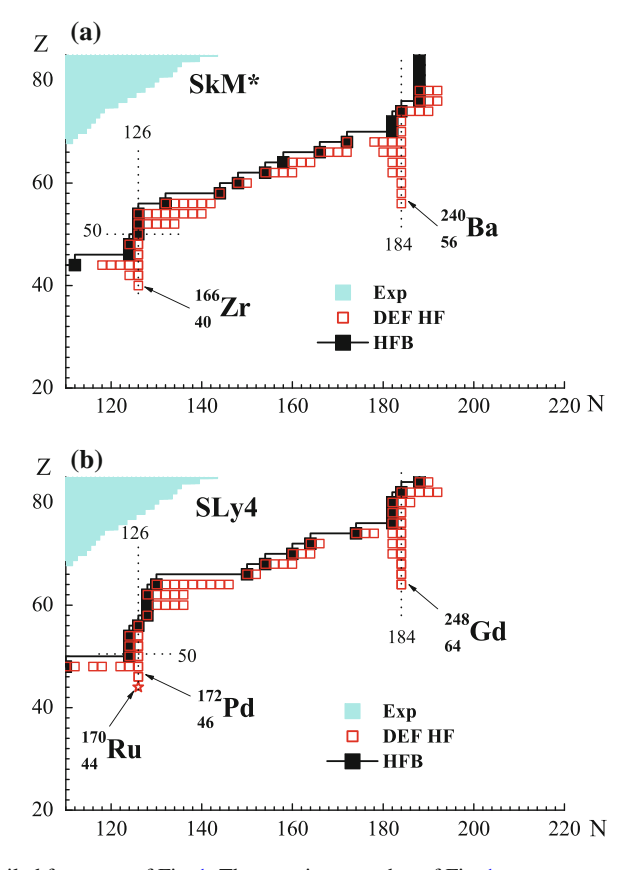


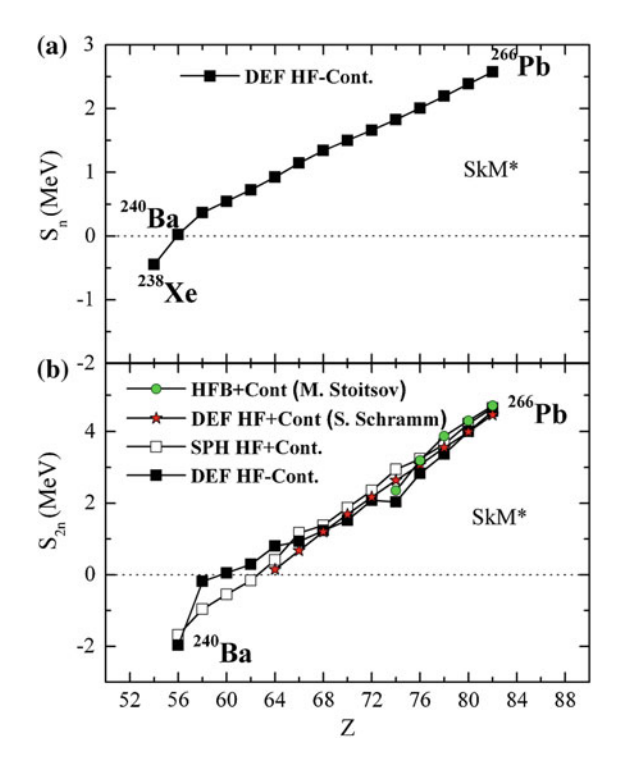
Fig. 2 A detailed fragment of Fig. 1. The notations are that of Fig. 1

marked with a star on Fig. 2b; its last filled level with quantum numbers $1i_{13/2}$ has a positive energy 0.27 MeV, but the centrifugal barrier, which corresponds to this state has a height of 9.28 MeV. One can see that that the peninsulas broaden with higher Z. Such broadening of peninsulas allows for some nuclei lying at these peninsulas a correct evaluation of two–neutron separation energies $S_{2n} = E(Z, N-2) - E(Z, N)$. The shift of the drip line compared to HFB calculations results from the different conditions for its determination, namely, zero one neutron separation energy (in the Koopman's approximation) in our case and zero chemical potential in the HFB method.

Figure 3 shows one neutron separation energies for the isotone chain N=184 (SkM* forces). One can see that S_n and S_{2n} decrease monotonically. The nucleus 240 Ba lies on the edge of stability peninsula, its one neutron separation energy is very small $S_n=0.024\,\mathrm{MeV}$ (DEF HF calculation) and $0.064\,\mathrm{MeV}$ (SPH HF calculation). The last filled one–particle level is $1\,j_{15/2}$, which has the HF potential with the centrifugal barrier height of $8.58\,\mathrm{MeV}$.

104 K.A. Gridnev et al.

Fig. 3 One and two-neutron separation energies for the series of isotones corresponding to N = 184 for SkM* forces, a One neutron separation energies in DEF HF calculations without continuum states in the BCS scheme. b Two-neutron separation energies. Dark sauares are DEF HF calculations (without continuum in the BCS). Light squares are SPH HF calculations with continuum states. Red stars are DEF HF in grid calculations with continuum states. Green circles are HFB calculations [1]



Two-neutron separation energies for isotones corresponding to N=184 are shown in Fig. 3b. For Z=56,58,60 and N=184 we used the binding energies of the isotopes, which are not stable against one neutron emission. This might, of course, reduce the precision of S_{2n} values. One can see that DEF HF, SPH HF and HFB calculations are in good agreement. The nucleus 248 Gd, which has Z=64 has a positive S_{2n} value. Thus for N=184 the stability peninsula contains isotopes that are stable against both one and two-neutron emission. Let us emphasize again that accounting for continuum states hardly affects the values of S_{2n} when N=184. This is a consequence of N=184 being a magic number.

In conclusion, using DEF HF (oscillator basis and grid) and SPH HF approaches with Skyrme forces we show that stability peninsulas, which contain nuclei stable against either 1n or 2n emission or both, may exist beyond the conventional theoretically predicted 1n drip line. The peninsulas are formed at N=32,58,82,126,184, which are either magic or new magic numbers. This was shown for various choices of Skyrme forces. All isotones with such neutron numbers are spherical. Since stability peninsulas lie along magic neutron numbers, the obtained results should not depend strongly on the way of accounting pairing correlations. All this indicates that the neutron drip line may have a more complicated structure than it was assumed earlier.

References

- 1. M.V. Stoitsov et al., Phys. Rev. C 68, 054312 (2003)
- 2. K.A. Gridnev et al., Eur. Phys. J. A 25(S01), 353 (2005)
- 3. K.A. Gridnev et al., Int. J. Mod. Phys. E 15, 673 (2006)
- 4. V.N. Tarasov et al., Bull. Russ. Acad. Sci. Phys. 71, 747 (2007)
- 5. V.N. Tarasov et al., Int. J. Mod. Phys. E 17, 1273 (2008)
- 6. V.N. Tarasov et al., Bull. Russ. Acad. Sci. Phys. 72, 842 (2008)
- 7. V.N. Tarasov et al., Phys. Atom. Nucl. **71**, 1283 (2008)
- 8. V.N. Tarasov et al., Bull. Russ. Acad. Sci. Phys. 74, 1559 (2010)
- 9. V.N. Tarasov et al., in *Book of Abstracts of LX*, ed. by A.K. Vlasnikov. International Conference on Nuclear Physics (NUCLEUS-2010), (St. Petersburg, 2010), p. 55
- 10. V.N. Tarasov et al., Phys. Atom. Nucl. **75**, 17 (2012)
- S. Schramm, D. Gridnev, V.N. Tarasov, D.V. Tarasov, W. Greiner, Int. J. Mod. Phys. E 21, 1250047 (2012)
- 12. G. Audi et al., Nucl. Phys. A 729, 337 (2003)

Part III Nuclear Fission

Dynamics of Collinear Ternary Fission

Wolfram von Oertzen, K.R. Vijayaraghavan and M. Balasubramaniam

Abstract True ternary fission of heavy nuclei has been predicted under conditions of large Z^2/A -parameters, and a decay into three fragments of comparable masses has been predicted repeatedly. Studies for these ternary decays with third fragments with masses around A=40 have been done using the missing mass approach with two FOBOS-detectors in coincidence at 180° . A new kind of radioactive fission decay, the so called collinear cluster tri-partition (CCT) has been discovered as reported in Refs. [1, 2], namely for spontaneous fission of 252 Cf(sf) and with neutron induced fission in 235 U(n, fff). We discuss the dynamics of the collinear ternary fission decay in a model, where the ternary decay is considered to be a sequential process of two binary decays, with two neck ruptures in a strongly deformed (hyperdeformed) nucleus. The kinetic energy of the third fragments are calculated as well as the potential energy surfaces are discussed for the ternary collinear decay.

1 Introduction: Ternary Fission

The phenomenon of ternary fission for heavy nuclei has been discussed already 40–50 years ago. These decays can easily be predicted using the liquid drop model [3–6]. True ternary fission, with comparable masses of the fragments, appears with a higher Q-value as compared to binary fission, because the three fragments are all closer to the maximum of the values of $E_{\rm B}/N$ (binding energy/nucleon). A particular feature for larger values of the charges of the three fragments is the fact, that the emission of the three fragments occurs collinearly. This has been predicted also in

Dedication This paper is dedicated to the 70th birthday of Michail Itkis, a highly appreciated colleague and friend.

W. von Oertzen (⊠)

Helmholtz Zentrum Berlin, Hahn Meitner Platz 1, 14109 Berlin, Germany e-mail: oertzen@helmholtz-berlin.de

M. Balasubramaniam · K.R. Vijayaraghavan Department of Physics, Bharathiar University, Coimbatore 641046, India e-mail: m.balou@gmail.com

© Springer International Publishing Switzerland 2015 W. Greiner (ed.), *Nuclear Physics: Present and Future*, FIAS Interdisciplinary Science Series, DOI 10.1007/978-3-319-10199-6_11 110 W. von Oertzen et al.

theoretical earlier work e.g. [5, 6] and references therein. This fact has been neglected in the earlier experiments, see Refs. [7, 8], and therefore has remained undiscovered until recently, see in particular Refs. [1, 2].

2 The Collinear Ternary Fission Process

In the recent analysis of the fragmentation potentials of the true ternary fission process in Ref. [9], the potentials for oblate and prolate (collinear) geometries have been compared (see Figs. 1 and 2). The shapes for touching spheres are shown in Fig. 1, the dominant part of the differences between the two geometries are due to the *Coulombinteraction*. From the fragmentation potentials the relative yields (the yield for α 's can not be obtained correctly) can be predicted by the statistical model and they are shown in Fig. 2. We observe, that for third fragments A3, heavier than $M_3 = 35$ (the crossing point of the two curves for the yields with the two geometries), the prolate (collinear) fission for comparable three fragments will dominate by many orders of magnitude. Looking into the calculations of Ref. [9], it can be easily understood that this effect is due to the dominance of the Coulomb interaction, the nuclear potential is weak in comparison.

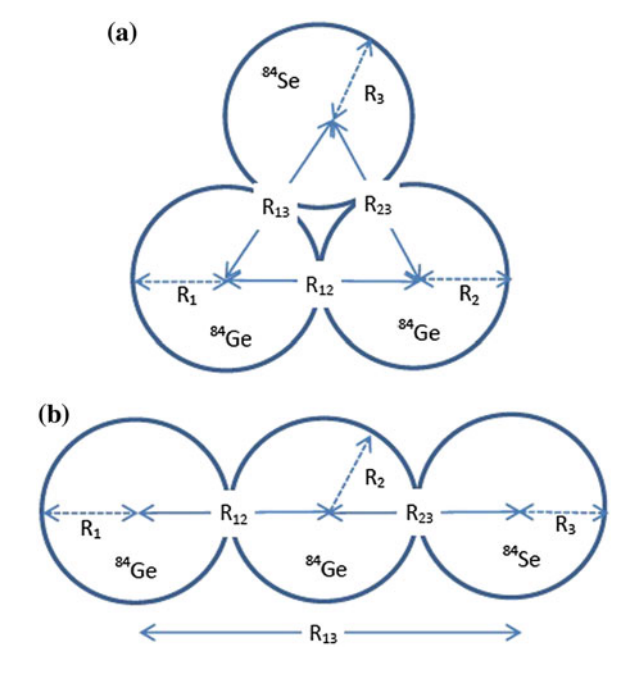
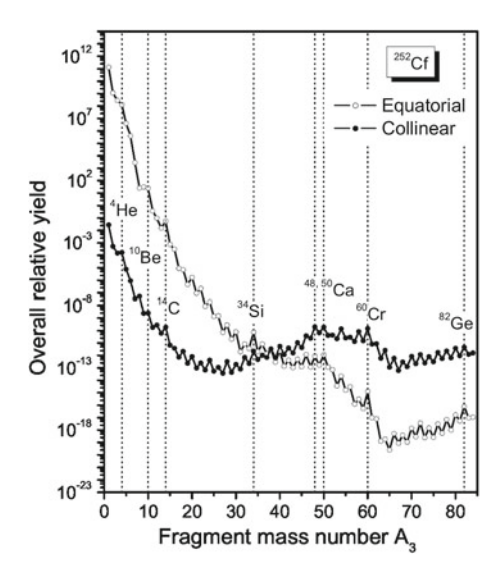


Fig. 1 The two geometries of three clusters in the ternary decay (true ternary fission). The fragmentation potentials of the two arrangements are calculated, see Ref. [9]. a Equatorial, b collinear

Fig. 2 Curves for relative yields in ternary decays of ²⁵²Cf(sf) are compared (from Ref. [9]) for oblate (equatorial, triangular) and prolate (collinear) geometries. Prolate fission dominates for heavier third fragments, A₃



2.1 Some Experimental Facts

Previous experiments have mainly concentrated to observing light particle emission perpendicular to the fission axis, see Refs. [7, 8]. According to Ref. [9] true ternary fission is dominated by prolate (collinear) ternary geometries and the corresponding fission yields are many orders of magnitude larger then those for oblate (triangular) geometries. Actually, in an experiment devoted for the establishment of true ternary fission in an triangular geometry for ²⁵²Cf(sf), a detector set-up was used to detect three coincident masses with the possible heaviest third particle, by Schall et al. [10], with four segments of gridded ionisation chambers (covering each a range of 80°). These ionisation chambers have been previously used in a system called "Diogenes", they imply a lower energy threshold of 25 MeV, which was set in order to reduce background. This experiment gave a lower limit for true ternary decays of 1×10^{-8} , relative to binary decays. The yield with this limit is connected to larger masses of the three particles (and relative angles of ca. 120°) with a central nuclear fragment at around A = 35 - 50. This experimental result once more emphasizes, as discussed above, that true ternary fission will occur collinearly. In Ref.[1] the process was therefore called collinear cluster tri-partition (CCT).

The fact, that true ternary decay in nuclei with large charges, has to occur *collinearly* was shortly discussed in [11]. Collinear decay has been neglected in the work on fission in the last decades [7, 8], thus it came as a surprise that it has been observed in the work presented in Refs. [1, 2], there the ternary decay is observed by the missing mass method. In a binary coincidence with two Fobos-detectors [12] placed at 180°, two vectors of the ternary decay are completely determined (two angles, two energies, two masses). In the sequential decay (see Ref. [13])

112 W. von Oertzen et al.

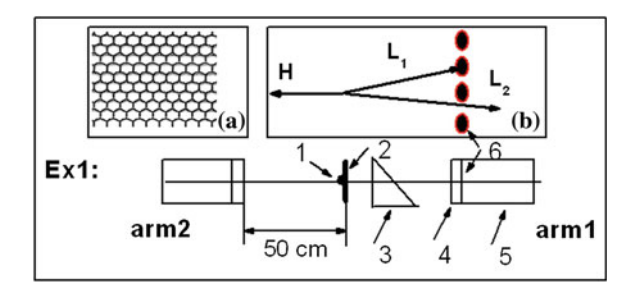


Fig. 3 The geometry of the experimental arrangements with the Fobos-detectors from Ref. [1]: ternary decay from the Cf-source (marked with label I) with one fragment (H) moving to the left and the intermediate fragment to the right, splitting into two (L1 and L2) lighter fragments. The entrance of the main Fobos-detectors has a support-grid with a beehive-structure (a). The angular dispersion of the two lighter fragments due to the passage through the backing of the source (and the blocking one of them on the support-grid), creates a missing mass event in the coincidences of M1 and M2

two fragments are emitted in the direction opposite to the first fragment. The latter two are emitted towards arm1 at a relative angle of 0° , however, they are dispersed to small relative angles by passing through dispersive media, namely, the backing of the source or target: $50 \,\mu\text{g/cm}^2$ of (Al_2O_3) , and the foils of the start detector positioned only in one of the detector arms, in arm1. This produces an angular dispersion (see Ref. [14] for details) between the two fragments of 0.5° , traveling to the ionisation chamber towards arm1. With this circumstance and the support grid (beehive-honey-comb) in front of the main Bragg-ionisation counter, separating its high pressure gas region from the low pressure PPAC (Parallel Plate Counters), a blocking of one of the fragments can occur. These give position information in x, y, (and timing signals) and block one of the fragments, while the other passes though the grid, see Refs. [1, 2] and Fig. 3. In the final analysis the differences of the coincident counts (arm1–arm2) is taken. In this experiment a relative yield of 4.3×10^{-3} per binary fission has been observed (Fig. 4).

As a test for the observed phenomenon we show the experimental results with similar conditions from Refs. [1, 2] for neutron induced fission 235 U(n, fff) using thermal neutrons from the reactor of JINR at Dubna. Also in this experiment with a target of $100\,\mu\text{g/cm}^2$ uranium, the support has been an Al_2O_3 backing of $50\,\mu\text{g/cm}^2$ pointing to arm1. The target was integrated in a special start detector to obtain a very compact device for the time of flight measurements (TOF), which give a mass resolution of $2{\text -}3$ a.m.u. In total 1.6×10^6 events have been recorded in this experiment with 235 U(n, ff). In this case the projections of coincident events on the M_s - and the M_1 -axis are shown in Fig. 5. Whereas the projection on M_1 shows again a bump for the Ni-isotopes, the missing mass bump in the M_s -spectrum is lower in mass, then in the case of 252 Cf(fff), implying the dominance of the Sn and Ni-clusters, and resulting in a smaller ternary central fragment.

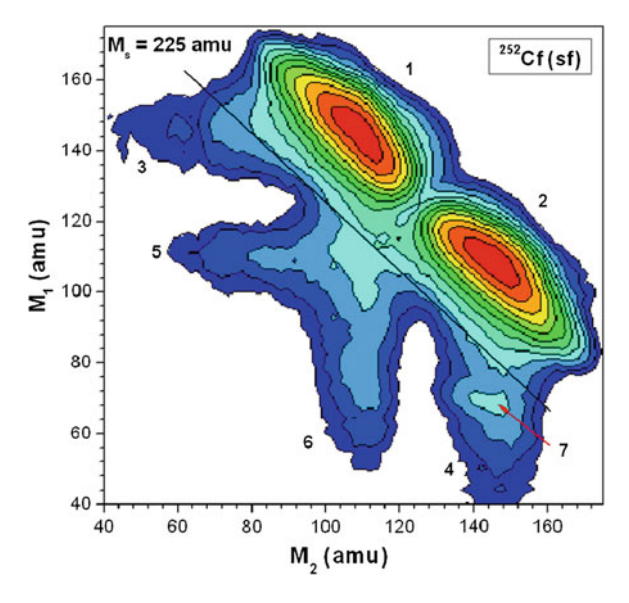


Fig. 4 The binary coincidences of two registered masses in Fobos-detectors, M1 and M2, at relative angles of 180° . The missing mass events are created due to the dispersion of the two fragments moving towards arm1, after passage through the backing of the source, and the blocking of one (see Fig. 3). Missing mass events appear *below* the region of the coincidences of M1 and M2, from binary fission. Note the *line* with (M1 + M2) = 225 shown for illustration. The missing mass events (a broader bump) are *centered* around the peak labeled 7, with a missing mass of A3 = (40-48)

3 The Phase Space and Potential Energy Surface (PES) of Ternary Fission Decay

One of the major objections of the referees of the papers published (Refs. [1, 2]) has been the high yield of 4.3×10^{-3} relative to the binary fission observed. Other objections were connected to the fact that with the detection of Ni-isotopes in the coincidences with 132 Sn, mostly Ca-isotopes have been observed as the missing fragments. Also the collinearity of the fragments had been questioned, we give the result of a calculation of the ternary fission valley at the end of this paper (see Figs. 9 and 10). In the following we clarify the circumstances leading to the high yield of the observed phenomena, mainly determined by the phase space of the process. All these questions are connected to a proper appraisal of the phase space. The latter problem is connected to the potential energies for different configurations. With Ca at the center we have a $10\,\text{MeV}$ deeper value of PES (see Figs. 6 and 7).

W. von Oertzen et al.

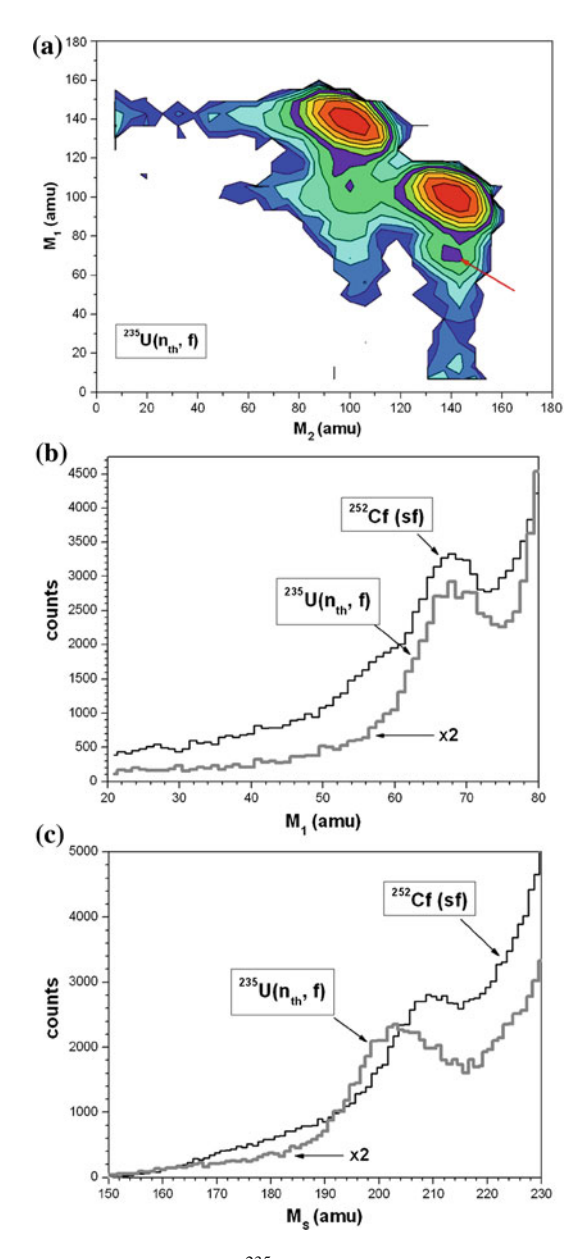


Fig. 5 The results of the fission reaction 235 U(n, fff) measured with a modified FOBOS (mini-Fobos) set-up. For technical details we refer to the paper on CCT by Pyatkov et al. [1]. For the comparison with other systems the projections onto the axis with the sum M_s of the registered masses are shown. The projection on M_1 shows the dominance of the Sn and Ni-clusters, the projection on M_s shows for 235 U(n, fff) the shift towards smaller mass, implying a smaller total mass and a smaller mass for the central ternary fragments, isotopes of S and Ar, instead of Ca in the case of 252 Cf(ffff)

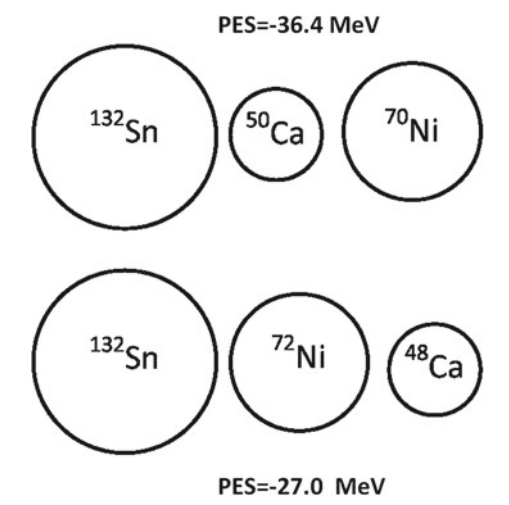


Fig. 6 Geometrical arrangements for the potential energies (dominated by the Coulomb interaction) of two collinear geometries of the three clusters (Sn + Ca + Ni), illustrating the difference in the PES, for different central fragments

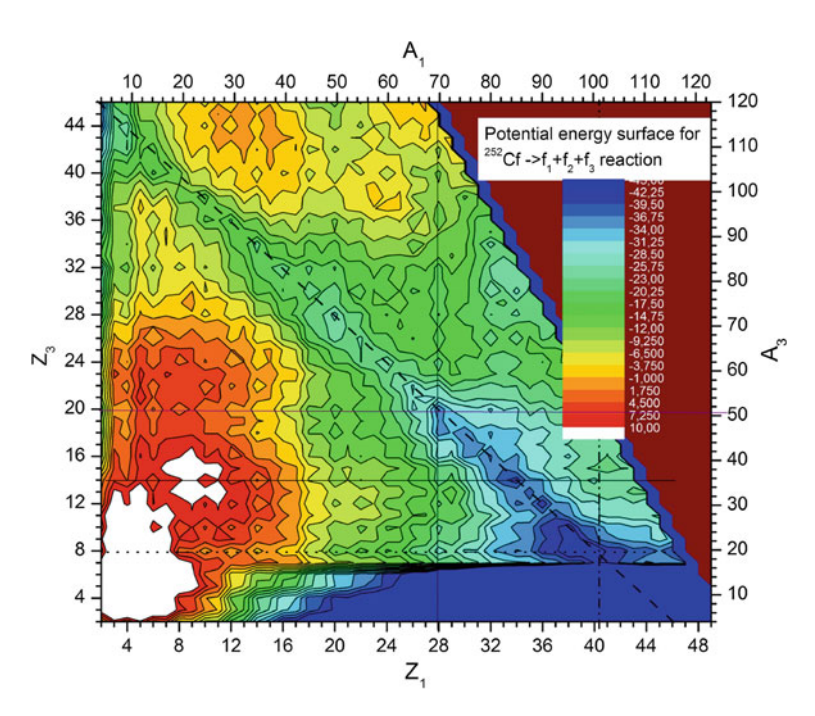


Fig. 7 The potential energy surface (PES) for the ternary decay of 252 Cf(fff), for the range of fragments (Z_3 , Z_1) with (A_3 , A_1) between 10 and 80. This gives a potential valley, with two minima for the different order of the two charges (Z_3 , Z_1) as (20, 28) or (28, 20), (*courtesy of A. Nazirov*)

W. von Oertzen et al.

3.1 The Phase Space of Ternary Fission Decay

Fission decay is proceeding as a statistical decay, see also Ref. [15], from an equilibrated compound nucleus as formulated in the Hauser-Feshbach theory of the decay of compound nuclei. The potential energy surfaces (PES, and *Q*-values) govern the range of momenta, the number of pairs of fragments, with the ranges in mass and charge favored in the decay. The most important ingredients in this model describing the total decay probability are enumerated below. There is principally no model dependence, the statistical factors are active, when the fragments are separated at the scission point. The factors governing the decay probability are:

- (1) The penetration factors in the sequence of binary channels,
- (2) The phase space of the decay:
 - (a) Q-values for the different channels (fragment combinations). Momentum range in each channel.
 - (b) number of open channels, combinations (A3, A1) allowed by the Q-values,
 - (c) number of excited states in each fragment in the different channels,
- (3) Statistical factors, spin and spin-multiplicity of these states, formed in different fragment combinations. As the most important factor we discuss the PES.

In the calculations of Vijay et al. [13], using the assumption of a sequential decay (two neck ruptures in a short time sequence) as illustrated in Fig. 8, the PES and kinetic energies in different fragment combinations have been calculated. In this figure we show a PES-Q-value-surface for the various fragment combinations. We find, that in the mass ranges of M1 and M2 (48–54) and (133–128), there are 30 fragment combinations for decay-channels with favorable Q-values. In the fragments due to favorable conditions (Q-values), the number of excited states, in the average (N = 5, or more) can be populated, with spins up to 6^+ (many spins are observed

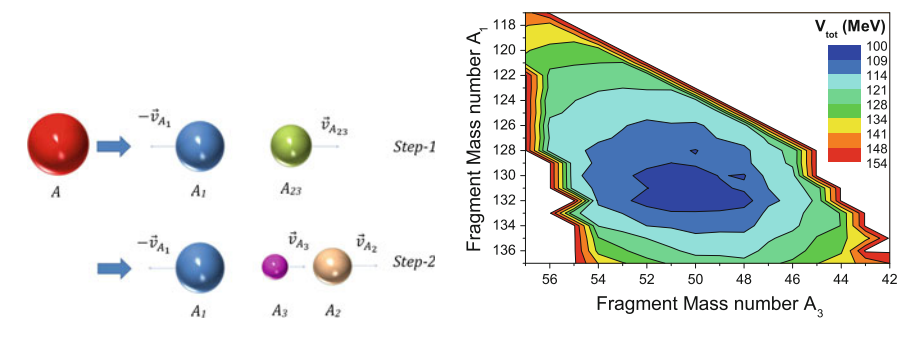


Fig. 8 The sequential ternary fission decay of the collinear arrangements of the three clusters (Sn + Ca + Ni). With this assumption, the *Q*-value ranges $(right \ side)$ and the kinetic energies of the fragments have been calculated, see Ref. [13]

in γ -spectroscopy of fission fragments, see Ref. [16] and citations therein). The average spin multiplicities would be $\langle M \rangle = 10$. With higher momenta due to the rather high Q-values for "true ternary fission", a total phase space factor of 5,000 or more is expected, as the factor to be multiplied to the probability for a single isotopecombination, and if compared to single isotope light particle emission, as observed in previous work on "ternary fission" [7]. This fact explains the large relative yield of CCT mentioned before, it refers to a bump of ternary fission fragments in the mass spectrum, similar to the "bumps" observed in binary fission.

3.2 Potential Energy Surface for Three Clusters

The potential energy surface (PES) for ternary decays has been calculated by Nazirov [17], Vijayaraghavan et al. [13] and Balasubramanian et al. [18]. We see particular minima (with optimal Q-values) in the PES, in Fig. 7, giving rise to higher yields for the favored mass combinations, mostly combinations of clusters, nuclei with closed shells in the neutron or proton number.

A major item influencing the fission decay is the available potential energy. We inspect the PES as calculated by Nazirov [17] shown in Fig. 7. We note two different minima for the charge-numbers (Z_1-Z_3) in either order (20,28) or (28,20), the latter with a deeper valley, favoring the Ca-Isotopes as central fragments.

Another question has been the collinearity of the ternary decay. We have calculated the energy of the collinear three-body arrangement, as function of the deviations from a straight line [18], defined by an angle θ , as shown in Fig. 9. The result is shown in Fig. 10. The Coulomb energy is again the dominating factor, it is screened for the clusters at the borders in the linear arrangement. A valley with a strong minimum for $\theta = 0$ appears, forcing the decay into a strictly collinear geometry.

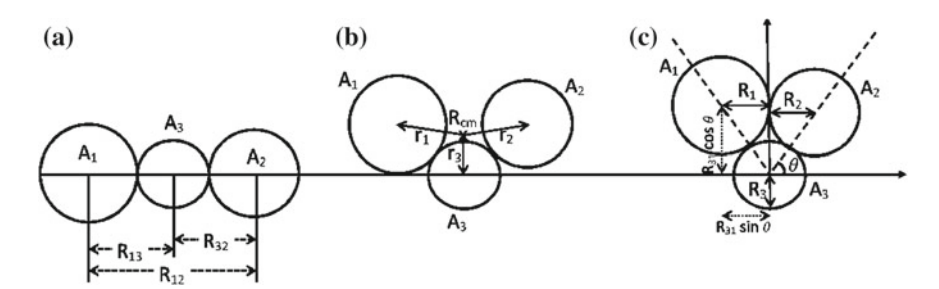


Fig. 9 The different orientations \mathbf{a} , \mathbf{b} and \mathbf{c} of three charges for the ternary decay of 252 Cf(fff), with an angle θ , giving a potential valley, into which the collinear decay will be confined [18]

118 W. von Oertzen et al.

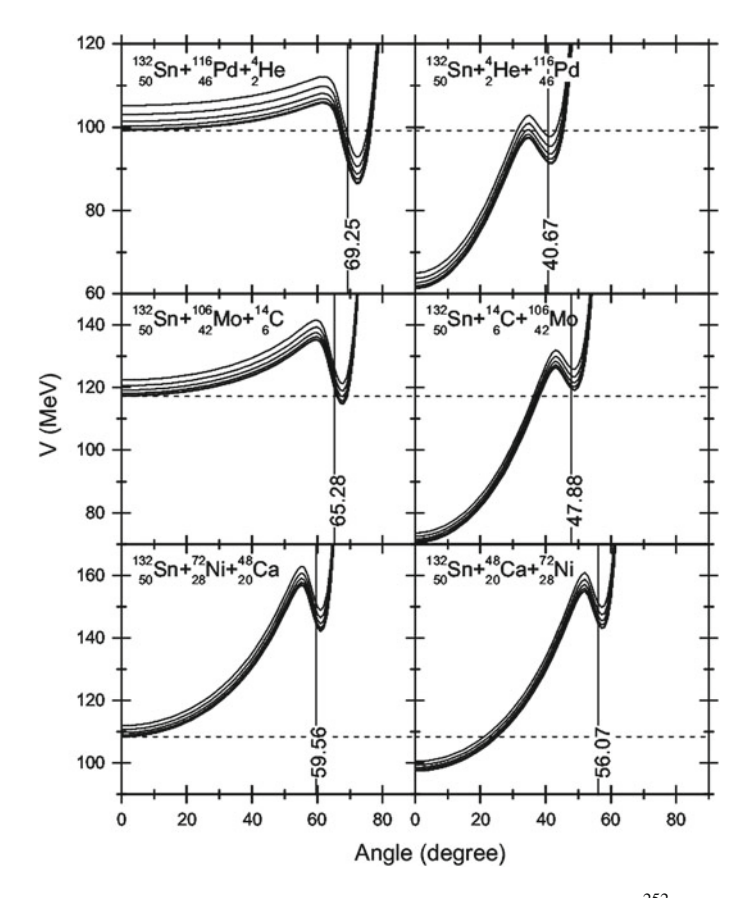


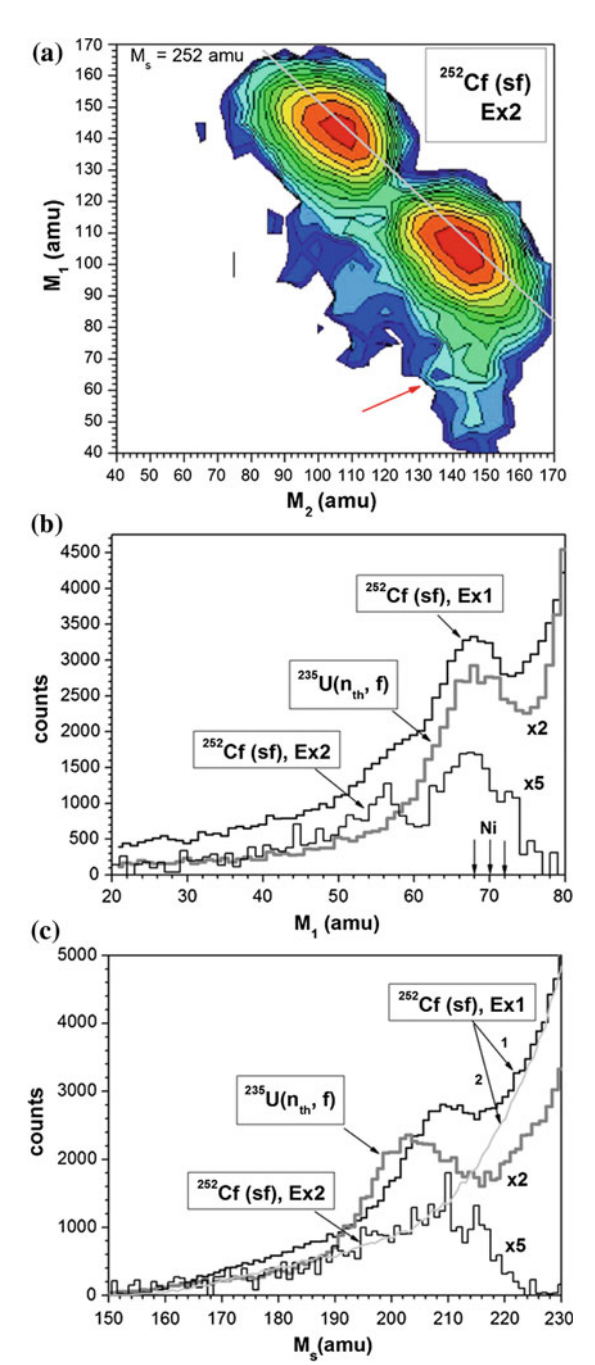
Fig. 10 The potential valleys created by three charges in the ternary decay of 252 Cf(fff) for deviations from the collinear geometry (see Fig. 9). The figure shows the steep increase of the potential energy if the orientation of the central Ni- or Ca-clusters changes, deviating from the collinear geometry with an angle θ (Fig. 9). Note the deeper valley for the case that Ca is the central fragment

4 Recent Results and Perspectives for Future Work

Recent work on true ternary fission was concerned with neutron coincidences and using Pin-diodes (instead of Fobos-detectors) for the measurements of TOF and energy. We show in Fig. 11 the result of the 252 Cf(ff, n) in coincidence with neutrons and measured with pin-diodes, instead of Fobos-counters. The background due to the scattering on the entrance support grid (see Fig. 3) has disappeared. The projections onto the M_1 and M_s axis are also shown for three cases, this experiment, as well as for the previous ones with Fobos for 252 Cf(ff, n) and for 235 U(n, fff). The essential features are very similar in all three cases (for details see Refs. [1, 2]).

We summarize, that the missing mass method for the study of collinear ternary decays has given consistent results for three independent experiments, for different

Fig. 11 Spontaneous fission in coincidence with neutrons of ²⁵²Cf(ff) in comparison with the fission reaction ²³⁵U(n, ff) measured with the Fobos (mini Fobos) set-up. For technical details we refer to the paper on CCT by Pyatkov et al. [1]. The projection on M₁ shows the dominance of the Sn and Ni-clusters, the projection on M_s shows for $^{235}U(n, ff)$ the shift towards smaller total mass, implying also smaller masses for the ternary fragments (isotopes of S and Ar). Note the lower background due to the use of pin-diodes



120 W. von Oertzen et al.

nuclei and for different detector systems. Further studies are planned with neutron coincidences, and registering the three fragments in coincidence. A unique way to study the collinear ternary (or multiple) decay will be by fission in flight after Coulomb excitation. Such experiments could be realized with inverse kinematics [19] at the fragment separator FRS at GSI (see also Refs. [20, 21]), and with the FRS's at other laboratories (MSU, RIKEN, FAIR). These experiments can be performed at energies up to 1.0 GeV/u. In this case the large momentum of the center of mass of the decaying nucleus will boost all decay vectors to high energies, allowing the registration in a multiple coincidence of all three (or more) fragments.

References

- 1. YuV Pyatkov et al., Eur. Phys. J. A 45, 29 (2010)
- 2. YuV Pyatkov et al., Eur. Phys. J. A 48, 94 (2012)
- 3. W.J. Swiatecki, *Proceedings of the Second UN Conference on the Peaceful Uses of Atomic Energy*, Geneva, vol. 15 (United Nations, Geneva, 1958), pp. 651
- 4. V.M. Strutinsky et al., Nucl. Phys. 46, 639 (1963)
- 5. H. Diehl, W. Greiner, Nucl. Phys. A 229, 29 (1974)
- 6. D.N. Poenaru, R.A. Gherghescu, W. Greiner, Nucl. Phys. A **747**, 182 (2005)
- 7. F. Gönnenwein, Nucl. Phys. A. **734**, 213 (2004). (also F. Gönnenwein, in EurophysicsNews 36/1, 11 (2005))
- 8. C. Wagemans, *The Nuclear Fission Process* (CRC Press Inc., Boston, 1991)
- 9. K. Manimaran et al., Phys. Rev. C 83, 034609 (2011)
- 10. P. Schall et al., Phys. Lett. B **191**, 339 (1987)
- W. von Oertzen, Y.V. Pyatkov, D. Kamanin, Acta Phys. Polonica 44, 447 (2013). (Zakopane Conference 2012)
- H.G. Ortlepp, W. Wagner, C.M. Herbach et al., Nucl. Instr. Meth. A 403, 65 (1998). (also, C.M. Herbach et al. Nucl. Phys. A 712, 207 (2002))
- 13. K.R. Vijayaraghavan et al., Eur. Phys. J. A 48, 27 (2012)
- 14. T. Haninger et al., Nucl. Phys. A 572, 294 (1994)
- 15. R.B. Tashkodajaev, A.K. Nazirov, W. Scheid, Eur. Phys. J. A 47, 136 (2011)
- 16. Y.X. Luo et al., Nucl. Phys. A **874**, 32 (2012). (and refs. to prior work)
- 17. A. Nazirov, JINR, Dubna, private communication
- 18. K.R. Vijayaraghavan, M. Balasubramaniam, W. von Oertzen, to be published
- 19. K.-H. Schmidt et al., Nucl. Phys. A 665, 221 (2000)
- 20. M. de Jong, C. Böckstiegel, H.-G. Clerc et al., Nucl. Phys. A **616**, 363 (1997)
- 21. A. Heinz, K.-H. Schmidt, A.R. Junghans et al., Nucl. Phys. A 713, 3 (2003)

General Laws of Quantum and Statistical Mechanics Governing Fission

Karl-Heinz Schmidt and Beatriz Jurado

Abstract It is shown that many of the apparently complex empirical features of low-energy fission can be explained by general laws of quantum and statistical mechanics. Early studies with the two-centre shell model have shown that the shells of the separated fragments decisively influence the microscopic properties of the fissioning system already way before scission. This lead us to postulate the separability of macroscopic and microscopic features of the potential energy surface, of the friction and of the inertia on the fission path. According to this postulate, only the macroscopic properties are specific to the compound nucleus, while the microscopic properties are attributed to the nascent fragments. The fragment shells may strongly differ from the shells of the separated fragments, because the Coulomb force favours strongly elongated shapes on the fission path. Scarce experimental information on prompt-neutron yields indicates that the thermal energy available at scission is fully transferred to the heavy fragment. This is explained by the laws of statistical mechanics that lead to an energy-sorting process. The semi-empirical model GEF was developed on the basis of these ideas.

1 Introduction

Nuclear fission is characterized by a huge number of final configurations and a rich variety of observables. The protons and neutrons of the fissioning system can be divided in more than thousand different ways between the two fragments. In addition, the fragments can be produced in a variety of shapes and a wide range of excitation

K.-H. Schmidt (⋈) · B. Jurado

CEN Bordeaux-Gradignan, Chemin du Solarium, B. P. 120,

33175 Gradignan, France

e-mail: schmidt-erzhausen@t-online.de

B. Jurado

e-mail: jurado@cenbg.in2p3.fr

energy and angular momentum. This is why nuclear fission is one of the best suited processes for studying the dynamical properties of microscopic systems.

Most effort is presently invested in modelling nuclear fission with stochastic [1] and with self-consistent [2] approaches. In the present contribution, however, it will be shown that a systematic view on the large body of experimental data reveals the dominant influence of general laws of quantum and statistical mechanics on the fission process. These are responsible for some very peculiar and unexpected dynamical features of the system.

2 Localization of Wave Functions in a Di-nuclear System

2.1 Systematics of Fission-Fragment Distributions

Figure 1 gives an overview on the measured mass and nuclear-charge distributions of fission products from low-energy fission. Fission of target nuclei in the actinide region, mostly induced by neutrons, shows predominantly asymmetric mass splits. A transition to symmetric mass splits is seen around mass 258 in spontaneous fission of fusion residues.

Electromagnetic-induced fission of relativistic secondary beams covers neutrondeficient nuclei from mass 204 to 234 [3]. A transition from asymmetric to symmetric fission occurs around mass 226. A pronounced double-humped structure close to

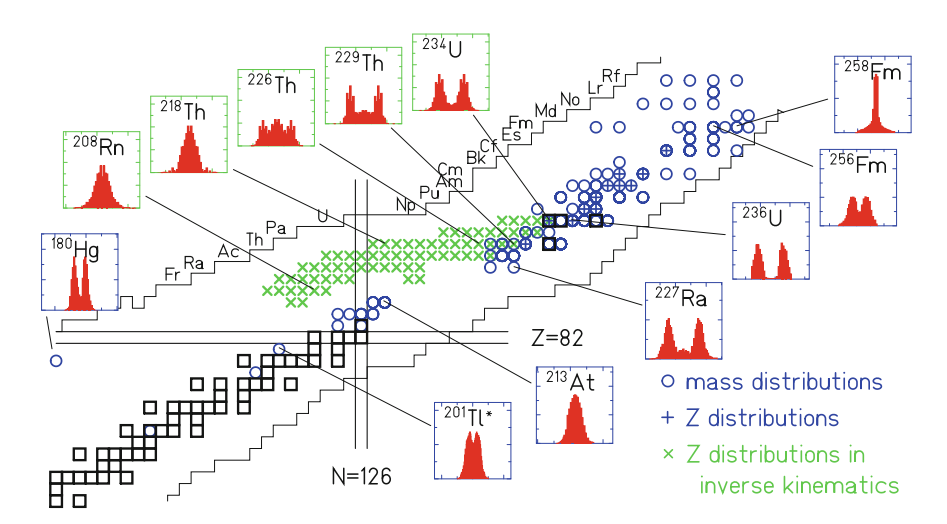


Fig. 1 General view on the systems for which mass or nuclear-charge distributions have been measured from [4]. The distributions are shown for 12 selected systems. *Blue circles (blue crosses)* Mass (nuclear-charge) distributions, measured in conventional experiments [5, 6] and references given in [3]. *Green crosses* Nuclear-charge distributions, measured in inverse kinematics [3]

symmetry appears in ²⁰¹Tl [5] and in ¹⁸⁰Hg [6]. It is difficult to observe low-energy fission in this mass range. Thus, ²⁰¹Tl could only be measured down to 7.3 MeV above the fission barrier due to its low fissility. Only ¹⁸⁰Hg was measured at energies close to the barrier after beta decay of ¹⁸⁰Tl. For ²⁰¹Tl it was observed that the structure weakens strongly with increasing excitation energy [5]. Considering this trend and extrapolating it to energies close to the fission barrier, the fission characteristics of these two nuclei, ²⁰¹Tl and ¹⁸⁰Hg, are rather comparable. Also other nuclei in this mass region show similar features [7].

In the range where asymmetric fission prevails, e.g. from 227 Ra to 256 Fm, the light and the heavy fission-product components gradually approach each other with increasing mass of the fissioning nucleus, see Fig. 1. A quantitative analysis revealed that the mean mass of the heavy component stays approximately constant [9] at about A=140. This has been explained by the influence of a deformed ($\beta\approx0.6$) fragment shell at N=88 and the combined influence of the spherical shells at N=82 and Z=50 [10].

Newer data on Z distributions over long isotopic chains [3, 11], however, revealed very clearly that the position in neutron number varies systematically over more than 7 units, while the position in proton number is approximately constant at Z=54, see Fig. 2. The rather short isotopic sequences covered in former experiments did not show this feature clearly enough and gave the false impression of a constant position in mass, although indications for a constant position in Z in proton-induced

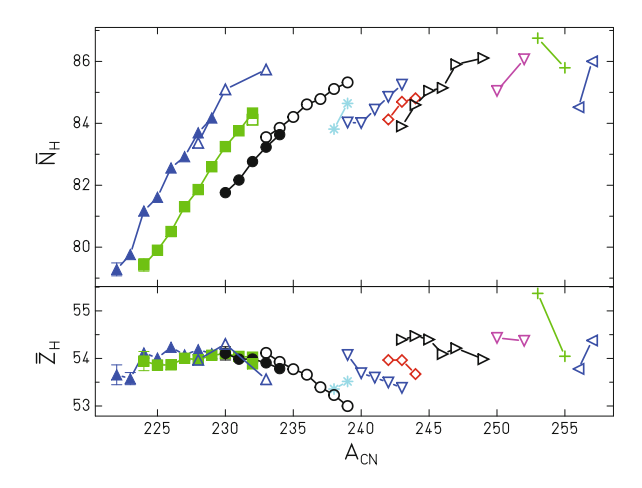


Fig. 2 Mean neutron and proton number of the heavy component in asymmetric fission before prompt-neutron emission in the actinide region from thorium to einsteinium from [4]. The lines connect the data for a fixed element. The values were deduced from measured mass and nuclear-charge distributions using the semi-empirical GEF code [8] for the correction of charge polarization (the deviation of the N/Z ratio of the primary fragments before emission of prompt neutrons from the N/Z value of the fissioning nucleus) and prompt-neutron emission. *Open symbols* denote results from conventional experiments, *full symbols* refer to an experiment with relativistic projectile fragments of ²³⁸U [3] (See [8, 11] for references of the underlying experimental data.)

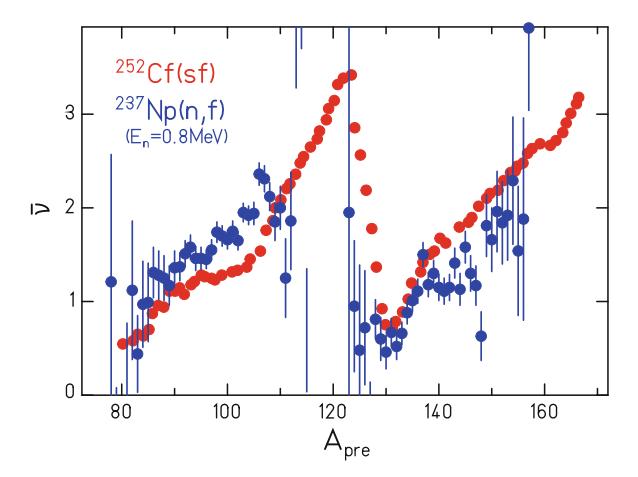


Fig. 3 Measured prompt-neutron yields as a function of the pre-neutron fragment mass for 0.8 MeV neutron-induced fission of ²³⁷Np [13] and spontaneous fission of ²⁵²Cf [14]

fission have already been deduced previously [12]. Only for the most neutron-rich systems, the curves in the upper and in the lower panel have about the same slopes with opposite signs, which indicates an approximately constant position in mass.

2.2 Mass-Dependent Prompt-Neutron Yields

In Fig. 3, the measured mass-dependent prompt-neutron yields are shown for two representative systems, with rather different mass, ²³⁷Np(n,f) [13] and ²⁵²Cf(sf) [14]. It seems that the prompt-neutron yields for the same fragments are very close for the two systems. The larger total prompt-neutron yield for ²⁵²Cf(sf) is essentially caused by the shift of the light fission-fragment group to heavier masses, where the prompt-neutron yield increases strongly.

2.3 Separability Principle

When the two-centre shell model became available, it was possible to study the single-particle structure in a di-nuclear potential with a necked-in shape. Investigations of Mosel and Schmitt [15] revealed that the single-particle structure in the vicinity of the outer fission barrier already resembles very much the sequence of single-particle levels in the two separated fragments directly after scission. They explained this result by the general quantum-mechanical feature that wave functions in a necked-in potential are already essentially localized in the two parts of the system.

This finding immediately leads to the expectation that the shells on the fission path that are responsible for the complex structure of fission modes are essentially given by the fragment shells. Potential-energy surfaces of fissioning systems calculated

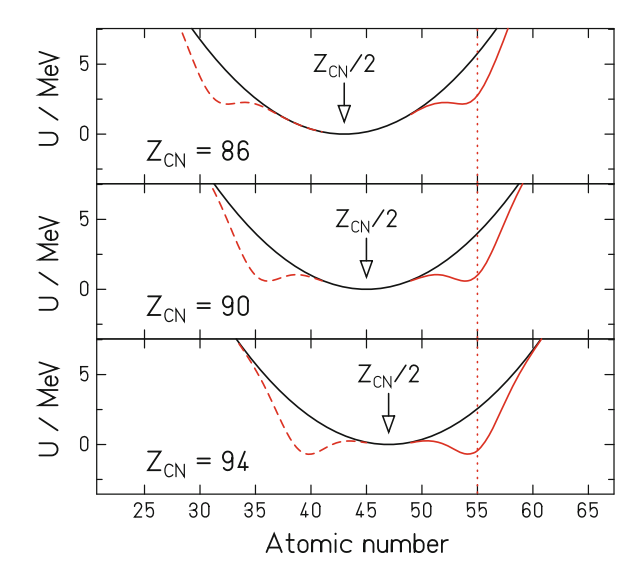


Fig. 4 Schematic illustration of the potential energy for mass-asymmetric shape distortions on the fission path, after an idea of Itkis et al. [17]. The *black curve* shows the macroscopic potential that is minimum at symmetry, while the *red curve* includes the extra binding due to an assumed shell at Z = 55

with the macroscopic-microscopic approach (e.g. Ref. [16]) support this assumption. Itkis et al. [17] quoted this feature as a qualitative argument to explain the systematic features of the fission-fragment distribution depicted in Fig. 1. Figure 4 illustrates the interplay of macroscopic and microscopic contributions to the potential-energy surfaces near the transition from single-humped mass distributions to double-humped mass distributions around mass number A=226. Also the prompt-neutron yields which are sensitive to the shape of the fragments at scission seem to be mostly specific to the nature of the fragment and independent from the fissioning system, see Fig. 3.

A more quantitative test of the role of fragment shells for the fission-fragment properties has been performed recently. Since only the macroscopic potential is specific to the fissioning system, while the shells on the fission path are the sum of the neutron- and proton shells of the two fragments, the shells can be determined by an un-folding procedure from the body of measured fission-fragment distributions. In this spirit, named separability principle, the GEF code [8] is based on the empirical positions of the fission channels as illustrated in Fig. 2 and on a unique set of shell-strength parameters for all fissionning systems. The effective temperatures are given by a suitable rather simple parameterisation as a function of the initial excitation energy of the fissionning system and the calculated potential-energy gain from saddle to scission. The fission-fragment distributions are deduced from the population of the quantum oscillators in mass asymmetry in the different fission valleys in statistical equilibrium. Figure 5 illustrates that the measured fission-fragment distributions are very well reproduced with this approach.

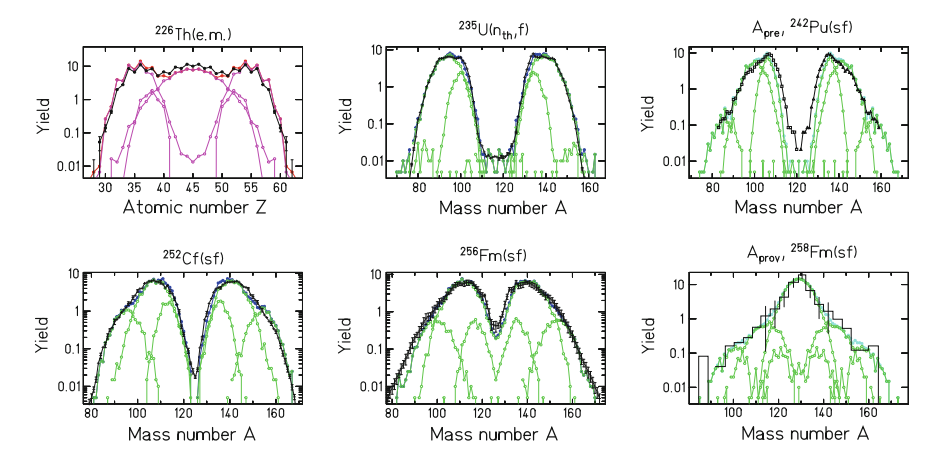


Fig. 5 Mass and Z distributions of fission fragments from spontaneous fission (sf), thermal-neutron-induced fission (nth,f) and electromagnetic-induced fission (e.m.). (In most cases the post-neutron masses are shown. A_{prov} is the "provisional mass" that is directly deduced from the ratio of the kinetic energies of the fragments and, thus, it is not corrected for neutron emission.) Measured or evaluated data (*black lines*, respectively histogram) are compared with predictions of the GEF code [7] (*pink and green lines*). The contributions of different fission channels are shown. (See [7] for references of the data.) Figure from [4]

3 Energy Sorting

3.1 Energy-Dependent Prompt-Neutron Yields

Data on the variation of prompt-neutron yields as a function of the initial excitation energy of the fissionning system are scarce and their uncertainties are often rather large. Figure 6 presents one of the most reliable results of this kind. It shows the prompt-neutron yields of the system ²³⁷Np(n,f) for two energies of the incoming neutrons. The additional energy introduced by the 5.5-MeV neutrons obviously enhances the prompt-neutron yields in the heavy fission-fragment group, only, while the neutron yields in the light group remain unchanged.

3.2 Nuclei in Contact—a Microscopic System of Coupled Thermostats

There is increasing evidence [18, 19] that the nuclear level density in the regime of pairing correlations essentially deviates from the widely so-called Fermi-gas level-density formula that had been derived by Bethe [20] for a system of non-interacting Fermions. Due to the gradual breaking of Cooper pairs, the effective number of degrees of freedom of the nucleus increases strongly, leading to a large heat capacity,

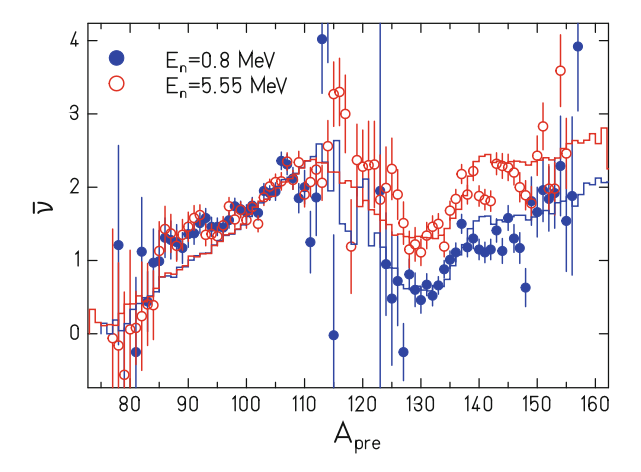


Fig. 6 Measured prompt-neutron yield in ²³⁷Np(n,f) as a function of pre-neutron mass at two different incident-neutron energies [13] (data points) in comparison with the result of the GEF code [8] (histograms) figure from [23]

and, therefore, the level density as a function of excitation energy is well approximated by an exponential function. This means that the nuclear temperature in the regime of pairing correlations is essentially constant.

The early manifestation of fragment shells on the fission path, mentioned above, indicates that the fragments acquire their individual characteristics long before scission. Thus, the fissioning nucleus represents a very interesting system of two microscopic objects that behave as coupled thermostats with a limited total energy. Driven by entropy, thermal energy is exchanged between the nascent fragments by transfer of particles through the neck [21, 22]. Since the nuclear temperature is grossly proportional to $A^{2/3}$, this process leads to an energy sorting, where essentially all thermal energy is concentrated in the heavy fragment [23]. This explains the enhanced prompt-neutron yield for the higher initial excitation energy shown in Fig. 6. Of course, this process ends at scission, and the deformation energy of the individual fragments at scission that is dissipated after scission remains in the respective fragment and represents the main source of the saw-tooth like behaviour of the mean mass-dependent prompt-neutron fission yield.

4 Conclusion

The nuclear fission process provides a unique test object for studying the dynamical behaviour of two microscopic objects with different structural and thermodynamical properties in contact. The relative velocity is so low that the heating of the system due to the window formula of the one-body dissipation, which normally dominates in heavy-ion reactions, is negligible.

Experimental data on the mass-dependent prompt-neutron yields reveal that the fissioning system on the way to scission represents a unique system of microscopic thermostats with a fixed total energy in contact. These thermostats act like two heat baths with different temperatures, leading to a transport of essentially all available thermal energy to the heavy fragment.

A nucleus in the regime of pairing correlations is certainly one of the smallest thermostats to be found in nature, offering the possibility to study the combined influence of quantum structure and statistical mechanics.

It was shown that major trends of the general dynamic behaviour of the fissioning system are driven by general laws of quantum and statistical mechanics.

Acknowledgments This work was supported by the European Commission within the Sixth Framework Programme through EFNUDAT (project no. 036434) and within the Seventh Framework Programme through Fission-2010-ERINDA (project no.269499), and by the Nuclear-Energy Agency of the OECD.

References

- J. Randrup, P. Moeller, A.J. Sierk, Fission-fragment mass distributions from strongly damped shape evolution. Phys. Rev. C 84, 034613 (2011)
- H. Goutte, J.F. Berger, P. Casoli, D. Gogny, Microscopic approach of fission dynamics applied to fragment kinetic energy and mass distributions in ²³⁸U. Phys. Rev. C. 71, 024316 (2005)
- 3. K.-H. Schmidt, S. Steinhaeuser, C. Boeckstiegel, A. Grewe, A. Heinz, A.R. Junghans, J. Benlliure, H.-G. Clerc, M. de Jong, J. Mueller, M. Pfuetzner, B. Voss, Relativistic radioactive beams: a new access to nuclear-fission studies. Nucl. Phys. A. 665, 221 (2000)
- K.-H. Schmidt, B. Jurado, Final excitation energy of fission fragments. Phys. Rev. C 83, 061601(2011)
- 5. M.G. Itkis, N.A. Kondrat'ev, S.I. Mul'gin, V.N. Okolovich, A.Ya. Rusanov, G.N. Smirenkin: Mass asymmetry of symmetric fission of nuclei with A approximately 200. Sov. J. Nucl. Phys. **52**, 601 (1990)
- A.N. Andreyev, J. Elseviers, M. Huyse, P. Van Duppen, S. Antalic, A. Barzakh, N. Bree, T.E. Cocolios, V.F. Comas, J. Diriken, D. Fedorov, V. Fedosseev, S. Franchoo, J.A. Heredia, O. Ivanov, U. Koester, B.A. Marsh, K. Nishio, R.D. Page, N. Patronis, M. Seliverstov, I. Tsekhanovich, P. Van den Bergh, J. Van De Walle, M. Venhart, S. Vermote, M. Veselsky, C. Wagemans, T. Ichikawa, A. Iwamoto, P. Moeller, A.J. Sierk, New type of asymmetric fission in proton-rich nuclei. Phys. Rev. Lett. 105, 252502 (2010)
- S.I. Mulgin, K.-H. Schmidt, A. Grewe, S.V. Zhdanov, Shell effects in the symmetric-modal fission of pre-actinide nuclei. Nucl. Phys. A 640, 375 (1998)
- 8. K.-H. Schmidt, B. Jurado, *Prompt-Neutron and Prompt-Gamma Emission from a General Description of the Fission Process* (JEF/DOC 1423, OECD Nuclear-Energy Agency, Paris, 2012), http://www.cenbg.in2p3.fr/GEF.
- 9. J.P. Unik, J.E. Gindler, L.E. Glendenin, K.F. Flynn, A. Gorski, R.K. Sjoblom, in *Proceedings of Symposium on Physics and Chemistry Fission*, Rochester, 1973. Fragment mass and kinetic energy distributions for fissioning systems ranging from mass 230 to 256, vol. 2 (IAEA, Vienna, 1974), p. 19
- B.D. Wilkins, E.P. Steinberg, R.R. Chasman, Scission-point model of nuclear fission based on deformed-shell effects. Phys. Rev. C 14, 1832 (1976)

- C. Boeckstiegel, S. Steinhaeuser, K.-H. Schmidt, H.-G. Clerc, A. Grewe, A. Heinz, M. de Jong, A.R. Junghans, J. Mueller, B. Voss, Nuclear-fission studies with relativistic secondary beams: analysis of fission channels. Nucl. Phys. A 802, 12 (2008)
- D.M. Gorodisskiy, S.I. Mulgin, V.N. Okolovich, A.Ya. Rusanov, S.V. Zhdanov, Isotopic and isotonic effects in fission-fragment mass yields of actinide nuclei. Phys. Lett. B 548, 45 (2002)
- 13. A.A. Naqvi, F. Kaeppeler, F. Dickmann, R. Mueller, Fission fragment properties in fast-neutron-induced fission of 237Np. Phys. Rev. C **34**, 218 (1986)
- O.V. Zeynalova, Sh. Zeynalov, M.A. Nazarenko, F.-J. Hambsch, S. Oberstedt, Cross correlation method application to prompt fission neutron investigation. AIP Conf. Proc. 1487, 207 (2012)
- U. Mosel, H.W. Schmitt, Potential energy surfaces for heavy nuclei in the two-center model. Nucl. Phys. A 165, 73 (1971)
- P. Moeller, A.J. Sierk, T. Ichikawa, A. Iwamoto, R. Bengtsson, H. Uhrenholt, S. Aberg, Heavyelement fission barriers. Phys. Rev. C 79, 064304 (2009)
- M.G. Itkis, V.N. Okolovich, A.Ya. Rusanov, G.N. Smirenkin, Asymmetric fission of the preactinide nuclei. Z. Phys. A 320, 433 (1985)
- M. Guttormsen, R. Chankova, M. Hjorth-Jensen, J. Rekstad, S. Siem, A. Schiller, D.J. Dean, Free energy and criticality in the nucleon pair breaking process. Phys. Rev. C 68, 034311 (2003)
- K.-H. Schmidt, B. Jurado, Inconsistencies in the description of pairing effects in nuclear level densities. Phys. Rev. C 86, 044322 (2012)
- 20. H.A. Bethe, An attempt to calculate the number of energy levels of a heavy nucleus. Phys. Rev. **50**, 332 (1936)
- J. Randrup, Theory of transfer-induced transport in nuclear collisions. Nucl. Phys. A 327, 490 (1979)
- K.-H. Schmidt, B. Jurado, Thermodynamics of nuclei in thermal contact. Phys. Rev. C 83, 014607 (2011)
- K.-H. Schmidt, B. Jurado, Entropy-driven excitation-energy sorting in superfluid fission dynamics. Phys. Rev. Lett. 104, 212501 (2010)

How Rare Is Cluster Decay of Superheavy Nuclei?

D.N. Poenaru, R.A. Gherghescu, W. Greiner and N.S. Shakib

Abstract Superheavy nuclei produced until now are decaying by α emission and spontaneous fission (SF). For atomic numbers larger than 121 cluster decay (CD) has a good chance to compete. While the majority of calculated α decay (α D) half-lives are in agreement with experimental data within one order of magnitude and CD are also very well accounted for, the discrepancy between theory and experiment can be as high as ten orders of magnitude for SF. Further improvement of accuracy comes from finding the optimal parameters of our models: analytical superasymmetric fission model, universal curve and semiempirical formula. For SF we study the nuclear dynamics based on potential barriers computed by the macroscopic-microscopic method and employing various nuclear inertia variation laws. Applications are illustrated for 284 Cn and even-even Z=118-124 parent nuclei.

1 Introduction

In the region of heavy nuclei with atomic number Z=87-96, the measured 14 C, 20 O, 23 F, $^{22,24-26}$ Ne, 28,30 Mg, and 32,34 Si cluster radioactivities (CD) [1] confirmed our predictions of 1980 [2, 3] and shows up as a rare phenomenon in a huge background of α particles.

Neutron deficient superheavy (SH) nuclei with Z = 104 - 118 synthesized by fusion reactions [4–8] are decaying mainly by alpha emission (αD) or in a few cases by spontaneous fission (SF). Production of SHs closer to the β -stability line could be possible in the future [9].

Dedicated to Prof. Mikhail Itkis's 70th Anniversary.

D.N. Poenaru (🖾) · R.A. Gherghescu · N.S. Shakib Horia Hulubei National Institute of Physics and Nuclear Engineering, PO Box MG-6, 077125 Bucharest-Magurele, Romania e-mail: Dorin.Poenaru@nipne.ro; poenaru@fias.uni-frankfurt.de

W. Greiner · D.N. Poenaru Frankfurt Institute for Advanced Studies, J. W. Goethe University, Ruth-Moufang-Str. 1, 60438 Frankfurt, Germany D.N. Poenaru et al.

Our calculations [10, 11] have shown a trend toward a branching ratio $b = T_{\alpha}/T_c$ relative to αD larger than unity for heavier SHs with Z > 121. Despite the good agreement between theory and experiment for αD [12] and CD [13, 14], in the regions of the nuclear chart which are not experimentally reached there is a large uncertainty of the calculated half-lives as a consequence of the differences of calculated atomic masses by different models. We continue our systematic search by using new mass tables: experimental AME12 [15] available for neutron deficient SHs up to Z = 118 and theoretical ones WS-10 and WS3-11 [16, 17] well extended up to the neutron drip line.

For SF we refer to the recent publications [18–20] as well as to the earlier ones [21–24].

In the three decay modes mentioned above (α D, CD, SF), from one parent nucleus ${}^{A}Z$, one obtains an emitted particle (or a light fragment) ${}^{A_2}Z_2$, and a daughter (heavy fragment) ${}^{A_1}Z_1$:

$${}^{A}Z \rightarrow {}^{A_{2}}Z_{2} + {}^{A_{1}}Z_{1}$$
 (1)

In the present work we consider the competition of SF, by performing calculations using the Werner–Wheeler approximation [25, 26] for the nuclear inertia and the two-center shell model [27, 28] to obtain the input for Strutinsky's [29] shell and pairing corrections to the macroscopic [30, 31] deformation energy. We also try some simple laws of variation of nuclear inertia allowing to obtain an agreement with experiment.

2 Alpha and Cluster Decay

The nuclear decay modes we study (αD , CD and SF) are explained by quantum tunneling through the potential barrier.

The decay constant

$$\lambda = \ln 2/T = \nu S P_s \tag{2}$$

is expressed by a product of three model dependent quantities ν , S and P_s where ν is the frequency of assaults on the barrier per second, S is the preformation probability and P_s is penetrability of external barrier. In the equation above $T = T_\alpha$ or $T = T_c$ or $T = T_f$ (for fission). According to our method the preformation in a fission theory is given by the penetrability of the internal part of the barrier.

For α D and CD we are using our ASAF (analytical superasymmetric fission) model [32, 33] employing Myers-Swiatecki's liquid drop model [34] adjusted with a phenomenological correction, E_{cor} , and the UNIV (universal curve) [13]. For α D we also have the semFIS (semiempirical model) [14] based on fission theory.

Unlike the majority of other models exhibiting large deviations from experimental values in the vicinity of the magic number of neutrons (e.g. N=126) semFIS model behaves well around hence at least for the even-even emitters $\sigma=0.225$ compared to 0.420 for ASAF. For 147 even-odd, 130 odd-even, and 113 odd-odd α emitters,

ones for a children, before and after optimization of 71574							
Group	n	σ_{ASAF}	σ_{ASAF}^{opt}	σ_{UNIV}	h_{UNIV}	σ_{semFIS}	
e-e	188	0.420	0.420	0.358	0.023	0.225	
e-o	147	0.720	0.714	0.641	0.573	0.527	
о-е	130	0.651	0.643	0.564	0.428	0.436	
0-0	113	0.869	0.869	0.805	0.963	0.603	

Table 1 The standard rms deviations of calculated half-lives ($\log_{10} T_{\alpha}$) compared to experimental ones for α emitters, before and after optimization of ASAF

UNIV and semFIS model values are included

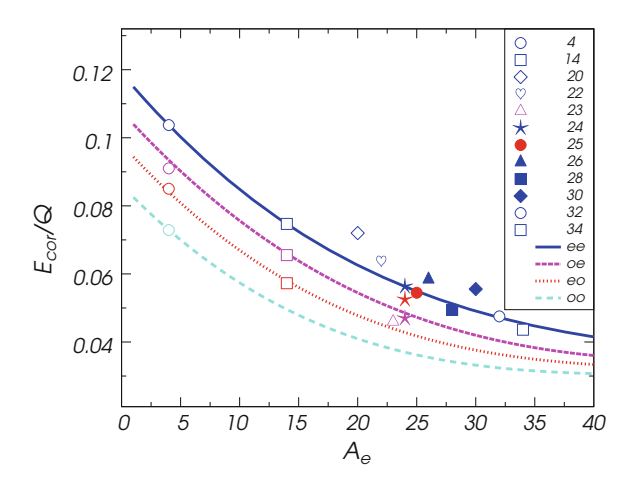


Fig. 1 The ratio of the correction energy to the Q value versus mass number of the emitted cluster in four groups of parent nuclei: even-even, odd-even, even-odd, and odd-odd. The points correspond to the experimental values

the standard deviations within semFIS, UNIV and ASAF are given in Table 1. As can be seen in this table, for αD the improvement of ASAF after optimization is not very important because practically the four points at $A_e=4$ in Fig. 1 are lying on the four smooth curves; anyway the semFIS values are better.

The optimization of ASAF model consists in choosing the best values of the parameters (see Fig. 1). For emitted cluster with mass numbers larger than 19, the experimental points are more or less scattered around the smooth lines we choose to improve the ASAF model. Consequently after optimization we can reproduce better the experimental data on αD , ¹⁴C radioactivity of all kind of parent nuclei, as well as ²⁴Ne, ²⁸Mg, and ^{32,34}Si radioactivities of even-even parent nuclei which are either on the smooth line or very close to it.

For universal curve (UNIV model) the values given in tables are slightly different from previous publications [13] for αD and [12] for CD because we included more experimental data for αD (578 compared to 534 α emitters) and new Q-values calculated using AME12 mass table [15]. h_{UNIV} is the hindrance factor fitted to experimental data. The largest deviations for e-e αD within UNIV model are:

D.N. Poenaru et al.

ones for CD, before and after optimization of ASA						
Group	n	σ_{ASAF}	σ_{ASAF}^{opt}	σ_{UNIV}	h _{UNIV}	
e-e	16	0.975	0.681	0.565	-0.388	
e-o	6	2.014	1.791	0.859	0.593	
о-е	5	0.303	0.391	0.674	0.583	

Table 2 The standard rms deviations of calculated half-lives ($\log_{10} T_c$) compared to experimental ones for CD, before and after optimization of ASAF

UNIV model values are included

1.330-1.071 and -1.194 for 114 Ba 210 Po and 218 U α emitters (daughters 110 Xe 206 Pb and 214 Th), respectively. For e-o emitters $\sigma_{UNIV}=0.641$ and there are 15 deviations who's absolute value is over one order of magnitude, of which 5 are over 1.5:1.582,-1.686,-1.611,-1.733,-1.512 for 199 Rn 215 Ra 217 Th, 251 Cf and 279 Ds parents. There are 13 deviations over one order of magnitude for o-e α emitters of which just one is over 1.5:-1.611 for 281 Rg. From 23 deviations over one order of magnitude for o-o parent nuclei, 6 are over 1.5:1.570,1.769,1.638,2.238,-1.644 and -1.550, for 158 Lu, 164 Ta, 166 Ir, 228 Ac, 218 Pa, and 274 Rg, respectively. There is only one case, 228 Ac, with a deviation larger than 2 within ASAF, UNIV, and semFIS: 2.220,2.238,2.037.

For 16 even-even cluster emitters we obtained $\sigma_{ASAF}^{opt} = 0.681$ compared to $\sigma_{ASAF} = 0.975$ before optimization, as shown in Table 2. The largest deviations of 1.222, 1.188, and 2.654 for 20 O radioactivity of 228 Th, 26 Ne emission from 234 U, and 30 Mg radioactivity of 236 U, respectively before optimization became 1.001, 0.673, and 1.965 after optimization. Optimized UNIV model with $h_{UNIV} = -0.388$ performs slightly better: $\sigma_{UNIV} = 0.565$ with only one deviation over 1 for 30 Mg radioactivity of 236 U: 1.148. For 20 O radioactivity of 228 Th and 26 Ne emission from 234 U one has: 0.809 and -0.908, respectively.

For 6 even-odd cluster emitters we obtained $\sigma^{opt}_{ASAF}=1.791$ compared to $\sigma_{ASAF}=2.014$ before optimization. The largest deviations of 2.841 and 3.230 for 24 Ne radioactivity of 235 U, and 25 Ne emission from 235 U before optimization became 2.553 and 2.956 after optimization. Again within UNIV model we have $\sigma_{UNIV}=0.859$ with largest deviations of -1.114 and 1.160 for 24 Ne radioactivity of 235 U, and 25 Ne emission from 235 U, respectively.

For 5 odd-even cluster emitters we obtained $\sigma_{ASAF}^{opt} = 0.391$ compared to $\sigma_{ASAF} = 0.303$ before optimization. There is no very large deviation exceeding one order of magnitude in this case. It happens that here we have the best result for ASAF. The σ_{ASAF} after optimization is slightly higher because we adopted a smoother law of variation of $E_{cor}/Q = f(A_e)$. This time UNIV model with $\sigma_{UNIV} = 0.674$ is less performant compared to ASAF; the largest deviation of -0.915 corresponds to 23 F radioactivity of 231 Pa. There are only two cases with deviations larger than 2 (within ASAF model): 24,25 Ne from 235 U: 2.553 and 2.956.

Predicted CD and αD half-lives for even-even SH nuclei with Z=118-124 are compared in Fig. 3. These nuclides are chosen as we expect to observe in this region in the future the competition of CD.

3 Spontaneous Fission

From Eq. (2) by denoting $P = SP_s = \exp(-K)$ the half-life, T, expressed in seconds, is calculated as

$$T = \frac{\ln 2}{\nu P} = \frac{h \ln 2}{2} \frac{1}{E_{\nu} P} \; ; \quad K = \frac{2\sqrt{2m}}{\hbar} \int_{R_a}^{R_b} \{B(R)[E(R) - Q]\}^{1/2} dR \tag{3}$$

where h is the Planck constant, $E_v = hv/2$ is the zero point vibration energy, K is the action integral, R_a and R_b are the turning points $[E(R_a) = E(R_b) = Q]$, B is the dimensionless inertia in units of the nucleon mass m, Q is the released energy expressed in MeV.

Nuclear inertia may be calculated either classically within the Werner–Wheeler approximation [25, 26] or with the cranking formula [35]. The potential energy surface in a multidimensional hyperspace of deformation parameters $q_1, q_2, ..., q_n$ gives the generalized forces acting on the nucleus. The information concerning how the system reacts to these forces is contained in a tensor of inertial coefficients, or the effective mass parameters $\{B_{ij}\}$ [36]. In contrast to the potential energy E = E(q), which only depends on the nuclear shape, the kinetic energy

$$E_k = \frac{1}{2} \sum_{i,j=1}^n B_{ij}(q) \frac{dq_i}{dt} \frac{dq_j}{dt}$$

$$\tag{4}$$

also includes the change in time of this shape. By choosing the distance between fragments, R, as deformation coordinate, the inertia at the touching point of the two fragments is equal to the reduced mass $\mu = (A_1A_2/A)m$ in a binary system. When we only consider one deformation coordinate, R, the inertia tensor becomes a scalar, R. An example of the nuclear inertia for the decay of 284 Cn into 138 Ba and 146 Ba is given by full line (W–W) in Fig. 2.

As shown in Table 3, we are not able to reproduce the experimental half-life if we use a Werner–Wheeler nuclear inertia, known to be too small. We concentrate on the particular splitting giving the shortest half-life for the quantum tunneling from the 2nd minimum of the potential barrier which is the lowest in energy. In the right-hand side of the Table 3 we compare the results obtained by combining the Werner–Wheeler nuclear inertia with potential barriers calculated only with shell corrections (W–W no pairing) and by including both shell and pairing corrections (W–W with pairing) for the tunneling from the 1st minimum higher in energy, implying two fission barriers. In the following we disregard the calculations without pairing (which are not correct despite giving closer half-life to the experiment) as we did in the left-hand side of the table.

To increase the half-life we need a smaller penetrability, hence a larger action integral, or for a given potential barrier, a larger nuclear inertia. In order to fulfill the requirement mentioned above it should approach the reduced mass at the touching

D.N. Poenaru et al.

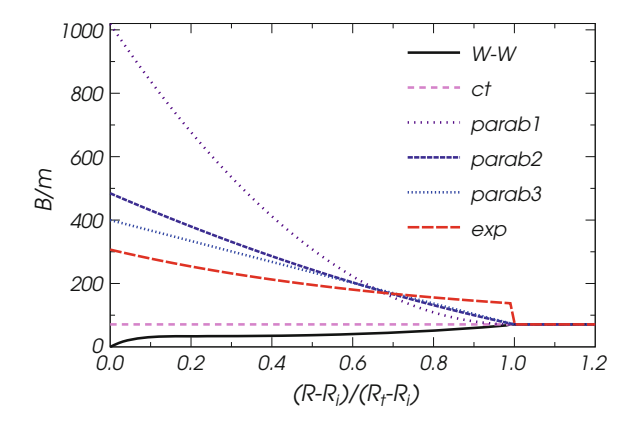


Fig. 2 Nuclear inertia variations for the SF of 284 Cn with light fragment 138 Ba. Besides W–W (Werner–Wheeler) and ct $(B/m=A_{\mu})$, which are not large enough to fit the data, the three parabolic approximations and the exponential one correspond to Eqs. (5–8) with parameters B_i or d, g fitted to reproduce the experimental half-life

Table 3 Decimal logarithm of SF half-lives $\log_{10} T_f(s)$ of 284 Cn along various paths leading from the 2nd or from the 1st minimum to a final state with a given light and heavy fragment

Light	From 2			From 1			
frag	B var	B=ct.	W–W	B = ct.	W-W with pairing	W-W no pairing	
¹³⁸ Ba	-0.98	-7.90	-10.44	-1.81	-6.32	-3.63	
¹³⁰ Cd	_	-8.03	-10.15	11.79	-13.97	-12.67	
¹³² Sn	_	-5.51	-7.97	-7.68	-10.63	-8.68	
¹⁴² Ba	_	-4.37	-7.52	-0.04	-4.72	0.50	
¹⁴⁰ Ce	_	-1.64	-6.52	1.64	-6.52	-4.57	

Experimental value: $\log_{10} T_f^{exp}(s) = -0.98$

point. As may be seen from the table by simply taking $B = B_t = \text{const}$ we can come closer to experiment by a few orders of magnitude.

We can do better, to reproduce exactly the experiment, by further increasing the inertia; we consider four different laws of variation for the nuclear inertia: three decreasing parabolic functions and an exponential variation. These functions represent a smooth approximation of the cranking inertia. Since we choose for the independent deformation parameter the separation distance of the fragments, R, or equivalently the normalized quantity $\xi = (R - R_i)/(R_t - R_i)$ we should have always at the touching point $R = R_t = R_1 + R_2$ and beyond, $R > R_t$, a nuclear inertia equal to the reduced mass; in units of nucleon mass, m, $B_t = A_{\mu} = A_1 A_2/A$.

We use a parabolic approximation $B = B(\xi)$ with one free parameter, B_i , which can be adjusted to fit the experimental data. By requesting a smooth matching (vanishing first derivative) at the touching point with $B_t = A_\mu$ we have:

$$B(\xi) = (B_i - B_t)(\xi - 1)^2 + B_t \tag{5}$$

The nuclear inertia is given in units of the nucleon mass m. In order to increase the $\log_{10} T_f(s)$ from -10.44 to -0.98 we need to take a very large value of the parameter $B_i = 1018.50$ compared to the final $B_t = 70.94$. Consequently we may try another law of variation with a slower decrease from B_i toward B_t . Let's make

$$B(\xi) = \frac{B_i - B_t}{3} (\xi - 1)^2 + \frac{4B_t - B_i}{3}$$
 (6)

This time the parameter $B_i = 484.50$ is smaller. Another parabolic law could be

$$B(\xi) = (a - \xi)^2 + c \tag{7}$$

with $a = (B_i - B_t + 1)/2$ and $c = B_i - a^2$. In this case $B_i = 400.05$ is even smaller. We had also used an exponential law

$$B(\xi) = B_t \{ 1 + d \exp[g(0.75 - \xi)] \}$$
 (8)

inspired from [21]; it was recently employed in Ref. [18]. Figure 2 illustrates different laws of variation $B = B(\xi)$. The exponential law had d = g = 1.2765 in order to fit the experimental half-life.

Few fission channels could be efficiently used to test different methods of calculating SF half-lives of ^{284}Cn who's experimental value is known. We know from the mass distributions of fission fragments that few splittings give the largest yield, very likely explained by shell effects (spherical and/or deformed magic numbers of neutrons and protons). Consequently we can guess that the following channels would be among those major splittings: $^{284}\text{Cn} \rightarrow ^{132}\text{Sn} + ^{152}\text{Sm}; \rightarrow ^{130}\text{Cd} + ^{154}\text{Gd}; \rightarrow ^{138}\text{Ba} + ^{146}\text{Ba}; \rightarrow ^{142}\text{Ba} + ^{142}\text{Ba}; \rightarrow ^{140}\text{Ce} + ^{144}\text{Xe}.$ The largest reduced mass is obtained at symmetry, where also the touching point separation distance reaches its maximum.

The potential barriers are calculated within macroscopic-microscopic method. The phenomenological deformation energy is of Yukawa-plus-exponential type [30] for binary systems with different charge densities [31]. The microscopic two center shell model [27, 28] was used to obtain the nuclear level schemes—the input data for shell and BCS pairing corrections [14]. With one exception (140 Ce light fragment) the 1st minimum is higher in energy than the 2nd one which means that the ground state of 284 Cn is well deformed and the shape isomer is almost spherical.

In our calculation using Werner–Wheeler inertia for a given mass asymmetry $\eta=(A_1-A_2)/A=0.0282$ (light fragment 138 Ba) we obtained $\log_{10}T_f(s)=-4.12$ when the tunneling was taken from the 2nd (lowest in energy and well deformed) minimum with no pairing and -10.44 with pairing. If we consider the starting point of tunneling the first minimum (smaller deformation and higher energy—very likely a shape isomer) at $\eta=0.0845$ (130 Cd light fragment) then the corresponding numbers are even further from the experimental one: -12.67, and -13.97, respectively.

For the SH nucleus ²⁸⁴Cn the SF half-life was measured [37] $T_f^{exp} = 104$ ms, i.e. $\log_{10} T_f(s) = -0.98$. Theoretical values already published are the following:

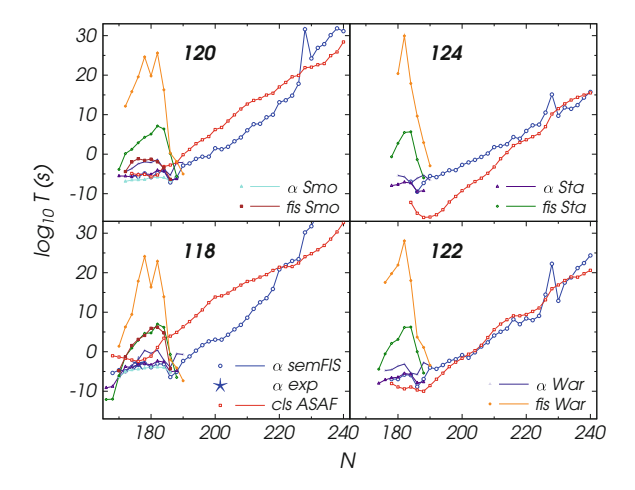


Fig. 3 Comparison of theoretical half-lives for α D, CD and SF for neutron numbers $N \le 206$. On the *line* of β -stability $N_{\beta} = 194$, 198, 202, 206 for Z = 118, 120, 122, 124, respectively. The proton *drip-line* position according to the mass tables from [16, 17] are $N_p = 169$, 174, 179, 183 or 184

 $\log_{10} T_f(s) = 0.60$ [38]; 2.36 [20]; -9.15 [19]. One can also make calculations with simple relationships leading to -3.93 [24], and -4.43 [22]. The closest value to the experimental one was obtained by using a dynamical approach [38]. Predictions for the heavier even-even SHs with Z = 118 - 124 are given in Fig. 3. By taking into account that on the line of β -stability one has $N_{\beta} = 194$, 198, 202, 206 for Z = 118, 120, 122, 124 it is clear that SF half-lives in Fig. 3 refer to neutron deficient nuclei; there are no numbers for nuclides with N > 190.

4 Competition of the Three Decay Modes for Z = 118 - 124

In Fig. 3 we can see how behave the various decay modes (α D, CD, SF) in the region of the heaviest SHs with atomic numbers Z=118-124. Only even-even parent nuclei are considered. The three publications mentioned above [19, 20, 23] give not only SF half-lives, but also α D half-lives in the region of neutron deficient SHs. α D half-lives predicted by all models we considered are not very far from each-other and they are close to the experimental point for $^{294}118$. CDs are calculated only by us.

For SF there are very large differences from model to model. In Refs. [18, 23] we only found calculations for the isotopes of Z=118,120 nuclei. The Bao [18] half-lives of Z=118 isotopes are shorter than that given by Smolanczuk [23], but for Z=120 they are longer, except for $^{294}120$. The data by Staszczak [19] are in good agreement with Smolanczuk when Z=118, but for Z=120 the Staszczak half-lives are longer. Much longer SF half-lives are predicted by Warda [20] which nevertheless

are closer to Staszczak for heavier neutron numbers approaching N=190. There are no predictions for N>190.

We extend these calculations, using semFIS for αD and ASAF for CD, for a broader range of neutron numbers using the theoretical mass tables [16, 17]. For even-even neutron deficient isotopes of the elements 118 and 120 αD is the dominant decay mode (shortest half-life). For few isotopes of the elements 118, 120, and 122 SF may compete with αD . CD is the most important decay mode (gives the shortest half-life) of the element 124. It could also be important for several neutron-rich isotopes of 118, 120, and 122. From this point of view the element 122 is a transitional one because the dominance of CD may alternate with that of αD when the neutron number is increased.

In conclusion we should stress the need to make reliable calculations for spontaneous fission half-lives of heavy and SH nuclei and the need to extend these calculations for superheavy nuclei closer to the line of β -stability and for neutron-rich nuclei. Our ASAF and UNIV models may reproduce both α and cluster decays with deviations not larger than two orders of magnitude, except for α D of ²²⁸Ac and ^{24,25}Ne radioactivities of ²³⁵U. Within ASAF, UNIV, and semFIS models the deviations for 513 (88%), 524 (90%), and 554 (95%) α emitters out of the total of 578, are under one order of magnitude. Similarly, ASAF and UNIV may reproduce 23 (85%), and 24 (89%) experimental data from the total of 27 cluster emissions with deviations under one order of magnitude.

Acknowledgments This work was partially supported by FIAS and partially within IDEI Programme under contracts 43/05.10.2011 and 42/05.10.2011 with UEFISCDI, Bucharest.

References

- 1. R. Bonetti, A. Guglielmetti, Rom. Rep. Phys. **59**, 301–310 (2007)
- Encyclopaedia Britannica Online, 2011. Web http://www.britannica.com/EBchecked/topic/ 465998/
- 3. A. Sandulescu, D.N. Poenaru, W. Greiner, Sov. J. Part. Nucl. 11, 528–541 (1980)
- 4. C.E. Duellmann et al., Phys. Rev. Lett. 104, 252701 (2010)
- 5. S. Hofmann, G. Münzenberg, Rev. Mod. Phys. **72**, 733–767 (2000)
- 6. K. Morita et al., J. Phys. Soc. Jpn. **76**, 045001 (2007)
- 7. G. Münzenberg, Rep. Prog. Phys. **51**, 57–104 (1988)
- 8. Y.T. Oganessian, J. Phys. G: Nucl. Part. Phys. 34, R165–R242 (2007)
- 9. V.I. Zagrebaev, W. Greiner, Phys. Rev. C 87, 034608 (2013)
- 10. D.N. Poenaru, R.A. Gherghescu, W. Greiner, Phys. Rev. Lett. 107, 062503 (2011)
- 11. D.N. Poenaru, R.A. Gherghescu, W. Greiner, Phys. Rev. C 85, 034615 (2012)
- 12. D.N. Poenaru, R.A. Gherghescu, W. Greiner, J. Phys. G: Nucl. Part. Phys. 39, 015105 (2012)
- 13. D.N. Poenaru, R.A. Gherghescu, W. Greiner, Phys. Rev. C 83, 014601 (2011)
- D.N. Poenaru, W. Greiner, ed. by, C. Beck. *Clusters in Nuclei*, Vol. 1. Lecture Notes in Physics 818, chap. 1, pp. 1–56. (Springer, Berlin, 2010)
- M. Wang, G. Audi, A.H. Wapstra, F. Kondev, M. MacCormick, X. Xu, B. Pfeiffer, Chin. Phys. C 36, 1603–2014 (2012)
- 16. M. Liu, N. Wang, Y. Deng, X. Wu, Phys. Rev. C 84, 014333 (2011)
- 17. N. Wang, M. Liu, X. Wu, Phys. Rev. C 81, 044322 (2010)

D.N. Poenaru et al.

- 18. X. Bao, H. Zhang, G. Royer, J. Li, Nucl. Phys. A 906, 1–13 (2013)
- 19. A. Staszczak, A. Baran, W. Nazarewicz, Phys. Rev. C 87, 024320 (2013)
- 20. M. Warda, J.L. Egido, Phys. Rev. C 86, 014322 (2012)
- J. Randrup, S.E. Larsson, P. Möller, S.G. Nilsson, K. Pomorski, A. Sobiczewski, Phys. Rev. C 13, 229–239 (1976)
- 22. K.P. Santhosh, R.K. Biju, S. Sahadevan, Nucl. Phys. A 832, 220–232 (2010)
- 23. R. Smolanczuk, Phys. Rev. C 56, 812–824 (1997)
- 24. C. Xu, Z. Ren, Y. Guo, Phys. Rev. C 78, 044329 (2008)
- 25. R.A. Gherghescu, W. Greiner, D.N. Poenaru, Phys. Rev. C 52, 2636–2642 (1995)
- 26. R.A. Gherghescu, D.N. Poenaru, Phys. Rev. C 72, 027602 (2005)
- 27. R.A. Gherghescu, W. Greiner, G. Münzenberg, Phys. Rev. C **68**, 054314 (2003)
- 28. W. Greiner, J.A. Maruhn, *Nuclear Models* (Springer, Berlin, 1996)
- 29. V.M. Strutinsky, Nucl. Phys. A **95**, 420–442 (1967)
- 30. H.J. Krappe, J.R. Nix, A.J. Sierk, Phys. Rev. C 20, 992–1013 (1979)
- 31. D.N. Poenaru, M. Ivaşcu, D. Mazilu, Comp. Phys. Commun. 19, 205–214 (1980)
- 32. D.N. Poenaru, R.A. Gherghescu, W. Greiner, ed, by W. Greiner. *Exciting Interdisciplinary Physics*, pp. 91–101 (Springer, Heidelberg, 2013)
- 33. D.N. Poenaru, D. Schnabel, W. Greiner, D. Mazilu, R. Gherghescu, At. Data Nucl. Data Tables 48, 231–327 (1991)
- 34. W.D. Myers, W.J. Swiatecki, Nucl. Phys. A 81, 1–60 (1966)
- 35. D.N. Poenaru, R.A. Gherghescu, W. Greiner, Europ. Phys. J. A 24, 355–359 (2005)
- M. Brack, J. Damgaard, A. Jensen, H.C. Pauli, V.M. Strutinsky, G.Y. Wong, Rev. Mod. Phys. 44, 320–405 (1972)
- G. Audi, F. Kondev, M. Wang, B. Pfeiffer, X. Sun, J. Blachot, M. MacCormick, Chin. Phys. C 36, 1157–1286 (2012)
- 38. R. Smolanczuk, J. Skalski, A. Sobiczewski, Phys. Rev. C 52, 1871–1880 (1995)

New Kind of Nuclear Multi-body Decay (CCT)—Status and Perspectives of Studies

D.V. Kamanin, Yu.V. Pyatkov, A.A. Alexandrov, I.A. Alexandrova, N. Mkaza, N.A. Kondratyev, E.A. Kuznetsova, G.V. Mishinsky, V. Malaza, A.O. Strekalovsky, O.V. Strekalovsky and V.E. Zhuchko

1 Introduction

The present paper is devoted to the observation of a new kind of ternary decay of low-excited heavy nuclei. This decay mode has been called by us "collinear cluster tri-partition" (CCT) in view of the observed features of the effect, that the decay partners fly apart almost collinearly and at least one of them has magic nucleon composition. CCT is observed together with conventional binary and ternary fission. It could be one of the rare fission modes but for the moment it is not matter-of-fact. For instance, many years have passed between the experimental discovery of the heavy ion radioactivity and working out of a recognized theory of the process.

At the early stage of our work the process of "true ternary fission" (fission of the nucleus into three fragments of comparable masses) was considered to be undiscovered for low excited heavy nuclei. Another possible prototype—three body cluster radioactivity—was also unknown. The most close to the CCT phenomenon, at least kinematically, stands so called "polar emission" [1], but only very light ions (up to isotopes of Be) were observed so far.

From the theoretical side there are numerous indications on possible ternary decays of the low excited heavy nuclei with comparable masses of the decay products. Swiatecki [2] has shown within the framework of the liquid drop model (LDM) that fission into three heavy fragments is energetically more favorable than binary fission for all nuclei with fission parameters $30.5 < Z^2/A < 43.3$. In 1963 Strutinsky

D.V. Kamanin (⊠) · A.A. Alexandrov · I.A. Alexandrova · N.A. Kondratyev · E.A. Kuznetsova · G. V. Mishinsky · A.O. Strekalovsky · O.V. Strekalovsky · V.E. Zhuchko · Y.V. Pyatkov Joint Institute for Nuclear Research, 141980 Dubna, Russia e-mail: kamanin@jinr.ru

Y.V. Pyatkov

National Nuclear Research University "MEPHI", 115409 Moscow, Russia

N. Mkaza · V. Malaza Faculty of Military Science, Military Academy, University of Stellenbosch, Saldanha 7395, South Africa

© Springer International Publishing Switzerland 2015 W. Greiner (ed.), *Nuclear Physics: Present and Future*, FIAS Interdisciplinary Science Series, DOI 10.1007/978-3-319-10199-6_14 [3] has calculated the equilibrium shapes of the fissioning nucleus and has shown, that along with the ordinary configuration with one neck, there is the possibility of more complicated elongated configurations with two and even three necks, at the same time it was stressed, that such configurations are much less probable. Later Diehl and Greiner [4, 5] have shown a preference for prolate over oblate saddlepoint shapes for the fission of a nucleus into three fragments of similar size. Such pre-scission configurations could lead to almost collinear separation of the decay partners, at least in a sequential fission process. Results demonstrating a decisive role of shell effects in the formation of the multi-body chain-like nuclear molecules were obtained by Poenaru et al. [6]. We want to refer as well on very recent theoretical articles, devoted to unusual ternary decays of heavy nuclei including CCT [7–10]. The authors analyze the potential energy of different pre-scission configurations leading to ternary decays, and the kinetic energies of the CCT partners [11] are calculated for a sequential decay process. These results, being strongly model dependent can be considered as only the first step in the description of the CCT process.

Bearing in mind both theoretical and experimental background mentioned we came to the conclusion, that collinear tri-partition of low-excited heavy nuclear systems would be a promising field of research. The basic results obtained so far are represented here.

2 The Most Pronounced Manifestation of the CCT

The bulk of our results were obtained within the framework of the "missing-mass" approach. With the two-arm spectrometers binary coincidences have been measured, with a special mechanism, which blocks the registration of a third fragment, as explained below and in Fig. 1. This means that only two fragments were actually detected in each fission event and their total mass, the sum M_s will serve as a sign of a multi-body decay if it is significantly smaller than the mass of the initial system.

Figure 2 shows in a logarithmic scale the two-dimensional distribution $(M_2 - M_1)$ of the two registered masses of the coincident fragments [13]. In the FOBOS setup used in the experiment M_1 is defined as the fragment mass derived from the arm pointing towards the detector arm with the additional dispersive (scattering) materials. Only collinear fission events with a relative angle of $180 \pm 2^{\circ}$ were selected, which corresponds to the typical angular spread for conventional binary fission fragments. The "tails" in the mass distributions marked 3–6 in Fig. 2a extending from the regions (1) and (2) which are used to mark the conventional binary fission, are mainly due to the scattering of fragments on both the foils and on the grid edges of the "stop" avalanche counters and the ionization chambers. We emphasize the small but important asymmetry in the experimental arrangement for the two arms, which consists in the thin source backing $(50 \, \text{mg/cm}^2 \, \text{of Al}_2 \text{O}_3)$ of the target and the "start" detector foil located only in arm 1 (Fig. 2a). An astonishing difference in the counting rate and in the shapes of the "tails" (3) and (4) attracts attention. In

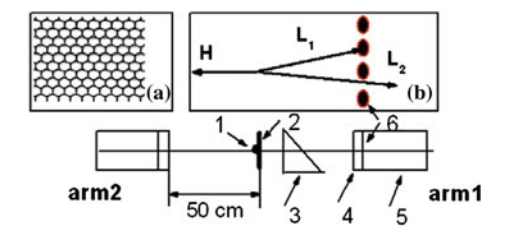


Fig. 1 Scheme for coincidence measurements of two fission fragments of 252 Cf(sf). The experiment has been performed at the FOBOS setup [12]. Here: I Cf source, 2 source backing, 3 micro-channel plate (MCP) based timing "start" detector, 4 position sensitive avalanche counter (PSAC) as "stop" detector, 5 ionization chamber (BIC) with the supporting mesh, 6 the mesh of the entrance window. The front view of the mesh is shown in the insert (a), an enlarged mesh section is presented in the insert (b). After passage of the two fragments through the source backing, two light fragments LI and L2, are obtained with a small angle divergence due to multiple scattering. In (b) we show that one of the fragments (LI) can be lost hitting the metal structure of the mesh, while the fragment L2 reaches the detectors of the $arm\ I$. The source backing (2) exists only on one side and causes the mentioned angular dispersion in the direction towards the $right\ arm I$

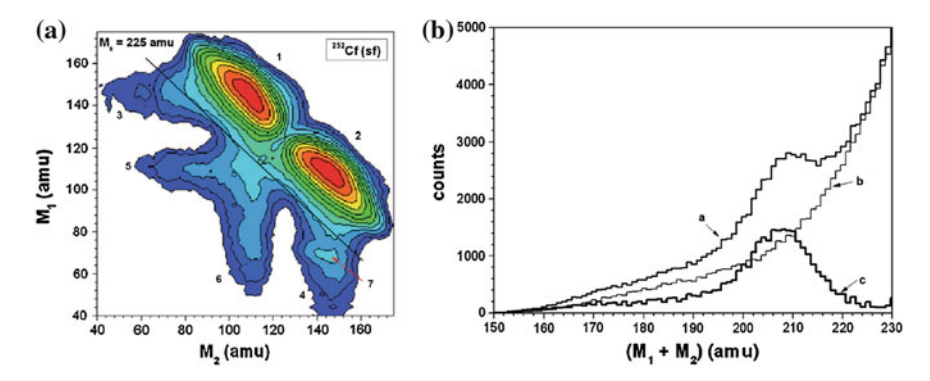


Fig. 2 a Contour map (in logarithmic scale, the steps between the lines are approximately a factor 2.5) of the mass—mass distribution of the collinear fragments of 252 Cf (sf), detected in coincidence in the two opposite arms of the FOBOS spectrometer. The specific bump in arm1 is indicated by an *arrow*. **b** the spectra of the summed masses M_s for the "tails" (4 and 3) shown as spectrum a and b, respectively, are compared. The result of the subtraction of spectrum, **b**, from spectrum, **a**, (difference spectrum) is marked as c

the case shown in Fig. 2a there is a distinct bump, marked (7), on top of the latter "tails" (4). The bump is located in a region corresponding to a large "missing" mass. The statistical significance of the events in the structure (7) can be deduced from Fig. 2b, where the spectra of total (summed) masses M_s for the "tails" (4) and (3) are compared. The yield of the events in the difference spectrum c, is $(4.7 \pm 0.2) \times 10^{-3}$ relative to the total number of events in the distribution shown in Fig. 2a. It is only a lower limit of the yield because the following reason. If both fragments (L1 and L2 in Fig. 1) pass on and enter into the (BIC), we register a signal corresponding to the sum of the energies of the two fragments. In this case the event will be treated as

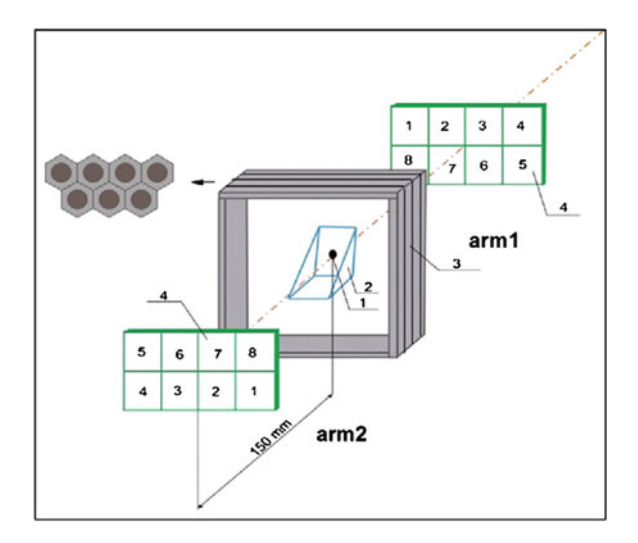


Fig. 3 Scheme of the COMETA setup, which consists of two mosaics of eight PIN-diodes each (4), MCP based start detector (2) with the ²⁵²Cf source inside (1), and a "neutron belt" (3) consisting of 28 ³He-filled neutron counters in a moderator. The cross section of the belt is marked by the *arrow*

binary fission with the usual parameters. The existence of the bump with the similar yield was confirmed in two other experiments carried out at the modified FOBOS spectrometer [14].

As it was stressed a specific supporting grid in the FOBOS detecting modules provides selecting of the ternary events. At the same time it serves a source of the scattered fragments forming the "tails" (Fig. 2a) simulating missing mass events. This effect is essentially suppressed in the mosaic COMETA spectrometer (Fig. 3) which lets to detect in principal all the partners of the ternary decay.

This methodically quite different experiment confirms our previous observations concerning the structures in the missing mass distributions. In this case there is no tail due to scattering from material in front of the E-detectors. Figure 4a shows the region of the mass distribution for the FFs from 252 Cf (sf) around the "Ni"-bump ($M_1 = 68 - 80$ amu, $M_2 = 128 - 150$ amu). The structures are seen in the spectrometer arm facing the source backing only. No additional selection of the fission events has been applied in this case, the experiment has no background. A rectangular-like structure below the locus of binary fission is bounded by magic nuclei (their masses are marked by the numbered arrows) namely 128 Sn (1), 68 Ni (2), 72 Ni (3). In Fig. 4b we show the projection of the linear structure seen at the masses 68 and 72 amu. Two tilted diagonal lines with $M_s = 196$ amu and $M_s = 202$ amu (marked by number 4) start from the partitions 68/128 and 68/134 (all the nuclei to be magic), respectively.

The result for the measured charges (Fig. 5) confirms the previous finding with the mass distributions, namely the existence of an additional bump linked with Ni isotopes ("Ni"-bump) in the arm with the scattering medium.

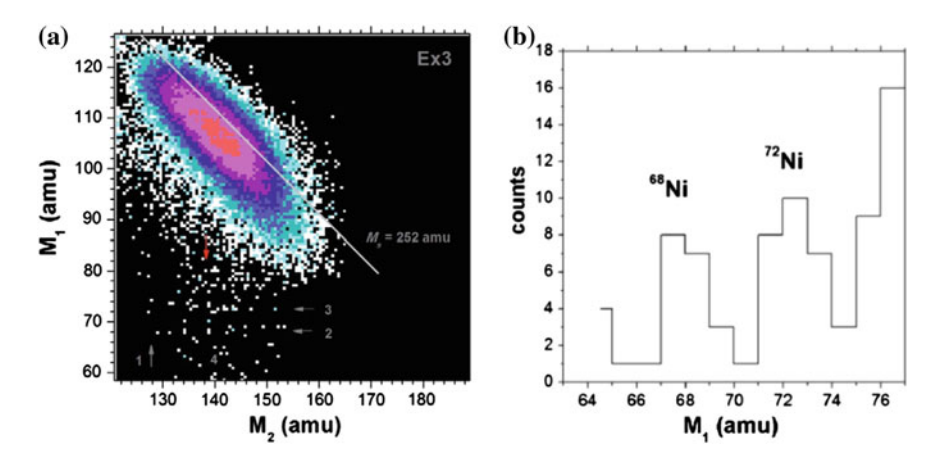


Fig. 4 Region of the mass–mass distribution for the FFs from ²⁵²Cf (sf) around the CCT-bump (similar to this marked by the *arrow* in Fig. 2a). Result was obtained at the COMETA setup. No additional gates were applied. The background of scattered fragments is very *low* due to the use of PIN-diodes (absence of a grid before the surface). An internal structure of the "bump" seen as the *horizontal lines* from points (marked by the *arrows*, 2 and 3) is shown in Fig. 4b, as a projection

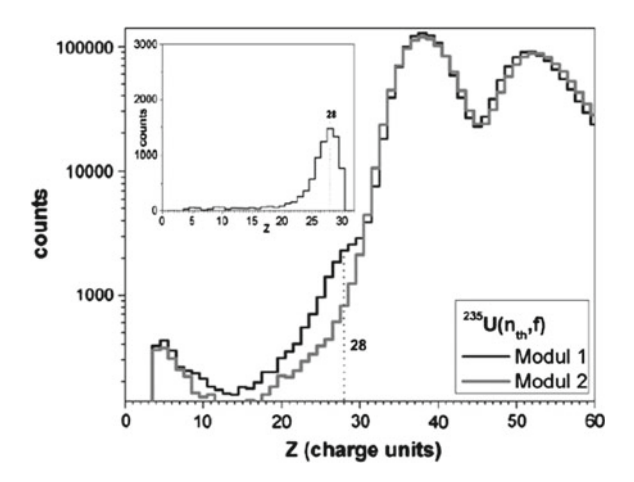


Fig. 5 Nuclear charge spectra for the FF from the reaction 235 U (n_{th} , f), the FF are detected in the two opposite spectrometer arms. A difference in the yields (bump) presented in the *upper* panel in a linear scale is visible for the charges around Z = 28 (isotopes of Ni)

One of the decay modes which contribute to the bump and manifests itself by the tilted ridges $M_1 + M_2 = \text{const}$ can be treated as a new type of cluster decay as compared to the well-known heavy ion or lead radioactivity. Key features of both are summed up in Fig. 6. The relatively high CCT yield can be understood if one assumes collective motion through hyper-deformed pre-scission shapes of the mother systems, which is supported by the fact that the linear arrangement realizes the lowest

D.V. Kamanin et al.

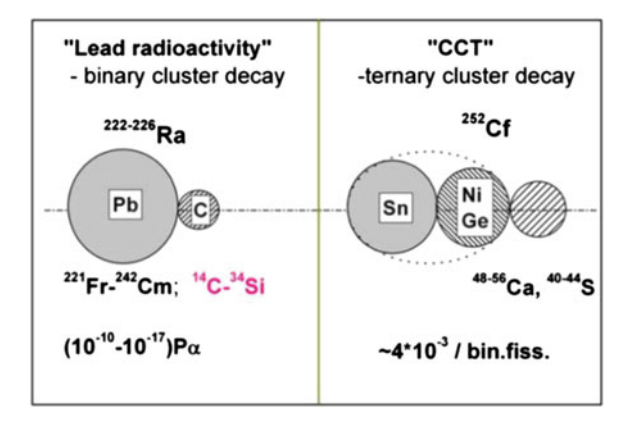


Fig. 6 Cluster scheme for the comparison of the lead radioactivity with collinear cluster tri-partition

Coulomb potential energies of three clusters. We also emphasize, that the \mathcal{Q} values for ternary fission are by 25–30 MeV more positive, again due to the formation of magic fragments, as in binary fission. The ternary fission process must be considered to proceed sequentially, with two neck ruptures in a short time sequence characteristic for binary fissions.

3 Conclusions from the Neutron Gated Data

The results of our previous experiments let us to assume that there are several CCT modes [15], with the middle fragment of the three-body pre-scission chain with very low velocity after scission. Such fragments are expected to emit neutrons almost isotropically. The neutrons emitted from the moving binary fission fragments are focused predominantly along the fission axis. In order to exploit this difference for revealing the CCT events, the "neutron belt" was assembled in a plane perpendicular to the symmetry axis of the spectrometer (Fig. 3). According to modeling and previous experiments, the detection efficiency is estimated to be \sim 5 and \sim 12 % for the neutrons emitted in binary fission and from an isotropic source, respectively. The array of neutron counters of the similar geometry was exploited earlier at the modified FOBOS spectrometer [14]. One of the results obtained at the COMETA setup is presented in Fig. 7.

As can be inferred from the figure, the rectangular structure seen in its upper right corner is bounded by the nuclei with the masses in the vicinity of known magic nuclei (shown in the brackets). These masses (except of double magic ¹³²Sn) were calculated based on the unchanged charge density hypothesis for the fission of the ²⁵²Cf nucleus. Actually we know that at least three neutrons were emitted in each fission event presented in the figure. A change in the nuclear composition of the mother system can lead to a shift of the masses of the magic nuclei if neutrons were emitted from

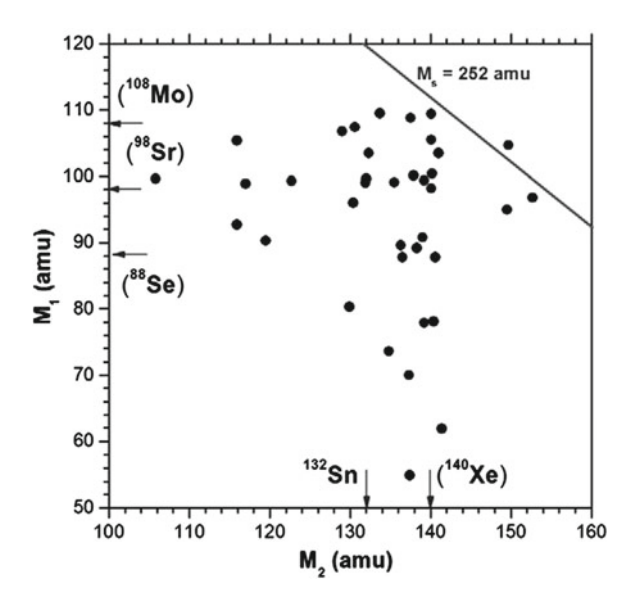


Fig. 7 Results obtained at the COMETA set-up: mass–mass distribution of the FFs from 252 Cf (sf) under the condition that three neutrons (n=3) were detected in coincidence and an additional selection with the gate in the FF velocity-energy distribution [14]

the decaying system (pre-scission neutrons). Likely this is what we observe here. For the upper right corner of the rectangle both mass and charge conservation laws are met only if the upper side of the rectangle corresponds to $^{109}_{43}$ Tc nucleus while mass 140 amu corresponds to the isotope combination of $^{140}_{55}$ Cs.

The structure manifests itself exclusively thanks to the difference of the neutron sources for the fragments appearing in both binary fission and CCT, respectively. These two decay modes must differ in the neutron multiplicity or/and in their angular distributions of the emitted neutrons in order to provide the higher registration efficiency for neutrons linked with the CCT channel. At the same time the excitation energy of the system at the scission point defined as $E_{\rm ex} = Q - {\rm TKE}$ (where Q is the reaction energy, TKE is the total kinetic energy of all the decay fragments), is known from our experimental data. It does not exceed $E_{\rm ex} = 30\,{\rm MeV}$. This value of the excitation energy is high enough to allow for the emission of three or four neutrons, which corresponds almost to the mean neutron multiplicity of binary fission. Thus the neutron source linked with the new CCT channels must have a much smaller velocity as compared to conventional binary fragments, or it can be almost at rest in the extreme case [11]. The latter agrees with the hypothesis put forward above that we deal with the pre-scission neutrons at least for very light missing masses.

Thus, the neutron gated data confirm an existence of the rectangular structures bounded by the magic nuclei in the FF correlation mass distributions. Analysis of the structures let to suppose that at least some of the CCT modes are linked with the emission of four pre-scission neutrons on the average.

D.V. Kamanin et al.

Table 1 Mass conservation law is met in the events presented

Point number	Decay scheme
1	128 Sn + 32 Mg + 80 Ge +2n
	112Ru
2	132 Sn + 68 Ni + 42 S
	¹¹⁰ Ru
3	130 Sn + 72 Ni + 40 S
	112Ru

4 Results from the Triple Coincidences

Evidently, for almost collinear decay partners a probability of their independent detection even by the spectrometer of high granularity decreases rapidly with multiplicity. Nevertheless ternary events caused by multi-body decays were detected in our experiments at the mosaic spectrometers. For instance, ternary events observed in the reaction $^{238}\text{U} + ^4\text{He} (40\,\text{MeV})$ [16] are presented below. In the following three events magic or double magic Sn nuclei were detected as the heaviest fragments (Table 1). Corresponding light fragment (deformed magic nucleus) was clusterized in the scission point forming di-nuclear system. Presumably, its breakup appears to occur due to inelastic scattering on the material of the start-detector. Such hypothesis is based on the fact that a momentum conservation law is not met in all three events.

In the next set of events the decaying system was also fully clusterised i.e. its mass was exhausted by two magic constituents. "Initial" clusters undergo fragmentation leading to formation of two di-nuclear systems. In contrast with previous case both "initial" clusters are relatively soft deformed nuclei. Some examples of the events under discussion are presented in Table 2. Really detected fragments are shown in bold.

Table 2 Di-nuclear systems based on deformed magic constituents

Point	Decay scheme	Point	Decay scheme
no.		no.	
1	121 Ag $+^{23}$ F $+^{65}$ Mn $+^{33}$ Al	4	140 Xe $+^{25}$ Ne $+^{62}$ Cr $+^{15}$ C
	144Ba 98Sr		¹⁶⁵ Gd ⁷⁷ Zn
2	113 Ru $+^{31}$ Mg $+^{78}$ Ni $+^{20}$ Ne	5	$134 \text{Te} + 30 \text{ Ne} + 50 \text{Ca} + 27 \text{ Ne} + \mathbf{n}$
	¹⁴⁴ Ba ⁹⁸ Sr		¹⁶⁴ Gd ⁷⁷ Zn
3	$\frac{^{130}\text{Sn} + ^{14}\text{C} + ^{62}\text{Cr} + ^{33}\text{Mg} + 3\text{n}}{}$	6	110 Tc + 11 Be + 62 Cr + 58 V
	¹⁴⁴ Ba ⁹⁵ Rb		¹²¹ Ag ¹²¹ Ag

5 Perspectives

In order to increase radically the registration efficiency in the cinematically complete experiments i.e. with the direct registration of all (three and more) decay partners we are developing new methodical approaches. The following one is among them. A digital image of the current pulses from the two CCT partners hitting the same PIN-diode during registration gate can be obtained using fast flesh-ADC ("double-hit" technique). Both energy and time-reference linked with each signal from PIN diode will be calculated event by event. In our recent experiments in addition to standard analog electronics the multichannel 5GC/s switched capacitor waveform digitizer DT5742 was set. Signals from all detectors were connected to active splitters and fed to proper inputs of our standard DAQ electronics and to the digitizer in order to compare different approaches of the FF spectrometry.

6 Conclusions

- 1. Clear manifestations of a new kind of at least ternary decay of low excited heavy nuclei (CCT) were observed so far in series of our experiments [17].
- 2. Close to collinear kinematics of the recession of the decay products and magic composition of at least one of them are the key features of new decay.
- 3. The properties of isotropic neutron sources can be assigned to some of the multiple CCT modes.

Our congratulation timeline for Prof. Itkis!





D.V. Kamanin et al.

References

- 1. E. Piasecki et al., Nucl. Phys. A255, 387 (1975)
- 2. W.J. Swiatecki, in *Proceedings of the Second UN Conference on the Peaceful Uses of Atomic Energy*, vol. 15. (United Nations, Geneva, 1958), p. 651
- 3. V.M. Strutinsky et al., Nucl. Phys. 46, 639 (1963)
- 4. H. Diehl, W. Greiner, Phys. Lett. **B45**, 35 (1973)
- 5. H. Diehl, W. Greiner, Nucl. Phys. A229, 29 (1974)
- 6. D.N. Poenaru et al., Phys. Rev. C59, 3457 (1999)
- 7. R.B. Tashkhodjaev et al., Eur. Phys. J. **A47**, 136 (2011)
- 8. K. Manimaran et al., Phys. Rev. C83, 034609 (2011)
- 9. K. Manimaran et al., Eur. Phys. J. **A45**, 239 (2010)
- 10. V.I. Zagrebaev et al., Phys. Rev. C81, 044608 (2010)
- 11. K.R. Vijayaraghavan et al., Eur. Phys. J. A48, 27 (2012)
- 12. H.-G. Ortlepp et al., NIM A403, 65 (1998)
- 13. Yu.V. Pyatkov et al., Eur. Phys. J. A45, 29 (2010)
- 14. Yu.V. Pyatkov et al., Eur. Phys. J. A48, 94 (2012)
- Yu.V. Pyatkov et al., in ed. by Y.T. Oganessian et al. Proceedings of the International Conference of Nuclear Physics Nuclear Shells – 50 Years", Dubna, 1999, (World Scientific, 2000), p. 301
- 16. Yu.V. Pyatkov et al., Int. J. Mod. Phys. **E17**, 2226 (2008)
- 17. D.V. Kamanin, Y.V. Pyatkov, Clusters in Nuclei vol. 3. ed. by C. Beck. Lecture Notes in Physics 875, 183 (2013)

Possible Production of Neutron-Rich Heavy Nuclei in Fissile Spallation Targets

Igor Mishustin, Yury Malyshkin, Igor Pshenichnov and Walter Greiner

Abstract In recent years the interest of researchers is attracted to a new type of neutron sources using so-called Acceleration Driven Systems (ADS), where primary neutrons are produced in a spallation target irradiated by an intensive proton beam. We propose to use spallation targets made of fissile materials in order to increase the neutron flux due to the (n, fission) reaction. Such targets can be used for the incineration of nuclear waste (Minor Actinides) and for generating extra strong neutron fields for production of new elements in neutron capture reactions. We have developed a Monte Carlo model for ADS (MCADS) using the Geant4 toolkit. In this talk we present our studies on the physical conditions in such spallation targets and on the possibility of synthesizing transuranic elements in multiple neutron capture reactions.

1 Preface

It is my pleasure to present this talk on this conference dedicated to 70th anniversary of Prof. Itkis. I wish Mikhail excellent health, joy of life and new great discoveries in physics.

2 Introduction: Multiple Neutron Capture Reactions

In a medium containing neutrons different types of nuclear reactions are possible depending on the neutron energy. Apart of the elastic scattering, the main reaction types are fission and neutron capture, which dominate respectively at higher and

I. Mishustin (☒) · Y. Malyshkin · I. Pshenichnov · W. Greiner Frankfurt Institute for Advanced Studies, 60438 Frankfurt, Germany e-mail: mishustin@fias.uni-frankfurt.de

I. Mishustin

National Research Center "Kurchatov Institute", 123182 Moscow, Russia

I. Pshenichnov

Institute for Nuclear Research, Russian Academy of Sciences, 117312 Moscow, Russia

© Springer International Publishing Switzerland 2015 W. Greiner (ed.), *Nuclear Physics: Present and Future*, FIAS Interdisciplinary Science Series, DOI 10.1007/978-3-319-10199-6_15 152 I. Mishustin et al.

lower energies with the boarder line around 1 MeV. Generally, the average number of neutrons captured by a nucleus A in time Δt is given by the formula:

$$\Delta N = f \,\sigma_{nA} \,\Delta t,\tag{1}$$

where $\sigma_{nA} = (1 \div 3)$ b = 10^{-24} cm² is the cross section of (n, γ) reaction and $f = \langle v \frac{dn}{dv} \rangle$ is the neutron flux averaged over the velocity distribution.

The possibility to capture many neutrons in nuclear explosions was considered already in 60s and 70s, see, e.g., Refs. [1, 2], and recently in Refs. [3, 4]. In this case the neutron flux is about $3 \times 10^{30} \frac{n}{s \text{ cm}^2}$, and the explosion time $\Delta t \simeq 1 \, \mu \text{s}$, therefore:

$$\Delta N_{\text{expl}} = f \ \Delta t \ \sigma_{nA} = 3 \times 10^{30} \frac{\text{n}}{\text{s cm}^2} \times 10^{-6} \text{ s} \times 10^{-24} \text{ cm}^2 \simeq 3,$$

assuming that $\sigma_{nA} \simeq 1$ b. As shown in [4], macroscopic quantities of super heavy elements (SHE) located on the Island of Stability can be produced in multiple nuclear explosions.

In ordinary fission reactors the average neutron flux does not exceed about 10^{15} n/(s cm²), and the nuclei up to Z=100 (Fm) can be produced by this method [5]. In this talk we consider the possibility of producing neutron-rich (super)heavy nuclei in ADS with fissile spallation targets (U, Am, ...). In this case the neutron flux could be as large as 6×10^{16} n/(s cm²) (see below). Since the (n, γ) reaction is only efficient at relatively low energies, $E_n < 1$ MeV, the flux of such neutrons is about twice lower. On the other hand, the target can be irradiated for a long time, say 1 year. Then taking $\sigma_{nA} = (1 \div 2)$ b, one obtains:

$$\Delta N_{ADS} \simeq 3 \times 10^{16} \frac{\text{n}}{\text{s cm}^2} \times 3 \times 10^7 \text{s} \times (1 \div 2) \times 10^{-24} \text{cm}^2 \simeq (1 \div 2)$$

If all other reactions are ignored, the distribution of nuclides in the number of captured neutrons follows a Poisson distribution, see, e.g., Ref. [3]. With a simple-minded correction to fission it can be written as:

$$P_n(\bar{n}) = \frac{\bar{n}^n e^{-\bar{n}}}{n!} (1 - q_{\text{fission}})^n \tag{2}$$

where $q_{\rm fission} \simeq \frac{1}{2}$ is the probability of fission on each single step. With $\bar{n}=2$ and $q_{\rm fission}=\frac{1}{2}$ the probability of capture of 20 neutrons, i.e. to produce isotopes with atomic mass A+20, can be estimated as 6×10^{-20} . For a small Am target with mass of about 40 kg the number of nuclei in the target is $\sim 10^{26}$, therefore $\sim 10^6$ nuclei with the mass of A+20 can be accumulated after 1 year of operation.

Neutrons suitable for transmutation of MA in the spallation targets should have hard spectrum, thus no moderating materials are required. In contrast, neutrons suitable for SHE production should have softer spectrum to increase efficiency of neutron

capture reactions. Therefore, such targets should include some moderating material. However, too intensive moderation of neutrons would suppress neutron breeding in fission reactions. A special investigation is required to find an optimum.

3 Monte Carlo Model for Accelerator Driven Systems: MCADS

3.1 Description of the Code

For simulation of neutron production and transport in spallation targets irradiated by proton and deuteron beams we use our Monte Carlo model for Accelerator Driven Systems (MCADS) described and tested in several publications [6–9]. Its main features are:

- Based on Geant4 toolkit (currently version 9.4 p01) [10];
- Employs several cascade models for the fast initial stage of pA and dA interactions, and evaporation, multi-fragmentation and Fermi break-up models for the slow de-excitation of residual nuclei;
- Includes secondary interactions of fast neutrons, protons and fragments in the target;
- Capability to visualize target volumes, histories of primary protons and all secondaries:
- Flexible scoring techniques to calculate neutron flux, heat deposition and leakage of particles from the target;
- Ability to work with minor actinides (MA).

Several extensions of the Geant4 source code and additional data libraries are needed [8, 9] for the proton- and neutron-induced reactions and elastic scattering on transuranic nuclei.

Among other characteristics the yields of newly produced and destroyed nuclides are calculated. Knowing the beam intensity and the exposition time the final abundances of the isotopes in the target can be calculated. As an example, neutron flux and heat deposition distributions inside a cylindrical 241 Am target irradiated by a 600 MeV proton beam are shown on Fig. 1.

When dealing with fissile materials one must control the criticality of the target. This can be done with MCADS by calculating the neutron multiplication factor k (the ratio between numbers of neutrons in two subsequent generations). Obviously, the target should not exceed so-called critical mass which corresponds to the condition k=1. As an illustration, in Fig. 2 we show the time dependence of neutron number in cylindrical 241 Am targets after an impact of a single proton. The targets have same lengths of 15 cm and different radii from 4 to 11 cm. As one can see, in the target with radius of about $106 \, \text{mm} \ k=1$ and the number of neutrons stays constant. For larger targets the supercritical regime is reached (k>1) and the number of neutrons grows with time.

I. Mishustin et al.

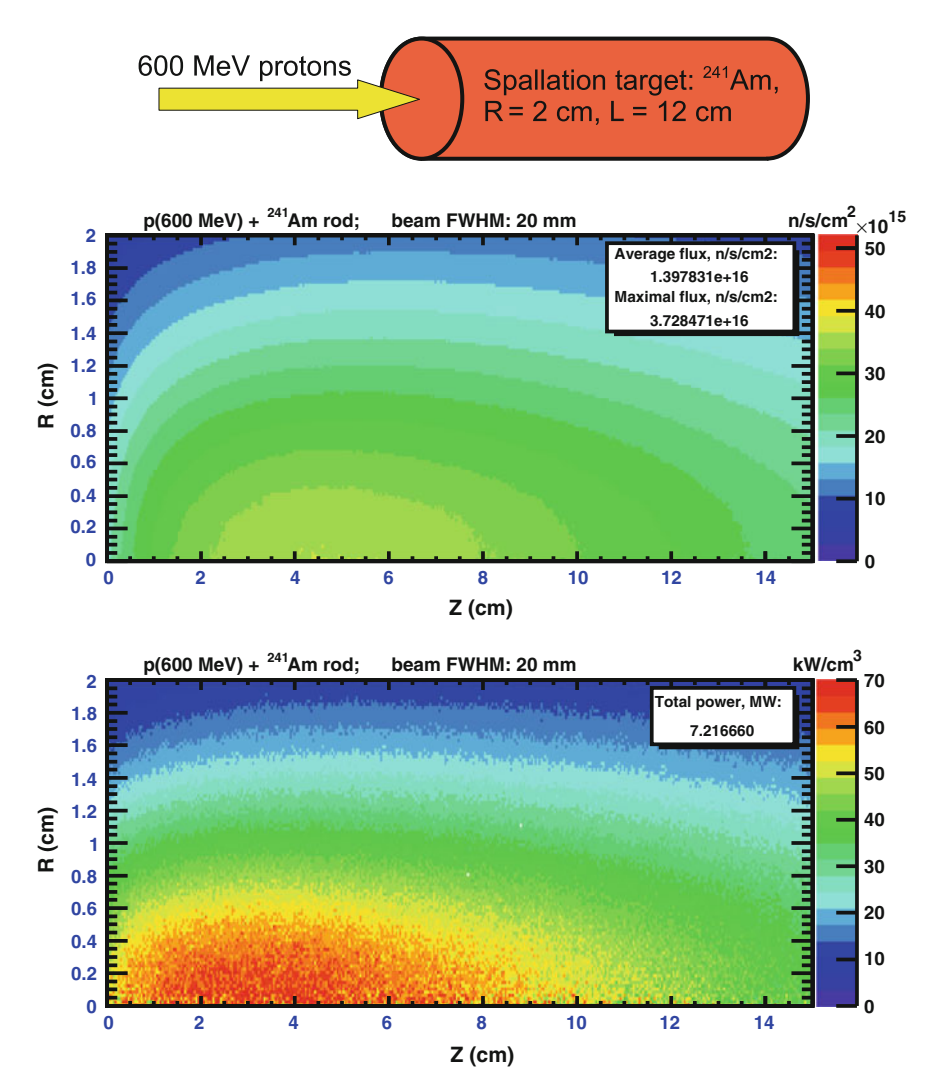
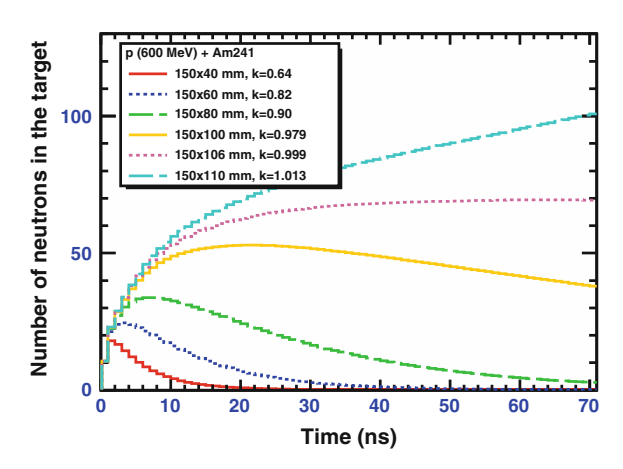


Fig. 1 Spatial distributions of neutron flux and energy deposition in the pure ²⁴¹Am target

3.2 NuCoD: Nuclide Composition Dynamics

The NuCoD (Nuclide Composition Dynamics) code is created to take into account decay chains of produced nuclides, which are important for modeling long time irradiation of spallation targets. This allows us to perform calculations with a target composition changing in time. The modeling process is a sequence of steps consisting of (a) Monte Carlo simulation with a fixed target, (b) calculation of radioactive chains and (c) target composition update and preparing input for the next step.

Fig. 2 Number of neutrons in Am targets of 15 cm length and different radii as a function of time



In practical simulations there is no need to include in the target all the isotopes produced in the previous step. First of all, this is too expensive in terms of computational time. However, many isotopes which are present in the target do not influence significantly the yields of the isotopes we are interested in. Secondly, the total number of atoms of some isotopes in the target may be very small, many orders of magnitude less than the number of generated events in Monte Carlo modeling. This means that these isotopes most probably will not be hit even once and we will not get the products of the interactions on these nuclei. To avoid these problems, the following technique was used.

Instead of modeling one target containing all the isotopes with "real" abundances, a set of special targets is used. The first one, the "base" target, contains only isotopes with relative abundances exceeding a threshold value of 0.001. MCADS modeling with this target gives amounts of newly produced isotopes and consumed ones. Besides, for every low-yield isotope, which we are interested in, a separate calculation with modified material composition is performed. In each of these calculations the abundance of a given isotope is scaled up to 0.005 and a corresponding scale factor is stored. Combining all the results, the isotope composition variation due to primary and secondary nuclear reactions is calculated for the current step. Then radioactive decays are simulated.

4 Validation

Isotope abundances in a Pb target irradiated by protons were simulated with NuCoD. The calculated yields of spallation products at the depth of 6 cm were compared with experimental data from [11] and with results of calculations with the CASCADE/INPE code [12], see Fig. 3. The target was assembled from ten sections and had a diameter of 20 cm and a total length of 60 cm. It was irradiated by a 1 GeV

156 I. Mishustin et al.

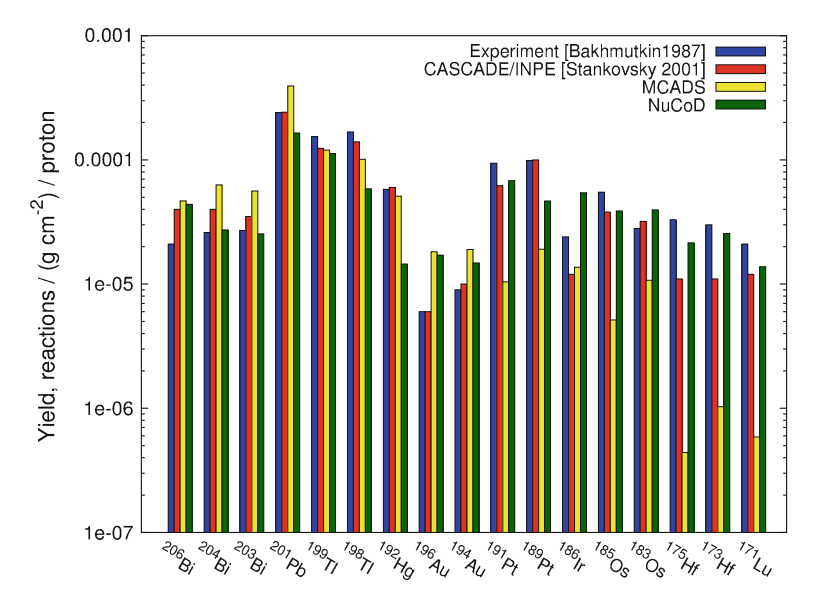


Fig. 3 Yields of spallation products in the lead target calculated with CASCADE/INPE [12], MCADS and NuCoD (this work) and compared with experimental data [11]. The cylindrical target section has a diameter of 20 cm and a length of 6 cm. The yields are measured and calculated at the back side of the section. For more details see [11]

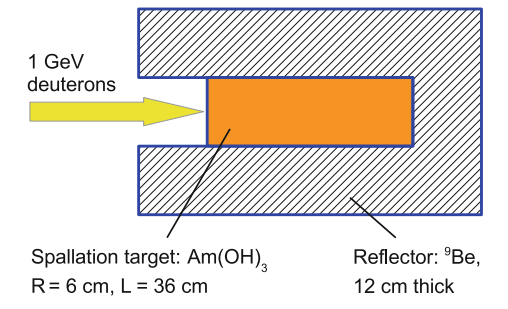
proton beam with a current of $0.3\,\mu\mathrm{A}$ for 3 h. In the experiment [11] the γ -spectra measurements started 7 h after the termination of the beam and were continuing for 8 days.

From Fig. 3 one can conclude that CASCADE/INPE and MCADS are not able to describe the isotope yields accurately, but CASCADE/INPE predicts closer values to the experimental data. The reason is that both these codes calculate prompt yields and don't take into account radioactive decays of reaction products. In contrast, NuCoD calculates decay chains and notably improves the accuracy of MCADS calculations, especially in the region of lighter elements (from Pt to Lu), where corresponding abundances are significantly increased due to decays of heavier elements.

5 Results

Production of heavy transuranic elements, up to Fm, was calculated with NuCoD in a cylindrical target irradiated by a 1 GeV deuteron beam with a current of 20 mA. The target made of Am(OH) $_3$ has radius of 6 cm and length of 36 cm, see Fig. 4. Due to the lack of information on the americium hydroxide properties the density was set to $10 \, \text{g/cm}^3$, which corresponds to the mass of the target of 40.7 kg. The hydrogen in this compound plays a role of a moderator, where the neutrons transfer on average 1/2

Fig. 4 Spallation target with a reflector for SHE production



of their energy in each n-H collision. With decreasing neutron energy the probability of capture increases and, therefore, the rate of neutron-rich elements production also increases. In order to prevent, at least partly, the leakage of neutrons, the target was covered by a 12 cm layer of beryllium. Beryllium has a very low neutron capture cross section and by this reason is widely used as a neutron reflector in reactors.

The isotope ratio of americium was set approximately as in spent nuclear fuel 241 Am : 243 Am = 3 : 2. Nuclei of 243 Am are of the most importance for the production of SHE, because the probability to capture a certain number of neutrons decreases very fast with a number of required captures. By this reason it is assumed that elements with atomic numbers A > 243 are mostly produced by multiple capture of neutrons on 243 Am and heavier products. The calculated average number of neutrons captured on 243 Am or heavier nuclei is about $\bar{n}(0.5y) = 0.6$ for 6 months and $\bar{n}(1y) = 1.2$ for 1 year of irradiation, which is more precise than it was estimated in the Introduction.

The isotope maps of nuclides produced after 5 days (one time step between the target composition updates), 1 month and 6 months of irradiation are presented in Fig. 5. The first map represents the isotopes produced before the first target composition update, i.e. direct output of MCADS simulation corrected for radioactive decays. Hence, on this map one can see only secondaries of (d, Am), (p, Am) and (n, Am) reactions and their decay. The main path of TRU elements production, starting from ²⁴³Am, is shown by thick arrows up to ²⁴⁹Bk. Produced in neutron capture ²⁴⁴Am undergoes β^- -decay with the half-life of $t_{1/2} = 10$ h. Resulting longlived isotope 244 Cm ($t_{1/2} = 18$ years) can capture one more neutron. The next four isotopes of Cm have half-life times of several thousands years and longer, so that they can be accumulated in the target after corresponding number of (n, γ) reactions. Isotope ²⁴⁹Cm has half-life time of 64 min and decays into relatively long-lived ²⁴⁹Bk $(t_{1/2} = 320 \,\mathrm{days})$. Heavier isotopes are produced in a similar way, see thin arrows on Fig. 5 up to fermium. The isotopes ^{254–256}Fm have half-life times of 2.5–20 h and undergo α -decay or spontaneous fission and thus drop out from the chain of neutron capture reactions. This region on the map of isotopes is called "fermium gap" and further move to the heavier isotopes is practically impossible. As seen from Fig. 5, the relative abundance of Fm isotopes in the considered spallation target is extremely low, $\sim 10^{-17}$.

I. Mishustin et al.

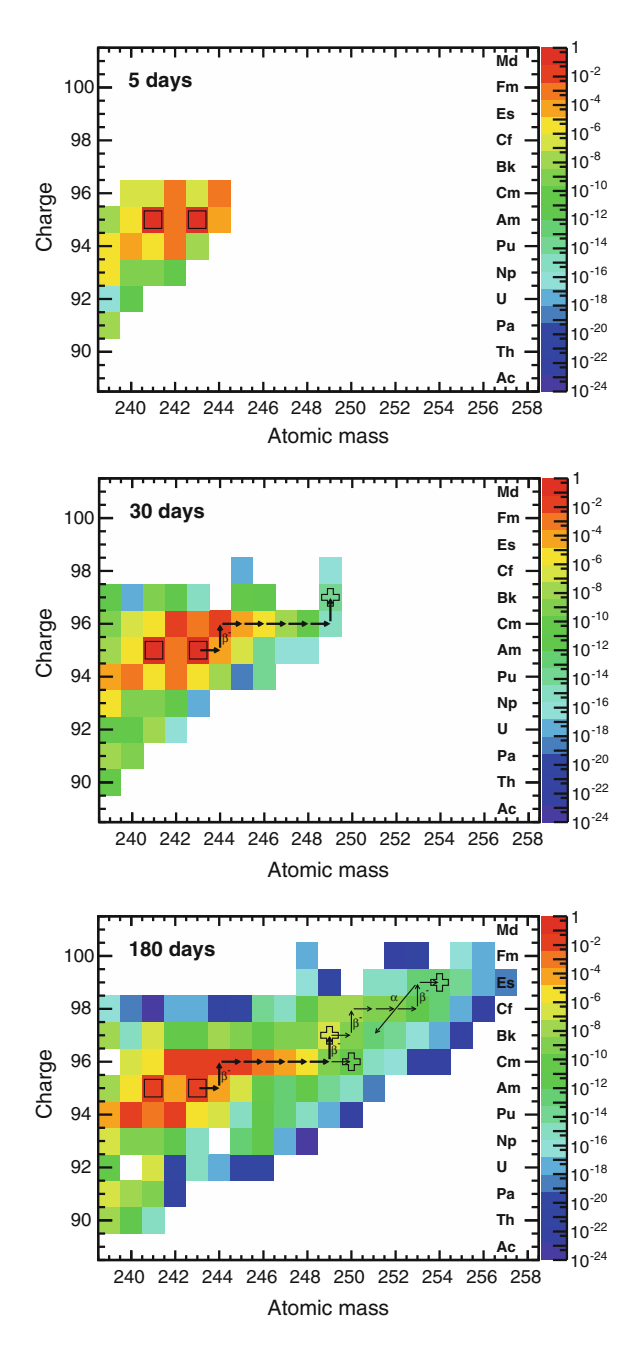


Fig. 5 Calculated maps of isotope abundances after 5 days (top), 30 days (middle) and 180 days (bottom) of irradiation. The initial isotopes, 241 Am and 243 Am, are marked with the squares, the crosses indicate 249 Bk, 250 Cm and 254 Es

Production of 250 Cm and 254 Es is suppressed by the fast β^- -decay of 249 Cm and the α -decay of 253 Es, respectively. However, the situation may change in the case of pulse-mode accelerator with pulse duration of $\sim 1~\mu s$ and very intensive bunches of protons.

Relative abundances of 243 Am, 244,246 Cm, 249 Bk and fission products as functions of time are shown in Fig. 6. As one can see, the abundance of 244 Cm raises rapidly at the beginning and after \sim 135 days exceeds the 243 Am abundance. In order to produce 246 Cm three neutrons must be captured by one nucleus. This means that 246 Cm can be seen only after three steps. This inaccuracy of the modeling method is only noticeable on the first steps and then becomes negligible. The abundance level corresponding to the mass of 10 mg for nuclides with atomic mass of about 250 is drawn by the black dashed line. 249 Bk reaches this level after 150 days.

Abundances of some long-lived isotopes after 2, 4 and 6 months of irradiation are presented in the Table 1. One can see that 249 Bk exceeds the required level of several mg for a fusion target fabrication [13]. 249 Cf can also reach this level after some cooling time after the irradiation termination due to the β^- -decay of 249 Bk ($t_{1/2} = 320$ days).

An increase of irradiation time should strongly enhance the yields of produced neutron-rich elements. Indeed, if the irradiation time is prolonged by a factor of 2, i.e. from 6 months to 1 year, the corresponding amounts of neutron-rich nuclei with n captured neutrons will increase by a factor $F(n) = 0.55 \times 2^n$ (see Eq. 2). For 257 Es n = 14 and $F(14) \simeq 10^4$. According to the results of NuCoD calculations the mass of accumulated 257 Es is 3×10^{-11} mg (see Table 1) after half a year of irradiation. However, it was assumed that 257 Es does not decay, while in reality it has a

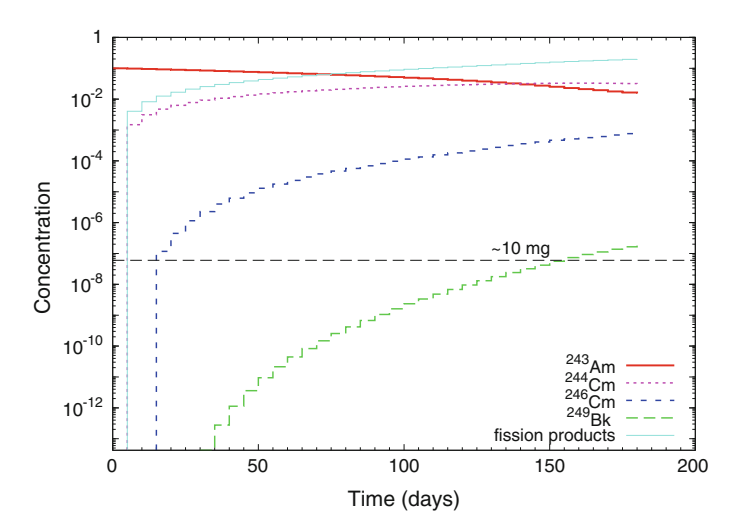


Fig. 6 Time evolution of the abundances of 243 Am, 244 Cm, 246 Cm, 249 Bk and fission products in the target calculated with NuCoD. The abundance corresponding to the mass of 10 mg is presented by a dashed black line (valid for elements with atomic mass A of \sim 250)

I. Mishustin et al.

Table 1 Abundance of ²⁴⁹Bk, ^{249,251}Cf, ²⁵⁰Cm, ²⁵⁴Es and ²⁵⁷Es after 2, 4 and 6 months of a continuous irradiation by a 1 GeV deuteron beam with a current of 20 mA

Isotope	Mass (mg)				
	2 months	4 months	6 months		
²⁴⁹ Bk	7.5×10^{-3}	1.6	32		
²⁴⁹ Cf	1.0×10^{-4}	0.042	1.2		
²⁵⁰ Cm	2×10^{-7}	1.1×10^{-4}	4.1×10^{-3}		
²⁵¹ Cf	2×10^{-6}	8.2×10^{-3}	0.55		
²⁵⁴ Es	10^{-14}	10^8	1.4×10^{-5}		
²⁵⁷ Es	_	3×10^{-15}	3×10 ⁻¹¹		

half-life time of about 8 days and undergoes β^- -decay into 257 Fm, which has a half-life time of 100 days. This means that calculated mass of 257 Es actually corresponds to 257 Fm. Multiplying 3×10^{-11} mg by the factor F(14) one can obtain that the mass of accumulated 257 Fm should be of the order of 10^{-7} mg.

6 Conclusions

After extensive MCADS+NuCoD simulations we came to the following conclusions:

- (1) Elimination of long-lived radioactive waste, e.g., MA is feasible with advanced ADS technologies using fissile targets (5 kg/year in a single target);
- (2) With high neutron fluxes at such facilities one can also produce significant amounts of neutron-rich heavy elements in (n, γ) reactions;
- (3) Synthesis of super-heavy elements in measurable amounts is in principle possible at operation times of several years.

Acknowledgments The authors thank Valeri Zagrebaev for fruitful discussions. Our calculations were performed at the Center for Scientific Computing (CSC) of the Goethe University, Frankfurt am Main. We are grateful to the staff of the Center for support.

References

- 1. G.I. Bell, Phys. Rev. 158, 1127 (1967)
- 2. H.W. Meldner, Phys. Rev. Lett. 28, 975 (1972)
- 3. A. Botvina, I. Mishustin, V. Zagrebaev, W. Greiner, Int. J. Mod. Phys. 19, 2063 (2010)
- 4. V.I. Zagrebaev, A.V. Karpov, I.N. Mishustin, W. Greiner, Phys. Rev. C 84, 044617 (2011)
- 5. G.T. Seaborg, Annu. Rev. Nucl. Sci. 18, 119 (1968)
- 6. Yu. Malyshkin, I. Pshenichnov, I. Mishustin, W. Greiner, EPJ Web Conf. 21, 10006 (2012)
- Yu. Malyshkin, I. Pshenichnov, I. Mishustin, T. Hughes, O. Heid, W. Greiner, Nucl. Inst. Meth. B 289, 79 (2012)

- 8. Yu. Malyshkin, I. Pshenichnov, I. Mishustin, and W. Greiner, in *Proceedings of International Conferences on Nuclear Data for Science and Technology*, New York (2013)
- 9. Yu. Malyshkin, I. Pshenichnov, I. Mishustin, W. Greiner, in *Proceedings of the Joint International Conference of Supercomputing in Nuclear Applications and Monte Carlo* Paris (2013)
- 10. J. Apostolakis et al., Radiat. Phys. Chem. **78**, 859 (2009)
- 11. S.V. Bakhmutkin, A.A. Nosov, A.A. Rimskii-Korsakov, At. Energiy. 63, 2 (1986)
- A. Stankovsky, W. Saito, V. Artisyuk, A. Shmelev, Y. Korovin, J. Nucl. Sci. Technol. 38, 503 (2001)
- 13. V.I. Zagrebaev, A.V. Karpov, W. Greiner, Phys. Rev. C 85, 014608 (2012)

Part IV Heavy Ion Physics

FAIR—Cosmic Matter in the Laboratory

H. Stöcker and C. Sturm

Abstract To explore cosmic matter in the laboratory—this fascinating research prospect becomes available in 2018 at the Facility for Antiproton and Ion Research, FAIR. The new facility is being constructed within the next five years adjacent to the existing accelerator complex of the GSI Helmholtz Centre for Heavy Ion Research at Darmstadt/Germany, expanding the research goals and technical possibilities substantially. This includes new insights into the dynamics of supernovae depending on the properties of short-lived neutron-rich nuclei which will be investigated with intense rare isotope beams. New insights will be provided into the interior of stars by exploring dense plasmas with intense heavy-ion beams combined with a highperformance laser—or into neutron star cores by probing the highest baryon densities in relativistic nucleus-nucleus collisions at unprecedented collision rates. To the latter, the properties of hadrons play an important part which will be systematically studied by high precision hadron spectroscopy with antiproton beams at unmatched intensities. The worldwide unique accelerator and experimental facilities of FAIR will open the way for a broad spectrum of unprecedented fore-front research supplying a large variety of experiments in hadron, nuclear, atomic and plasma physics as well as biomedical and material science which will be briefly described in this article.

H. Stöcker (⊠) · C. Sturm GSI Helmholtzzentrum für Schwerionenforschung GmbH, Planckstraße 1, 64291 Darmstadt, Germany e-mail: h.stoecker@gsi.de

C. Sturm

e-mail: c.sturm@gsi.de

H. Stöcker

Judah M. Eisenberg Chair, Institut für Theoretische Physik, Goethe Universität, Max-von-Laue Str. 1, 60438 Frankfurt, Germany

H. Stöcker

Frankfurt Institute for Advanced Studies, Ruth-Moufang-Str. 1, 60438 Frankfurt, Germany

C. Sturm

Institut für Kernphysik, Goethe Universität, Max-von-Laue Str. 1, 60438 Frankfurt, Germany

© Springer International Publishing Switzerland 2015 W. Greiner (ed.), *Nuclear Physics: Present and Future*, FIAS Interdisciplinary Science Series, DOI 10.1007/978-3-319-10199-6_16 166 H. Stöcker and C. Sturm

1 Introduction

The new international facility Facility for Antiproton and Ion Research (FAIR in Europe [1–3]) is being constructed adjacent to the site of the GSI Helmholtz Centre for Heavy Ion Research at Darmstadt, Germany (see Fig. 1). It will substantially expand research goals by providing worldwide unique accelerator and detector facilities for a large variety of unprecedented fore-front science. The main thrust of FAIR research focuses on the structure and evolution of cosmic matter on a microscopic scale. This will deepen our understanding of fundamental questions such as:

- How does the complex structure of matter at all levels arise from the basic constituents and the fundamental interactions?
- How can the structure of hadronic matter be deduced from the strong interaction? In particular, what is the origin of hadron masses?
- What is the structure of matter under the extreme conditions of temperature and density found in astrophysical objects?
- What was the evolution and the composition of matter in the early Universe?
- What is the origin of the elements in the Universe?

To address these fundamental questions FAIR will provide an extensive range of particle beams from protons and their antimatter partners, antiprotons to ion beams of all chemical elements up to the heaviest (stable) one, uranium, with world record intensities. As a joint effort of more than 50 countries the new facility builds, and substantially expands, on the present accelerator system at GSI Helmholtz Centre for Heavy Ion Research, both in its research goals and its technical possibilities. Compared to the present GSI facility, the beam intensities will increase by a factor of 100 for primary beams and up to a factor of 10,000 for secondary radioactive beams with an excellent beam brilliance of primary as well as secondary beams. This will be achieved through innovative beam handling techniques, many aspects of which have been developed at GSI over recent years with the present accelerator complex. This includes in particular stochastic, laser and electron-beam cooling of high-energy, high-charge state ion beams in storage rings and bunch compression techniques. To realize parallel operation of the research programs the design of FAIR includes the superconducting double-ring synchrotrons SIS100 and SIS300. Both have a circumference of 1,100 m each and a magnetic rigidity of 100 and 300 Tm, respectively. Since a key feature of the new facility will be the generation of intense, high-quality secondary beams, the facility design contains a system of associated storage rings for beam collection, cooling, phase space optimization and experimentation (see Fig. 1).

After the official launch of the project in 2007, nine countries² signed the international agreement on the construction of FAIR on October 4th, 2010. Civil work

¹ This article is based on the FAIR Green Paper [4] and gives an update of former publications [5–9]. A copy of this manuscript will be published in [10, 11].

 $^{^2}$ In alphabetical order: Finland, France, Germany, India, Poland, Romania, Russia, Slovenia and Sweden.

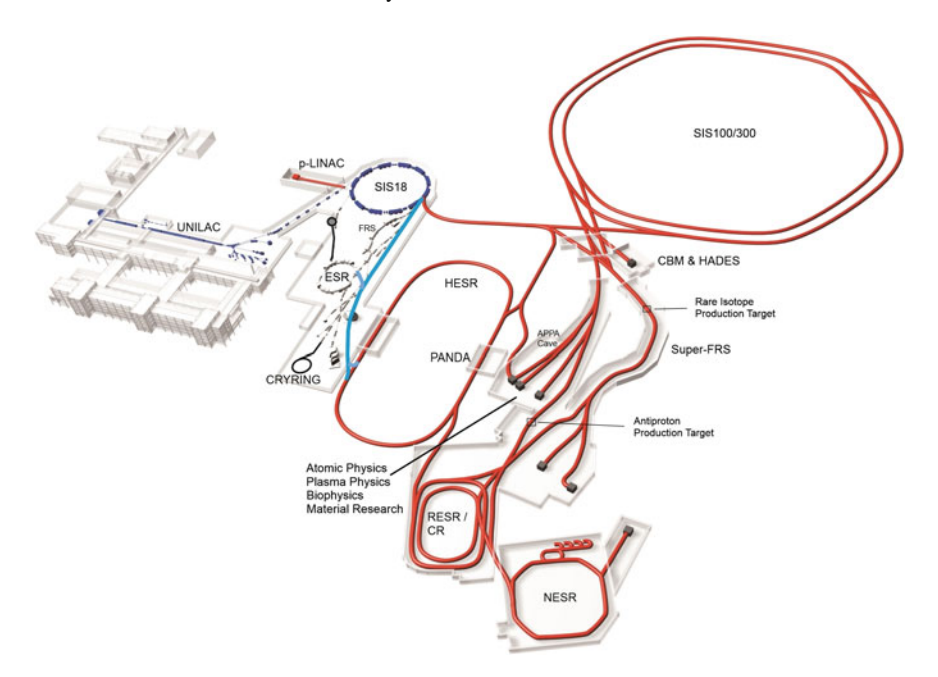


Fig. 1 The existing GSI facility is shown on the *left*, in *dark-blue* the existing accelerators and ion sources. On the *right* the new FAIR complex is displayed in *red* with its 100 and 300 Tm super conducting double-ring synchrotrons SIS100 and SIS300, detector areas (i) for atomic and plasma physics, biomedical and material sciences (APPA), (ii) for the relativistic nucleus-nucleus collision experiments CBM and HADES, (iii) for the radioactive beam facility (NuSTAR) and (iv) for the hadron physics detector system PANDA as well as the rare-isotope and antiproton production targets with storage rings. Possible *beam lines* for transport of protons and ions from SIS18 directly to the High Energy Storage Ring (HESR) and of antiprotons and ions from HESR to the ESR are shown with *light-blue* color. These *beam lines* are currently subject of detailed investigations

started in 2013, first beams will be delivered in 2018. The *Modularized Start Version* [3, 4] of FAIR consists of the superconducting synchrotron SIS100 which feeds primary beams for fixed-target experiments and production targets for secondary beams of rare isotopes and antiprotons with the two cooler-storage rings HESR (High Energy Storage Ring) and CR (Collector Ring). Detector areas for all scientific pillars are included. Following an upgrade for high intensities, the existing GSI accelerators UNILAC and SIS18 will serve as injectors. The facility will be completed by experimental storage rings enhancing capabilities of secondary beams and by the superconducting synchrotron SIS300 providing parallel operation of experimental programs as well as particle energies twenty-fold higher compared to those achieved so far at GSI.

168 H. Stöcker and C. Sturm

2 The Experimental Program of FAIR

The approved FAIR research program embraces 14 experiments. These form the four scientific pillars of FAIR and offer a large variety of unprecedented forefront research in hadron, nuclear, atomic and plasma physics as well as applied sciences. Already today, over 2,500 scientists and engineers are involved in the design and preparation of the FAIR experiments. The four scientific pillars are named

- APPA—Atomic Physics, Plasma Physics and Applications,
- CBM and HADES—Compressed Baryonic Matter,
- NuSTAR—Nuclear Structure, Astrophysics and Reactions,
- PANDA—AntiProton Annihilation in DArmstadt.

2.1 APPA—A Look into the Interior of Giant Planets and Stars

In the Universe at large, matter exists predominantly either as hot dense plasma in the interior of stars or in stellar atmospheres, as medium- or low-temperature dense plasma in the interior of giant planets, or as hot plasma of very low density in interstellar space. In particular the regime of dense plasmas is so far only scarcely explored, since it is difficult to approach experimentally. Intense heavy-ion beams provide an efficient tool to create large samples of this high-energy-density matter with volumes of the order of a few mm³ or even cm³ and lifetimes of the order of several tenths of nanoseconds by isochoric and uniform heating of solid matter. The uniform physical conditions and comparatively long life times facilitate application of a broad spectrum of the diagnostic tools for studying these states of matter. For Plasma physics the availability of high-energy, high-intensity ion-beams in unique combination with a petawatt-laser enables the investigation of high energy density matter in regimes of temperature, density and pressure not accessible so far [12]. It will allow probing new areas in the phase diagram and long-standing open questions of basic equation-of-state research can be addressed.

Atomic physics with highly charged ions [13, 14] will concentrate on two central research themes: (i) the correlated electron dynamics in extremely strong, ultrashort electromagnetic fields including the production of electron-positron pairs and (ii) fundamental interactions between electrons and heavy nuclei, in particular the interactions described by Quantum Electrodynamics, QED. Here bound-state QED in critical and supercritical fields is the focus of the research program. In addition, atomic physics techniques will be used to determine properties of stable and unstable nuclei and to perform tests of predictions of fundamental theories besides QED. Since FAIR is promising the highest intensities for relativistic beams of stable and unstable heavy nuclei, combined with the strongest available electromagnetic fields, for a broad range of experiments. This will then allow the extension of atomic physics research across virtually the full range of atomic matter, i.e. concerning the accessible ionic charge states as well as beam energies.

Very recently a realization scheme has been worked out for experiments with highly-charged heavy-ions at relativistic energies in the High-Energy Storage Ring HESR and at very low-energies at the CRYRING coupled to the present ESR (see Fig. 1) [15]. In particular, the storage ring HESR will be exploited for collision studies. Here, fundamental atomic processes can be investigated for cooled heavy-ions at well-defined charge states interacting with photons, electrons and atoms. These studies can be extended at the CRYRING (at ESR) to the low-energy regime where the atomic interactions are dominated by strong perturbations and quasi-molecular effects. Both facilities, the HESR and the CRYRING at the present ESR, will provide unprecedented physics opportunities already at the very early stage of FAIR operation.

FAIR will provide beams of high energy and very high intensity, whose biological effectiveness was never studied in the past, but whose contribution to the dose equivalent in space is very significant. It will be possible to investigate the radiation damage induced by cosmic rays and protection issues for Moon and Mars missions. Furthermore, the intense ion-matter interactions with projectiles of energies above 1 GeV/u will enable systematic studies of material modifications.

2.2 CBM and HADES—A Look into the Interior of Neutron Stars

The stability of neutron stars is guaranteed by the Pauli principle of nucleons together with the repulsive part of the nucleon-nucleon interaction. Therefore the structure of a neutron star is dictated by the strong interaction with the nuclear equation-of-state as key ingredient. The transition from the outer to the inner core of a neutron star is specified by the appearance of exotic phases, e.g. matter containing additional particles species carrying strangeness such as hyperons, pion or kaon condensed matter or deconfined quark matter. The question whether the interior of a neutron star is already in a (superconducting) quark phase is an active field of research. To explore nuclear matter densities beyond saturation density in the laboratory nucleus-nucleus reactions provide the only possibility.

The mission of high-energy nucleus-nucleus collision experiments worldwide is to investigate the properties of strongly interacting matter under these extreme conditions. At very high collision energies, as available at RHIC and LHC, the measurements concentrate on the study of the properties of deconfined QCD matter at very high temperatures and almost zero net baryon densities. Results from lattice QCD indicate that the transition from confined to deconfined matter at vanishing net baryon density is a smooth crossover, whereas in the region of high net baryon densities, accessible with heavy-ion reactions at lower beam energies, a first-order phase transition is expected [16]. Its experimental confirmation would be a substantial progress in the understanding of the properties of strongly interacting matter.

170 H. Stöcker and C. Sturm

Complementary to high-energy nucleus-nucleus collision experiments at RHIC and LHC, the CBM experiment [17–19] as well as HADES [20–25] at SIS100/300 will explore the QCD phase diagram in the region of very high baryon densities and moderate temperatures by investigating heavy-ion collision in the beam energy range³ 2–35 AGeV. This approach includes the study of the nuclear matter equation-of-state, the search for new forms of matter, the search for the predicted first order phase transition to the deconfinement phase at high baryon densities, the QCD critical endpoint, and the chiral phase transition, which is related to the origin of hadron masses.

In the case of the predicted first order phase transition, basically one has to search for non-monotonic behavior of observables as function of collision energy and system size. The CBM experiment at FAIR is being designed to perform this search with a large range of observables, including very rare probes at these energy regime like charmed hadrons. Produced near threshold, their measurement might be well suited to discriminate hadronic from partonic production scenarios. The former requires pairwise creation of charmed hadrons, the latter the recombination of c-quarks created in first chance collisions of the nucleus-nucleus reaction. Ratios of hadrons containing charm quarks as a function of the available energy may provide direct evidence for a deconfinement phase.

The properties of hadrons are expected to be modified in a dense hadronic environment which is eventually linked to the onset of chiral symmetry restoration at high baryon densities and/or high temperatures. The experimental verification of this theoretical prediction is one of the most challenging questions in modern strongly interacting matter physics. The dileptonic decays of light vector mesons (ρ, ω, ϕ) provide the tool to study such modifications since the lepton daughters do not undergo strong interactions and can therefore leave the dense hadronic medium essentially undistorted by final-state interaction. For these investigations the ρ meson plays an important role since it has a short lifetime and through this a large probability to decay inside the reaction zone when created in a nucleus-nucleus collision. As a detector system dedicated to high-precision di-electron spectroscopy at beam energies of 1–2 AGeV, the modified HADES detector at SIS100 will measure e^+e^- decay channels as well as hadrons [23–25] in collisions of light nuclei up to 10 AGeV beam energy. In addition and complementary, the CBM experiment will cover the complete FAIR energy range by measuring both the e^+e^- and the $\mu^+\mu^-$ decay channels.

Most of the rare probes like lepton pairs, multi-strange hyperons and charm will be measured for the first time in the FAIR energy range. The goal of the CBM experiment as well as HADES is to study rare and bulk particles including their phase-space distributions, correlations and fluctuations with unprecedented precision and statistics. These measurements will be performed in nucleus–nucleus, proton–nucleus, and proton–proton collisions at various beam energies. The unprecedented beam intensities will allow to study extremely rare probes with high precision which have not been accessible by previous nucleus-nucleus experiments at the AGS, SPS and the beam energy scan program (BES) at RHIC.

³ Light nuclei up to 44 AGeV.

Complementary to the CBM program at FAIR and at about the same time as FAIR the Nuclotron-based Ion Collider facility NICA will come into operation at the Joint Institute for Nuclear Research (JINR) in Dubna [26]. The main goal of the project is to study hot and dense strongly interacting matter in nucleus-nucleus collisions at center-of-mass energies $\sqrt{s_{NN}} = 4-11 \,\text{GeV}$ with the Multi-Purpose Detector (MPD). As a collider, NICA achieves higher collision energies while CBM will perform experiments with up to 4 orders of magnitude higher collision rates.

2.3 NuSTAR—Rapid Nuclear Processes in Supernovae and the Elemental Abundances in the Universe

Reactions between nuclei play a decisive role in many astrophysical processes in the universe. Nuclear structure effects and the dynamics of nuclear reactions are directly reflected in the various evolutionary stages of stars, in the light curves of stellar explosions, and in the elemental abundance distributions in the Universe. Unstable nuclei, far away from stability, are involved and their properties determine the fate of the relevant astrophysical processes. The radioactive beam facility at FAIR offers world-wide unique experimental opportunities for this area of research.

The main scientific thrusts in the study of nuclei far from stability are aimed at three areas of research: (i) the structure of nuclei, the quantal many-body systems built by protons and neutrons and governed by the strong force, towards the limits of stability, where nuclei become unbound, (ii) nuclear astrophysics delineating the detailed paths of element formation in stars and explosive nucleosynthesis that involve short-lived nuclei, (iii) and the study of fundamental interactions and symmetries exploiting the properties of specific radioactive nuclei.

The central part of the NuSTAR programme at FAIR [27, 28] is the high acceptance Super-FRS with its multi-stage separation that will provide high intensity mono-isotopic radioactive ion beams of bare and highly-ionized exotic nuclei at and close to the driplines. This separator, in conjunction with high intensity primary beams with energies up to 1.5 AGeV, is the keystone for a competitive NuSTAR physics programme. This opens the unique opportunity to study the evolution of nuclear structure into the yet unexplored territory of the nuclear chart and to determine the properties of many short-lived nuclei which are produced in explosive astrophysical events and crucially influence their dynamics and associated nucleosynthesis processes.

⁴ Au + Au collisions at FAIR: $E_{\text{kin}} = 2-35 \,\text{AGeV}$, $\sqrt{s_{NN}} = 2.7-8.3 \,\text{GeV}$.

172 H. Stöcker and C. Sturm

2.4 PANDA—The Structure of Hadrons and the Generation of Mass in the Visible Universe

In the evolution of the universe, microseconds after the big bang, a coalescence of quarks and gluons to hadrons occurred associated with the generation of hadron masses. The elementary light quarks, the up and down quarks that make up the nucleon, have very small masses amounting to only a few percent of the total mass of the nucleon. Most of the baryon's masses, and hence of the visible universe stems from the QCD interaction. The generation of mass is thus associated with the confinement of quarks and the spontaneous breaking of chiral symmetry, one of the fundamental symmetries of QCD in the limit of massless quarks.

The big challenge in hadron physics is to achieve a quantitative understanding of strongly interacting complex systems at the level of quarks and gluons. In $p\bar{p}$ -annihilation, particles with gluonic degrees of freedom as well as particle-antiparticle pairs are copiously produced, allowing spectroscopic studies with unprecedented statistics and precision. The PANDA experiment at FAIR [29–31] will bring new fundamental knowledge in hadron physics by pushing the precision barrier towards new limits. The charmonium ($c\bar{c}$) spectroscopy will take advantage of high-precision measurements of mass, width and decay branches. Particular emphasis is placed on mesons with open and hidden charm, which extends ongoing studies in the light quark sector to heavy quarks, and adds information on contributions of the gluon dynamics to hadron masses. The search for exotic hadronic matter such as hybrid mesons or heavy glueballs will profit by precise scanning of resonance curves of narrow states as well. Additionally, the precision gamma-ray spectroscopy of single and double hypernuclei will allow extracting information on their structure and on the hyperon-nucleon and hyperon-hyperon interaction.

Recently, much attention has been attracted by the observation at electron-positron colliders of the so-called X, Y and Z states with masses around 4 GeV as measured by experiments e.g. Belle at KEKB [32], BESIII at BEPC [33] and others. These heavy mesons show very unusual properties, whose theoretical interpretation is entirely open.

An extension of the FAIR antiproton facility to a $\bar{p}p$ -collider with a maximum center-of-mass energy $\sqrt{s^{\text{max}}}=30$ GeV [34] and luminosities of about $3\times 10^{30}\,\mathrm{cm^{-2}s^{-1}}$ [35] would allow to analyze these exotic objects and their beauty complements at quantal states not accessible to electron-positron colliders. FAIR would thus open the way to a rich spectrum of Beauty Physics by formation of beauty baryon-antibaryon pairs with a large variety of beauty, charm, strange and light quarks, as well as beauty mesons with spin $\neq 1$. Technically, the antiproton and proton beam would be stored and accelerated in opposite directions inside the HESR which would require a second injection point as well as a second electron cooler. Furthermore the PANDA detector can serve as the mid-rapidity detector system. This fascinating opportunity will enrich the PANDA physics program into new, unprecedented realms and will push the physics program of the High Energy Storage Ring HESR for decades to come.

3 Summary

The construction of the Facility for Antiproton and Ion Research, FAIR, has started in 2013, so that the first beams will be delivered in 2018. The scientific program of FAIR covers

- the investigation of bulk matter in the dense and hot plasma state, atomic physics of ultra-high electro-magnetic fields, material and biological research using intense, highly-stripped ions and high-intensity laser fields (APPA);
- the exploration of the QCD phase-diagram and the phase transition to the deconfinement phase at high baryon densities in high-intensity nucleus-nucleus collisions (CBM and HADES);
- the investigation of the nuclear chart and nuclear structure far from stability and of nuclear astrophysics with radio-active beams (NuSTAR);
- the exploration of the hadron structure, QCD vacuum, and the nature of the strong force in the non-perturbative regime of quantum chromo dynamics with high-energy beams of antiprotons (PANDA),

forming together the four scientific pillars. The design of FAIR includes the superconducting double-ring synchrotrons SIS100 and SIS300 to realize parallel operation of the research programs. Since a key feature of the new facility will be the generation of intense, high-quality secondary beams, the facility design contains a system of associated storage rings for beam collection, cooling, phase space optimization and experimentation.

The first phase of the FAIR project comprises the superconducting synchrotron SIS100 as well as experimental areas to perform experiments for all research pillars. It will allow to carry out an outstanding and world-leading research program in hadron, nuclear, atomic and plasma physics as well as applied sciences. Due to the high luminosity which exceeds current facilities by orders of magnitude, experiments will be feasible that could not be done elsewhere. FAIR will expand the knowledge in various scientific fields beyond current frontiers. Moreover, exciting synergy effects between the various research fields and instruments at FAIR in five parallel and crossed operation modes will prove what has been the basic idea of the FAIR communities: *four* scientific pillars with *one* machine.

References

- 1. H.H. Gutbrod et al. (eds.), FAIR Baseline Technical Report, ISBN 3-9811298-0-6 (2006)
- 2. W.F. Henning, FAIR: recent developments and status. Nucl. Phys. A 805, 502c (2008)
- 3. H. Stöcker, FAIR: challenges overcome and still to be met. in *Proceedings of EPAC08*, Published in Proceedings of Conference C0806233:moycgm01 (2008)
- Green paper of FAIR: the modularized start version, https://www.gsi.de/documents/DOC-2009-Nov-124-1.pdf. Accessed Oct 2009
- 5. C. Sturm, B. Sharkov, H. Stöcker, 1,2,3.. FAIR !. Nucl. Phys. A 834, 682c (2010)
- 6. H. Stöcker, C. Sturm, The FAIR start. Nucl. Phys. A **855**, 506 (2011)

 H. Stöcker, C. Sturm, The facility for antiproton and ion research FAIR: cosmic matter in the laboratory. Nucl. Phys. A 862–863, 92 (2011)

- 8. C. Sturm, H. Stöcker, The facility for antiproton and ion research FAIR. Phys. Part. Nucl. Lett. **8.** 865 (2011)
- H. Stöcker, C. Sturm, The facility for antiproton and ion research FAIR. Phys. J. Ro. 58, 1023 (2013)
- 10. H. Stöcker, C. Sturm, FAIR—cosmic matter in the laboratory, submitted to SLAC e-conference. in *Electronic Conference Proceedings*. http://www.slac.stanford.edu/econf/
- 11. H. Stöcker, C. Sturm, FAIR—cosmic matter in the laboratory. Astron. Nachr. http://www.an-journal.org. Wiley, Weinheim
- 12. I.V. Lomonosov, N.A. Tahir, Prospects of high-energy density matter research at the future fair facility at Darmstadt, Nucl. Phys. News **16**(1), 29 (2006)
- 13. Th Stöhlker et al., Atomic physics with highly-charged ions at the future FAIR facility: a status report. Nucl. Instr. Methods Phys. Res. B **261**, 234 (2007)
- Th Stöhlker et al., SPARC: The stored particle atomic research collaboration at FAIR. AIP Conf. Proc. 1336, 132 (2011)
- 15. Th. Stöhlker et al., SPARC collaboration: new strategy for storage ring physics at FAIR. Hyperfine Interact. (2014). doi:10.1007/s10751-014-1047-2
- B. Friman, C. Höhne, J. Knoll, S. Leupold, J. Randrup, R. Rapp, P. Senger (eds.), The CBM Physics Book, Lecture Notes in Physics, vol 814 (2011), pp. 1–994
- 17. P. Senger et al., CBM Collaboration, Compressed baryonic matter: experiments at GSI and FAIR. Phys. Part. Nucl. 39, 1055 (2008)
- 18. P. Senger et al., CBM Collaboration, Probing dense baryonic matter. Prog. Part. Nucl. Phys. **62**, 375 (2009)
- J. Heuser et al., CBM Collaboration, The compressed baryonic matter experiment at FAIR. Nucl. Phys. A 904–905, 941c (2013)
- G. Agakishiev et al., HADES Collaboration, The high-acceptance dielectron spectrometer HADES, Eur. Phys. J. A 41, 243 (2009)
- 21. G. Agakishiev et al., HADES Collaboration, Origin of the low-mass electron pair excess in light nucleus-nucleus collisions. Phys. Lett. B **690**, 118 (2010)
- 22. G. Agakishiev et al., HADES Collaboration, Dielectron production in Ar + KCl collisions at 1.76A GeV. Phys. Rev. C 84, 014902 (2011)
- 23. I. Fröhlich for the HADES Collaboration, Future perspectives at SIS-100 with HADES-at-FAIR, arXiv:0906.0091v2 [nucl-ex] (2009)
- P. Tlusty et al., HADES Collaboration, Future experiments with HADES at FAIR. AIP Conf. Proc. 1322, 116 (2010)
- K. Lapidus et al., HADES Collaboration, The HADES-at-FAIR project. Phys. Atom. Nucl. 75, 589 (2012)
- 26. V.D. Kekelidze et al., Status of the NICA Project, PoS (EPS-HEP 2013), p. 106
- 27. R. Krücken et al., NuSTAR Collaboration, The nustar facility at FAIR. J. Phys. G 31, S1807 (2005)
- 28. B. Rubio, T. Nilsson, NuSTAR. Nucl. Phys. News **16**, 9 (2006)
- 29. Physics performance report for PANDA: strong interaction studies with antiprotons. arXiv:0903.3905v1 [hep-ex]
- 30. K. Fohl et al., PANDA Collaboration, The PANDA detector at the future FAIR laboratory. Eur. Phys. J. ST **162**, 213 (2008)
- J.S. Lange for the PANDA Collaboration, The PANDA Experiment: hadron physics with antiprotons at FAIR. Int. J. Mod. Phys. A 24, 369 (2009)
- 32. Z.Q. Liu et al., Belle Collaboration, Study of $e^+e^- \to \pi^+\pi^- J/\psi$ and observation of a charged charmoniumlike state at Belle. Phys. Rev. Lett. **110**, 252002 (2013)
- 33. M. Ablikim et al., BESIII Collaboration, Observation of a charged $(D\bar{D}^*)$ -mass peak in $e^+e^-\to \pi^+(D\bar{D}^*)$ —at E=4.26 GeV. Phys. Rev. Lett **112**, 022001 (2014)
- 34. M. Strikmann, H. Stöcker, F. Maas, R. Maier, The authors have suggested to extend the present FAIR design by moderate changes into a full-fledged $\bar{p}p$ collider with $\sqrt{s}^{\text{max}} = 30 \text{ GeV}$ accessing the Beauty Baryon and Meson Physics at FAIR. manuscript in preparation (2013)
- 35. R. Maier, Private communication

Turbulence in Low Viscosity Quark-Gluon Plasma

László P. Csernai

Abstract Collective flow processes were the first phenomena showing that nuclear matter in heavy ion collisions can behave collectively, and not just as a set of independent nucleon nucleon collisions. The present highest energy experiments show the dominance of the fluid dynamical processes due to much higher particle multiplicities. In addition the possibility of new collective phenomena occurs which were known only in macroscopic systems up to now as rotation and turbulent instabilities.

1 The Beginnings of Fluid Dynamics for Heavy Ions

The role of fluid dynamical approach was recognized from the first high energy heavy ion experiments in the 1970s. This model uses the Equation of State (EoS) as the direct information characterizing the matter. The first theoretical predictions came from Walter Greiner's institute. The most important of these early works is Scheid et al. [1]. In this work the compression of nuclear matter in shock waves was first suggested as a basic process. The work by Scheid, Ligensa and Greiner discussed nuclear compressibility in such collisions earlier, while in another early subsequent work of Baumgardt et al. [2] possible experimental consequences were discussed. The importance of shock waves in a work by Chapline et al. [3], was pointed out also.

The first undebatable proof of collective flow was achieved by Gustafsson et al. [4]. This group constructed a large new detector in Berkeley, "The Plastic Ball", and this helped them to achieve undebatable results. Afterwards other groups confirmed the results, and by the flow observations are used to study the details of the equation of state and transport properties. The importance of transport properties, especially the viscosity and transport processes was recognized also [5–7].

Dedicated to Prof. Mikhail Itkis for his 70th birthday!

L.P. Csernai (⋈)

Department of Physics and Technology, University of Bergen, Allegaten 55, 5007 Bergen, Norway

176 L.P. Csernai

At the first heavy ion experiments the dominant flow patterns were the bounce off, side splash or directed flow, which led to a well defined azimuthal and polar direction in the reaction plane [8–11]. These typical flow patters were observed in Los Alamos model calculations [12, 13].

In a concerted theoretical effort it was shown that the fluid dynamical predictions are different from predictions of random nuclear cascade. Thus the experimental results proved the existence of collective flow [14]. This directed flow effect was then observed in different observables, including two-particle and multi-particle correlations, among nucleons and nuclear fragments [8–11].

After the first experimental work that confirmed the existence of collective flow the streamer chamber measurements could also confirm the collective flow, using a sensitive evaluation method developed by Danielewicz and Odyniecz [15]. This method was so sensitive that it could be used even in emulsion experiments [16].

The transport properties, viscosity and Reynolds number of the hot and compressed nuclear matter were also studied early [17] via energy and mass scaling of collective flow data.

The beam energy increased with time and it was predicted that the signature of QGP formation and the related softening of the EoS modifies the flow observables and lead to an appearance of the "third flow component" or "anti-flow" [18]. This was observed a few years later together with several other signals of QGP formation. In these observations the collective flow played an important role.

2 Dominance of Fluid Dynamics in Present Heavy Ion Studies

In 2010 studying heavy ion collisions at LHC energies in a high-resolution 3+1D fluid dynamical model we observed that the flow leads to collective rotation [19] in peripheral collisions, arising from the initial angular momentum [20], see Fig. 1. This rotation leads to a modification of the flow pattern, and the antiflow, characterized by the v_1 parameter weakens and peaks at angles which point more forward.

Unfortunately the v_1 parameter becomes very small at high, e.g. LHC energies, less than one per cent. Thus its measurement is not easy. Still the trend that the antiflow peak moves to more forward rapidities is seen in experiments up to the energy where the peak position could be identified.

At high energies the role of random fluctuations became obvious, and these random fluctuations became strong, exceeding the magnitude of the v_1 flow component. Flow harmonics were identified up to v_8 , having a maximum amplitude at v_3 , in central heavy ion collisions (where due to symmetry reasons all flow harmonics should have vanished). This in itself indicated the low viscosity of the underlying matter which enables large random fluctuations.

In fact, the stability of the flow requires a given amount of viscosity. This stability against turbulent instabilities is characterized by the dimensionless, Reynolds number:

$$Re = l_1 u_1 / v$$

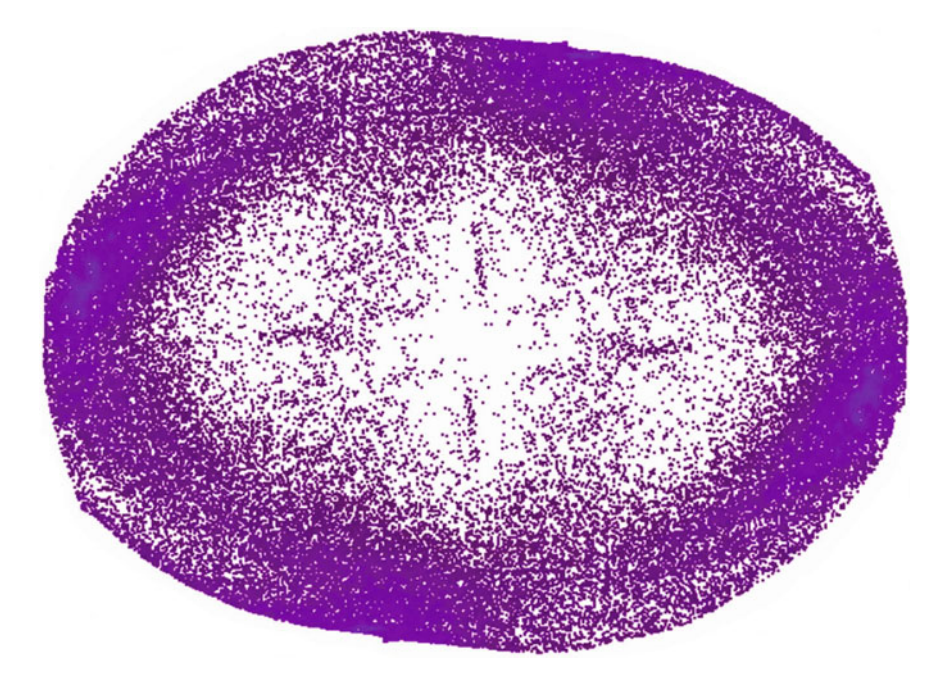


Fig. 1 The positions of the marker particles at a final stage of the flow development in the reaction plane of a heavy ion collision in a peripheral collision where the projectile is on the *top* and the projectile moves to the *right*. Only the participant matter is seen, the projectile and target spectator residues have moved away from the participants. The density of marker particles is proportional to the net baryon charge of the matter which is a conserved quantity. The marker particles rotate clockwise (to the *right* on the *top*). Notice that in the calculation by this time the position of the local maximum density appears on the *right*, i.e. at forward rapidities. It depends on the relative strength of rotation versus the radial expansion whether the peak can reach the positive rapidity side or not

where u_1 is the characteristic flow velocity, l_1 is the characteristic length scale of the flow pattern, η is the shear viscosity, $\nu = \eta/\rho$ is the kinetic viscosity, and ρ is the mass (or energy) density.

In a recent paper Kovtun, Son and Starinets have shown that in certain field theories, that are dual to black branes in higher space-time dimensions, we have the ratio $\eta/s = 1/4\pi$ [21]. Interestingly, this bound is obeyed by $\mathcal{N}=4$ supersymmetric $SU(N_c)$ Yang-Mills theory in the large N_c limit. Subsequently in our recent work with Kapusta and McLerran, [22] we pointed out that η/s has a minimum at the critical point of the QGP—Hadronic Matter phase transition. At pressures below the critical pressure there is a discontinuity in η/s , and at pressures above it there is a broad smooth minimum.

The simplest way to understand the general behavior is that for a dilute gas the mean free path is large, thus it is easy for a particle to carry momentum over great distances, leading to a large viscosity. In the other, liquid, phase the momentum transport can be accomplished by voids, that can be considered as quasi-particles, and their motion can transfer momentum. As the temperature is reduced at fixed

178 L.P. Csernai

pressure in a liquid, the density of voids increases, thus increasing the viscosity. The viscosity, normalized to the entropy, is observed to be the smallest at the critical temperature, the condition to transport momentum is the worst.

Apart of the low viscosity, the phase transition leads to critical fluctuations also. These fluctuations, and their multipolarity spectrum can identify and characterize the phase transition. This is discussed in a large number of publications, including [23, 24]. These fluctuations can shed light on the critical properties of the phase transition.

Another consequence of the low viscosity is turbulence. The most typical occurrence of turbulence is the Kelvin Helmholtz Instability (KHI) which is well known in macroscopic systems, as breaking waves on the sea in strong wind, or in the air with strong wind shear in different vertical layers. It was observed in low viscosity numerical fluid dynamical model calculations that the KHI may occur in heavy ion collisions under favorable conditions [25], see Fig. 2. The development of the KHI is dependent on several conditions, discussed in Ref. [25], but most importantly low viscosity is required. Thus, this phenomenon is a direct measure of the low viscosity.

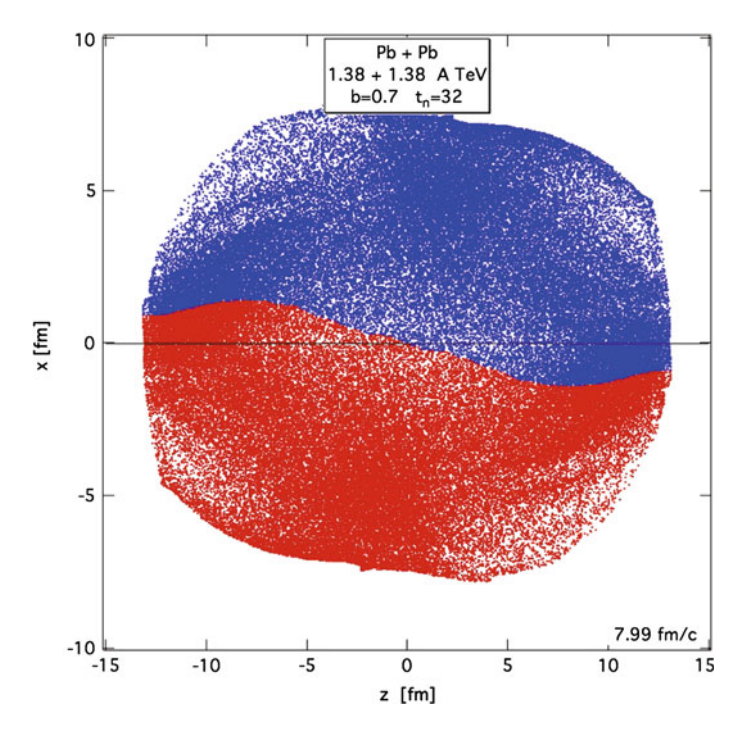


Fig. 2 (color online) The position of the marker particles in the reaction plane of a peripheral $(b=0.7b_{\rm max})$ Pb + Pb heavy ion reaction. The marker particles on the *upper*, projectile side are painted *red*, while on the *lower*, target side *blue*. The division line was originally at the exact *horizontal central plane*. In case of very *low* viscosity the dividing plane with time $(t=7.99\,{\rm fm/c})$ becomes a non-sinusoidal wave, which is the initial development of a Kelvin—Helmholtz Instability. The figure shows that the KHI increases the rotation considerably

Turbulent phenomena may occur also from random fluctuations. We have seen that these fluctuations are significant. In Ref. [26] vorticity arising from random fluctuations in the transverse plane were studied, and a maximum vorticity amplitude of 0.2 c/fm was found. Due to the fact that this vorticity is a product of random fluctuation in a sample of a large number of collisions the average integrated vorticity should vanish.

On the other hand the vorticity in the reaction plane is arising from the initial angular momentum, thus the plane of the rotation is the reaction plane, [x, z] plane and the rotation axis is the y axis. Due to the high angular momentum, $\approx 10^6 \hbar c$, at LHC energies, the vorticity vector is large and pointing into one direction, to the y direction. The amplitude of the vorticity reaches a maximum of 3 c/fm [27], which is more than an order of magnitude larger that the vorticity arising from random fluctuations.

3 Observation of Rotation and Turbulent Phenomena

The observation of the collective phenomena is not a trivial problem, although it has been practiced for more than three decades. The recent emphasis of random fluctuations has extended the evaluation methods to those classes of symmetries which would not occur in case of collisions without fluctuations.

Without fluctuations, the heavy ion collision is mirror symmetric across the reaction plane, as well as reflection symmetric with respect to the center of mass (c.m.) point. Thus in the early, lower energy experiments the longitudinal distribution along the z axis was antisymmetric across the c.m. point or with respect to the c.m. point of the rapidity coordinate. From the mirror symmetry across the reaction plane it followed that the distribution as function of the azimuth angle should be symmetric, so only cosine functions can be present in the in azimuthal angle Fourier series.

For random fluctuations these restrictions do not apply. The azimuthal multipole and longitudinal analysis should contain even and odd functions. This does not lead to any problem in exactly central collisions, where global flow patterns do not lead to specific angles.

The precise identification of the c.m. of the observed participant system would still be necessary for "exactly" central collisions, because random azimuthal fluctuations may be correlated with the longitudinal momentum in the c.m. system. Unfortunately this is not done yet in any of the recent experiments, although longitudinal fluctuations of the participant c.m. momentum are not negligible at high beam energies.

Several collective processes in peripheral collision are strongly correlated with the symmetry axes of the collision, such as the reaction plane and the c.m. momentum or rapidity. These include the directed flow, all odd flow harmonics, rotation, and all polarization effects, which are correlated with the reaction symmetries. If these symmetry axes and the c.m. are not identified, then these processes are not measurable or are not measured accurately.

For example if we intend to measure polarization of particles which are arising from the collective rotation in the reaction plane then it is necessary to identify the 180 L.P. Csernai

plane, the direction of the rotation, i.e. which is the projectile and target side, and the position of the rotation axis, i.e. the c.m. momentum of the participants. If this is not done with a given precision than the measurement of these collective phenomena is not possible.

In view of these general comments we discussed the effect of rotation on the directed flow, which turned out very sensitive and subject to significant perturbations from random fluctuations [19]. As the v_1 becomes small (\sim 1 % or less) at RHIC and LHC energies, other measurements were studied which are more sensitive to rotation and turbulence.

One of the consequences of rotation and local vorticity, which arises in a stratified shear flow, is the polarization of particles. This can happen due to equipartition of orbital rotation and spin due to local thermalization. It was shown that about 8–10 % Λ or $\bar{\Lambda}$ polarization can be reached in peripheral heavy ion collisions [28]. This is observable for Λ or $\bar{\Lambda}$ emitted into the $\pm x$ direction in the reaction plane and both the Λ or $\bar{\Lambda}$ will be polarized into the -y direction (i.e. transverse polarization). This is in contrast to electromagnetic effects where the Λ and $\bar{\Lambda}$ polarizations would be opposite. Of course to perform this measurement the event-by-event identification of the reaction plane, its direction, and the c.m. momentum are necessary. Otherwise the overall integration of all directions eliminates the effect as it happened in recent experiments at RHIC.

Another sensitive method of studying heavy ion reactions is the Hanbury-Brown, and Twiss (HBT) effect. This is widely used for identifying the size of the emitting source, and also the radial expansion speed, which also influences the observed effective radii. Furthermore, with the azimuthal HBT method the shape of the emission ellipsoid can also be determined.

Recently, a Differential HBT (DHBT) method was worked out, which is similarly sensitive to rotation and has advantages compared to the flow-harmonics type of analysis. The estimated signal is of the order of 10% also [29]. As in the previous case this also requires the identification of reaction geometry.

This is not a fundamental problem and at lower energies this was done earlier. Recently the shift of focus towards analysis of fluctuations, diverted attention from this, but we hope that the experimental teams will pay attention to this task.

In conclusion, we have a good perspective to continue the research along the lines and successes of the earlier research in this field.

Acknowledgments Enlightening discussions and kind hospitality from the Frankfurt Institute for Advanced Studies and the Helmholtz International Center for FAIR are gratefully acknowledged.

References

- W. Scheid, H. Müller, W. Greiner, Phys. Rev. Lett. 32, 741 (1974); W. Scheid, R. Ligensa, W. Greiner, Phys. Rev. Lett. 21, 1479 (1968); W. Scheid, W. Greiner. Z. Phys. 226, 364 (1969)
- 2. H. Baumgardt et al., Z. Phys. A **273**, 359 (1975)
- 3. G.F. Chapline, M.H. Johnson, E. Teller, M.S. Weiss, Phys. Rev. D 8, 135 (1973)

- 4. H.Å. Gustafsson, H.H. Gutbrod et al., Phys. Rev. Lett. **52**, 1590 (1984)
- 5. L.P. Csernai, H.W. Barz, Z. Phys A 296, 173 (1980)
- 6. G. Buchwald, L.P. Csernai, J. Maruhn, W. Greiner, H. Stöcker, Phys. Rev. C 24, 135 (1981)
- L.P. Csernai, I. Lovas, J. Maruhn, A. Rosenhauer, J. Zimányi, W. Greiner, Phys. Rev. C 26, 149 (1982)
- 8. L.P. Csernai, W. Greiner, Phys. Lett. **99B**, 85 (1981)
- H. Stöcker, L.P. Csernai, G. Graebner, G. Buchwald, H. Kruse, R.Y. Cusson, J. Maruhn, W. Greiner, Phys. Rev. C 25, 1873 (1982)
- L.P. Csernai, W. Greiner, H. Stöcker, I. Tanihata, S. Nagamiya, J. Knoll, Phys. Rev. C 25, 2482 (1982)
- 11. H.W. Barz, L.P. Csernai, W. Greiner, Phys. Rev. C 26, 740 (1982)
- 12. A.A. Amsden et al., Phys. Rev. C 15, 2059 (1977)
- 13. A.A. Amsden et al., Phys. Rev. Lett. **35**, 905 (1975)
- H. Stöcker, C. Riedel, Y. Yariv, L.P. Csernai, G. Buchwald, G. Graebner, J. Maruhn, W. Greiner, K. Frankel, M. Gyulassy, B. Schürmann, G. Westfall, J.D. Stevenson, J.R. Nix, D. Strottmann, Phys. Rev. Lett. 47, 1807 (1981)
- 15. P. Danielewicz, G. Odyniecz, Phys. Lett. B **157**, 146 (1985)
- 16. L.P. Csernai, P. Freier, J. Mevissen, H. Nguyen, L. Waters, Phys. Rev. C 34, 1270 (1986)
- A. Bonasera, L.P. Csernai, Phys. Rev. Lett. 59, 630 (1987); A. Bonasera, L.P. Csernai,
 B. Schürmann, Nucl. Phys. A 476, 159 (1988)
- 18. L.P. Csernai, D. Röhrich, Phys. Lett. B **458**, 454 (1999)
- 19. L.P. Csernai, V.K. Magas, H. Stöcker, D.D. Strottman, Phys. Rev. C 84, 024914 (2011)
- 20. V. Vovchenko, D. Anchishkin, L.P. Csernai, Phys. Rev. C 88, 014901 (2013)
- 21. P.K. Kovtun, D.T. Son, A.O. Starinets, Phys. Rev. Lett. 94, 111601 (2005)
- 22. L.P. Csernai, J.I. Kapusta, L.D. McLerran, Phys. Rev. Lett. 97, 152303 (2006)
- 23. L.P. Csernai, G. Mocanu, Z. Neda, Phys. Rev. C 85, 068201 (2012)
- D.J. Wang, L.P. Csernai, D. Strottman, Cs. Anderlik, Y. Cheng, D.M. Zhou, Y.L. Yan, X. Cai, B.H. Sa. Eur. Phys. J. A 48, 168 (2012)
- 25. L.P. Csernai, D.D. Strottman, C. Anderlik, Phys. Rev. C 85, 054901 (2012)
- 26. S. Floerchinger, U.A. Wiedemann, JHEP 11, 100 (2011); and. J. Phys. G 38, 124171 (2011)
- 27. L.P. Csernai, V.K. Magas, D.J. Wang, Phys. Rev. C 87, 034906 (2013)
- 28. F. Becattini, L.P. Csernai, D.J. Wang, Phys. Rev. C 88, 034905 (2013)
- 29. L.P. Csernai, S. Velle, D.J. Wang, Phys. Rev. C 89, 034916, arXiv:1305.0396v2 [nucl-th] (2014)

Parallelization of Kinetic Theory Simulations

Jim Howell, Wolfgang Bauer, Dirk Colbry, Rodney Pickett, Alec Staber, Irina Sagert and Terrance Strother

Abstract Numerical studies of shock waves in large scale systems via kinetic simulations with millions of particles are too computationally demanding to be processed in serial. In this work we focus on optimizing the parallel performance of a kinetic Monte Carlo code for astrophysical simulations such as core-collapse supernovae. Our goal is to attain a flexible program that scales well with the architecture of modern supercomputers. This approach requires a hybrid model of programming that combines a message passing interface (MPI) with a multithreading model (OpenMP) in C++. We report on our approach to implement the hybrid design into the kinetic code and show first results which demonstrate a significant gain in performance when many processors are applied.

W. Bauer · A. Staber

Department of Physics and Astronomy, Michigan State University,

East Lansing MI 48824, USA e-mail: bauer@pa.msu.edu

A. Staber

e-mail: staberal@msu.edu

D. Colbry · R. Pickett

Institute for Cyber-Enabled Research, Michigan State University,

East Lansing MI 48824, USA e-mail: colbrydi@msu.edu

R. Pickett

e-mail: picke1@mail.lcc.edu

J. Howell (⊠)

Department of Computer Science and Engineering, Michigan State University,

East Lansing MI 48824, USA e-mail: howell20@msu.edu

I. Sagert

Center for Exploration of Energy and Matter, Indiana University,

Bloomington IN 47408, USA e-mail: isagert@indiana.edu

T. Strother

XTD-6, Los Alamos National Laboratory, Los Alamos NM 87545, USA

© Springer International Publishing Switzerland 2015 W. Greiner (ed.), *Nuclear Physics: Present and Future*, FIAS Interdisciplinary Science Series, DOI 10.1007/978-3-319-10199-6_18

1 Computational Many-Body Methods

During the last two or three decades computational approaches have become the 'third leg' of science, complementing the more traditional theoretical and experimental/observational approaches. In particular in studies of dynamical systems additional insights can be obtained from large-scale computer simulations. Among the most popular approaches are molecular dynamics simulations with explicit two-body interactions, kinetic theory approaches solving Boltzmann like equations with mean field and two-body collision terms, and hydrodynamics studies, which are based on short mean-free-path assumptions.

In nuclear physics, in particular, the field of heavy ion reactions at intermediate and high energies has been studied extensively on the basis of hydrodynamics [1–7], kinetic theory [8–19], and molecular dynamics [20–25] methods. Since the physical phenomena in heavy ion collisions require spatial resolution of on the order of 10^{-15} m and time resolution of on the order of 10^{-24} s, direct observations are not possible, and careful modeling of reaction dynamics is essential for any meaningful comparison with experimental observables. Thus methods like the ones just listed are indispensable tools for heavy ion physics. In particular, one can show that several of these approaches have identical results in certain analytic test cases, which increases our degree of confidence in the simulation results [3, 26, 27].

During the last few years our group has begun to apply the heavy ion modeling expertise to the problem of supernova explosion. The preferred tool to study these explosions has been hydrodynamics simulations for the baryons, coupled to Boltzmann transport for the neutrinos [28–35]. However, it can be shown that kinetic theory based models can treat the baryon and neutrino transport on the same footing within the framework of a coupled transport theory [36], similar to the coupled transport relativistic transport theory for baryons, mesons, and resonances for heavy ion collisions [16]. This enables us to conduct fully relativistic 3 + 3 dimensional studies of supernova core collapses [37–41]. In order for these studies to be able to provide reliable predictions that can be compared to observables, however, one has to utilize a very large number of test particles, on the order of 10⁸. This, in turn, requires the use of modern multi-processor environments with effective algorithms for parallelization. The present manuscript describes such algorithms and our implementation.

2 Initial Simulation Setup

Our kinetic simulation code models hydrodynamic shock waves by tracking the collisions of millions of particles over a set number of time steps. Each collision is determined by the distance of closest approach method. Hereby, each particle looks for its nearest collision partner at every time step. The naive approach to this type of collision detection problem is to compare the position and velocity of every particle to

every other particle in the simulations to find a collision partner. The computational complexity of such an algorithm scales with the total number of particles N as $O(N^2)$. For smaller-scale problems, this algorithm is sufficient. However, for largerscale problems the amount of computation time required to run such a simulation is unreasonable. Achieving a minimal processing time is a common challenge for computationally demanding computer models. Parallelization is a key ingredient in these simulations as it divides up the workload among multiple processors. The algorithm we chose is conceptually simple. The simulation space is divided up into a grid of cells or so-called bins. Hereby, each bin is represented by a pointer. The grid is thereby setup as a multidimensional array of pointers. The number of bins in the x, y, and z dimensions and the size of the simulation space in each dimension are set by the user. The characteristic length scale of the system corresponds to the width of a bin, Δx , and is therefore determined from the size of simulation space and the number of bins. The mean free path must be set significantly smaller than the characteristic length scale to ensure the simulation is fluid-like. We use an adaptive time step size $\Delta t = \Delta x / v_{\text{max}}$, where v_{max} is the maximum speed of the particles. With that, we can ensure that no particle can escape its scattering neighborhood within a single time step. Furthermore, if the difference between the average particle velocity and the maximum velocity is sufficiently small, this modification guarantees that the time steps will not be too small. Each particle is an instance of a class that contains a particle's velocity, position, mass, effective radius, and two particle pointers. One pointer is used to identify the collision partners, while the other is to connect particles that are located within the same bin via a linked list.

At the beginning of the simulation, all particles are initialized within a box. The boundary conditions of the box can be set as reflective, absorptive, or periodic and depend, like the exact initialization of the particles, on the particular test being run. Particles are sorted into their respective bins by appending them to a linked list based upon their initialized position. Once all of the particles have been sorted, output data is processed and printed to a file.

When output is complete, the binary collision detection phase of the program starts. This is the most computationally intensive part of the program, and we make use of the cell linked list structure to achieve greater computational efficiency. Our program loops through all bins, with every particle in a bin being compared to all of the other particles in the neighboring bins (26 bins in three dimensions and 8 bins in two dimensions). A particle is considered as a collision partner if the following criteria are met:

The collision partners

- are located within each other's collision neighborhood,
- are within each other's effective radii,
- and reach their distance of closest approach within the next time step.

If a potential collision partner is found, the pointer of the searching particle is set to point to this new collision partner. If a closer collision partner is found later in the search, then that pointer is updated accordingly to the new particle. In this way, each particle finds its closest collision partner without searching through the entire J. Howell et al.

simulation space. The computational efficiency of this algorithm scales as

$$O(B \times N_{\rm bin}^2/P),\tag{1}$$

where B is the number of bins, $N_{\rm bin}$ is the maximum number of particles per bin, and P is the number of processors. As opposed to scaling exponentially with the total number of particles, our code scales exponentially with the number of particles per bin, which can be controlled by using a large number of bins when there many particles. Note that the binary collision detection step does not update any particle properties other than the pointers to collision partners.

The number of processors P resides in the denominator of Eq. (1) due to the parallelization of the binary collision detection phase. We use OpenMP to create a new slave thread for each processor in addition to the processor running the master thread. Since OpenMP uses a shared memory model, every thread can access the same set of pointers and variables. Each thread searches approximately an equal number of bins for scattering partners. No two threads are allowed to compute the same bin and its collision neighborhood. This is a simple approach for keeping the workload of all of the processors roughly the same. However, in tests with shock fronts, some bins can have drastically higher particle densities and velocities than others. These bins can take significantly more computational time than bins with lower particle densities, which creates a load imbalance. When a load imbalance occurs, some processors complete their computation before others and have to wait for the other processors to finish before proceeding. A more sophisticated approach to dividing up the workload, for example an adaptive bin size, will be considered in future versions of this code. At the end of the binary collision step, all of the slave threads share their information with the master thread and subsequently close. The code beyond this point executes in serial on the master thread.

The final stage of the simulation updates particles' positions and velocities. Two particles only collide if they have both found each other as a collision partner in the binary collision detection phase. If this occurs, the particles' positions and velocities are calculated accordingly, and boundary conditions are applied to particles that come in contact with the walls of the simulation space. The program will then loop back to the part of the code that sorts the particles into their bins, and then repeat the steps described above.

3 Algorithm Optimization

Timing studies show that our algorithm can be optimized by using a low average number of particles per bin, with some caveats. Figure 1 illustrates that the relationship between computation time and number of particles per bin is nearly linear when the average number of particles per bin is significantly greater than one. This indicates that decreasing the number of particles per bin can significantly improve computation time. However, at roughly three particles per bin, the total wall time

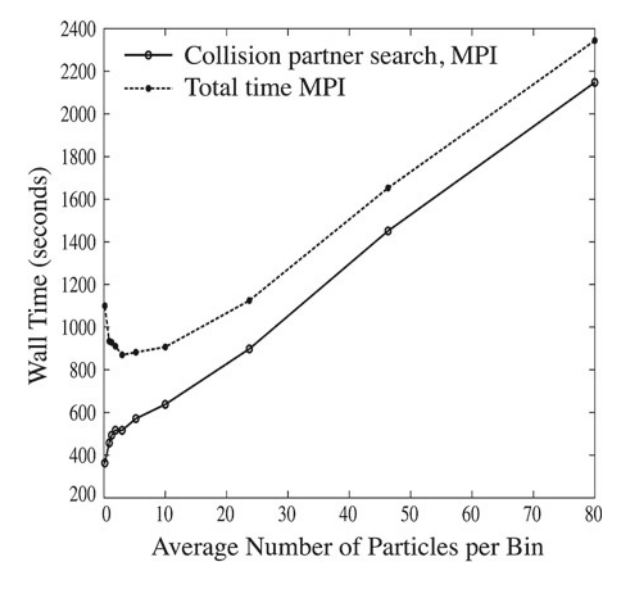


Fig. 1 Timing study for the wall time of our initial simulation as a function of the average number of particles per bin. Each test was initialized with 10^8 particles in three dimensions, with all of the particles having the same initial speed, random velocity directions, and random positions. The number of time steps taken in each test ranges from 20 to 206. The tests with a lower average number of particles per bin take more time steps to maintain the same elapsed simulation time. Each test produced a total of 40 output files

reaches a minimum, and the correlation between the total simulation time and binary collision detection time begins to diverge. Below this value, the total computation time starts to increase and the binary collision detection computation time starts to decrease. Further testing is needed to understand the cause of this divergence, and how using a low number of particles per bin could effect shock fronts.

One limitation to this optimization method is high random access memory usage. Our code uses a multidimensional array of pointers to sort the particles. Increasing the number of bins increases the size of that array. In 2D simulations, this memory increase is generally not large enough to be a significant limitation, but for 3D simulations this can be a constraint for simulations with $\gg 10^8$ particles and a correspondingly large number of bins. Nonetheless, modern supercomputers can usually handle this amount of memory consumption.

Furthermore, changing the number of bins affects the time step size of the simulation. Our code has an adaptive time step that is proportional to Δx . For a square or cubic simulation space, increasing the number of bins in the simulation decreases the time step size, and the simulation will need approximately twice as many time steps to reach the same simulation time. To negate this potential drawback, a time step counter ensures that output is only generated at a specified time interval. This allows a user to maintain the same amount of output regardless of the time step size. To control for the adaptive time step issue, all of the tests were run with the same amount of total output and elapsed simulation time.

J. Howell et al.

4 Hybrid Simulations

Implementing MPI is generally more difficult than implementing OpenMP. OpenMP uses straightforward preprocessor directives called pragmas that signal to the compiler when a section of code can be parallelized. The creation, destruction, and communication of threads is established automatically by compiler at these points, and most of the complex details are hidden from the user. One can implement more specific control over threads with work sharing constructs and through the manipulation of environmental variables to optimize performance. One advantage of using OpenMP is that a program can still use the same compilers after parallel pragmas have been added. This allows for incremental parallelization, without the need for creating separate files for an OpenMP version of the code. OpenMP pragmas ordinarily are placed before the most computationally intensive loops of the program, and the remainder of the code executes serially. One limitation of this method of parallelization is that simulations cannot run on multiple nodes simultaneously, because nodes use a distributed memory system.

In contrast, using MPI requires a better understanding of parallelization and the code that it is being applied to. MPI uses a standardized set of library routines to pass bits of information and instructions from one processor to another. Often, this type of parallelization involves determining how to break a large problem into smaller pieces that share information between each other with MPI function calls. This process is referred to as domain decomposition. Domain decomposition can require a significant amount of code rewriting, particularly if it is being considered after a code already been developed. An abstraction called ghost cells are frequently used in conjunction with domain decomposition. Ghost cells are copies of neighboring cells from different nodes, which allow each node to have access to the information from other nodes.

The benefits of using MPI are that it allows: for finer control of parallelization, for parallelization of the entire code, and a parallelized code to run on a distributed memory system. By implementing a hybrid of both OpenMP and MPI, we can gain the benefits of both types of parallelization, while mitigating some of the drawbacks of each. There are various ways to structure a hybrid code. A standard method that we use in our code is to create one MPI thread per node and use MPI routines to communicate between each node. OpenMP is used to create additional threads on each node in the binary collision detection phase.

For domain decomposition, we divide the simulation space by the number of nodes in use. The number of rows in our simulation must be evenly divisible by the number of nodes to split up the simulation space into equal parts. For example, if a simulation with 12 rows is running on four nodes, then the grid of the simulation space is split up into four domains of three rows each. Each domain is executed on a different node. In this case, the two nodes designated to handle the middle of the simulation space both have two neighboring domains: one domain above and one domain below. The middle domains have one empty row added above, and one empty row added below their normal simulation space. These extra rows are used to store

a row of ghost cells that they receive from their respective neighboring domains. A node designated to run the bottom part or the top part of the simulation space is a special case. In this case, a node has only one neighboring domain, because it lies on the boundary of the simulation space. In practice, there can be an arbitrary number of middle domains, but there are always two special case domains on the boundaries. Figure 2 demonstrates this example.

We have added four stages of communication between nodes to our simulation. The first stage of communication transfers rows of ghost cells from neighboring nodes. The second phase syncs the adaptive time step of all the nodes. The third phase sends the collision information of the ghost particles found in the collision detection phase. The lasts phase of communication transfers the real particles between nodes.

In the first stage of communication, we count the number of ghost particles that will be sent from each node and send that information to the neighboring nodes. This information allows each node to know how many ghost particles it will receive. In the example with four nodes described above, each middle domain has a total five rows. The first and the fifth rows are the ghost rows used for storing information received from other nodes. The second and the fourth rows contain the particle information that is sent to neighboring nodes. These particles are packed into a contiguous memory storage, sent individually with an MPI send function, and received with an MPI receive function. For the middle nodes, all of the particles in the second row are sent to the node above in the simulation space and copied into that node's fifth row. All of the particles in the fourth row are sent to the node below in the simulation space and copied into that node's first row. For the special case nodes, the top node sends the particle information from its fourth row to the first row of the node below, and the bottom node sends particle information from its second row to the fifth row of the node above. Once the first communication phase is complete, all of the nodes' ghost rows are filled with copies of particles from the neighboring rows of other

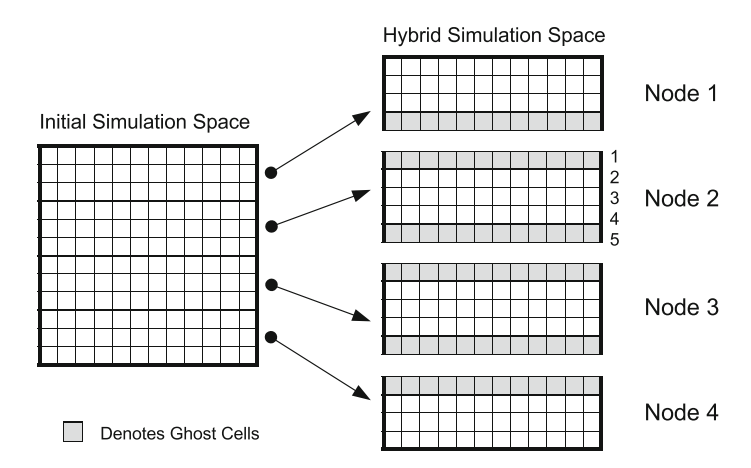


Fig. 2 Initial and hybrid simulation spaces

190 J. Howell et al.

nodes. This enables the binary collision detection phase to find all of the potential collision partners for particles in the second and fourth rows.

The second stage of communication is brief but important. Since all of the nodes are essentially running separate simulations that intermittently communicate with their neighbors, each node can develop a different maximum particle velocity. Our adaptive time step is derived from the maximum particle velocity, so each domain can have different sized time steps if they are not synced. By using an MPI reduce function, all of the nodes can acquire a global maximum particle velocity, and use that information to set their adaptive time steps to the same value.

The third communication phase sends collision partner information found in the binary collision detection step from particles in the second and fourth rows to the ghost particle copies of themselves. The pointers must be converted into particle ID integers, since pointers are not meaningful when transferred to other nodes. In our four node example, if a real particle in the fourth row has found a ghost particle as a collision partner in the fifth row, then that particle's collision information will be sent to the first row of the node below. The pointers of the corresponding ghost particle will be updated with this information. This process repeats until all of the particles in the second and fourth rows with ghost particle collision partners have sent their collision information. Without this information, there is no way of determining if the ghost particle in the fifth row has also found the real particle in the fourth row as a collision partner.

The lasts phase of communication occurs after the collisions have been calculated. Once the particles' positions and velocities have been updated, and boundary conditions have been applied, the code counts the number of particles with coordinates outside of their respective domain spaces. Particles are removed from the domains that they are leaving and added to the domain that they are entering. In our four node example, if a real particle lies in the first row of a middle node, it will be transferred to fourth row the node above, and if a real particle lies in the fifth row of a middle node, it will be transferred to the second node of the node below. Each node has its own coordinate system, so the particles' positions are transformed accordingly. The program either stops after this point or loops back to the part of the code that sorts particles into their bins, depending on the number of time steps.

The advantage of our hybrid code is that each node runs almost entirely in parallel. The drawback is that there is significant overhead and processing time required to send the data of millions of particles between nodes. Also, each node produces a separate output file, which are combined after the simulation is complete. Yet, as the empirical timing studies in Fig. 3 show, the binary collision detection phase of hybrid code scales well with an increasing number of processors. Furthermore, this setup should allow the code to run with hundreds or thousands of processors, and should greatly reduce job scheduling times.

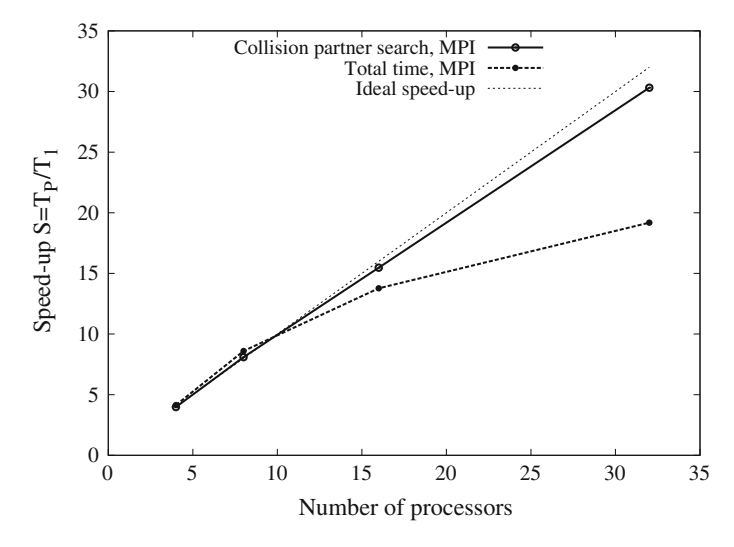


Fig. 3 Timing test for the speed-up of our hybrid implementation as a function of the number of processors (4, 8, 16, and 32 nodes with one processor per node) used in the calculation. The *dotted line* shows the theoretical maximum speedup possible. Each test was initialized with 40,000,000 particles in two dimensions, with all of the particles having the same initial speed, random velocity directions, and random positions. Each test produced a total of two output files per node

5 Outlook

So far our hybrid code has only been developed in two dimensions for an initialization in which all of the particles have random positions, random velocity vector directions, and reflective boundary conditions. This scenario is ideal for parallelization since each processor has approximately the same workload. The initializations for the supernova simulations are more complex and will require more careful consideration for implementation in the hybrid version. The supernova tests with shock fronts will probably not scale as well. One solution for this issue is to use dynamic bins sizes on the level of the OpenMP implementation, and dynamic domain sizes on the level of the MPI implementation. Areas of higher density would have smaller bins sizes and domain sizes than areas of lower density.

Acknowledgments The authors would like to thank the Blue Water Undergraduate Petascale Education Program and Shodor for their financial and educational support. Furthermore, this work used the Extreme Science and Engineering Discovery Environment (XSEDE), which is supported by National Science Foundation grant number OCI-1053575. I.S. is thankful to the Alexander von Humboldt foundation and acknowledges the support of the High Performance Computer Center and the Institute for Cyber-Enabled Research at Michigan State University.

192 J. Howell et al.

References

- 1. W. Scheid, H. Müller, W. Greiner, Phys. Rev. Lett. 32, 741 (1974)
- 2. H. Stöcker, J.A. Maruhn, W. Greiner, Phys. Rev. Lett. 44, 725 (1980)
- 3. I. Bouras et al., Phys. Rev. Lett. **103**, 032301 (2009); I. Bouras et al., Phys. Rev. C **82**, 024910 (2010); I. Bouras et al., Phys. Lett. B **710**, 641 (2012)
- 4. M. Luzum, P. Romatschke, Phys. Rev. C 78, 034915 (2008)
- 5. H. Song, U.W. Heinz, J. Phys. G 36, 064033 (2009)
- 6. B. Schenke, S. Jeon, C. Gale, Phys. Lett. B 702, 59 (2011)
- 7. J. Novak et al., Phys. Rev. C 89, 034917 (2014)
- 8. C.-Y. Wong, Phys. Rev. C 25, 1460 (1982)
- 9. G.F. Bertsch et al., Phys. Rev. C 29, 673 (1984)
- 10. H. Kruse et al., Phys. Rev. Lett. 54, 289 (1985)
- 11. W. Bauer, G.F. Bertsch, W. Cassing, U. Mosel, Phys. Rev. C 34, 2127 (1986)
- 12. H. Stöcker, W. Greiner, Phys. Rep. 137, 277 (1986)
- 13. G.F. Bertsch, S. Das, Gupta. Phys. Rep. **160**, 189 (1988)
- 14. P. Schuck et al., Prog. Part. Nuc. Phys. 22, 181 (1989)
- 15. W.G. Gong, W. Bauer, C.K. Gelbke, S. Pratt, Phys. Rev. C 43, 781 (1991)
- 16. S.J. Wang, B.-A. Li, W. Bauer, J. Randrup, Ann. Phys. **209**, 251 (1991)
- 17. B.-A. Li, C.M. Ko, W. Bauer, Int. J. Mod. Phys. E 7, 147 (1998)
- 18. Z.W. Lin et al., Phys. Rev. C C 72, 064901 (2005)
- 19. B.-A. Li, L.W. Chen, C.M. Ko, Phys. Rep. 464, 113 (2008)
- 20. L. Wilets, E.M. Henley, M. Kraft, A.D. MacKellar, Nucl. Phys. A2(82), 341 (1977)
- 21. A.R. Bodmer, C.N. Panos, Phys. Rev. C 15, 1342 (1977)
- 22. J. Aichelin, A. Rosenhauer, G. Peilert, H. Stöcker, W. Greiner, Phys. Rev. Lett. 58, 1926 (1987)
- 23. H. Feldmeier, Nucl. Phys. A 515, 147 (1990)
- 24. J. Aichelin, Phys. Rep. 202, 233 (1991)
- 25. H. Feldmeier, J. Schnack, Rev. Mod. Phys. 72, 655 (2000)
- I. Sagert, D. Colbry, T. Strother, R. Pickett, W. Bauer, JPCS 458, 012031 (2013). arXiv:1210.8084
- 27. I. Sagert, W. Bauer, D. Colbry, R. Pickett, T. Strother, J. Phys.: Conf. Ser. 458, 012031 (2013)
- 28. J.R. Wilson, *Numerical Astrophysics* (Jones and Bartlett, Boston, 1985)
- 29. M. Herant, W. Benz, W.R. Hix, C.L. Fryer, S.A. Colgate, Astrophys. J. 435, 339 (1994)
- 30. C.L. Fryer, A. Heger, Astrophys. J. **541**, 1033 (2000)
- A. Mezzacappa, M. Liebendörfer, O.E.B. Messer, W.R. Hix, F.-K. Thielemann, S.W. Bruenn, Phys. Rev. Lett. 86, 1935 (2001)
- 32. C.L. Fryer, M.S. Warren, Astrophys. J. 574, L65 (2002)
- 33. T.A. Thompson, A. Burrows, P.A. Pinto, Astrophys. J. 592, 434 (2003)
- 34. A. Heger et al., Astrophys. J. **591**, 288 (2003)
- 35. R. Buras, M. Rampp, H-Th Janka, K. Kifonidis, Phys. Rev. Lett. 90, 241101 (2003)
- 36. W. Bauer, Acta Phys. Hung. A 21, 371 (2004)
- 37. T. Bollenbach, MSU, M.S. Thesis (2002)
- 38. T. Strother, W. Bauer, Int. J. Mod. Phys. E 16(4), 1073 (2007)
- 39. T. Strother, W. Bauer, Prog. Part. Nucl. Phys. 62, 468 (2009)
- 40. T. Strother, MSU, Ph.D. Thesis (2009)
- 41. T. Strother, W. Bauer. J. Phys.: Conf. Ser. 230, 012027 (2010)

Part V Supercritical Fields

Probing Supercritical Fields with Real and with Artificial Nuclei

Joachim Reinhardt and Walter Greiner

Abstract In the presence of strong electric fields the vacuum state of Quantum Electrodynamics (QED) becomes unstable and decays through the spontaneous production of electron-positron pairs. This is expected to occur, e.g., in constant electric fields exceeding a critical strength of $E_{\rm cr} \simeq 1.3 \cdot 10^{18}$ V/m and also in hypothetical atoms with a nuclear charge exceeding the critical value $Z_{\rm cr} \simeq 172$. We discuss how supercritical quasiatoms can be created transiently in collisions of two heavy ions and discuss experimental signatures. We also report on an analogue of supercritical QED which has been found in solid-state physics. The electron states in the material graphene obey an effective Dirac-like equation. Depositing charged impurity atoms on the surface of a graphene sheet one can construct artificial supercritical atoms.

1 Supercritical Atoms in QED

Strong fields and the related occurrence of nonperturbative effects play an important role in many areas of physics. This is obvious in the area of strong interactions, characterized by a large coupling constant $\alpha_s \simeq 1$. However, strong-field effects can occur even when the fundamental coupling constant is small, as it is in Quantum Electrodynamics which is characterized by the fine structure constant $\alpha \simeq 1/137 \ll 1$. In the following we will concentrate on strong and, to be more specific, on "supercritical" electric fields in atomic physics. For references we refer the reader to the book [1].

When atomic structure is extrapolated from the known boundary of chemical elements into the region $Z=170\dots190$ one finds that the inner-shell electrons gain tremendously in binding energy. In particular, the $1s_{1/2}$ -state and also the next higher $2p_{1/2}$ state traverse the gap between the positive and negative energy continuum

J. Reinhardt (⋈)

Institute for Theoretical Physics, Johann Wolfgang Goethe University, Frankfurt am Main, Germany e-mail: jr@th.physik.uni-frankfurt.de

W. Greiner

Frankfurt Institute for Advanced Studies, Johann Wolfgang Goethe University, Frankfurt am Main, Germany e-mail: greiner@fias.uni-frankfurt.de

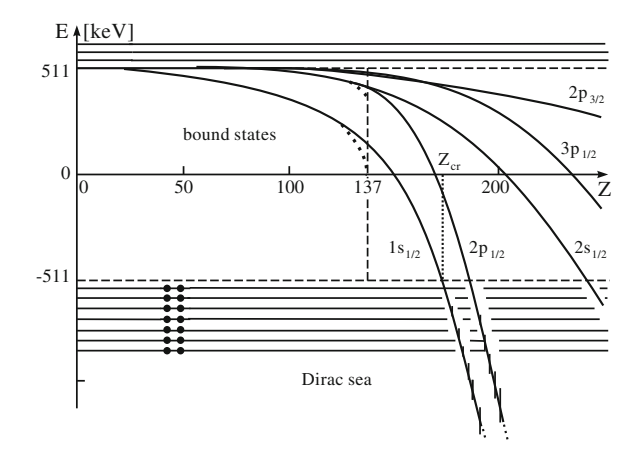


Fig. 1 Atomic binding energies as function of nuclear charge Z

solutions of the Dirac equation. The total energy E_{1s} becomes negative at Z=150 and is predicted to reach the value -m (i.e., a binding energy of twice the electron mass, 2m=1.022 MeV) at the critical nuclear charge $Z_{\rm cr}\simeq 172$. This dramatic increase in binding is caused by relativity. It turns out that already in relativistic classical mechanics the orbit of a particle bound by a Coulombic potential -Ze/r becomes instable when the potential strength exceeds a critical valued (dependent on angular momentum). The particle will fall into the center on a spiral path. (Mathematically this stems from the fact that the relativistic energy-momentum relation is quadratic, resulting in an attractive $1/r^2$ term on par with the repulsive centrifugal energy barrier.) The instability occurs also in quantum mechanics: Solving the Dirac equation for a point like central charge one finds that all bound states with the relativistic angular momentum quantum number $\kappa=\pm 1$, i.e., all $ns_{1/2}$ and $np_{1/2}$ states, cease to exist at a charge value $Z_0\alpha=1$ or $Z_0\simeq 137$. This "collapse of the wave function" is the quantum analogue of the classical spiralling fall into the center.

Applied to atomic physics, however, this collapse at $Z \simeq 137$ is an artifact since the divergence of the Coulomb potential gets truncated owing to the final size of the nucleus. As a consequence, as described above the bound states can be traced continuously beyond $Z = Z_0$ [2], although with steeply increasing binding energy and rapidly shrinking spatial extension. Instead, a qualitative change is expected at the critical charge $Z_{\rm cr}$: The 1s state leaves the discrete spectrum and merges with the lower continuum of the Dirac equation which it enters as a narrow *resonance*. The physics of this "supercritical" state was clarified in the early 1970s by our group in Frankfurt [3] and by another group in Moscow [4].

The history of this topic dates back to the early days of relativistic quantum mechanics when Oscar Klein discovered that scattering off an electrostatic potential barrier V_0 which exceeds the height of 2 mc² leads to anomalous behaviour of the transmission and reflection coefficients. In 1931 F. Sauter derived the transmission coefficient for "tunneling through the gap of the Dirac equation" for a potential

barrier of finite width a as $T \simeq \exp\left[-\pi mc^2/(V_0/a)(\hbar/mc)\right] = \exp\left(-E_{\rm cr}/E\right)$. This expression displays a nonanalytic dependence on the electric field strength E and is exponentially suppressed unless E reaches the value of the *critical field strength*

$$E_{\rm cr} = \frac{\pi m^2 c^3}{e\hbar} \simeq 1.3 \cdot 10^{18} \frac{\rm V}{\rm m} \ .$$
 (1)

It soon became clear, in particular through the work Heisenberg and his student Euler, that the vacuum of QED is a dynamical polarizable medium in which an external field can induce the production of virtual and (provided the field is strong enough) also real electron-positron pairs. An elegant formulation of this vacuum instability later was given in 1951 by Schwinger so that today one often refers to "Schwinger pair creation" in strong electric fields.

The existence of this mechanism is generally accepted, but in QED it has eluded direct experimental verification so far. Macroscopic ultrastrong electrostatic fields $E \simeq E_{\rm cr}$ are unattainable in the laboratory. On an atomic scale, however, this is not true: The electric field strength at the surface of a nucleus exceeds $E_{\rm cr}$ by about three orders of magnitude. Nevertheless in ordinary atoms pair creation does not occur because the created electron quantum mechanically would not fit into the narrow well of the Coulomb potential. This changes when atomic structure is extrapolated from the known region of chemical elements by about a factor of two. As discussed above, supercriticality sets in at $Z_{\rm cr} \simeq 172$ when the $1s_{1/2}$ state "dives into the lower continuum" and is transformed into a resonance.

In the language of Dirac's hole picture, if an empty bound state enters the lower continuum it will get filled by a sea electron which can tunnel through the classically forbidden gap of the Dirac equation, leaving behind a hole, i.e., a positively charged positron, which escapes to infinity. This is just an instance of the Schwinger mechanism for pair creation. The process also has been termed "spontaneous pair creation" or "decay of the vacuum" of QED. The difference to Schwinger pair creation in a constant electric field is that in supercritical atoms the strong field is confined to a small region in space which can harbour only a small number of created electrons. I.e., pair creation is stopped by "Pauli blocking" when the available electron states are occupied. In a weakly supercritical atom (172 < Z < 185) just two positrons (spin degeneracy) can be produced in this way.

In a world with a fine structure constant α somewhat larger than our physically realized value supercritical atoms would be an everyday phenomenon. It would be impossible to fully ionize heavy atoms since their inner shells would be filled by "electron capture from the vacuum" (bound-free pair creation). The supercritical atoms would exhibit narrow resonances in the scattering of positrons.

1.1 Supercritical Heavy Ion Collisons

As it happens, stable nuclei with a supercritical charge do not exist in nature. However, it is possible to assemble such a charge $Z = Z_1 + Z_2$ for a short time interval

in close collisions of two very heavy nuclei. In this way charge values of up to $Z \simeq 190$ can be attained experimentally. It has been suggested to look for the signs of supercriticality in "supercritical quasimolecules". The solution of the Dirac equation with two Coulomb centers shows that the critical binding will be reached, e.g., in U+U collisions at an internuclear distance of $R_{\rm cr} \simeq 34 \, {\rm fm}$ (unscreened) [5, 6]. However, the colliding nuclei move on their Rutherford trajectories which causes the wave functions and binding energies to vary rapidly with time and also leads to strong dynamically induced transitions. This makes it necessary to solve the *time dependent two-center Dirac equation*.

This problem can be attacked in a number of ways. The direct brute-force approach of solving the coupled partial differential equations numerically is quite demanding. Instead, using tools from atomic collision theory one can expand the time-dependent Dirac wave function Ψ into a complete set of basis states φ_j :

$$\Psi_i(\mathbf{r}, t) = \sum_j a_{ij}(t)\varphi_j(\mathbf{R}(t), \mathbf{r}) e^{-i\chi_j(t)}.$$
 (2)

Here the indices *i* and *j* run over the full spectrum of the Dirac equation, *i* designates the initial state $(t \to -\infty)$ of the electron under consideration. $\chi_j(t)$ is a time dependent phase factor.

The physics of the collision is encoded in the set of expansion amplitudes $a_{ij}(t)$. They satisfy a set of coupled ordinary differential equations in time, the coupled channel equations (infinite in principle but truncated in practical calculations). The reliability of such a calculation depends on the choice of the expansion basis φ_j . At bombarding energies not much above the nuclear Coulomb barrier (i.e., $E/A \simeq 6$ MeV) the ion velocity $v \simeq 0.1c$ is comparatively slow so that the relativistic inner-shell electrons have time to adjust to the nuclear Coulomb field. This gives justification for using adiabatic basis states (superheavy quasimolecules).

For the description of inner-shell excitation and pair production in very heavy systems it was found sufficient to include only states with angular momentum j = 1/2 ($s_{1/2}$ and $p_{1/2}$) and, furthermore, to approximate the two-center potential by its lowest-order term in the multipole expansion (the monopole approximation). This framework has been employed with considerable success to calculate various atomic excitation processes in heavy ion collisions, cf. the review [7].

Collisions with $Z_1+Z_2>Z_{cr}$ pose an extra challenge for the calculation. The combined nuclear charge is sufficiently large to let the quasimolecular 1s-state enter the Dirac sea at critical distance R_{cr} . Then in the adiabatic picture the 1s state vanishes from the bound spectrum, becoming admixed to the lower continuum as a narrow resonance. A method was developed [8] which introduces a normalizable state $\tilde{\varphi}_r$ for the supercritical 1s-state. With the help of a projection operator technique then a matching set of modified resonance-free continuum states $\tilde{\varphi}_E$ can be constructed. As a consequence, in the coupled channel equations an additional coupling term between the supercritical 1s state and the negative continuum arises

$$\langle \varphi_{1s} | \partial/\partial t | \varphi_E \rangle \longrightarrow \langle \tilde{\varphi}_{1s} | \partial/\partial t | \tilde{\varphi}_E \rangle + i \langle \tilde{\varphi}_{1s} | H | \tilde{\varphi}_E \rangle .$$
 (3)

These "induced" and "spontaneous" couplings act coherently over the course of the collision, both contributing to the production of positrons. In principle there is a qualitative difference between them: The spontaneous coupling acts also for a stationary nuclear charge configuration. It is related to the decay width of the supercritical resonance at energy $E=E_r$ through the formula $\Gamma_r=2\pi |\langle \tilde{\varphi}_r|H|\tilde{\varphi}_{E_r}\rangle|^2$.

For undelayed elastic collisions the contribution from the spontaneous coupling constitutes only a small fraction of the produced positrons. Furthermore the time-energy uncertainty relation leads to a large collision broadening. Accordingly, the calculations do not yield a significant change in the shape of the predicted positron spectra for such collisions when going from subcritical to supercritical systems.

Experiments investigating the production of positrons in heavy ion collisions at the Coulomb barrier have been carried out for more than a decade, starting in the late 1970s, mainly at the UNILAC accelerator at GSI [9]. This was part of a comprehensive experimental program to study a variety of atomic-physics excitation processes such as *K-hole production*, δ-electron and positron emission, and quasimolecular X-ray radiation. The theory sketched above turned out to be very successful in describing the dynamics of the electron shell (including the electron-positron field) in heavy ion collisons. The absolute values, impact-parameter and nuclear-charge dependences, ionization rates, intensities and spectral shapes of electron and positron production in most cases could be explained on a quantitative basis.

No direct proof of "supercriticality" has been found. However, from the heavy ion collision experiments we can be quite sure that the underlying picture on which our understanding of QED of strong fields is based—in particular the very steep increase in binding energy and the near-collapse of the wave functions predicted in the presence of strong Coulomb fields—is indeed realized in nature.

1.2 Collisions of Bare Nuclei

It should be noted that the experiments searching for positron creation in heavy ion collisions so far were performed by colliding partly stripped projectile ions with solid state targets. Under these conditions bound-free pair production is suppressed by *Pauli blocking*: The K shell initially is occupied and can contribute to pair creation only after being emptied through ionization, which at best takes place in a few percent of the collisions. Bound-free pair creation thus could be studied much more cleanly if the required holes were brought in right from the start, i.e., by using *fully stripped ions*.

Heavy ions can be stripped bare quite easily at high beam energies. In fact, bound-free pair creation has been first observed at the Bevalac using 1 GeV/nucleon U^{92+} beams [10]. In the present context, however, we are interested in *slow* collisions allowing the formation of quasimolecular electron states. Experimentally this could be achieved by either by slowing down the ions after stripping [11] or in colliding-beam experiments. There are two variants of the latter option, either colliding two beams of

equal velocity under a small relative angle or colliding two collinear beams having different velocites. The feasibility of the latter option presently is studied at Dubna [12].

The consequences of the transition to collisions of fully stripped ions for positron creation have been studied theoretically in [8, 13]. Apart from a sizable increase in binding energy the main effect will be the removal of Pauli blocking. Since in a completely stripped system bound-free pair production with the electron ending up in the 1s state can proceed unimpeded as a one-step process, the positron production cross section is predicted to grow by up to two orders of magnitude. Nearly all created electrons end up in bound states (mostly 1s and 2 $p_{1/2}$).

Let us quote some numbers [13] for collisions of fully stripped $U^{92+} + U^{92+}$ at an energy slightly below the Coulomb barrier, $E_{\rm cm} = 680$ MeV corresponding to E/A = 5.7 MeV/u in a fixed target experiment. Here the number of produced positrons in central collisions (impact parameter b = 0) is predicted to be $N_{e^+}^{\rm bare} = 1.06 \cdot 10^{-2}$, out of which $1.04 \cdot 10^{-2}$ end up in bound states. This is to be compared with $N_{e^+}^{F=3} = 2.93 \cdot 10^{-4}$ for GSI-type fixed-targed experiments with a Fermi-surface F = 3, i.e., the lowest three $s_{1/2}$ and $p_{1/2}$ levels are initially occupied. The enhancement in the rate of produced positrons clearly reflects the removal of Pauli blocking. At larger impact parameters b the effect is even more pronounced since the rate of inner-shell holes dynamically induced in non-bare collisions gets further reduced. For the total positron cross section we expect $\sigma_{e^+}^{\rm bare} = 105$ mb as compared $\sigma_{e^+}^{F=3} = 2.3$ mb, an enhancement by a factor of 46.

It should be mentioned that essentially half of the advantage gained in bare-onbare collisions can be achieved already with fully ionized projectiles impinging on neutral target atoms since in this case half of the K-holes (assuming $Z_1 = Z_2$) brought in by the projectile ion will be transferred to the $1s\sigma$ state.

Collisions of fully stripped ions offer a further advantage: Significant information can be obtained by simply measuring the ion's change of charge state. The observation of, e.g., a transition $U^{92+} \rightarrow U^{91+}$ would prove that bound-free pair production has occurred, even if the emitted positron is not measured. This of course assumes that background processes like electron capture from rest gas atoms can be excluded. A less trivial background process would be bound-free pair conversion from the de-excitation of Coulomb excited nuclei.

Does the foregoing discussion mean that successful experiments with fully stripped ions would positively confirm the occurrence of spontaneous pair creation and the decay of the neutral vacuum? We would argue that this question is not so clear cut. Let us look at the results shown in Fig. 2 which depict positron creation in various sub- and supercritial systems at a collision energy of E/A = 5.9 MeV/u. Figure 2a refers to non-stripped fixed-target experiments, Fig. 2b to collisions of bare nuclei. The number of produced positrons is drawn as a function of the distance of closest nuclear approach $R_{\rm min}$, reflecting the impact parameter dependence. The combined charges $Z = Z_1 + Z_2$ range from Z = 164 (Pb+Pb) over Z = 174 (Pb+U) and Z = 184 (U+U) to Z = 190 (U+Cf). We observe a steeply falling impact parameter dependence for the E = 3 case where because of the (initial) Pauli blocking of the inner shells a larger amount of energy has to be transferred from the nuclear motion to create

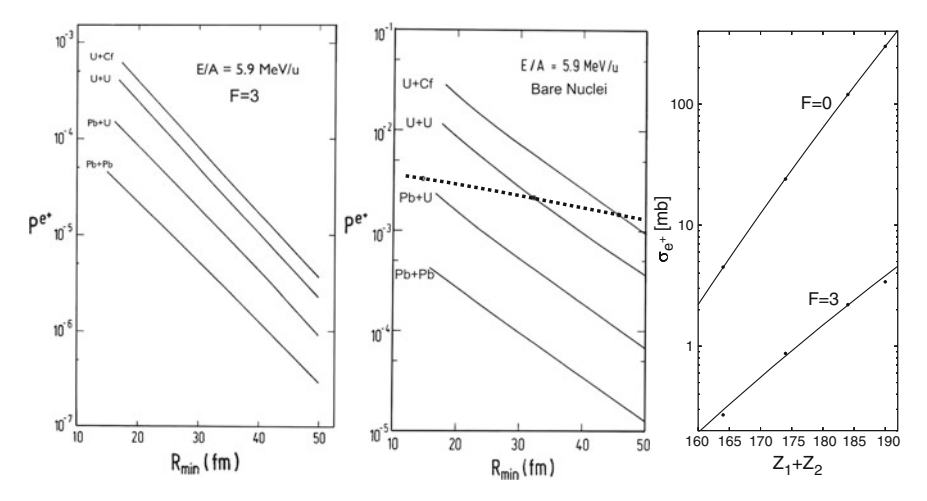


Fig. 2 Number of produced positrons as function of the distance of closest approach R_{\min} for various collision systems $(Z_1 + Z_2 = 164 \dots 190)$ at impact energy $E_{\text{Lab}}/A = 5.9$ MeV/u. a The inner shells are initially occupied (F = 3). b Bare nuclei (F = 0). The dashed line indicates the border of the supercritical region. c Dependence of the total cross section for positron creation as a function of the combined nuclear charge for filled inner shells (F = 3) and bare nuclei (F = 0). Adapted from [8]

a pair, either in a continuum-continuum transition or through multi-step processes. In the fully ionized case (F = 0) the fall-off with impact parameter is less steep.

The curves for different collisions systems look very similar, i.e., there is *no qualitative difference* between the predicted positron creation rates in subcritical and supercritical systems. In Fig. 2b the border of the region where supercriticality is expected to set in is marked by a dotted line. The curves do not significantly change. This is also true for the total positron cross section σ_{e^+} , see Fig. 2c which grows smoothly when increasing the nuclear charge. Note, however, the extreme slope of the curves: For F=0 a 16% increase of Z leads to an increase of the positron cross section by a factor of nearly 70. The Z dependence can be well parametrized by a power law with a remarkable large exponent:

$$\sigma_{e^+} \propto Z^n$$
 with $n \simeq 29$ for $F = 0$ and $n \simeq 17$ for $F = 3$. (4)

Figure 3 demonstrates that also the shape of the energy spectrum of positrons is not expected to change markedly when going to collisions of fully stripped ions.

The lack of qualitative distinguishing features and step-like threshold behaviour when going from the subcritical to the supercritical region results from the shortness of the collision time. For example, in U + U the internuclear distance falls below the critical value $R_{\rm cr}$ for only $\Delta t_{\rm cr}=2.5$ zs (the zeptosecond 1 zs = 10^{-21} s is the appropriate unit of time here). This leads to a *dynamical width* or *Heisenberg broadening* of the quasimolecular 1s state of $\Gamma_{\rm dyn}=\hbar/\Delta t_{\rm cr}\simeq 300$ keV. Actually, one may argue that an extra factor of π should be included here [14], leading to a broadening of the order of 1 MeV. This completely blurs the transition between subund supercritical systems.

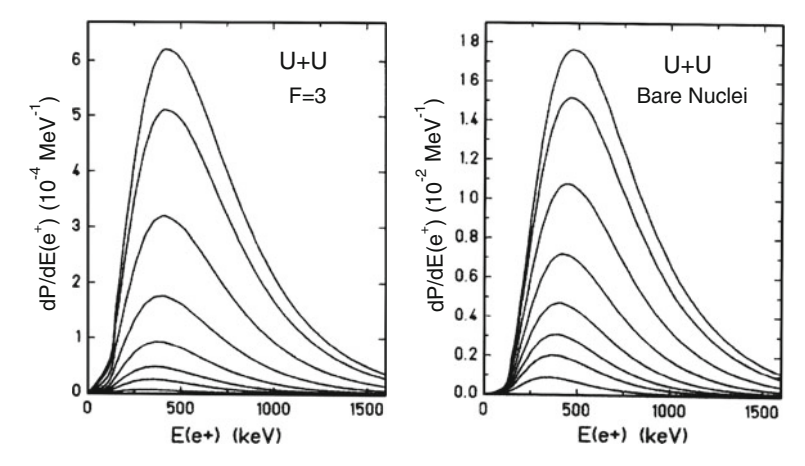
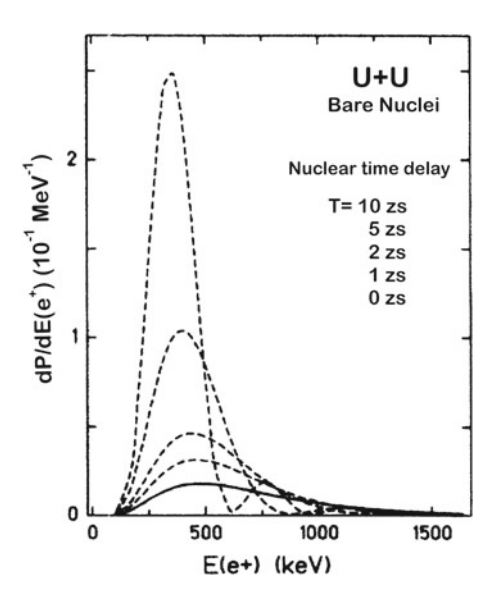


Fig. 3 Energy spectra of positrons produced in U + U collisions at E/A = 5.7 MeV/u for various impact parameters between b = 0 (top most) to b = 40 fm (lowest curves). a Non-bare collisions (F = 3). b Collisions of bare nuclei (F = 0). From [13]

To put it differently: Our notion of supercriticality is based on stationary atomic states and thus, when describing collisions uses the adiabatic (quasimolecular) picture. The dynamical wave function, however, does not behave fully adiabatically.

To find a *qualitative* experimental signal for supercriticality the dynamical broadening should be reduced. In principle this could be done [15] by looking for positron creation in collisions at energies above the Coulomb barrier which exhibit a *nuclear time delay* (either through friction or through the actions of the attractive nuclear force). Quantitative calculations assuming arbitrarily inserted time delays *T* were performed in [14]. As shown in Fig. 4 for the same collisions as in Fig. 3b delays of

Fig. 4 Energy spectra of positrons produced in central U+U collisions at E/A=5.7 MeV/u. Full curve same as b=0 curve in Fig. 3b. Dashed curves Assuming nuclear delay times from 1 to 10 zs. From [13]



a few zs lead to strong enhancement of positron production, e.g., by a factor of 15 for T=10 zs. In addition, a positron line structure emerges which narrows down for large delays according to $\Delta E_{fwhm} \simeq 5.56\hbar/T$. The corresponding behaviour for subcritical systems is very different, leading to a reduction of positron production with increasing delay time.

This would be the ultimate proof that spontaneous positron production has been observed. Whether collisions with sufficient time delay can be observed, however, is an open question. The problem of nuclear time delay is discussed in some detail in the talks by H. Backe and S. Heinz at this conference.

2 Supercritical Atoms in Solid State Physics?

Quite recently, the study of supercritical atoms has received a boost from a rather unexpected side, i.e. from the study of graphene in solid state physics. Graphene—a two-dimensional crystals made from carbon atoms—is a material with many extraordinary properties, like large tensile strength and thermal conductivity, support of high current densities etc. It is the "mother" of many nanosystems like carbon nanotubes, nonoribbons, fullerenes, and also of graphite. Nevertheless, the discovery of graphene had to wait until 2004, although it turned out to be quite easy to produce through micromechanical cleavage [16]. In 2010 A.K. Geim and K.S. Novoselov were awarded the Nobel prize for discovering graphene. Presently graphene is in the focus of research worldwide, not the least because of its many possible technological applications. In 2013 the European Union has declared graphene research a "flaship program" funded by 1 billion euros.

In the course of these studies it turned out that graphene possesses electron states which (quite accidentally) obey an ultrarelativistic energy-momentum dispersion relation and can be described by (massless) Dirac fermions which interact with a strongly increased fine structure constant. Inserting charged impurities on a graphene sheet allows to create "artificial atoms" which can become supercritical. We will give a brief non-expert overview of this subject and the recent experimental discovery of supercritical states [17].

2.1 Electronic Structure of Graphene

Since it is relatively easy to understand how the ultrarelativistic dispersion relation comes about we will give a short derivation of the energy bands of graphene. For details see the reviews [18, 19] and references therein. The valence-shell electrons of the carbon atoms form hybridized sp^2 orbitals which give rise to the covalent σ bonds forming stable hexagonal benzene rings which combine to build up a honeycomb lattice. In addition there are π electrons (one per carbon atom, arising from the $2p_z$ state) forming lobes orthogonal to the lattice plane (see Fig. 5a). The honeycomb

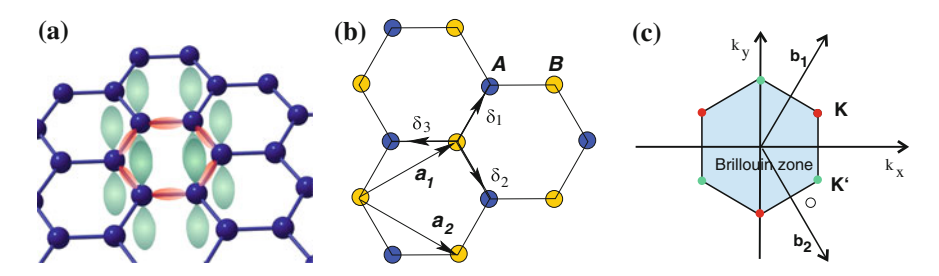


Fig. 5 a Schematic sketch of the electron structure of graphene. The hybridized sp^2 bonds (red) form hexagonal benzene rings. In addition there are p_z states (green) orthogonal to the plane. **b** The honeycomb lattice of graphene is composed of two triangular sublattices (blue and yellow). **c** The Brillouin zone of graphene. **b**₁ and **b**₂ are the reciprocal lattice vectors

structure can be thought as consisting of two interpenetrating *triangular sublattices* A and B, marked yellow and blue in Fig. 5b.

The Bravais lattice unit vectors depicted in Fig. 5b have the form

$$\mathbf{a}_1 = \frac{a}{2}(3, \sqrt{3}), \quad \mathbf{a}_2 = \frac{a}{2}(3, -\sqrt{3}).$$
 (5)

while the three nearest-neighbour vectors (connecting atoms from the two sublattices) are

$$\delta_1 = \frac{a}{2}(1, \sqrt{3}), \quad \delta_2 = \frac{a}{2}(1, -\sqrt{3}), \quad \delta_3 = -a(1, 0).$$
 (6)

Here a=1.42 Å is the carbon-carbon nearest-neighbour distance. The Brillouin zone also has a hexagonal shape, see Fig. 5c. The corner points of the hexagon will play a special role in the following. Two of them are non-equivalent. They are called the *Dirac points*:

$$\mathbf{K} = \frac{2\pi}{3a} \left(1, \frac{1}{\sqrt{3}} \right), \quad \mathbf{K}' = \frac{2\pi}{3a} \left(1, -\frac{1}{\sqrt{3}} \right). \tag{7}$$

The description of the electron structure [20, 21] can be based on the *tight binding approximation*. One assumes that electron states are localized at one atom and are influenced (in a first step) only by their *nearest neighbours*. Using second quantization the most simple ansatz for the interaction Hamiltonian is

$$\hat{H} = t_1 \sum_{\mathbf{A}} \sum_{i=1}^{3} (\hat{a}^{\dagger}(\mathbf{A})\hat{b}(\mathbf{A} + \boldsymbol{\delta}_i) + \text{h.c.})$$
 (8)

Here \hat{a}^{\dagger} creates an electron at lattice site $\mathbf{A} = n_1 \mathbf{a}_1 + n_2 \mathbf{a}_2$ and \hat{b} annihilates an electron at neighbouring site $\mathbf{A} + \boldsymbol{\delta}_i$. The *hopping parameter t*₁ describes the interaction

strength. Transformed to momentum space (8) becomes an integral over the Brillouin zone Ω_B

$$\hat{H} = \int_{\Omega_B} \frac{d^2k}{(2\pi)^2} \left(\hat{a}^{\dagger}(\mathbf{k}), \, \hat{b}^{\dagger}(\mathbf{k}) \right) \begin{pmatrix} 0 & t_1 \gamma_{\mathbf{k}} \\ t_1 \gamma_{\mathbf{k}}^* & 0 \end{pmatrix} \begin{pmatrix} \hat{a}(\mathbf{k}) \\ \hat{b}(\mathbf{k}) \end{pmatrix}$$
(9)

with $\gamma_{\mathbf{k}} = e^{i\mathbf{k}\cdot\boldsymbol{\delta}_1} + e^{i\mathbf{k}\cdot\boldsymbol{\delta}_2} + e^{i\mathbf{k}\cdot\boldsymbol{\delta}_3}$.

This Hamiltoniann can be easily diagonalized, leading to the energy spectrum:

$$E_{\mathbf{k}} = \pm t_1 |\gamma_{\mathbf{k}}| = \pm t_1 \sqrt{3 + 2\cos(k_y a\sqrt{3}) + 4\cos(k_y a\frac{\sqrt{3}}{2})\cos(k_x a\frac{3}{2})}$$
 (10)

One finds two symmetric bands π^* and π with positive and negative energies. Inspecting the function $E_{\bf k}$ one finds that the bands touch at the corners of the Brillouin zone, i.e., at the Dirac points (7): $E_{\bf K}=E_{{\bf K}'}=0$. The full energy surface is shown in Fig. 6. We are particularly interested in the region surrounding the Dirac points were the gap between the π and π^* bands vanishes. Taking the low-energy limit on can expand about the Dirac point ${\bf K}$ according to ${\bf k}={\bf K}+{\bf q}$ assuming $qa\ll 1$. Expansion of the factors $e^{i{\bf k}\cdot\delta_i}$ leads to (up to a phase factor)

$$\gamma_{\mathbf{q}} \simeq -\frac{3a}{2}(q_x + iq_y) \tag{11}$$

The resulting expression for the energy then reads

$$E_{\mathbf{q}} = \pm \frac{3a}{2} t_1 |\mathbf{q}| = \pm \hbar v_F |\mathbf{q}|. \tag{12}$$

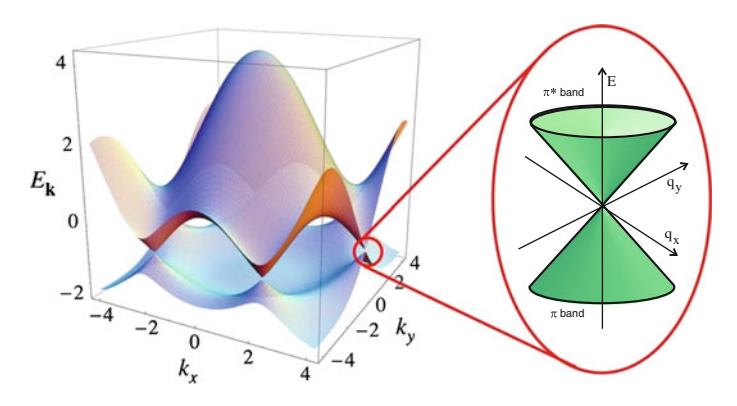


Fig. 6 Energy spectrum of electrons in the hexagonal lattice. The inset shows the cone-shaped energy spectrum in the vicinity of one of the Dirac points. The calculation includes also the effect of next-to-nearest neighbour couplings. Adapted from [18]

Here we have introduced the Fermi velocity

$$v_F = \frac{3a}{2\hbar} |t_1| \simeq 10^6 \text{ m/s} \simeq \frac{1}{300} c \text{ (with } t_1 \simeq -3\text{eV})$$
 (13)

Most interestingly, Eq. (12) corresponds to the dispersion relation of ultrarelativistic particles $E = c|\mathbf{p}|$, though with the much smaller Fermi velocity v_F instead of the velocity of light c. We have found that graphene is a zero-gap semiconductor with massless "ultrarelativistic" quasiparticles which, however, move at a velocity 300 times smaller than the speed of light.

The connection to relativistic quantum mechanics goes beyond the dispersion relation. Following [21] one can introduce an effective low-energy Hamiltonian

$$\hat{H}_{\text{eff}} = -i\hbar v_F \int d^2 r \,\hat{\Psi}^{\dagger} \boldsymbol{\sigma} \cdot \nabla \hat{\Psi}(\mathbf{r})$$
 (14)

with the Pauli matrices $\sigma = (\sigma_x, \sigma_y)$. The corresponding wave equation reads

$$-i\hbar v_F \boldsymbol{\sigma} \cdot \nabla \psi(\mathbf{r}) = E\psi(\mathbf{r}) \tag{15}$$

This is identical to the *massless Dirac equation* (i.e. the Weyl equation). The wave functions $\psi(\mathbf{r})$ are two-component spinors. Note, however, that the intrinsic degree of freedom is not the electron spin. Rather it is a "pseudospin" related to the localization of the electron on one of the two sublattices A and B! (There is a further degree of freedom called "valley symmetry": The presence of the second Dirac point \mathbf{K}' leads to an extra degeneracy factor 2.)

2.2 Supercritical States in Graphene

According to the discussion above, the electron bands π^* and π of graphene are an analogue of the relativistic particle and antiparticle states (electron and positron continua) of QED. However, there is a marked difference: Because of $v_F \ll c$ the effective fine structure constant is much larger:

$$\alpha_G = \frac{e^2}{\epsilon \hbar v_F} \simeq \frac{300}{\epsilon} \alpha \simeq 1. \tag{16}$$

Here $\epsilon \simeq 2.5$ is the dielectric constant of graphene. This lead to the idea, that an analogue of strong-field QED can be studied experimentally on the eV instead of MeV scale: Impurities with a very modest charge inserted into graphene should behave as artificial supercritical atoms!

This idea was first studied quantitatively by Shytov et al. and by Pereira et al. [22, 23] who solved the 2D massless Dirac equation in the presence of an external

Coulomb potential.

$$(-i\boldsymbol{\sigma}\cdot\nabla + V(r))\boldsymbol{\psi} = E\boldsymbol{\psi}$$
 with $V(r) = \frac{\beta}{r}$, $\beta = -Z\alpha_G$. (17)

These studies showed that the system does not allow for true bound states (since there is no gap in the energy spectrum). However, for a Coulomb strength parameter exceeding a *critical coupling*, $|\beta| > \beta_{cr}$, *resonances* (quasibound states) emerge. In contrast to QED atoms ($Z\alpha_{cr} = 1$ for point nuclei) the critical coupling strength was found to be $\beta_{cr} = \frac{1}{2}$.

The electron states are illustrated in Fig. 7 which shows the scattering phase shifts in the lower continuum E < 0. For supercritical coupling ($\beta = -0.8$, red and $\beta = -1.2$, blue) the phaseshifts show the telltale jumps in phase shift by π indicative for the presence of resonances.

The calculations also showed that, as in QED, in supercritical systems "real vacuum polarization" sets in which screens the inserted charge. Note that the calculations use a cut-off radius for the 1/r-potential, typically on the scale of 1 nm.

A handle for measuring the supercritical state is the *local density of states* (LDOS)

$$\nu(E, r) = \frac{4}{\pi \hbar \nu_F} \sum_{i} |\psi_i(k_E, r)|^2$$
 (18)

where $k_E = |E|/\hbar v_F$ and the sum runs over the relevant angular momentum channels in the continuum.

Fortunately, experimental solid state physics provides a tool for measuring the LDOS of a sample as a function of energy and spatial position: *Scanning tunneling microscopy* (STM). In an STM microscope a sharp tip of atomic extension scans over a probe and measures the electric current *I* the tip draws from the surface as a

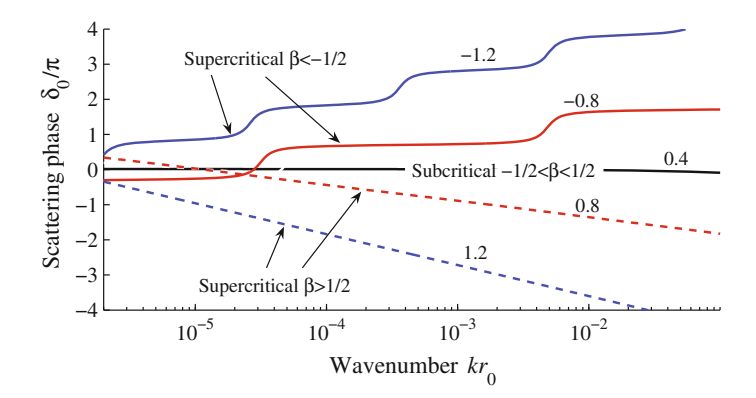


Fig. 7 Phaseshift for states in the lower continuum of the 2D Coulomb problem. The *blue* and *red full curves* referring to supercritical coupling show the presence of resonances. *Dashed curves* repulsive coupling does not produce resonances. From Shytov et al. [22]

consequence of the tunnelling effect. The current depends on the relative voltage V between tip and probe and it can be shown from the laws governing the tunnel effect that the derivative of I with respect to V is proportional to the local density of states

$$v(E,r) \propto \frac{dI}{dV}$$
 (19)

This technique is known as differential conductance mapping spectroscopy. By modulating V with an oscillating a.c. component this derivative is easily measured. In the attempt to observe the supercritical state one further problem had to be solved: How to introduce a sufficiently large impurity charge into graphene. The net charge of a single impurity atom turned out to be too low. M.F. Crommie and his collaborators [17] deposited Calcium dimers (Ca₂) on the surface of a graphene sheet (sitting on a flake of Boron nitride which in turn rested on a substrate of Silicon and Silicon dioxide). Each such dimer was found to posses a positive charge of about 0.6e which is subcritical. However, an STM allows to "shuffle around" impurity atoms on a surface. In this way clusters of up to 5 Ca₂ dimers sitting closely together were formed.

The result of the experiment [17] with N=1, 3 and 5 Ca₂ dimers is shown in Fig. 8. The insets show the positions of the Calcium dimers as seen by the STM. The curves depict the differential conductance dV/dI (and thus the LDOS) as a function of the bias voltage V. A change of V corresponds to changing the energy E and thus allows to scan the band structure of the investigated material. The various curves in each subpicture correspond to a different distances from the charge center, in the range of about $r=2\dots 20$ nm. The vertical dashed line marks the position of the Dirac point. The structure of the dV/dI curves is quite involved; for a detailed understanding it is necessary, to include, e.g., phonon-assisted inelastic tunneling of electrons and the finite quasiparticle width. However, the appearance of a clear narrow maximum in the vicinity of the charge center in the N=5 case is obvious. This is interpreted as evidence for an "atomic collapse state" in graphene with a supercritical impurity charge. This interpretation corroborated by the at least semiquantitative agreement with theoretical calculations based on this concept.

What is the relevance of the experiment by Crommie and collaborators? Their measurement roughly corresponds to the observation of an atom in QED with $Z > Z_{\rm cr}$ displaying a supercritical filled K-shell. Owing to the instability of very heavy nuclei such an observation cannot be made in the case of real QED. The best one can hope for is to find evidence for supercriticality through the emission of positrons in the collision of (preferentially bare) heavy ions on a time scale of 10^{-21} s to 10^{-20} s. Therefore it is tempting to take the filled and empty bands in graphene as a model for the electron-positron vacuum in QED. One should keep in mind that QED is believed to be a fundamental field theory (embedded in the standard model) while the Dirac-like band structure refers to quasiparticle excitation in an effective low-energy approximation. The energy and lengths scales are 1 MeV and 100 fm compared to 1 eV and 10 nm, respectively. And there are considerable qualitative differences between the systems: graphene is two-dimensional and massless while QED is three-dimensional and massive.

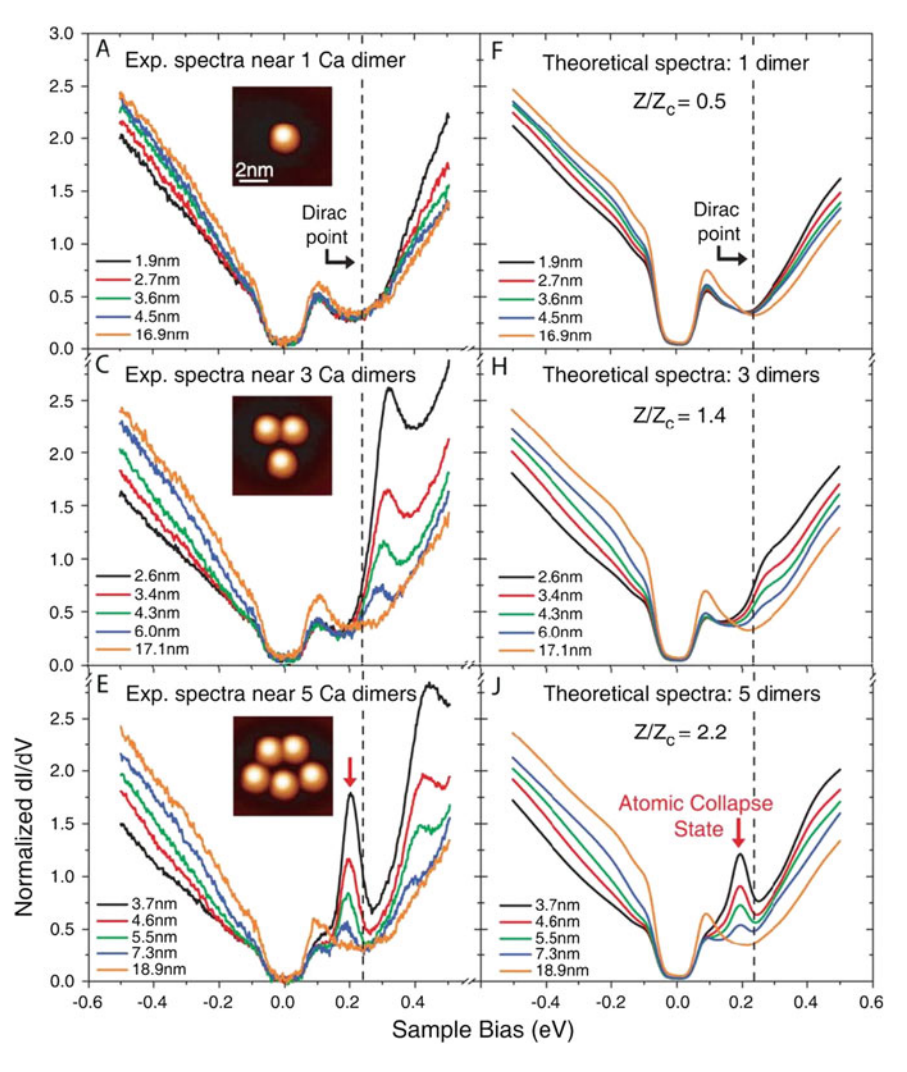


Fig. 8 STM measurements of dV/dI for graphene with N=1,3, and 5 charged impurity clusters (calcium dimers) put on *top*. In the *lowest* row the supercritical "atomic collapse state" shows up (arrow). Left experiment, right calculation. Adapted from Crommie et al. [17]

The big advantage of graphene, of course, is its experimental accessibility. Supercritical "collapse states" in graphene can be investigated in table-top experiments. There is quite a number of parameters that can be varied (doping, back-gate voltage, bi-layer graphene, …) allowing for further study. E.g., static molecules with two charged impurities in graphene might be investigated; the corresponding two-center Dirac equation already has been studied theoretically [24]. Also the "Klein paradox", i.e. anomalous transmission coefficients for high potential barriers can be

studied experimentally in graphene [25], in contrast to QED where the necessary microscopic potential steps are not available.

References

- W. Greiner, B. Müller, J. Rafelski, Quantum Electrodynamics of Strong Fields (Springer, Berlin, 1985)
- 2. I. Pomeranchuk, Y. Smorodinsky, J. Phys. USSR 9, 97 (1945)
- 3. B. Müller, J. Rafelski, W. Greiner, Z. Phys. 257, 62,183 (1972)
- 4. Y. Zel'dovich, V.S. Popov, Sov. Phys. Usp. 14, 673 (1972)
- B. Müller, J. Rafelski, W. Greiner, Phys. Lett. B 47, 5 (1973); B. Müller, W. Greiner, Z. Naturforsch. 31a, 1 (1976)
- 6. V.S. Popov, Phys. Atom. Nuclei **64**, 367 (2001)
- 7. U. Müller, G. Soff, Phys. Rep. 246, 101 (1994)
- 8. J. Reinhardt, B. Müller, W. Greiner, Phys. Rev. A 24, 103 (1981)
- H. Backe et al., Phys. Rev. Lett. 40, 1443 (1978); C. Kozhuharov et al. ibid. 42, 376 (1979); J. Schweppe et al., ibid. 51, 2261 (1983); T. Cowan et al., ibid. 54, 1761 (1985); M. Clemente et al., Phys. Lett. B 137, 41 (1984); H. Tsertos et al., ibid. 162, 273 (1985)
- A. Balkacem, H. Gould, B. Feinberg, R. Bossingham, W.E. Meyerhof, Phys. Rev. Lett. 71, 1514 (1993)
- 11. GSI, SPARC Technical Design Report (2006)
- 12. Y. Oganessian, G. Ter-Akopian, Private communication (2013)
- U. Müller, T. de Reus, J. Reinhardt, B. Müller, W. Greiner, G. Soff, Phys. Rev. A 37, 1449 (1988)
- J. Reinhardt, U. Müller, B. Müller, W. Greiner, Z. Physik, A 303, 173 (1981); U. Müller, G. Soff, T. de Reus, J. Reinhardt, B. Müller, W. Greiner, Z. Physik A 313, 263 (1983)
- 15. J. Rafelski, B. Müller, W. Greiner, Z. Physik A 285, 49 (1978)
- K.S. Novoselov, A.K. Geim, S.V. Morozov, D. Jiang, Y. Zhang, S.V. Dubonos, I.V. Grigorieva, A.A. Firsov, Science 306, 666 (2004)
- 17. Y. Wang, D. Wong, A.V. Shytov, V.W. Brar, S. Choi, Q. Wu, H. Tsai, W. Regan, A. Zettl, R.K. Kawakami, S.G. Louie, S.S. Levitov, M.F. Crommie, Science **340**, 734 (2013)
- A.H. Castro Neto, F. Guinea, N.M.R. Peres, K.S. Novoselov, A.K. Geim, Rev. Mod. Phys. 81, 109 (2009)
- M.I. Katsnelson, K.S. Novoselov, Solid State Commun. 143, 3 (2007); A.K. Geim, Science 324, 1530 (2009)
- 20. P.R. Wallace, Phys. Rev. 71, 622 (1947)
- 21. G.W. Semenoff, Phys. Rev. Lett. 53, 2449 (1984)
- A.V. Shytov, M.I. Katsnelson, L.S. Levitov, Phys. Rev. Lett. 99, 236801(2007); ibid. 99, 246802 (2007)
- 23. V.M. Pereira, J. Nilsson, A.H Castro Neto. Phys. Rev. Lett. 99, 166802 (2007)
- 24. O.O. Sobol, E.V. Gorbar, V.P. Gusynin, Phys. Rev. **B88**, 205116 (2013)
- M.I. Katsnelson, K.S. Novoselov, A.K. Geim, Nat. Phys. 2, 620 (2006); A.F. Young, P. Kim. Nat. Phys. 5, 222 (2009)

Zepto-Second Atomic Clock for Nuclear Contact Time Measurements

Hartmut Backe

Abstract Renewed interest in search for the spontaneous decay of the neutral vacuum by emission of positrons in overcritical nuclear collision systems prompted the question of how to find experimental triggers for the required long sticking times in the order of 10^{-20} s in dissipative heavy ion collisions [1]. A survey of various conceivable experimental methods led to the conclusion that the most promising way may be either to search directly for the positron line [2] or to investigate the shape of δ -electron spectra [3, 4], both as function of the total kinetic energy loss or a large mass transfer between the collision partners. The δ -electron-spectroscopy tool has been employed in a previous experiment for the dissipative U + Au collision system at an uranium beam energy of 8.65 MeV/u [5] in which nuclear contact times in the order of only 1 zs = 1 × 10^{-21} s were deduced.

1 Introduction

Although more than 40 years ago predicted by Walter Greiner and coworkers, the observation of spontaneous positron creation in superheavy nuclear systems is still an experimental challenge, see, e.g., Refs. [6, 7]. An ideal experiment would be based on a chemical element with an atomic number greater than the critical charge $Z_c = 173$ for which the binding energy of the lowest bound state exceeds twice the rest mass of the electron. For such an atom inner shell ionization would result in a narrow positron line originating from a transition of an electron of the negative energy continuum into the vacancy. The just described spontaneous decay of the neutral vacuum is a pure Gedanken experiment, since it is well known that elements with atomic numbers exceeding Z_c do neither exist in nature nor can be produced artificially by a nuclear fusion reaction of two colliding heavy ions. However, a supercritical nuclear charge can at least be assembled for a short period of time in a close collision of two very heavy ions like uranium on uranium. Unfortunately, such a collision lasts only for about 1 zs = 10^{-21} s which is much too short for the creation of spontaneous positrons requiring about a factor of 10-100 more time. Therefore, it was proposed by

Institute for Nuclear Physics, Johannes Gutenberg-University, 55099 Mainz, Germany e-mail: backe@kph.uni-mainz.de

H. Backe (⊠)

212 H. Backe

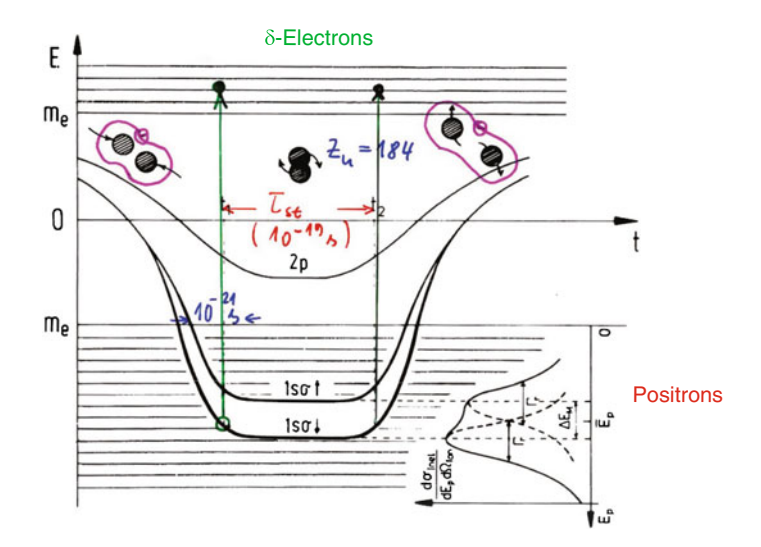


Fig. 1 Schematic representation of the correlation diagram for the inner electronic shells in an inelastic U + U collision as function of time. The resonances in the positron continuum are indicated together with the relevant widths [2]

Rafelski, Müller and Greiner [2] already in the year 1978 to delay the process between the colliding partners by means of nuclear reactions, see Fig. 1. Electrons from the $1s_{\sigma}$ atomic shell of the quasi-molecule are excited due to the strong dynamics in the approaching phase of the nuclei and the remaining hole may decay spontaneously by positron emission during the sticking phase. While the dynamics without sticking results in a broad positron spectrum with a width of typically 660 keV, the monochromatic positron lines may have widths down to about a few keV.

In a dissipative heavy ion collision the dinuclear system rotates for a certain time before the collision partners separate again. Since the impact parameter in the entrance channel is not an observable, the angular momentum cannot be determined experimentally and, consequently, also not the time the dinuclear system exists. However, it is generally accepted that during the nuclear contact a neck is formed through which nucleons are exchanged and kinetic energy is dissipated. In such a picture a correlation should exist between the sticking time, i.e. the time at which the neck exists, and both, the dissipated energy, which is signaled as total kinetic energy loss (T_{KEL}) in the exit channel, and the number of totally transferred nucleons. According to calculations of Zagrebaev et al. [1] rare subclasses of the reaction products with large mass transfers are connected with sticking times in the order of $10 \, \text{zs}$. From an experimental point of view such subclasses must be selected and be used as a trigger on the positron detection system, in order to suppress the majority of events with short contact times.

The article contributes to the question how sticking times in the order of $10\,\mathrm{zs}$ may be found experimentally. In Sect. 2 a brief overview is given on experimental methods for life time measurements between $10^{-21}\,\mathrm{s}$ and $10^{-19}\,\mathrm{s}$. It turns out that the

only viable method to search for sticking times in the $10\,\text{zs}$ range, without employing an efficient positron detection system, may be based on δ -electron spectroscopy. The principle of this method will be explained in Sect. 3. In Sect. 4 an experiment [5] is reviewed with the conclusion that some concepts proposed in Ref. [1] to prepare the long sticking were already followed up in this U + Au experiment at $8.65\,\text{MeV/u}$. Some facts will be repeated which might hamper a clean separation of subclasses with long sticking times in dissipative collisions. The article closes with a discussion and conclusions at Sect. 5.

2 Survey of Experimental Methods for Search of Long Sticking Times

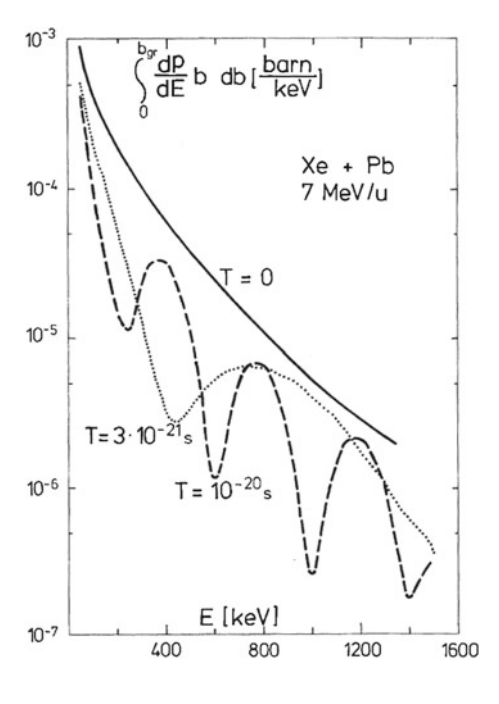
The conceptional simplest experimental method would be to search directly for a narrow positron line emitted in coincidence with a certain subclass of reaction products which belong to long sticking times. A successful experiment would prove both, the existence of very long nuclear sticking times and the spontaneous decay of the neutral vacuum. Such an approach was pursued at the early GSI experiments at beam energies close to the Coulomb barrier [8, 9]. However, after some euphoria triggered by the observation of monochromatic positron lines only shortly later it was already recognized that these lines were not connected with the spontaneous decay of the neutral vacuum [10, 11]. The particle detection systems used in these early experiments were rather simple, allowing in essence only for the detection of binary encounters in the exit channel. The challenge in resumed future experiments will be to maintain the large positron detection efficiency of the early experimental setups and to combine this feature with a modern and efficient heavy ion detection system. The latter must be able to determine for dissipative heavy ion collisions both, T_{KEL} and masses of the separated binary system before fission. Such an experimental setup is supposedly rather involved. Therefore, the question to be addressed in the following will be, whether there are other more efficient experimental methods for a search of the wanted long nuclear contact times in a preparatory experiment without employing already a sophisticated positron detection system.

Already in the year 1978 Kaun and Karamyan pointed out in an internal report [12] that the crystal blocking effect might be employed to distinguish between dynamical positron creation and subsequent nuclear positron emission from internal pair decay of excited nuclear levels. The latter is an important background process which must be subtracted in any experiment. With the blocking technique, for a concise description of this technique see, e.g., Ref. [13], direct evidence for very long fission times of uranium-like nuclei at very high excitation energies has been reported [14]. More recently this method has been applied for the investigation of the role of nuclear shell structures in the superheavy elements formation [15, 16]. However, this technique is only sensitive to lifetimes in the range between $3 \times 10^{-19} \, \mathrm{s}$ and $10^{-16} \, \mathrm{s}$ [17] and probably can not be applied to search for lifetimes in the order of $10^{-20} \, \mathrm{s}$.

Other conceivable experimental methods are based on atomic clocks. One of them utilizes the characteristic X-ray fluorescence emitted either during the time 214 H. Backe

the intermediate superheavy complex exists or from one of the separated nuclei. The latter method is not suited for a lifetime measurement of the dinuclear system. Instead, it has been employed for the investigation of the fission dynamics of uranium-like nuclei in uranium-uranium collisions [18] as well as for some lighter systems [19]. Recently, the former method has been used to estimate the mean characteristic time for fusion followed by fission in ²³⁸U+⁶⁴Ni reactions at 6.6 MeV/u [20, 21]. However, for an estimate of the time a superheavy nuclear complex exists, such a method is only applicable if its lifetime matches about with the lifetime of a K-vacancy. Soff et al. [22] calculated for a superheavy nucleus with atomic number of Z = 188 and a radius of 9.4 fm that the fastest transition with a decay width of $0.383\,keV$ is a M1 transition from the $2s_{1/2}$ to the $1s_{1/2}$ ground state. The corresponding decay width by spontaneous positrons emission is about 15 keV [23]. The corresponding numbers estimated for a nucleus with an atomic number of 184 and a radius of 9.23 fm are 0.24 keV for the radiative transition and 8 keV for the spontaneous positron decay [23], assuming an $(\hbar\omega)^3$ scaling of the radiative transition rate. The transition energy for uranium was taken from Fig. 2 of Ref. [25]. However, these numbers were obtained for spherical nuclei neglecting screening. An estimate for the U + U collision system at minimum distance of approach of 15 fm, including screening, results in a positron decay width of 1.2 keV at a resonance energy of 210 keV and a somewhat reduced M1 transition width which may still be in the order of 0.14 keV. Since the total decay width with inclusion of all atomic orbitals may be about a factor of two larger, it can be estimated that about 25 % of the K vacancies may decay radiatively. The emission spectrum would be a broad distribution at

Fig. 2 Differential emission probability with respect to kinetic δ -electron energy. A coincidence with created ls_{σ} formation is assumed. Integration over all impact parameters $b \le b_{\text{grazing}}$ that lead to a nuclear reaction has been performed. The nuclear delay times T = 0, 10^{-21} s, and 10^{-20} s are considered. Figure taken from Ref. [4]



X-ray energies around 1 MeV. The additional broadening of about $66 \, \text{keV}$ originating from the assumed lifetime of the giant nuclear complex of $10^{-20} \, \text{s}$ can be neglected completely.

It should be mentioned that atomic clock methods applied for deep inelastic collisions will most probably suffer from the huge background created by γ rays emitted by the excited nuclei in the exit channel. Since such background components remain constant, regardless of the sticking time, they mask the atomic clock signals all the more, the shorter the sticking time will be. Assuming a total decay width of 0.28 keV for radiative X-ray transitions, the transition rate corresponds to 4.3×10^{17} /s which results in a time interval of 10^{-20} s in only a fraction of 0.43 % X rays per vacancy formed in the entrance channel of the collision. Extremely good statistics may be required to separate the expected rather small signal unambiguously from the background.

Another class of experimental methods to search for contact times in the order of $10\,\mathrm{zs}$ is based on interference phenomena. The atomic inner shell ionization probability can be affected by the nuclear reaction time which causes time-dependent interference effects between the amplitudes describing the ionization of the innershell electrons during the approach and the separation phases of the two colliding nuclei. This effect has been observed experimentally in the yield of characteristic X-rays by Nessi et al. [24]. Another more direct approach which is based on a spectroscopy of δ electrons will be described in the following section.

3 Principle of Contact Time Measurements with δ -electron Spectroscopy

The principle of nuclear contact time measurements employing this method will also be explained by means of Fig. 1. In the phase when the two nuclei approach each other, an electron from the $1 \, \mathrm{s}_\sigma$ orbital may be excited into the positive energy continuum. This process is described by the amplitude a_i which is given in the monopole approximation by simply the Fourier transform of $\dot{R}(t)/R(t)$ with R(t) the time dependent distance of the two colliding nuclei [4]. During the sticking phase of duration T an amplitude $a_{st}=0$ results assuming $\dot{R}(t)/R(t)$ to be zero. In the exit channel the excitation amplitude is a_o the absolute value of which might be reduced in comparison to $|a_i|$ in case of a damping of the kinetic energy during the contact phase. The total amplitude is given by

$$a_{if} = a_i + a_{st} + a_o$$

$$= \frac{d(E_\delta, Z_u)}{\hbar \omega} \left[\int_{-\infty}^0 \frac{\dot{R}_i(t')}{R_i(t')} e^{i\omega t'} dt' + \int_0^T 0 \times e^{i\omega t'} dt' + \int_0^\infty \frac{\dot{R}_o(t'-T)}{R_o(t'-T)} e^{i\omega t'} dt' \right]$$

$$(1)$$

216 H. Backe

with $\omega = (E_{\delta} - E_{1s_{\sigma}})/\hbar$ and $d(E_{\delta}, Z_u)$ a constant depending essentially only on the united nuclear charge number $Z_u = Z_p + Z_t$ of the projectile and the target nucleus. With the substitution t = t' - T one obtains

$$a_{if} = a_i(\omega) + e^{i\omega T} a_o(\omega). \tag{2}$$

This important Eq. (2) expresses that the two phasors add coherently into the complex plane whereby the second one rotates by an angle ωT resulting in interference maxima and minima as function of $E = E_{\delta} - E_{1s_{\sigma}}$. The corresponding exact theory has been developed by Soff et al. [4]. Fig. 2, taken from this reference, clearly demonstrates that δ -electron spectroscopy should be applicable for a measurement of sticking times in the order of $10 \, \mathrm{zs}$.

4 Contact Time Measurements for the Deep Inelastic $^{238}\text{U} + ^{197}\text{Au}$ Collision System with δ -electron Spectroscopy

If the two colliding nuclei come in close contact in a deep inelastic collision, the repulsive nuclear forces cause a rotation by an angle θ of the di-nuclear system before the nuclei separate again, see Fig. 21 of Schröder et al. [26]. If this angle were known, the nuclear contact time could simply be determined by the formula $T = J\theta/L$, with J the moment of inertia of the di-nuclear system, and $L = Mbv_0$ the angular momentum. The latter depends on the mass M of the projectile, its velocity v_0 at infinity and the impact parameter b. Unfortunately, only the angle in the exit channel can be measured. The impact parameter is not an observable. Experimental evidence on fragment-mass distributions suggests that during the time the two constituents of the intermediate double-nucleus system interact with each other, a mass equilibration process proceeds which is accompanied by a damping of the relative kinetic energy into other degrees of freedom. It is generally accepted that the total kinetic energy loss T_{KEL} signifies the total interaction time T, i.e. $L = L(T_{KEL})$. This view is supported by classical dynamical calculations [27–29] which show that the energy loss is a monotonic function of the initial angular momentum and the total interaction time.

The consequence of this picture of a deep inelastic collision for the design of an experimental setup is, that it must be able to determine T_{KEL} and the mass transfer. The setup which fulfills this requirements is shown in Fig. 3, left panel. It allows the measurement of the complete kinematics for binary, ternary and quadruple reactions. In the latter, one or both colliding particles undergo fission, respectively.

With this experimental setup the δ -electron spectra for the 238U+197Au ternary reaction at a beam energy of 8.65 MeV/u have been measured as function of T_{KEL} , see Fig. 3, right panel [31]. The insets show the contact time distributions which were used to reproduce the measurement as good as possible. For further details see the papers of P. Senger et al. [31] and J. Stroth et al. [5].

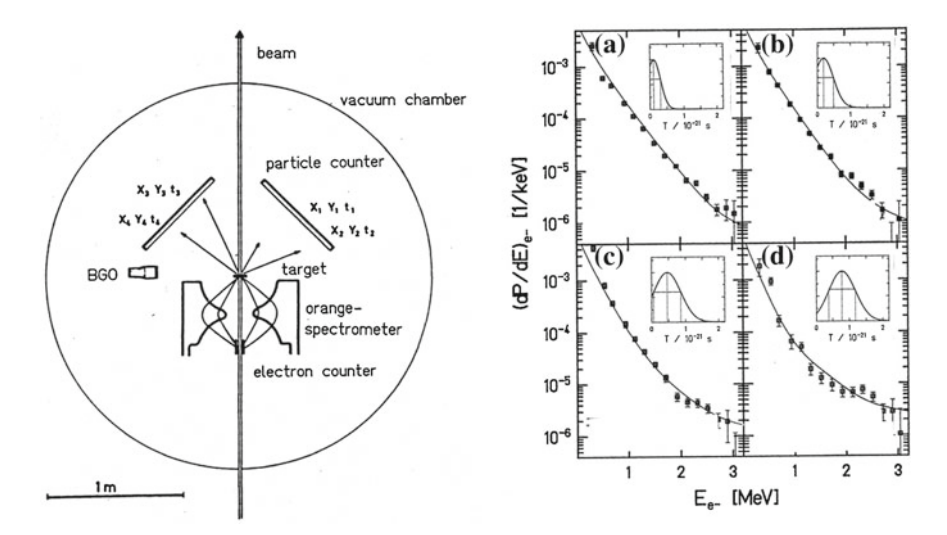


Fig. 3 Left panel Experimental setup [5]. The parallel plate particle counters with a size of $91 \times 91 \,\mathrm{cm}^2$ and a resolution $\delta x = \delta y = 2 \,\mathrm{mm}$ (FWHM) allow a measurement of the velocity vectors of up to four particles in the exit channel. For that purpose advantage is taken of the beam time structure which is delivered in bunches with a duration of typically 0.4 ns. These numbers allow a measurement of the total kinetic energy loss with an accuracy $\delta T_{KEL} = 40 \,\mathrm{MeV}$, a mass resolution $\delta m = 5 \,\mathrm{u}$, and the scattering angle in the CM system with an accuracy $\delta \theta_{CM} = 0.5^\circ$. Electrons are measured with an orange spectrometer [30] located in backward direction. The BGO detector measures the γ-ray spectrum from which the conversion electron background can be determined. Right panel δ-electron spectra for the $^{238}\mathrm{U} + ^{197}\mathrm{Au}$ ternary reaction at a beam energy of 8.65 MeV/u for various T_{KEL} : $T_{KEL} = 100 \,\mathrm{MeV} \,\mathrm{ams}$ $T_{KEL} = 190 \,\mathrm{MeV} \,\mathrm{bms}$ $T_{KEL} = 280 \,\mathrm{meV} \,\mathrm{cm}$ $T_{KEL} = 350 \,\mathrm{meV}$ (d). The insets show the contact time distributions as used for the best fits (full lines) [31]

In addition, δ -electron spectra were generated belonging to different mass windows, see Fig. 4. Within statistical errors the spectrum for the larger mass transfer, window VI, shows no significant difference in comparison with the spectrum of window V belonging to low mass transfer. Indeed, these spectra resemble that ones taken for window III with about the same T_{KEL} . These experimental observations indicate that all events have the same nuclear contact time, regardless of the mass diffusion. Obviously, the nuclear trajectories during the sticking phase are rather similar. Such a behavior could be explained in a picture in which the nuclei form at rupture a long neck which constricts statistically at different locations [32].

It can be concluded that long contact times of up to $10\,\mathrm{zs}$ as predicted by the analysis of deep inelastic collisions with the schematic model of Schröder at al. [26] could not be verified by the analysis of the experimental δ -electron spectra, neither as function of the T_{KEL} nor of the mass drift. However, it must be conceded that δ -electron spectra under the condition of very large mass transfer could not be generated because of lack of sufficient statistics.

218 H. Backe

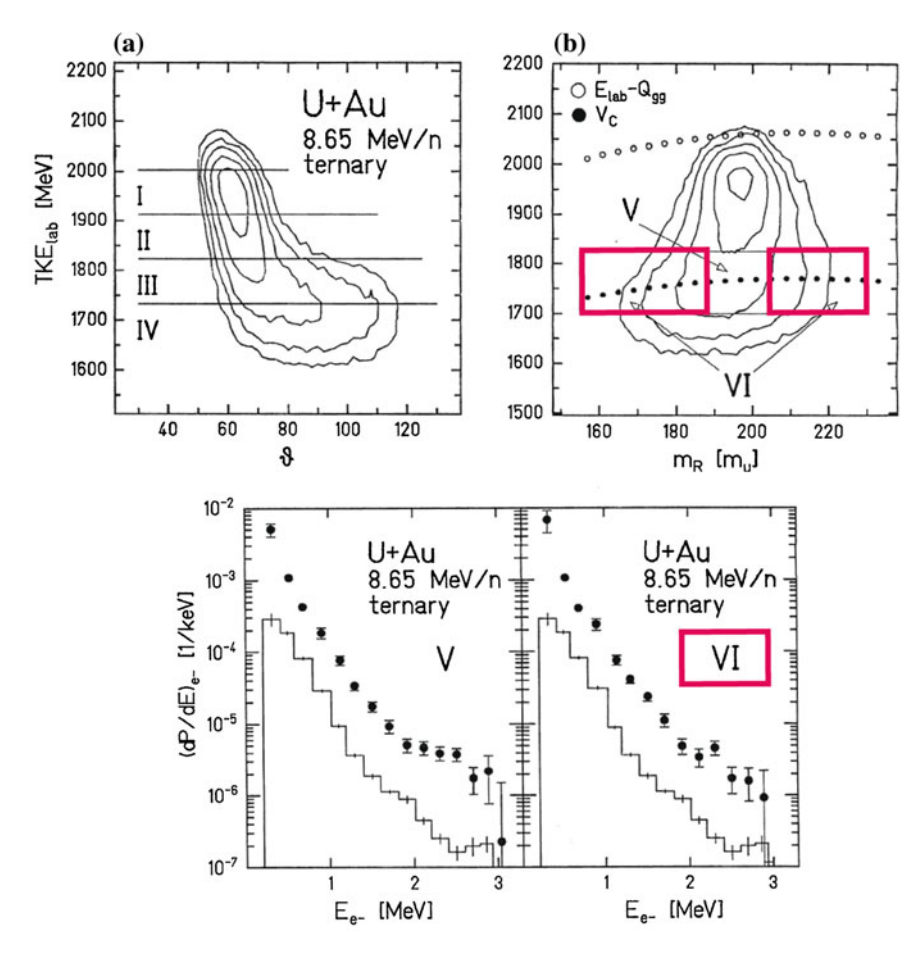


Fig. 4 Wilczyński diagram a and mass diffusion plot b for ternary reactions of U + Au at E/A = 8.65 MeV. The roman numbers (I–VI) indicate the different sub classes in total kinetic energy and mass diffusion for which δ -electron spectra were generated. The conversion electron background as indicated by the *histogram* has not been subtracted. Taken from Ref. [32]

With the tool of δ -electron spectroscopy nice results have been obtained by the TORI group on the subject of elastoplasticity in dissipative Pb + Pb collision at 12 MeV/u [35]. However, it would be worthwhile to re-investigate whether the first-order adiabatic perturbation theory approach holds for the analysis of this collision system, or not. As pointed out in a recent paper [34], the excess electron yield observed for the U+Pd ($Z_u=138$) collision system at conditions when nuclear forces become important is most likely of dynamical origin. The dynamics under the influence of the nuclear forces can probably not anymore be analyzed with scaling laws derived on the basis of first-order adiabatic perturbation theory. The reason may be found in its breakdown if the system Hamiltonian, characterized by \dot{R}/R , changes too rapidly.

5 Discussion and Conclusions

As the survey of possible experimental methods for the search of nuclear contact times in the order of 10^{-20} s in superheavy collision systems has shown, there are only two viable experimental methods, either to search directly for the spontaneous positron line or to employ the zs-atomic clock. With the latter, which is based on δ -electron spectroscopy, sticking times in dissipative collisions of uranium and gold nuclei at 8.65 MeV/u not longer than $1.5 \cdot 10^{-21}$ s have been deduced [5]. The sticking times about a factor of 10 longer derived on the basis of a pure kinematical model are not related to observables on which experimentally can be triggered. The preparation of well defined kinematical conditions as, e.g., T_{KEL} or a very asymmetric mass transfer suffers from the fact that diffusion processes or a statistical rupture, once the nuclei have formed a neck, do probably not allow to prepare a single well defined sticking time.

It should be mentioned that the search of the spontaneous positron line will also suffer from the huge background created by internal pair decay of the excited nuclei in the exit channel. For instance, at a total decay width for K holes by spontaneous positron emission of 1.2 keV, the transition rate corresponds to 1.2×10^{18} /s which results in a time interval of 10^{-20} s in only a fraction of 1.8 % positrons per vacancy formed in the entrance channel of the collision. Extremely good statistics and rather sophisticated experimental methods are required to separate the expected small signals unambiguously from the background to which, in addition, also the dynamically produced positrons belongs.

Unfortunately, even now about 30 years after the very suggestive Fig. 1 has been published neither the spontaneous positron peak has been observed nor the model dependent predictions of long sticking times in dissipative nuclear collisions have been verified by an atomic clock experiment. The nice positron peaks which were claimed to be observed by not only one group at GSI in the 80th and early 90th finally disappeared, for references see [7]. It remains a challenge to observe the mentioned effects at GSI, GANIL, FAIR or elsewhere. Experimentalists feel confident to address again the subject of spontaneous positron emission [36]. However, a long way must be gone to attain again the maturity of the experimental setups already reached at GSI and Argonne more than 20 years ago.

Acknowledgments Fruitful discussions with J. Stroth, P. Senger, J. Reinhardt, H. Feldmeier, G. Wolschin, V. Zagrebaev, and W. Greiner are gratefully acknowledged.

References

- 1. A. Karpov, V. Zagrebaev, W. Greiner, Int. J. Mod. Phys. E 20(Suppl. 1), 263–280 (2011)
- 2. J. Rafelski, B. Müller, W. Greiner, Z. Phys. A 285, 49-52 (1978)
- 3. J. Reinhardt, B. Müller, W. Greiner, G. Soff, Z. Phys. A 292, 211–212 (1979)
- 4. G. Soff, J. Reinhardt, B. Müller, W. Greiner, Phys. Rev. Lett. 43, 1981–1984 (1979)

- J. Stroth, H. Backe, M. Begemann-Blaich, K. Bethge, H. Bokemeyer, M. Dahlinger, W. Konen,
 P. Kosmadakis, S. Mojumder, P. Senger, K. Stiebing, Z. Phys. A 357, 441–455 (1997)
- 6. J. Reinhardt, W. Greiner, Rep. Prog. Phys. 40, 219–295 (1977)
- J. Reinhardt, W. Greiner, Supercritial fields and the decay of the vacuum. In: *Topics in Heavy Ion Physics, Memorial Symposium for Gerhard Soff* ed. by W. Greiner, J. Reinhardt. April 25–26, 2005, Frankfurt, Germany, pp. 151–162, EP Systema Bt. Budapest, 2005. ISBN 963-869-340-1
- 8. J. Schweppe, A. Gruppe, K. Bethge, H. Bokemeyer, T. Cowan, H. Folger, J.S. Greenberg, H. Grein, S. Ito, R. Schule, D. Schwalm, K.E. Stiebing, N. Trautmann, P. Vincent, M. Waldschmidt, Phys. Rev. Lett. **51**, 2261–2264 (1983)
- 9. M. Clemente, E. Berdermann, P. Kienle, H. Tsertos, W. Wagner, C. Kozhuharov, F. Bosch, W. Koenig, Phys. Lett. B 137, 41–46 (1984)
- T. Cowan, H. Backe, M. Begemann, K. Bethge, H. Bokemeyer, H. Folger, J.S. Greenberg, H. Grein, A. Gruppe, Y. Kido, M. Kluver, D. Schwalm, J. Schweppe, K.E. Stiebing, N. Trautmann, P. Vincent, Phys. Rev. Lett. 54, 1761–1764 (1985)
- H. Tsertos, E. Berdermann, F. Bosch, M. Clemente, P. Kienle, W. Koenig, C. Kozhuharov, W. Wagner, Phys. Lett. B 162, 273–276 (1985)
- 12. K.H. Kaun, S.A. Karamyan, JINR P 7–11420, Dubna 1978, GSl-tr-9/78 (translation P. Strehl)
- M. Morjean, J.L. Charvet, A. Chbihi, M. Chevallier, C. Cohen, D. Dauvergne, R. Dayras, A. Drouart, J.D. Frankland, D. Jacquet, R. Kirsch, M. Laget, P. Lautesse, A. L'Hoir, A. Marchix, L. Nalpas, M. Parlog, C. Ray, C. Schmitt, C. Stodell, L. Tassan-Got, C. Volant. Eur. Phys. J. D 45, 27–31 (2007)
- F. Goldenbaum, M. Morjean, J. Galin, E. Liénard, B. Lott, Y. Périer, M. Chevallier,
 D. Dauvergne, R. Kirsch, J.C. Poizat, J. Remillieux, C. Cohen, A. L'Hoir, G. Prévot,
 D. Schmaus, J. Dural, M. Toulemonde, D. Jacquet, Phys. Rev. Lett. 82, 5012–5015 (1999)
- J.U. Andersen, J. Chevallier, J.S. Forster, S.A. Karamian, C. Broude, F. Malaguti, A. Uguzzoni, Phys. Rev. C 78, 064609 (2008)
- M. Morjean, D. Jacquet, J.L. Charvet, A. L'Hoir, M. Laget, M. Parlog, A. Chbihi, M. Chevallier, C. Cohen, D. Dauvergne, R. Dayras, A. Drouart, C. Escano-Rodriguez, J.D. Frankland, R. Kirsch, P. Lautesse, L. Nalpas, C. Ray, C. Schmitt, C. Stodel, L. Tassan-Got, E. Testa, C. Volant, Phys. Rev. Lett. 101, 072701 (2008)
- 17. D. Jacquet, M. Morjean, Prog. Part. Nucl. Phys. **63**, 155–185 (2009)
- J.D. Molitoris, W.E. Meyerhof, Ch. Stoller, R. Anholt, D.W. Spooner, L.G. Moretto, L.G. Sobotka, R.J. McDonald, G.J. Wozniak, M.A. McMahan, L. Blumenfeld, N. Colonna, M. Nessi, E. Morenzoni, Phys. Rev. Lett. 70, 537–540 (1993)
- 19. H.W. Wilschut, V.L. Kravchuk, Nucl. Phys. A 734, 156–163 (2004)
- M.O. Frégeau, D. Jacquet, M. Morjean, E. Bonnet, A. Chbihi, J.D. Frankland, M.F. Rivet,
 L. Tassan-Got, F. Dechery, A. Drouart, L. Nalpas, X. Ledoux, M. Parlog, C. Ciortea,
 D. Dumitriu, D. Fluerasu, M. Gugiu, F. Gramegna, V.L. Kravchuk, T. Marchi, D. Fabris,
 A. Corsi, S. Barlini, Phys. Rev. Lett. 108, 122701 (2012)
- M. Morjean, A. Chbihi, M. Dasgupta, A. Drouart, J.D. Frankland, M.O. Frégeau, D.J. Hinde, D. Jacquet, L. Nalpas, M. Pârlog, C. Simene, L. Tassan-Got, E. Williams, 2nd Heavy Ion Accelerator Symposium for Fundamental and Applied Research (HIAS), in2p3-00812697, version 1–28 Jun 2013. Canberra, Australia (2013)
- 22. G. Soff, W. Greiner, J. Phys. B: At. Mol. Phys. 15, L681-L684 (1981)
- 23. J. Reinhardt, U. Müller, B. Müller, W. Greiner, Z. Phys. A 303, 173–188 (1981)
- M. Nessi, Ch. Stoller, E. Morenzoni, W. Wölfli, E. Meyerhof, J.D. Molitoris, E. Grosse, Ch. Michel, Phys. Rev. C 36, 143–151 (1987)
- H. Backe, Atomic physics of high-Z Systems—Les Houches. Session XXXVIII, 1982, in New Trends in Atomic Physics, ed. by G. Grynberg, R. Stora (Elsevier Science Publishers B.V, Amsterdam, 1984), pp. 697–777
- W.U. Schröder, J.R. Birkelund, J.R. Huizenga, K.L. Wolf, J.E. Viola Jr, Phys. Rep. 45, 301–345 (1978)
- 27. K. Siwek-Wilczyńska, J. Wilczyński, Nucl. Phys. A 264, 115 (1976)

- E. Gross, H. Kalinowski, J.N. De, Friction model for heavy ion collisions and its application to heavy ion fusion and deep inelastic reactions. In: *Classical and Quantum Mechanical Aspects* of *Heavy Ion Collisions*, ed. by H.L. Harney. Heidelberg, 1974, Lecture notes in physics, vol. 33. (Springer, Berlin, 1975), pp. 194–220
- 29. C. Riedel, G. Wolschin, W. Nörenberg, Z. Phys. A 290, 47-55 (1979) 253 (1980)
- 30. E. Moll, E. Kankeleit, Nukleonika 7, 180 (1965)
- P. Senger, H. Backe, M. Begemann-Blaich, H. Bokemeyer, P. Glässel, D.V. Harrach, M. Klüver, W. Konen, K. Poppensieker, K. Stiebing, J. Stroth, K. Wallenstein, Nuclear contact times in dissipative heavy ion collisions measured via δ-ray spectroscopy. In: *Physics of Strong Fields*, ed. by W. Greiner. Maratea (Italy) 1986. (NATO Adv. Study Inst. Ser. B 153, 423–439 (1987))
- 32. J. Stroth, Untersuchungen der Reaktionsdynamik von Schwerionenreaktionen via δ -Elektronenspektroskopie, Doctoral thesis, University of Mainz, 1990, GSI-90-28 report, Nov 1990, ISSN 0171–4546
- 33. H. Backe, Positronenerzeugung bei Schwerionenstössen, in *Present Status and Aims of Quantum Electrodynamics, Mainz 1980*, vol. 143, Lecture notes in physics, ed. by G. Gräff, E. Klempt, G. Werth (Springer, Berlin, 1981), p. 277
- 34. H. Backe, A zepto-second atomic clock for nuclear contact time measurements at superheavy collision systems. In: *Proceedings of the Symposium Advances in Nuclear Physics in Our Time*, Goa, India, 28 Nov– 2 Dec 2010, to be published
- M. Rhein, R. Barth, E. Ditzel, H. Feldmeier, E. Kankeleit, V. Lips, Ch. Müntz, W. Noerenberg,
 H. Oeschler, A. Piechaczek, W. Polai, I. Schall, Phys. Rev. Lett. 69, 1340–1343 (1992)
- C. Golabek, S. Heinz, W. Mittig, F. Rejmund, A.C.C. Villari, S. Bhattacharyva, D. Boilley,
 G. De France, A. Drouart, L. Gaudefroy, L. Giot, V. Maslov, M. Morjean, G. Mukherjee,
 Yu. Penionzkevich, P. Roussel-Chomaz, C. Stodel, Eur. Phys. J. A 43, 251–259 (2010)

Superheavy Nuclear Molecules

Sophie Heinz

Abstract We investigated the formation of nuclear molecules and the occurrence of time delays in collisions of the superheavy system 64 Ni + 207 Pb ($Z_1 + Z_2 = 110$) and of the giant system 238 U + 238 U ($Z_1 + Z_2 = 184$). In Ni + Pb we observed clear signatures for the formation of long-lived molecule-like nuclear systems which rotate by large angles of 180°. The results from U + U collisions revealed striking similarities to the ones from Ni + Pb showing that significant time delays must occur also in the heaviest accessible systems. The experiments were performed at the velocity filter SHIP at GSI and at the VAMOS spectrometer at GANIL.

1 Introduction

The formation of molecule-like nuclear systems in heavy ion collisions is an interesting phenomenon from different points of view. On one hand, nuclear MOlecules (MOs) are regarded by some theoretical models as first step of fusion and quasifission reactions. Therefore, the understanding of MO formation and properties is important for understanding the proceeding of these reactions and, therewith, for a successful application of fusion and quasi-fission reactions for the synthesis of new exotic nuclei like, e.g., superheavy elements. On the other hand, MOs can serve as a "laboratory" to study physics phenomena in very strong electric fields. An example is the predicted emission of spontaneous positrons in the field of nuclear systems with a total proton number $Z \geq 173$.

According to theoretical models, a nuclear molecule is formed after mutual capture of projectile and target nucleus due to the nuclear force and trapped for some time in a minimum ("pocket") of the nucleus-nucleus potential. During this time, a large amount of nucleons can be exchanged and kinetic energy is dissipated. The evolution of the MO can either result in reseparation after nucleon exchange (quasi-fission) or in complete fusion with formation of a compound nucleus. Due

to their short lifetimes, which are typically on the order of $(10^{-21}-10^{-19})$ s, MOs are not directly accessible in experiments. Information about their formation and evolution can only be obtained indirectly by studying exit channel characteristics like mass, charge, angular and energy distributions of deep inelastic binary reaction products.

First signatures of MO formation were observed in 1960 in collisions of ${}^{12}C + {}^{12}C$ at energies around the Coulomb barrier [2]. Resonances in the scattering excitation functions revealed a fine structure which was interpreted as due to "formation of high-spin quasi-molecular states with $\tau \sim 10^{-21} \, \mathrm{s}$ [2]. First theoretical works on the understanding and description of MOs followed 10 years later [10]. Around the same time, MO formation was indicated also in experiments with heavy systems. In one of the earliest experiments, 40 Ar + 232 Th ($Z_1 + Z_2 = 108$) [1], the energy spectra of transfer products revealed for certain scattering angles two well separated maxima. While the maximum at higher energy originated from elastic and quasi-elastic scattering events, the maximum at lower energy was interpreted by Wilczynski as due to "nuclear orbiting" [13]. The latter means that both nuclei stick together for some time and rotate about their centre of gravity. During this time energy is dissipated which leads to the observed second maximum at lower energy. From this observation, Wilczynski anticipated the possible existence of nuclear molecules: "The idea of nuclear orbiting in collisions with angular momenta near to the critical value implies another interesting effect which eventually could be found experimentally. If some of the colliding systems survive more than half of a revolution, ... such a phenomenon would strongly indicate the existence of nuclear molecules rotating in the dynamical force equilibrium" [13].

In the following decades, nuclear orbiting was observed in many further experiments and various collision systems but MOs which performed "half of a revolution" like predicted by Wilczynski were not revealed. Only recently we observed at the velocity filter SHIP at GSI structures in the velocity spectra of heavy target-like quasi-fission products from 64 Ni + 207 Pb ($Z_1 + Z_2 = 110$) collisions which can consistently be explained as signatures of MOs rotating by angles of 180° [3].

Another interesting question concerns the limits of possible MO formation with respect to the total nuclear charge of the system. With increasing $Z_1 + Z_2$ the Coulomb repulsion increases, the potential pocket becomes gradually flatter and the corresponding quasi-fission barrier decreases until it is so small that trapping, and thus MO formation, is no longer possible. Different theoretical models arrive at very different conclusions concerning the region of $Z_1 + Z_2$ where trapping can still occur. Calculations in the two-centre shell model with adiabatic potentials result in a noticeable time delay even in the heaviest systems like U + U while the two-centre shell model with diabatic potentials obtains no time delay and only direct reactions. From experimental side there are only few data existing on the heaviest systems. Therefore some years ago we investigated binary reactions in U + U at the VAMOS spectrometer (GANIL) and observed the so far clearest signatures for the occurrence of significant time delays even in such giant systems.

2 Observation of MO Formation in Collisions of 64 Ni + 207 Pb

At the velocity filter SHIP we investigated deep inelastic transfer reactions in the system $^{64}\text{Ni} + ^{207}\text{Pb}$ at beam energies around the Coulomb barrier. In these experiments we used SHIP to separate the target-like reaction products from background events. The particles which passed SHIP were implanted in a position sensitive silicon detector in the focal plane where they were identified by their α -decay properties. Velocity spectra were measured by scanning stepwise the electric and magnetic field values of SHIP which determine the velocity at which a particle can pass the filter. The velocity of a reaction product at fixed detection angle [(in the case of SHIP $(0\pm2^\circ)$] is a very sensitive probe for the reaction process (e.g. fusion, transfer, etc.) in which a nucleus has been created. A detailed description of the method and results can be found in [4].

A large region of α -emitters was populated in this experiment where we identified nuclei with $84 \le Z \le 89$. The velocity spectra were measured in the range (0.15-2.0) times the expected compound nucleus velocity $v_{\rm CN}$ (the accepted velocity window at a certain setting is $\Delta v/v = 0.1$ (FWHM)). In Fig. 1, the velocity spectra of the selected isotopes 212m At, 213 Rn, 213 Fr and 215 Ra (Z=85-88) measured at 5.92 MeV/u are shown. The velocities are normalized to $v_{\rm CN}$. The spectra revealed an unexpected double peak structure consisting of a pronounced maximum at velocities $v > 1.6 v_{\rm CN}$ and a small peak at $v < 0.4 v_{\rm CN}$ where the low-velocity peak becomes more pronounced with increasing proton number of the target-like

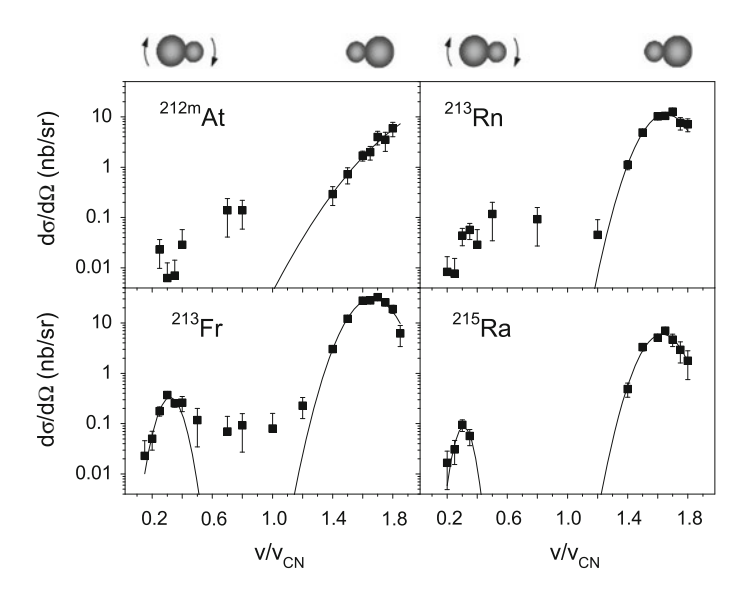


Fig. 1 Velocity spectra of the reaction products 212m At, 213 Rn, 213 Fr and 215 Ra measured at SHIP in reactions of 64 Ni+ 207 Pb at 5.92 MeV/u. The velocities are given in units of the compound nucleus velocity $v_{\rm CN}$

reaction product. For each isotope the two peaks are located symmetrically with respect to the compound nucleus velocity $v/v_{\rm CN}=1.0$.

On a first glance the observations would suggest complete fusion reactions with successive, very asymmetric fission of the excited compound nucleus (²⁷¹Ds) as origin of the isotopes. Due to the restricted acceptance angle of $(0\pm2^{\circ})$, only those fragments can enter the velocity filter which are emitted in beam direction. If the heavy fission fragment (At, Rn, etc.) is emitted into 0° with velocity v' in the centre-of-mass, its velocity in the laboratory system is $v = v' + v_{\rm CN}$. The centre-of-mass velocity v' is determined by the Coulomb barrier of the two fission fragments at the scission point (Viola energy). If the heavy fission fragment is emitted in backward direction in the centre-of-mass, it is still emitted in forward direction in the laboratory system but with a reduced velocity $v = -v' + v_{CN}$. The observed peak positions would be in accordance with the velocities expected for the heavy fragments after compound nucleus fission. However, a closer look to the data reveals that compound nucleus fission as origin of the observed nuclei is unlikely. Fusion-fission fragments are emitted isotropically in the centre-of-mass. Therefore one would expect the same intensity for the low- and high-velocity peak after efficiency corrections. But the yields of the low-velocity peaks are after corrections still about one order of magnitude lower than the yields of the high-velocity peaks. With increasing proton number of the detected reaction product, the yield of the low-velocity peak increases relative to the respective high-velocity peak. This indicates that the nuclei were rather produced in nonisotropic decays of an intermediate nuclear system than in compound nucleus fission. Also the measured cross-sections are more than three orders of magnitude larger than expected from compound nucleus fission. In addition, the measured isotopic distributions of the reaction products [4] cannot be explained with fusion-fission reactions but are typical for deep inelastic transfer or quasi-fission products, respectively.

The total of the observations can best be explained by assuming the formation of a molecule-like rotating nuclear system which decays before compound nucleus formation as will be shown in the following. If MO formation with successive quasifission is the origin of the observed isotopes, the high-velocity peak would result from quasi-fission after central collisions where the light projectile-like nucleus is emitted in backward direction and the target-like nucleus in beam direction, leading to a peak at $v = v' + v_{\rm CN}$. If the MO has angular momentum, it can rotate about its centre of gravity and if it is long-lived enough a rotation by 180° leads again to an alignment parallel to the beam axis where, however, projectile and target nucleus have changed their positions like indicated by the small drawings on top of Fig. 1. Therefore, if the reseparation occurs in this orientation, the projectile-like nucleus will be emitted in forward direction and the target-like nucleus in backward direction in the centre-of-mass. In the laboratory frame, the target-like nucleus is emitted in beam direction with a velocity $v = -v' + v_{\rm CN}$. Reaction products from other rotation angles are not accepted by SHIP.

The position of the velocity peaks is directly correlated with the kinetic energy of the corresponding target-like transfer product and can be used to calculate the total kinetic energy (TKE) in the exit channel by assuming a binary reaction process. The TKE values (in the centre-of-mass) obtained in this way are shown in Fig. 2 as a

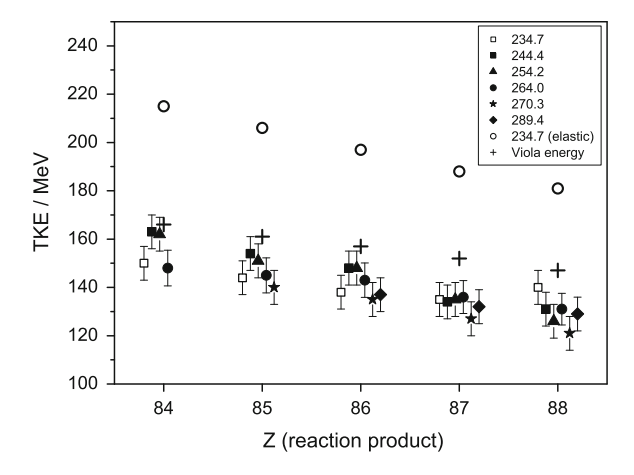


Fig. 2 Measured total kinetic energy (TKE) as a function of the proton number Z of transfer products created in reactions of 64 Ni $+^{207}$ Pb at beam energies of 4.80, 5.00, 5.20, 5.40, 5.53 and 5.92 MeV/u. The beam energies in the centre-of-mass are given in the inset. The data points for a fixed Z but for different beam energies are plotted with an offset for better discrimination. The energies expected from the Viola systematics are represented by the *crosses*. The *open circles* denote the TKE values expected from elastic kinematics at the lowest beam energy

function of the proton number Z of the target-like reaction product for the six investigated beam energies from 4.80 to 5.92 MeV/u. For all reactions leading to nuclei with $Z \geq 84$ the TKE values are located at or below the Viola energy for fission fragments from an equilibrated compound nucleus and they are independent of the bombarding energy. These are typical signatures for the formation of a compound system in a deep inelastic reaction where the exit channel nuclei reseparate with their Coulomb barrier energy. The low TKE values which decrease continuously with increasing number of transferred protons or nucleons, respectively, indicate also a considerable deformation of the fragments before reseparation. From the internuclear distance which can be determined from TKE, we deduced quadrupole deformations of $\beta_2 \approx 0.4$.

The deep inelastic nature of the reactions is also reflected by the behavior of the total kinetic energy loss (TKEL) which is given by $TKEL = E_{\rm cm} - TKE$. TKEL (normalized to $E_{\rm cm}$) is shown in Fig. 3(left) as a function of the number of transferred nucleons dA for the beam energy of 5.92 MeV/u. Here, dA is the number of transferred nucleons which lead to the expected primary transfer products with Z = 84 - 88 [4]. The slope of the curve reveals that a saturation value of about $0.5E_{\rm cm}$ is reached for a net transfer of 10 or more nucleons. This is typical for deep inelastic reactions where all kinetic energy above the barrier was transformed into excitation. Towards smaller values of dA a decrease of TKEL is indicated, meaning that the quasi-elastic region is entered for few nucleon transfer.

Assuming the scenario of rotating MOs, the ratio of the yields (i.e. decays), N_2/N_1 , in the low- and high-velocity peak must reflect the mean lifetimes of the MOs. From this, we calculated the lifetimes according to the decay law $dN/dt = -\lambda N$, where

228 S. Heinz

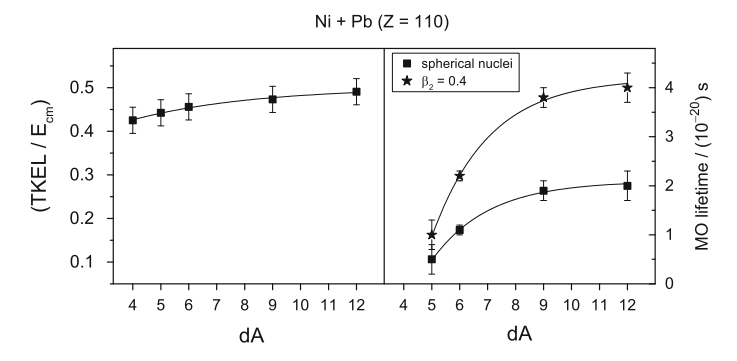


Fig. 3 Left Total kinetic energy loss (TKEL) for transfer reactions in 64 Ni + 207 Pb at 5.92 MeV/u as a function of the number of transferred nucleons dA. TKEL is normalized to the centre-of-mass energy $E_{\rm cm}$. Right Experimentally deduced lifetimes of nuclear molecules formed in collisions of Ni + Pb at 5.92 MeV/u as a function of the number of transferred nucleons

 λ is the decay constant of the MO. The lifetime $\tau = 1/\lambda$ is then obtained with $N_2/N_1 = \exp(-\lambda \Delta T)$ where ΔT is the time needed by the MO to perform a rotation by 180°. The value of ΔT is a function of the MO angular momentum and moment of inertia. For the critical angular momentum of MO formation in Ni + Pb we deduced a value of 50 \hbar from our own measurements and the experiment described in [12]. For the calculation of the lifetimes we used the corresponding average angular momentum $\langle L \rangle = 34 \,\hbar$. Concerning the moment of inertia, we regarded two limit cases. In one case we assumed spherical nuclei in the MO and in the other case deformed nuclei with $\beta_2 = 0.4$ like deduced from the TKE values. In the latter case, the moment of inertia is about two times larger. The lifetimes obtained for the two limit cases are shown in Fig. 3(right) as a function of the number of transferred nucleons. The data indicate that the lifetimes approach a limit value for the transfer of more than about 10 nucleons. This is very similar to the behavior of the TKEL values (Fig. 3, left). A possible, but still speculative, explanation for the saturation might be that the MO approaches the properties of a compound nucleus, meaning that the system reaches thermal equilibrium and the nucleons move without friction like in a "normal" mononucleus. However, more data on similar systems are needed to confirm this saturation before drawing final conclusions.

3 Time Delay in Reactions of ²³⁸U+²³⁸U

In 2006 we investigated binary reactions in collisions of $^{238}\text{U}+^{238}\text{U}$ at the VAMOS spectrometer at GANIL where we measured excitation functions of deep inelastic transfer products at five different beam energies between 6.09 and 7.35 MeV/u. The reaction products were detected at angles of $(35\pm5^\circ)$. For the identification of the reaction products we determined their mass by measuring time-of-flight and energy.

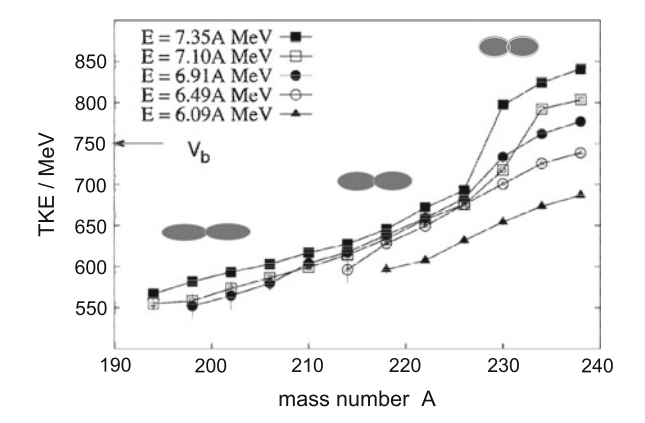


Fig. 4 Total kinetic energy (TKE) of binary reaction products from collisions of $^{238}\text{U}+^{238}\text{U}$ at beam energies of 6.09, 6.48, 6.91, 7.10 and 7.35 MeV/u. TKE is shown as a function of the mass number *A* of the detected reaction product. The drawings sketch the increasing deformation of the composite system U + U with increasing nucleon transfer

With this, a mass resolution of four units was obtained for nuclei in the region of uranium. A detailed description of the experimental method and results can be found in [5].

The mass spectra revealed a massive transfer of nucleons even at the lowest beam energies leading to transfer products with masses down to A = 190 which corresponds to a transfer of 50 nucleons (nuclei heavier than uranium were not observed). The most surprising and new result was revealed by the TKE of the reaction products which was calculated from the kinetic energy of the detected transfer product by assuming a binary reaction. TKE as a function of the mass number A of the detected transfer product is shown in Fig. 4. Two regions can be distinguished. For reaction products with 225 < A < 238, TKE is strongly beam energy dependent like expected for elastic and quasi-elastic reactions. However, for A < 225, TKE becomes within error bars independent of the beam energy. This is a typical signature of deep inelastic transfer reactions which is known since long time and was also revealed by the Ni + Pb reactions discussed in the previous section. In this experiment it was for the first time observed in such a giant system like U + U. The decrease of TKE with decreasing A indicates that the deformation of the compound system U + U becomes larger with increasing number of transferred nucleons. For reaction products with A < 225 we observed quadrupole deformations of 0.3 $< \beta_2 < 0.6$. β_2 -values of the order of 0.6 correspond usually to superdeformed nuclei with axis rations of 2:1 and are typical for the formation of two fragments from a fissioning compound nucleus. In comparison, in the quasi-elastic region (A > 225) we observed very similar deformation than for uranium ($\beta_2 = 0.27$).

So far, the results from U + U look very similar to the ones discussed for the system Ni + Pb in the previous section. The extrapolated Viola energy for the fission of a hypothetical compound system U + U leading to the observed reaction products

S. Heinz

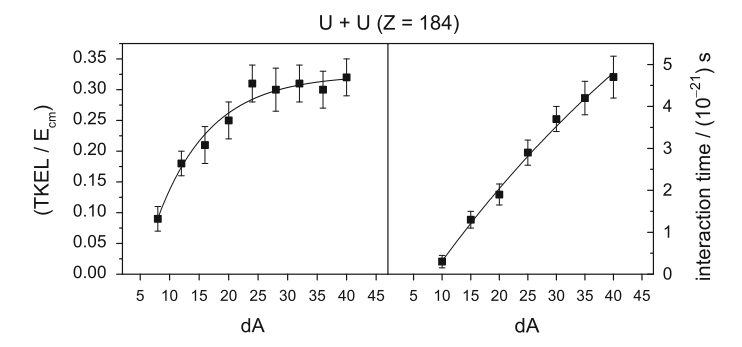


Fig. 5 Left Total kinetic energy loss (TKEL) for transfer reactions in 238 U + 238 U at 7.35 MeV/u as a function of the number of transferred nucleons dA. TKEL is normalized to the centre-of-mass energy $E_{\rm cm}$. Right Nuclear interaction times in collisions of U + U as a function of the number of transferred nucleons

is between 510 and 520 MeV. This means, that the observed TKE values are at least still 50 MeV higher than the expected Viola energy. However, the application of the Viola formula for U + U must rather be considered as a rough extrapolation because this system is far outside the range of nuclei where the empirical Viola formula has been established (for U + U the parameter $Z^2/A^{1/3} = 4336$ while the formula was deduced for compound nuclei with $Z^2/A^{1/3} < 2000$).

TKEL as a function of the number of transferred nucleons is shown in Fig. 5(left) for the beam energy 7.35 MeV/u. After a steep increase of TKEL for few-nucleon transfer, the curve approaches a saturation value for the transfer of about 30 or more nucleons which reveals the deep inelastic nature of the reactions. The overall slope of the curve is very similar to the one observed in collisions of Ni + Pb, see Fig. 3(left). It is also noteworthy that in Ni + Pb as well as U + U the saturation is reached after a net transfer of about 5 % of the total number of nucleons $(A_1 + A_2)$ in the respective system. The energy dissipation relative to the centre-of-mass energy is in Ni + Pb collisions 1.8 times larger than in collisions of U + U (TKEL depends on the beam energy and collision system; see, e.g., [11]).

The binary reaction products from U + U collisions reveal all features of deep inelastic transfer or quasi-fission reactions but the data do not allow to conclude if also trapping and MO formation occurred (full energy dissipation can also take place in deep inelastic scattering without MO formation). Nevertheless, the data indicate that significant time delays must occur in this system. Since the measured mass spectra of binary reaction products are typical for a diffusion process, we applied the diffusion model [8] to derive values for the time delay. According to this model, the interaction time τ increases linearly with the variance σ_A^2 of the mass distribution according to $\sigma_A^2 = 2D_A\tau$. The coefficient D_A is the mass diffusion coefficient which is $6.0 \times 10^{22} \, \mathrm{s}^{-1}$ for U + U at 7.5 MeV/u [9]. The experimentally deduced delay times are shown in Fig. 5(right) as a function of the net mass transfer dA (dA is also here related to the expected primary transfer products).

In total, the interaction times deduced for U+U are about one order of magnitude shorter than in Ni + Pb. One can notice that the interaction time increases with the number of transferred nucleons in the displayed region of dA (for dA > 40 the yield of transfer products was already too low to deduce reliable values for the interaction times). Around dA = 40 a slight tendency towards a flatter slope is indicated but no saturation is visible like in the system Ni + Pb (see for comparison Fig. 3, right). This might indicate that the system U+U does not approach equilibrium in a comparable measure as does the system Ni + Pb. From this one could deduce that the Coulomb repulsion in U+U is already so large that no MO formation can take place anymore. However, for a final answer, further experimental investigations of U+U, in particular at very low beam energies ($<6.5\,\text{MeV/u}$) and at further scattering angles are necessary.

Finally one has to note that the experimentally deduced interaction times are in good agreement with the values calculated in the two-centre shell model with adiabatic potentials where time delays of about 7×10^{-21} s were obtained for binary reactions of U+U with one Pb-like nucleus in the exit channel (corresponding to dA = 30) and correlated with an energy dissipation of more than 200 MeV [14].

4 Summary and Outlook

Our experiments on deep inelastic binary reactions in 64 Ni + 207 Pb revealed the formation of long-lived nuclear molecules which rotate by large angles of 180° . Lifetimes of up to 5×10^{-20} s were deduced for these systems from the experimental data. This well confirms theoretical models which assume the formation and trapping of a molecule-like nuclear system as first step of fusion and quasi-fission reactions in heavy systems. In addition, we studied binary reactions and the possible formation of nuclear molecules in the giant system 238 U + 238 U. Our data revealed all typical signatures for deep inelastic transfer reactions in U + U but no clear indication for MO formation. Nevertheless, a significant time delay of up to 5×10^{-21} s is revealed in collisions of U + U.

This opens two interesting applications for reactions in the heaviest systems. One is the search for spontaneous positron emission in supercritical electric fields of nuclei or nuclear systems with $Z \geq 173$ which was predicted many years ago [6, 7] but was not observed experimentally so far. The electric fields which appear in collisions of nuclear systems like U+U would be sufficiently high to allow this decay. The mean decay time for spontaneous positron emission is 10^{-19} s but delay times of 5×10^{-21} s would already enable the observation of the related monoenergetic positron line. For the observation of the line, binary reactions which lead to the longest lifetimes could be used as a trigger.

The other interesting application is the possible synthesis of new neutron-rich nuclei in the superheavy element region in deep inelastic transfer reactions with heaviest available projectile and target nuclei. Such isotopes cannot be accessed in fusion reactions due to the lack of sufficiently neutron-rich projectile and target

S. Heinz

nuclei. The application of deep inelastic transfer reactions in systems like U+U or U+Cm was suggested on basis of theoretical calculations [15]. An important point in these calculations is the occurrence of shell effects which would lead to a preferred emission of Pb-like transfer products, leading in turn also to an enhanced production of the complementary heavier transfer product which would be Z=102 for the system U+U. Shell effects have so far not been revealed by our or other experiments on collisions of the heaviest systems but are well known from the decay of lighter systems or nuclei, respectively. Therefore, the search for shell effects is a major goal of our next experiments on U+U.

References

- A.G. Artukh, G.F. Gridnev, V.L. Mikheev, V.V. Volkov, J. Wilczynski, Nucl. Phys. A 215, 91 (1973)
- 2. D.A. Bromley, J.A. Kuehner, E. Almqvist, Phys. Rev. Lett. 4, 356 (1960)
- V. Comas, S. Heinz, S. Hofmann, D. Ackermann, J. Heredia, F.P. Heßberger, J. Khuyagbaatar, B. Kindler, B. Lommel, R. Mann, Eur. Phys. J. A 48, 180 (2012)
- V. Comas, S. Heinz, S. Hofmann, D. Ackermann, J. Heredia, F.P. Heßberger, J. Khuyagbaatar, B. Kindler, B. Lommel, R. Mann, Eur. Phys. J. A 49, 112 (2013)
- C. Golabek, S. Heinz, W. Mittig, F. Rejmund, A.C.C. Villari, S. Bhattacharyva, D. Boilley, G. De France, A. Drouart, L. Gaudefroy et al., Eur. Phys. J. A 43, 251 (2010)
- 6. W. Greiner (ed.), Quantum Electrodynamics of Strong Fields (Plenum Press, New York, 1983)
- 7. J. Reinhardt, U. Müller, B. Müller, W. Greiner, Z. Phys. A **303**, 173 (1981)
- 8. C. Riedel, G. Wolschin, W. Nörenberg, Z. Phys. A **290**, 47 (1979)
- 9. C. Riedel, W. Nörenberg, Z. Phys. A 290, 385 (1979)
- 10. W. Scheid, W. Greiner, R. Lemmer, Phys. Rev. Lett. 25, 176 (1970)
- 11. W.U. Schröder, J.R. Huizenga, Annu. Rev. Nucl. Sci. 27, 465 (1977)
- 12. J. Töke, R. Bock, G.X. Dai, A. Gobbi, S. Gralla, K.D. Hildenbrand, J. Kuzminski, W.F.J. Müller, A. Olmi, H. Stelzer et al., Nucl. Phys. A **440**, 327 (1985)
- 13. J. Wilczynski, Phys. Lett. B 47, 484 (1973)
- 14. V. Zagrebaev, W. Greiner, J. Phys. G 31, 825 (2005)
- 15. V. Zagrebaev, W. Greiner, J. Phys. G 34, 825 (2007)

Part VI Astrophysics and Relativity

Compact Stars—How Exotic Can They Be?

S. Schramm, V. Dexheimer, R. Negreiros, J. Steinheimer and T. Schürhoff

Abstract Strong interaction physics under extreme conditions of high temperature and/or density is of central interest in modern nuclear physics for experimentalists and theorists alike. In order to investigate such systems, model approaches that include hadrons and quarks in a unified approach, will be discussed. Special attention will be given to high-density matter as it occurs in neutron stars. Given the current observational limits for neutron star masses, the properties of hyperonic and hybrid stars will be determined. In this context especially the question of the extent, to which exotic particles like hyperons and quarks affect star masses, will be discussed.

1 Introduction

Currently, the only way to investigate the properties of extremely dense and relatively cold strongly interacting matter is the study of the properties of neutron stars, or more general, compact stars. Depending on the equation of state, the central density of such an object might reach or even exceed the value of ten times the ground state density of nuclear matter. In this sense, neutron star physics complements the efforts by many ultra-relativistic heavy-ion experiments to create a hot fireball in the collision, which, depending on the collision energy, contain varying amounts of net baryonic density. Both of these areas can be comprised as investigation of strong interaction physics for hot and/or dense systems. In order to connect and relate results from the different regimes of density and temperature, models that can realistically describe all those conditions have to be developed and studied. In particular, this includes a quantitatively reasonable description of ground state nuclear matter and finite nuclei, as well as the correct asymptotic states at large values of temperature and density, i. e. quarks and gluons. Such an approach has been developed and refined over the recent years. In this article we will study some general observations within

S. Schramm (🖾) · V. Dexheimer · R. Negreiros · J. Steinheimer · T. Schürhoff FIAS, Johann Wolfgang Goethe-Universität, Ruth-Moufang-Str. 1, 60438 Frankfurt am Main, Germany

S. Schramm et al.

this theoretical approach related to the possibility of exotic matter in a neutron star, including hyperons, kaon condensates and quarks.

A main problem of extracting the equation of state of very dense matter via the study of neutron stars is that this matter is in the core of the star and, thus, not directly detectable (with the exception of neutrinos that can leave the star without secondary interactions). For theoretical modeling one therefore has to compare model results with the observational data available, including star masses, radii, temperature/cooling behavior, and rotational periods. Here, there are still relatively few data that can be used for cooling studies and the radii are very difficult to pin down to an accuracy of about 1 km or less. As a consequence, the main input for modeling is still the mass of the star. This is especially true, due to the recent accurate measurements of two heavy neutron stars PSR J1614-2230 of $M=1.97\pm0.04\,M_\odot$ [1] and PSR J0348-0432 with a value of $M=2.01\pm0.04\,M_\odot$ [2]. These high values point to a stiff equation of state at high densities. How to reconcile these numbers with theory will be discussed in the following.

2 The Hadronic Model

Within a simple (SU(2) isospin) description of a neutron star, the particles occurring in the cold star are neutrons, protons, and electrons. Studying the early, proto-neutron star phase, one also has to take into account neutrinos. As the new benchmark stellar masses are rather high, the best scenario is to have relatively few populated degrees of freedom inside of the star, as in this case filling up the energy levels of the particles leads to high fermi momenta, which in turn translates to high pressure and a stiff equation of state (EoS). Such a stiff EoS can support larger star masses against gravitational collapse than a soft EoS, therefore leading to larger maximum star masses. However, from the observation of many hypernuclei it is well established that at least the Lambda hyperon is bound in nuclear matter with a binding energy of about 30 MeV. There are indications of binding of Xi baryons in nuclear matter with a binding of around 20 MeV [3]. The situation of the Sigma hyperons is less clear, however, scattering and Sigma-atom data point to a repulsive potential of the Sigma [4]. Overall a realistic model for the description of dense (and hot) matter has to contain hyperons, i. e., should be constructed within a flavor-SU(3) scheme.

We have followed this path for a number of years, developing an effective chiral SU(3) hadronic model, in which the baryonic masses are largely generated by their coupling to scalar fields that attain a vacuum expectation value due to spontaneous symmetry breaking, analogously to simple chiral σ models.

The model is described in detail in various publications [7–9]. The key relations of the model are as follows. The effective baryon masses m_i^* read

$$m_i^* = g_{i\sigma}\sigma + g_{i\zeta}\zeta + g_{i\delta}\delta + \delta m_i. \tag{1}$$

The masses are generated by couplings to the scalar fields (σ, δ, ζ) whose expectation values are related to the scalar quark condensates, i.e. $\sigma \sim \langle \overline{u}u + \overline{d}d \rangle$, $\zeta \sim \langle \overline{s}s \rangle$, and $\delta \sim \langle \overline{u}u - \overline{d}d \rangle$. A mass term δm_i breaks chiral and SU(3) symmetry explicitly. The various couplings contained in the equation result from the SU(3) coupling scheme. Thus, the non-zero vacuum expectation values of σ and ζ generate the baryonic masses in the vacuum, while the change of the scalar fields at finite density or temperature is responsible for the scalar attraction. The other crucial relation defines the effective baryonic chemical potentials

$$\tilde{\mu}_i = \mu_i - g_{i\omega}\omega - g_{i\sigma}\rho - g_{i\phi}\phi, \tag{2}$$

where the different fields ω , ρ and ϕ are the analogous vector fields to the σ , δ , and ζ , respectively. The fields acquire non-zero mean fields in dense matter and, therefore, shift the effective chemical potentials of the particles. In the case of the isospin 0 fields ω and ϕ this leads to a reduction of the chemical potential, which corresponds to a repulsive interaction, whereas for the ρ the effect depends on the isospin of the baryon.

3 Results

With these preliminaries, we can address the topic of this article, the influence of exotic particles on the compact star solutions. Here, for the sake of simplicity, we will only consider static spherical stars, which can be solved straightforwardly by integrating the corresponding Tolman-Oppenheimer-Volkoff equations [10, 11]. Performing such a calculation for the purely hadronic case (and using the star-optimized coupling parameters) we obtain masses and radii of the stars as shown in the left panel of Fig. 1 [5]. The figure distinguishes the cases for a purely nucleonic star,

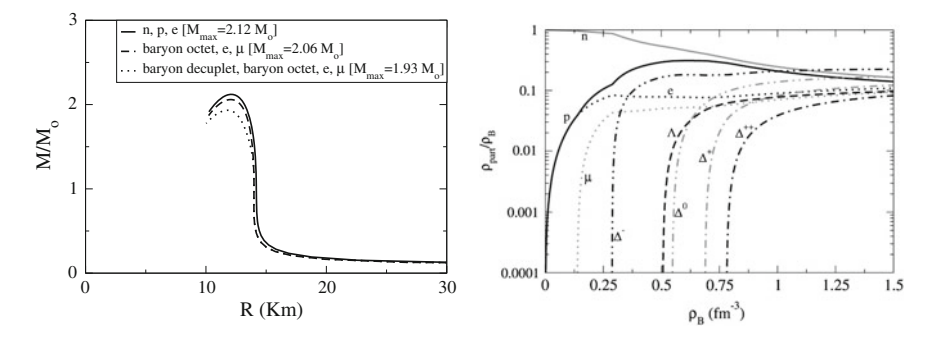


Fig. 1 Left Mass-radius diagram for compact stars in the chiral SU(3) model. The *curves* distinguish results for nucleonic particles only, nucleons and hyperons, and nucleons, hyperons, and Δ resonances, respectively. Right Normalized particle densities in the star including the Δ resonances. Δ 's largely replace hyperons inside the star [5]

S. Schramm et al.

a star with hyperons, i.e. a hyperstar, as well as solutions when in addition the baryon decuplet is included, which is synonymous to adding Δ baryons as the other states in the decuplet are too heavy to be populated. One can see that adding new degrees of freedom leads to a reduction of the maximum star mass, however, all scenarios are in good agreement with current observations. The right panel of Fig. 1 shows that the structure of a nucleonic star can be changed quite drastically by including Δ baryons. The fact that the hyperstar masses do not drop considerably compared to the nucleonic case originates from the fact that the model also includes the repulsive ϕ meson exchange between hyperons, which suppresses their densities.

In addition to adding strangeness to the system by including hyperons, a condensation of K^- mesons in very dense matter is in principle possible [12]. This results from the fact that a K^- consists of an anti-up quark and a strange quark. For the anti-quark the vector repulsion experienced by the baryons changes to a strong attraction. On the other hand the s quark in the meson does not couple strongly to the matter as long as there are not too many hyperons in the system, in sum leading to a strong attraction for the K^- in matter. There is a substantial amount of electrons (and some muons) in the star as the whole system has to be electrically neutral. In case the electron chemical potential becomes larger than the energy of a K^- at rest, the system will start to be neutralized by K^- instead of additional e^{-} . As the kaons are bosons, they can condense in the same zero-momentum state. This in turn leads to a strong reduction of the pressure of the system (no kinetic energy for the kaons), softening the equation of state considerably and therefore reducing star masses. However, a calculation of the effective kaon masses within the model shows that the condensation effect only shows up at densities of about $6 \rho_0$ and beyond, which are not reached in the center of the star within our model (Fig. 2) [6, 13]. Thus, kaon condensation does not affect the previously obtained results.

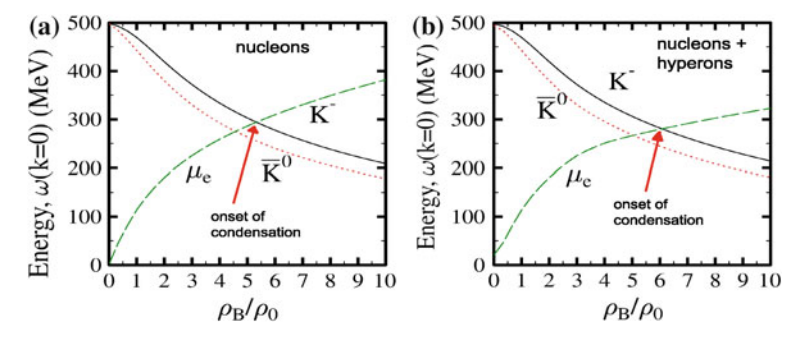


Fig. 2 Energy of K^- and \overline{K}^0 at rest as function of density. When the energy of the K^- drops below the electron chemical potential kaon condensation sets in. The *left panel* shows the result for nucleonic star matter, the *right panel* includes also hyperons [6]

4 The Effect of Quarks

At some unknown high density the system does not consist anymore of hadrons but of quarks. The main, unsolved question is when the transition to quark matter takes place. It is in principle quite possible that quarks only occur at densities larger than 6 to 10 times nuclear matter saturation density, which would imply that no neutron stars with a quark core, i. e. hybrid stars, would exist. In a simplified study we determine the general impact of a quark core. For that purpose we adopt a standard equation of state for the hadrons (G300 [14]) and a MIT bag model equation of state for the quarks. For the latter EoS we vary the bag constant [15, 16]. The results are shown in the left panel of Fig. 3. One can clearly see that the onset of the population of quarks, signaled by the sharp bend in the curves, leads either to reduced maximum masses of the stars or even to unstable solutions for the whole hybrid star branch. These calculations were done assuming non-interacting quarks in the quark core. Taking into account perturbative corrections due to the quark-quark interaction, the EoS of the quarks stiffens, stabilizing the hybrid star solutions (see Fig. 3, right panel). Changing the coupling constant to higher values stiffens the equation of state and the maximum star mass increases. The equations of state corresponding to these results can be seen in Fig. 4. In case that the first-order phase transition to quark matter generates a large jump in energy density, the masses of the compact stars are reduced. For a recent, even more schematic discussion of hybrid star properties assuming a simplified structure of the quark EoS, see [17].

A more realistic description of a quark phase can be obtained by coupling quarks to the system in a way very analogous to the PNJL model by introducing a Polyakov loop field Φ that describes the deconfinement phase transition [18, 19]. In this case, the quarks couple to the mean fields in the same form as the hadrons in Eqs. (1) and (2) with their own SU(3)-invariant coupling strengths, thus coupling hadrons and quarks in a unified description [20]. While the isospin-symmetric matter does not show any first-order phase transition at high densities (see [20]), star matter, i.e. charge neutral matter in β equilibrium, does. The latter transition is generated by

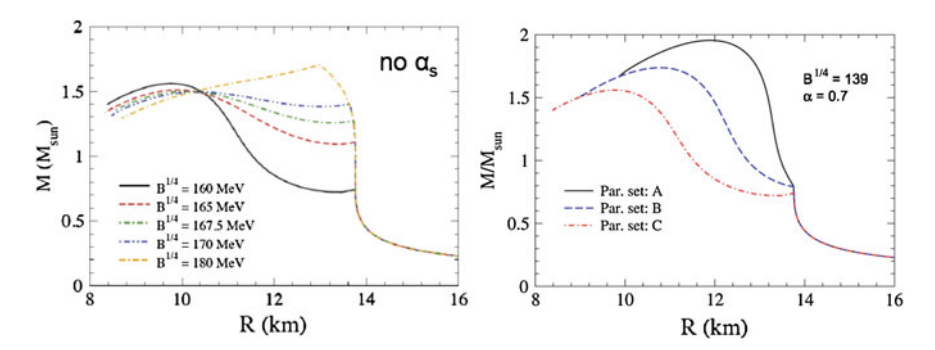


Fig. 3 *Left* Hybrid star mass-radius diagram for different choices of the vacuum pressure *B* are shown (compare Fig. 3). *Right* Similar calculation as on the *left*, including quark interactions

S. Schramm et al.

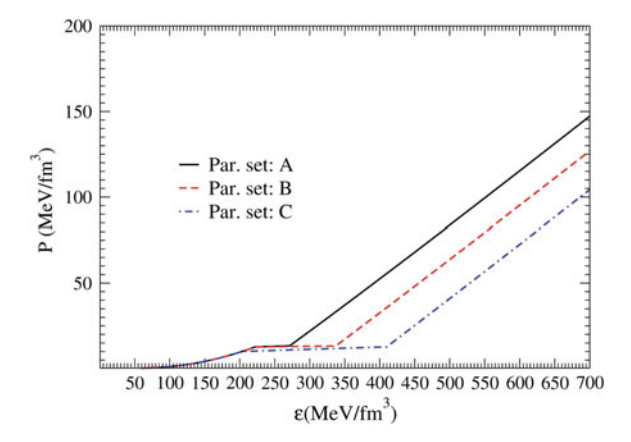
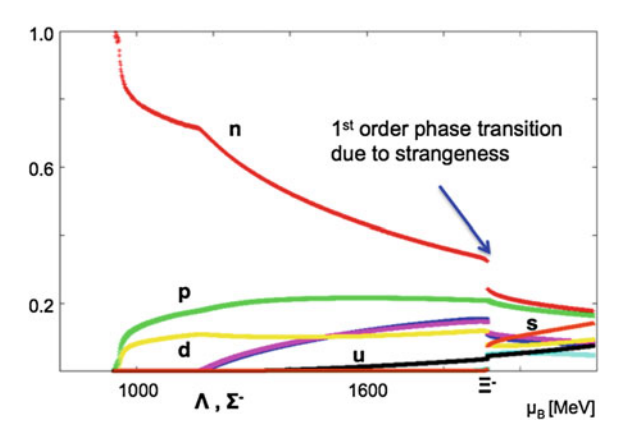


Fig. 4 Equation of state for hybrid star matter. Results for different bag pressures and interaction strengths are shown

Fig. 5 Baryon number densities of baryons and quarks inside of the hybrid star. Quarks already enter the system a long time before the first-order phase transition that leads to a jump in the s-quark densities



the strange quark sector and is therefore quite parameter-dependent and particularly sensitive to the coupling of the strange quark to the ϕ vector field. If one follows the baryon number densities contained in quark and hadron degrees of freedom, one can observe a very early onset of a mixed quark-hadron phase long before the first-order phase transition. The particle densities of star matter can be seen in Fig. 5. As the plot shows the baryon number densities, the corresponding quark densities have been multiplied by their baryon number 1/3. Here one can observe the jump of the strange quark density at the critical chemical potential. In Fig. 6 the mass-radius diagram for this approach can be seen with star masses of up to $\sim 2.2 M_{\odot}$. As in the previous schematic studies with the MIT bag model repulsive vector interactions in the quark sector have been used [21]. The results for different choices of the value are shown in the figure.

For very specific parameter choices of a strong vector coupling of the strange quark the mass-radius diagram shows a second family of stable compact stars with

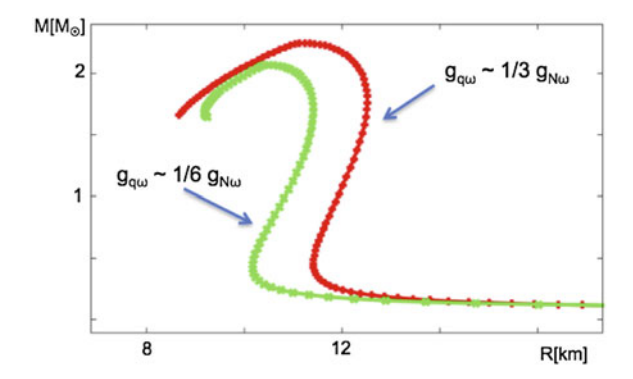
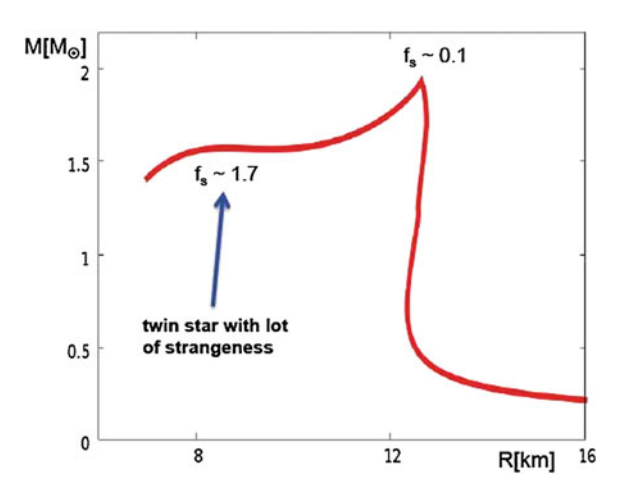


Fig. 6 Mass-radius diagram for compact stars within the quark-hadron (QH) model. The first-order transition causes a break for stable star solutions. *Two curves* for different choices of the quark vector-coupling are shown

Fig. 7 Mass-radius diagram for compact stars for specific fine-tuned parameters. A strangeness-rich stable twin-star solution appears



a large strangeness content of values of strange quarks per baryon number f_s larger than 1, and a distinctly smaller radius than the other stable branch, which also consists of hybrid stars albeit with very small strangeness content (Fig. 7).

Thus, the general solution for obtaining a sizable quark core in a hybrid stars seems to be to introduce a repulsive quark vector interaction that stiffens the quark equation of state. Note, however, that such an addition to models that contain quarks generates problems at the other end of the parameter space, i. e., at small chemical potential μ_B and high temperatures. In this case, lattice QCD simulations have determined the general behavior of the pressure of matter for small μ_B by calculating the Taylor coefficients for an expansion of the pressure in the chemical potential

$$P = P(\mu_q = 0, T) + c_2(T)\mu_q^2 T^2 + \cdots,$$
(3)

with the quark chemical potential $\mu_q = \mu_B/3$.

S. Schramm et al.

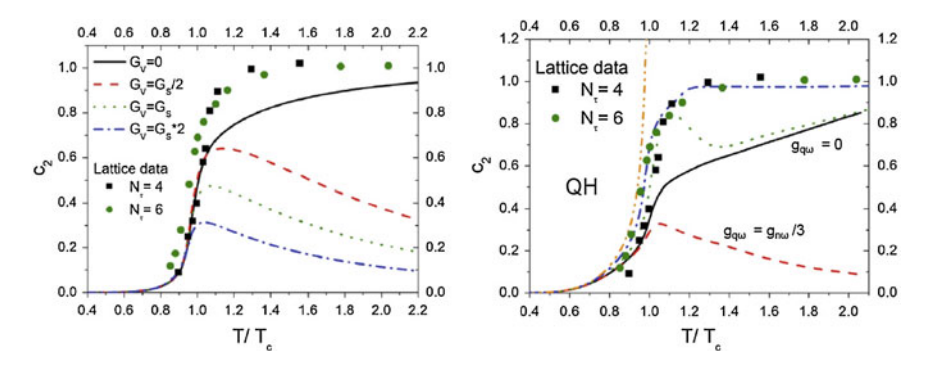


Fig. 8 Taylor coefficient c_2 of the expansion of the pressure in terms of chemical potential over temperature. Lattice QCD results are indicated by *circles* and *squares*. The *lines* show the results for different quark vector coupling. The *left panel* displays the results for the PNJL model, whereas the *right panel* contains the computed values for the quark-hadron model [22]

The panels in Fig. 8 shows the results for zero and finite quark-vector coupling for different model approaches. The results indicate that, independent of the specific model applied, the curves with a non-zero coupling strength deviate significantly from lattice data [23–25], far beyond any statistical or systematic error bars [22, 26]. Therefore, there is a currently unresolved problem with describing neutron stars that contain a sizable quark core and simultaneously achieving agreement with lattice data.

5 Conclusions

We have discussed compact star properties and the impact of exotic particles inside stars on the attainable maximum star masses. We have shown that in a reasonable flavor-SU(3) approach a 2-solar mass star, a so-called hyperstar, can be obtained, even when one includes effects of the Δ resonances. However, the amount of strangeness contained in the star through the population of hyperons is rather small. Considering a kaon condensate we have shown that the critical density for the onset of condensation in our model is too high to have any impact on star properties. If one extends the approach to consider quarks in the inner regions of the star (a hybrid star), we have demonstrated that a simple addition of a quark phase via a non-interacting MIT model leads to either strongly reduced masses or no stable hybrid star solutions at all. Interactions between the quarks that produce a stiffening of the equation of state can remedy this effect. In the generalized quark-hadron model, a heavy hybrid star of 2.2 solar masses is obtained without any phase mixing (as obtained in the usual Gibbs construction), as the quarks co-exist with hadrons without any first-order transition. A later phase transition is triggered by a large increase of the strange quark density. This value, however, is strongly parameter-dependent.

Finally we discussed the general problem with adopting a large quark-vector coupling in order to stiffen the quark equation of state and, in turn, obtain high-mass hybrid stars. Comparing results for small chemical potential with QCD lattice simulations shows a clear discrepancy generated by these interactions for very different model approaches. Thus, a consistent picture of a heavy hybrid star and agreement with lattice date is still elusive.

Acknowledgments We acknowledge the use of the CSC computer facilities at Frankfurt university for our work. T. Schürhoff is supported by the Nuclear Astrophysics Virtual Institute (NAVI).

References

- P.B. Demorest, T. Pennucci, S.M. Ransom, M.S.E. Roberts, J.W.T. Hessels, Nature 467, 1081 (2010)
- J. Antoniadis, P.C.C. Freire, N. Wex, T.M. Tauris, R.S. Lynch, M.H. van Kerkwijk, M. Kramer, C. Bassa et al., Science 340, 6131 (2013)
- 3. C.B. Dover, A. Gal, Ann. Phys. 146, 309 (1983)
- 4. T. Harada, Y. Hirabayashi, Nucl. Phys. A 759, 143 (2005)
- 5. V. Dexheimer, S. Schramm, Astrophys. J. 683, 943 (2008)
- 6. A. Mishra, A. Kumar, S. Sanyal, V. Dexheimer, S. Schramm, Eur. Phys. J. A 45, 169 (2010)
- P. Papazoglou, S. Schramm, J. Schaffner-Bielich, H. Stöcker, W. Greiner, Phys. Rev. C 57, 2576 (1998)
- 8. P. Papazoglou, D. Zschiesche, S. Schramm, J. Schaffner-Bielich, H. Stöcker, W. Greiner, Phys. Rev. C 59, 411 (1999)
- 9. S. Schramm, Phys. Rev. C 66, 064310 (2002)
- 10. R.C. Tolman, Phys. Rev. 55, 364 (1939)
- 11. J.R. Oppenheimer, G.M. Volkoff, Phys. Rev. 55, 374 (1939)
- 12. D.B. Kaplan, A.E. Nelson, Phys. Lett. B **175**, 57 (1986)
- 13. A. Mishra, S. Schramm, W. Greiner, Phys. Rev. C78, 024901 (2008)
- 14. N.K. Glendenning, Nucl. Phys. A 493, 521 (1989)
- 15. R.P. Negreiros, V. Dexheimer, S. Schramm, arXiv:1011.2233 [astro-ph.HE] (2010)
- 16. R. Negreiros, V.A. Dexheimer, S. Schramm, Phys. Rev. C 85, 035805 (2012)
- 17. M.G. Alford, S. Han, M. Prakash, Phys. Rev. D 88, 083013 (2013)
- 18. K. Fukushima, Phys. Lett. B **591**, 277 (2004)
- 19. C. Ratti, M.A. Thaler, W. Weise, Phys. Rev. D 73, 014019 (2006)
- 20. J. Steinheimer, S. Schramm, H. Stöcker, J. Phys. G 38, 035001 (2011)
- S. Schramm, V. Dexheimer, R. Negreiros, T. Schürhoff, J. Steinheimer, arXiv:1306.0989 [astro-ph.SR]
- 22. J. Steinheimer, S. Schramm, Phys. Lett. B 696, 257 (2011)
- 23. A. Bazavov et al. (HotQCD Collaboration), Phys. Rev. D **86**, 034509 (2012)
- M. Cheng, P. Hendge, C. Jung, F. Karsch, O. Kaczmarek, E. Laermann, R.D. Mawhinney, C. Miao et al., Phys. Rev. D 79, 074505 (2009)
- 25. S. Borsanyi, Z. Fodor, S.D. Katz, S. Krieg, C. Ratti, K. Szabo, JHEP 1201, 138 (2012)
- 26. P. Rau, J. Steinheimer, S. Schramm, H. Stöcker, arXiv:1308.4319 [hep-ph]

Observational Tests of the Pseudo-complex Theory of GR Using Black Hole Candidates

Thomas Boller and Andreas Müller

Abstract We have worked out astronomical tests of the pseudo-complex gravitational field theory (pc-GR) proposed by Hess and Greiner [1] going beyond our first paper on pc-GR tests [2]. Observational tests of the standard GR theory (standard-GR) and the pc-GR theory include (i) Galactic binaries, (ii) the Galactic Center, and (iii) supermassive black holes. For Galactic binaries with both relativistic Fe K line emission and OPO frequencies we have calculated the distances of both observational quantities to the central black hole. While the relativistic Fe K emission arises only within a few gravitational radii ($R_G = GM/c^2$) from the black hole with mass M, the QPO frequencies when related to Keplerian motions place their origin to much larger distances. This discrepancy is not understood so far. As very little has been done going beyond the phenomenological description of that problem, we applied the pseudo-complex theory to these Galactic black hole binaries and find that the Fe K and QPO emission is arising at quite similar radii from the black hole. While this is not any proof for the pc-GR, it is worth pointing out that both theories give different results. For the Galactic Center we show that the orbital frequencies of test particles are different in pc-GR and standard GR. In addition, we show that VLBI interferometry will result into the first direct image of the black hole in the GC and that ray-tracing images in both theories are different for the GC and can be used to probe standard GR and pc-GR. Finally, we argue that in supermassive black holes the OPO frequencies and the relativistic Fe K emission occur from the same physical origin. This further allows performing tests on pc-GR and standard GR from both observational quantities.

Max-Planck-Institut für extraterrestrische Physik, Giessenbachstrasse 1, Garching, Germany e-mail: bol@mpe.mpg.de

A Miiller

Excellence Cluster Universe, Boltzmannstrasse 2, Garching, Germany

T. Boller (⋈)

246 T. Boller and A. Müller

1 Introduction

GR theory has up to now withstood all experimental tests, (i) the spin down period in binary pulsars (Hulse-Taylor pulsar, e.g. [3]), (ii) the Shapiro delay, (iii) the deflection of light, and (iv) precession. Nevertheless, there are extreme situations in standard-GR, like the formation of a coordinate singularity at the Schwarzschild radius around black holes, which makes regions below the Schwarzschild radius not accessible for an external observer. In addition, the curvature diverges in standard-GR at the center of the black hole. This is illustrated in Fig. 1 with the Kretschmann scalar [4]. The Kretschmann scalar, one of several curvature invariants in standard-GR, shows how the curvature in the vicinity of the BH behaves. Far away from the black hole the spacetime is flat. If one approaches the black hole the spacetime curves strongly indicated by the hills and valleys. At r=0 the curvature diverges. This curvature singularity motivates the search for extensions of the standard-GR which prevent from such singularities where also physics breaks down.

The ansatz of the pc-GR theory was published by Hess and Greiner [1], which is that a pseudo-complex number X can be divided into a real part X_R and an imaginary part X_I with $I^2 = +1$. This results into a new Einstein equation and a metric tensor g_{00} and no coordinate singularity at r = 2m for a = 0 (see [6] and [2] for details). There is growing interest from galactic and extragalactic experts to perform tests going beyond standard-GR. Testing pc-GR is part of the Athena+ proposal for ESA's Large Mission program 2015–2030 [2, 7, 8]. The pc-GR is also part of the ALMA white paper for direct imaging of black holes (Section C05: Alternative theories of Gravity, Th. Boller, A. Müller, P. Hess, submitted to the ALMA consortium, 2013).

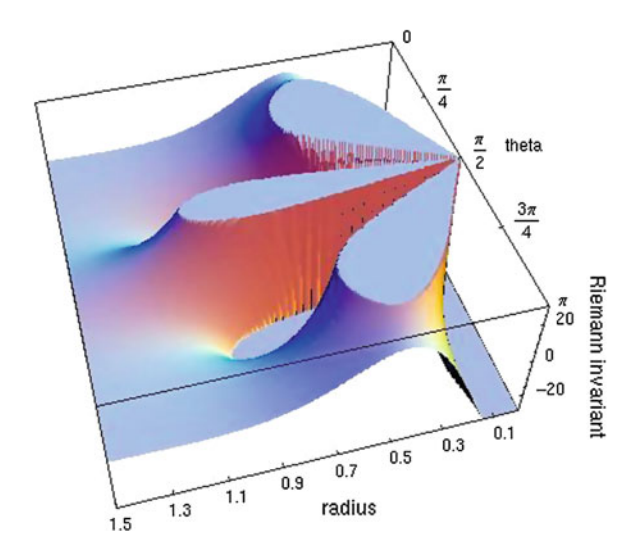


Fig. 1 Curvature as a function of radius and polodial angle ([4] based on [5])

Spin a	Mass (M_{sun})	QPO frequency (Hz)	Reference
0.92 ± 0.02	6.3 ± 0.5	126–446	Miller [10], Belloni [11]
0.5 ± 0.15	9.10 ± 0.61	134–284	Steiner [12], Belloni [11]
0.93 ± 0.01	>5.8	105–279	Reis [13], Miller [14],
			Hynes [15], Belloni [11]
0.52 ± 0.11	9.8 ± 0.9	115–443	Belloni[11]
	0.92 ± 0.02 0.5 ± 0.15 0.93 ± 0.01	$\begin{array}{c cccc} 0.92 \pm 0.02 & 6.3 \pm 0.5 \\ 0.5 \pm 0.15 & 9.10 \pm 0.61 \\ 0.93 \pm 0.01 & >5.8 \end{array}$	0.92 ± 0.02 6.3 ± 0.5 $126-446$ 0.5 ± 0.15 9.10 ± 0.61 $134-284$ 0.93 ± 0.01 >5.8 $105-279$

Table 1 Galactic Binaries with relativistic Fe K and OPO measurements

2 Tests on Galactic Binaries

2.1 The Sample

We searched the literature for Galactic Black hole binaries with both relativistic Fe K line emission, QPO measurements and dynamically constrained masses. Only a handful of objects were found to share these properties. They are listed in Table 1. The black hole spin is determined from fitting standard-GR to the relativistic Fe K line profile using relativistic disk line models (e.g. [9]). The black hole spin is determined under the assumption that the emission arises at the last marginally bound radius.

2.2 Deriving Fe K and QPO Emission Radii in Standard-GR

In the following we discuss each individual object and describe how the distances of the relativistic Fe K lines and the QPO distance have been determined. The distance of the relativistic Fe K emission is determined from fitting the line profile using standard-GR. It is assumed that the Fe K line emission arises from the last marginally stable orbit, an assumption which has been questioned in the literature (e.g. [16]).

The distance r(Fe K), the black hole mass M and the spin a are related by the relation $r(\text{Fe K}) = (\sqrt{M} + \sqrt{M \pm a})^2$. The measured (QPO) frequencies relate to the distance r(QPO) by applying a Kepler frequency $\Omega_K = (r^{3/2} - a)^{-1}$ [17]. The relativistic Fe K line fitting results in inner radii of about $2R_G$. The QPO frequencies, if associated with Keplerian, Vertical, and Radial motion, would place the QPOs at $10...50R_G$, and not within $2R_G$, as these systems are not thought to have truncated disks at high accretion rates. It is rather puzzling to have this discrepancy between QPO frequency and the inner radius. Very little has been done beyond phenomenological description and this is all speculative and there is no clear model to explain this. In the following we show the QPO frequencies as a function of the distance r to the black hole for pc-GR and standard-GR. The 68% confidence levels are indicated by the blue (standard-GR) and red (pc-GR) dashed areas.

248 T. Boller and A. Müller

2.2.1 GRO J1655-40

In Fig. 2 the QPO frequency as a function of black hole distance is shown for GRO J1655-40. In standard-GR the frequency is increasing with decreasing distance to the black hole, reaching infinity at the last stable orbit. In pc-GR a maximum value exists when a test particle is getting closer to the central black hole. At smaller distances the QPO frequency is decreasing, reaching zero at $4/3~R_G$. The QPO frequencies are higher for standard-GR compared to pc-GR. The 68 % confidence region for the Fe K emission line is marked with the vertical dashed lines. For GRO J1655-40, the Fe K emission region is between about 2.1 and 2.4 gravitational radii. In Fig. 3 we

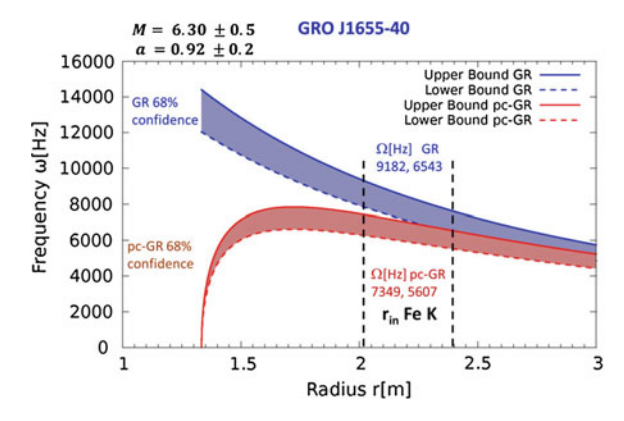


Fig. 2 Keplerian frequency as a function of distance (up to 3 gravitational radii) for GRO J1655-40 for standard GR (*blue dashed*) and pc-GR (*red dashed*)

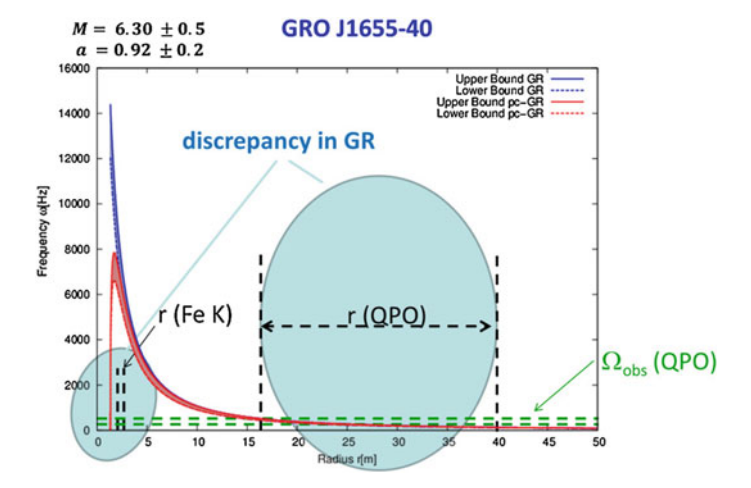


Fig. 3 Keplerian frequency as a function of distance (up to 50 gravitational radii) for GRO J1655-40 for standard GR (*blue dashed*) and pc-GR (*red dashed*)

show the QPO frequency-radius relation up to distances of 50 gravitational radii to illustrate the discrepancy of the Fe K and OPO emission regions.

While the Fe K emission arises from about 2 gravitational radii, the measured QPO frequencies translate into distances to the black hole between about 15 and $40 R_G$. This discrepancy is not yet understood.

2.2.2 XTE J1550-564, GX 339-4, XTE J1752-223

In Fig. 4 we show the corresponding plots for the remaining objects listed in Table 1. For all objects the emission regions of the Fe K line and the emission region of the QPO frequencies are not consistent in standard-GR. We do not argue that this suggests that standard-GR being not correct. We only show that under the assumptions for deriving the radii the emission regions in standard GR are different for the Fe K emission and the QPO region. However, as can be seen from Fig. 3, in pc-GR the radius of the Fe K emission appears consistent with the radius of the QPO emission region at distances below about 2 gravitational radii. In order to work that out in reliable detail, we have to fit the Fe K line profile with a relativistic pc-GR fitting routine, which is work in progress.

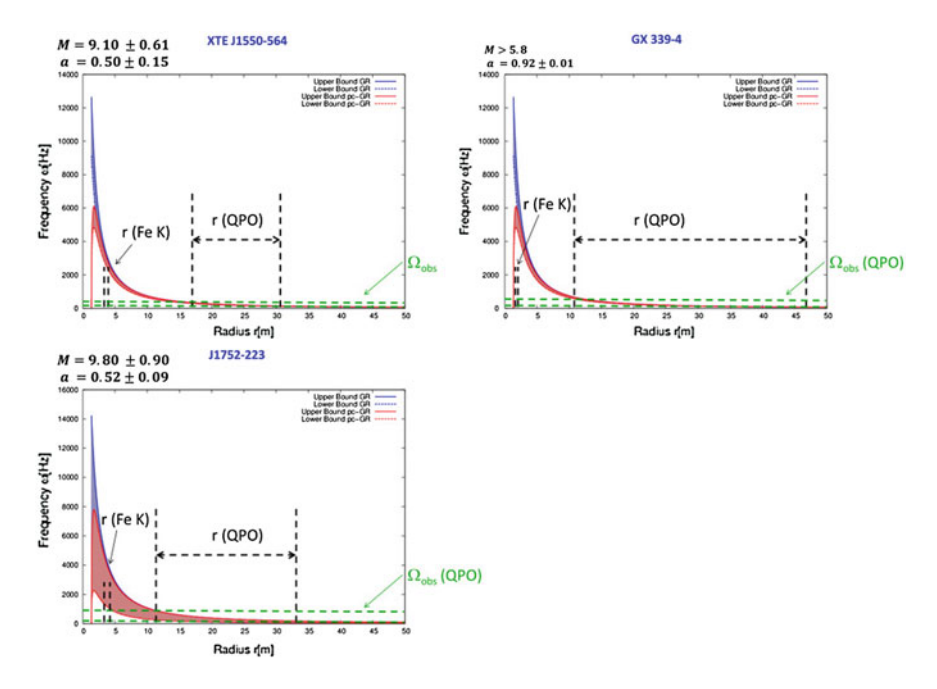


Fig. 4 Keplerian frequency as a function of the distance the Galactic black hole binaries XTE J1550-564, GX 339-4, and J1752-223 for standard GR (*blue dashed*) and pc-GR (*red dashed*). In standard-GR the Fe K emission line region is much closer to the black hole compared to the regions where the QPO frequencies arise

250 T. Boller and A. Müller

3 Tests on the Galactic Center

3.1 Timing and Spectral Parameters

NIR / X-ray spectroscopy and orbital motions from the infalling gas cloud [18] might provide additional tests for standard-GR and pc-GR. If parts of the gas cloud will approach distances smaller than about three gravitational radii and if observations will allow measuring the orbital frequencies via timing measurements and if relativistic Fe K line emission will become observable, then one can determine the radius of the Fe K line emission and the radius of the QPO emission. The test for standard-GR would be to measure the pair r(QPO) and r(Fe K) from the observations. If the radii are different within the errors, then one should apply pc-GR to measure r(QPO) and r(FeK). In pc-GR lower QPO frequencies (cf. [6]) are expected compared to standard-GR. In addition, the gravitational redshift is also reduced, resulting in different radii for the relativistic Fe K line compared to standard-GR. The infalling gas cloud provides a unique opportunity in this century to study accretion physics in the strong gravity regime. If a relativistic Fe K line is associated with the flare emission, from the line profile and the orbital frequency, we expect that both theories, GR and pc-GR, to be distinguished for the first time.

3.2 Ray-Tracing Images and VLBI Interferometry Observations

The first spatially resolved images of black holes will be observed within the next few years using the very long base-line interferometry technique at mm/sub-mm wavelength (mm-VLBI) in combination with the ALMA telescopes [19]. The microarcsec spatial resolution will allow obtaining images from the black hole in the Galactic Center and the gas emission from the innermost accretion processes. The same holds for the supermassive black hole in M87. These images are expected to provide new and crucial tests for the standard-GR and the pc-GR. As the gravitational redshift is different in both theories, the observed images can be compared with ray-tracing images. We have produced ray-tracing images for standard-GR and pc-GR [20]. With increasing spin a, the simulated images differ significantly due to the different gravitational redshifts. In Fig. 5 we show a simulated pc-GR black hole image and a simulated standard-GR image for a black hole spin of a = 0.9.

4 Test on Supermassive Black Holes

Relativistic Fe K emission and QPO frequencies are most probably associated in supermassive black holes. As an example we show in Fig. 6 the light curve of one of the most variable active galactic nuclei, IRAS 13224-3809 [21]. Persistent, rapid and

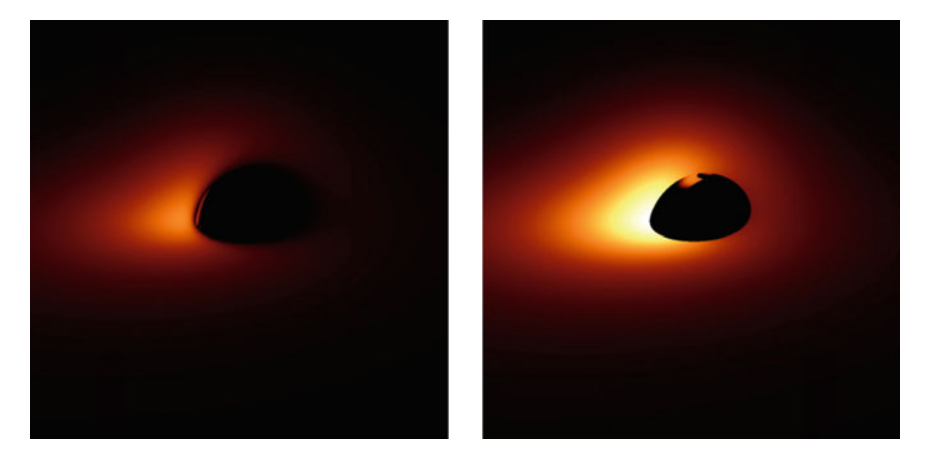


Fig. 5 Simulated images [20] for a supermassive black hole with spin a=0.9 and inclination 70° in standard-GR (*left*) and pc-GR (*right*). pc-GR black holes are brighter than standard-GR black holes due to the reduced gravitational redshift. This offers a unique possibility to test GR theories with upcoming spatially resolved images from the black hole in the Galactic Center and in M87

huge amplitude variations have been detected with a maximum amplitude variability of a factor of about 60 within only 1,200 s. The most plausible explanation for such type of variability is flux boosting. Temperature inhomogeneities in the accretion disc lead to flux variation in the observer's frame which scale as

$$\frac{f}{f'} = \delta^{3+\Gamma}$$

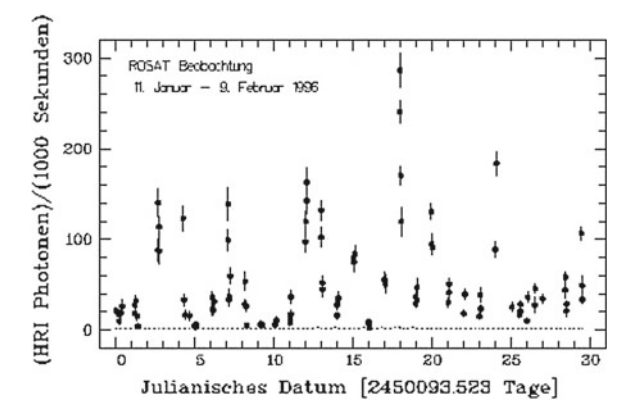


Fig. 6 30 day flux monitoring of the active galaxy IRAS 13224-3809 at X-ray with ROSAT in 1996. The strong and persistent flux variations are most probably due to flux boosting of temperature inhomogeneities in the accretion disc

252 T. Boller and A. Müller

where f is the flux in the observer's frame, f' is the rest frame flux, δ is the Doppler factor and Γ is the photon index. In Narrow-Line Seyfert 1 Galaxies [22] the large values of the photon index make these objects to the most highly variable objects at X-rays in the Universe. Temperature inhomogeneties in the accretion disc with factors of only about 2 result into flux variations in the observer's frame up to 100. As the blackbody-type emission of the temperature inhomogeneities in the disc scales with the temperature to the power of 4, these higher temperature regions are also associated with Fe K line emission, which is then strongly flux boosted in the observer's frame. Therefore Fe K line emission and QPO type variability should be physically linked. As shown in the previous Section, the pair of the Fe K emission r(Fe K) and of the quasi-periodic emission r(QPO) can be measured and compared to standard-GR and pc-GR, which will be a powerful test of modified GR theories.

5 Summary

We have shown that Galactic binaries, the Galactic Center, and supermassive black holes provide ideal test laboratories for modified GR theories. The discrepancy between the emission region of the Fe K line and the QPO emission regions in Galactic binaries is presently not understood in standard-GR. Spectral fitting of relativistic X-ray lines within the pc-GR theory is required to further address that problem.

The infalling gas cloud in the Galactic Center provides a unique opportunity in this century to study accretion physics in the strong gravity regime. X-ray and NIR observations will allow testing GR via QPO frequencies and relativistic line emission. mm-VLBI observations will allow to test "shadowing" towards the black hole in

the Galactic Center and in M87 within the next few years. Our gallery of pc-GR ray-tracing images will be used to compare the simulated images with the observed, spatially resolved images of the black holes and will provide the strongest test for standard and pc-GR theory in the very nearby future.

Acknowledgments The authors would like to wish Prof. Mikhail Itkis all the best for the future. The conference was held in honor of the 70th birthday of Prof. Mikhail Itkis.

References

- 1. P. Hess, W. Greiner, Int. J. Mod. Phys. E 18, 51 (2009)
- T. Boller, A. Müller, Exciting Interdisciplinary Physics, FIAS Interdisciplinary Science Series. ISBN 978-3-319-00046-6. Springer, Switzerland, p. 293 (2013)
- 3. C.M. Will, Phys. Uspekhi 37, 697 (1994)
- A. Müller, Lexikon der Astrophysik, http://www.wissenschaft-online.de/astrowissen/lexdt. html
- 5. R.C. Henry, ApJ **535**, 350 (2000)
- 6. T. Schönenbach, G. Caspar, P. Hess et al., MNRAS 430, 2999 (2013)
- 7. M. Dovciak, G. Matt, S. Bianchi, T. Boller et al., arXiv1306.2331 (2013)
- 8. K. Nandra, D. Barret, X. Barcons et al., arXiv1306.2307 (2013)

- 9. R. Ross, A.C. Fabian, MNRAS 358, 211 (2005)
- 10. J.M. Miller, C.S. Reynolds, A.C. Fabian, G. Miniutti, L. Gallo, ApJ 697, 900 (2009)
- 11. T.M. Belloni, A. Sanna, M. Mendz, MNRAS **426**, 1701 (2012)
- 12. J. Steiner, J. McClintock, G. Jeffrey, R. Narayan, R. Remillard, in 38th COSPAR Scientific Assembly, held 18–15 July 2010 in Bremen, Germany, p. 6
- 13. R.C. Reis, A.C. Fabian, R.R. Ross, G. Miniutti, J.M. Miller, C. Reynolds, MNRAS 387, 1489 (2008)
- J.M. Miller, J.M. Reynolds, A.C. Fabian, E.M. Cackett, G. Miniutti, J. Raymond, D. Steeghs, R. Reis, J. Homann, ApJ 679, 113 (2008)
- 15. R.I. Hynes, D. Steeghs, J. Casares, P.A. Charles., K. O'Brien, ApJ 609, 317 (2004)
- 16. C. Done, M. Middleton, M. Ward, MNRAS 434, 1955 (2013)
- 17. B. Aschenbach, A&A 425, 1075 (2004)
- 18. S. Gillesen et al., ApJ **774**, 44 (2013)
- 19. H. Falcke, R. Laing, L. Testi, A. Zensus, The Messenger 149, 50 (2012)
- 20. T. Schönenbach, G. Caspar, P. Hess et al., MNRAS 442, 121 (2014)
- 21. Th Boller, W.N. Brandt, A.C. Fabian, H. Fink, MNRAS **289**, 393 (1997)
- 22. Th Boller, W.N. Brandt, H. Fink, A&A **305**, 53 (1996)

Pseudo-complex General Relativity and Neutron Stars

Peter O. Hess, Isaac Rodríguez and Walter Greiner

Abstract The basic concepts of the pseudo-complex General Relativity (pc-GR) are presented. The pc-GR is finally applied to neutron stars. We discuss the TOV equations for the matter and the dark energy. It is shown that already with a simple coupling of the matter with the dark energy, neutron stars with six solar masses can be generated without difficulty.

1 Introduction

In this contribution we will give a brief overview on the pseudo-complex General Relativity (pc-GR) and what has been achieved up to now. The central part consists on basic concepts and some predictions, which can be measured in near future. Toward the end a preliminary consideration of neutron stars with the presence of dark energy will be given.

First of all, the motivation for this work has a long history. We are not the first who tried to extend the theory of General Relativity (GR). Einstein [1, 2] already applied an algebraic extension of his theory, introducing complex coordinates. His intention was to unify GR with Electrodynamics. There was another concern made by M. Born [3, 4] who complained that while in Quantum Mechanics the coordinates and momenta are treated on equal footing, in GR this is not the case because in the length element squared $ds^2 = g_{\mu\nu}dx^{\mu}dx^{\nu}$ coordinates dominate. Therefore he

P.O. Hess (⊠)

Circuito Exterior, Instituto de Ciencias Nucleares, UNAM, C.U., A.P. 70-543,

04510 Mexico, Mexico

e-mail: hess@nucleares.unam.mx

I. Rodríguez · W. Greiner

Frankfurt Institute for Advanced Studies, Johann Wolfgang Goethe Universität,

Ruth-Moufang-Str. 1, 60438 Frankfurt, Germany

e-mail: irodriguez@fias.uni-frankfurt.de

W. Greiner

e-mail: greiner@fias.uni-frankfurt.de

P.O. Hess et al.

proposed an extension of the length element to

$$d\omega^{2} = g_{\mu\nu}dx^{\mu}dx^{\nu} + \frac{l^{2}}{c^{2}}du^{\mu}du^{\nu}.$$
 (1)

The u^{μ} refers to the 4-velocity. Actually he used instead of u^{μ} the momenta p^{μ}/m , with m being the mass of a particle. We changed it here because (1) allows a more general treatment. E.R. Caianiello [5] recognized that this length element squared corresponds to the introduction of a maximal acceleration, or equivalent to a minimal length scale l, with the acceleration being lower or equal to 1/l. Here, we have a case where for dimensional reasons a length scale l appears, corresponding to a minimal length. This is a parameter, i.e., it is not affected by a Lorentz transformation! Commonly, when a minimal length appears, one assumes that it is a physical length affected by the Lorentz transformation (or the extended Poincaré transformation). Thus, when the minimal length, as a natural constant, is not allowed to be affected, one has to deform the Lorentz transformation, turning the treatment of the physical system extremely difficult. This is not necessary in Born's proposal. The length element squared in (1) is invariant and all known symmetries are maintained. The symmetry group is larger than the Lorentz group O(3, 1), namely U(3, 1) and the mathematics is nicely exposed in [6].

The idea of Born and Caianiello were intensively worked out in [7–16]. In [14–16] also non-symmetric metrics where considered. This algebraic extended theory is called *hermitian gravity* and well summarized in [17, 18].

In [19] all possible algebraic extension where investigated. The weak gravitational limit was considered and the corresponding field equations. It was shown that in most extensions so-called ghost solution exist, which are non-physical solutions, like the tachyons. Only when real or *pseudo-complex* variables are used, no ghost solutions appear. We introduced the notion of *pseudo-complex* (pc) which has to be explained in more detail further below. There are different notations in the literature, like hyperbolic, hyper-complex, para-complex, etc. The definition as introduced in [20, 21] is used. The important point is that a complex extension has problems and the only promising algebraic extension is to pc-coordinates, which was our motivation to formulate a pc-GR.

The use of pc-variables also proved to be of great advantage in field theory. As shown in [20, 21] its use permits to formulate a linear field theory which is automatically renormalized due to the appearance of a minimal length. The propagators are of the type Pauli-Villars, corresponding to a highly nonlinear field theory when no pc-variables and pc-fields are used. This might create some concern, because in the theory of Pauli-Villars one has to introduce a regularizing mass such that gauge symmetry is broken. In [22] a pc-field theory was developed and shown that in the pc-formulation gauge symmetry is perfectly maintained. Thus, a pc-extension leads to a simple theory with a complicated content, i.e. a great simplification! Pc-extensions where already proposed in the 60's and 70's [23–26], though in very mathematical terms.

There is also a philosophical reason to look for extensions of GR, besides the argument given by Born: GR predicts under extreme conditions the formation of a black hole. This happens when a very large mass contracts, then the collapse continues until a singularity in the center is formed. While this singularity can be discussed away by quantum effects, for us a more problematic phenomenon appears, namely an *event horizon*. Event horizons may appear in various forms. For example, all galaxies are flying away from us, due to the expansion of the universe, such that at very large distances they fly away at more than the speed of light, disappearing from us. This does not concern us, because it can be well understood due to expansion of space. In the case of a black hole the problem is different: A *nearby* observer (not too near but sufficiently far away) has no possibility to see inside a black hole, thus part of a *nearby space* is excluded from his world. From a philosophical point of view this is annoying. One can argue that the gravitational field is so strong that deviations may appear, such that this event horizon disappears. It helps to note that the GR, though very well tested in many ways, has not been tested up to now in such strong gravitational environments.

Another comment may be that the event horizon is only a coordinate singularity, because an infalling observers does not see it. This is true, but in our point of view a singularity, even a coordinate singularity, should not appear for *any* observer. Of course this is only a philosophical point of view.

Thus, we were motivated to extend the GR to a pc-GR. A first attempt has been published in [27] and a pc-Roberston-Walker model of the universe was discussed in [28]. The, for the moment, last version of pc-GR was published in [29].

This contribution is organized as follows: In Sect. 2 the pc-GR will be summarized. Also some experimental prediction were determined in [30]. Due to lack of space, we will not discuss them here but rather refer to the contribution of Boller [31]. At the end, neutron stars will be treated within the pc-GR, showing that stars with six solar masses can easily be generated.

2 Pseudo-complex General Relativity

First, we will shortly define pc-variables. A pc-variable is defined as $X = x_R + Ix_I$, with x_R being the pseudo-real and x_I the pseudo-imaginary component. The I has the important property that $I^2 = 1$, contrary to a complex variable. One can introduce the operators $\sigma_{\pm} = \frac{1}{2} (1 \pm I)$ and rewrite the coordinate in the form $X = X_+ \sigma_+ + X_- \sigma_-$, with $X_{\pm} = x_R \pm x_I$. The operators satisfy $\sigma_{\pm}^2 = \sigma_{\pm}$ and $\sigma_+ \sigma_- = 0$. Especially the last property shows that the pc-variables do not form a field but a ring, because one can multiply two variables, one proportional to σ_- and the other to σ_+ , and nevertheless the product is zero. This property is called a zero divisor. Mathematical manipulations, like multiplication, addition, etc., can be done independently in both components, which we will call zero-divisor components. A variable which is either proportional to σ_- or σ_+ has zero norm and can be considered as a generalized

P.O. Hess et al.

zero. The mathematics of such variables is nicely explained in [32, 33], including integration.

In pc-GR the pc-variables are $X^{\mu}=x^{\mu}+Iy^{\mu}=X^{\mu}_{+}\sigma_{+}+X^{\mu}_{-}\sigma_{-}$. We stay in the zero-divisor basis. In each component we can define a metric, i.e.,

$$g_{\mu\nu}(X) = g_{\mu\nu}^{+}(X_{+})\sigma_{+} + g_{\mu\nu}^{-}(X_{-})\sigma_{-},$$
 (2)

which is pseudo-complex and we restrict to a symmetric metric (in general non-symmetric metrics can be treated too).

In each zero-divisor component one can define covariant derivatives, Christoffel symbols, parallel displacement, etc., as is done in the standard GR.

The length square element takes the form

$$\begin{split} d\omega^{2} &= g_{\mu\nu}^{+} dX_{+}^{\mu} dX_{+}^{\nu} \sigma_{+} + g_{\mu\nu}^{-} dX_{-}^{\mu} dX_{-}^{\nu} \sigma_{-} \\ &= \left[g_{\mu\nu}^{R} \left(dx^{\mu} dx^{\nu} + dy^{\mu} dy^{\nu} \right) + 2 g_{\mu\nu}^{I} dx^{\mu} dy^{\nu} \right] \\ &+ I \left[g_{\mu\nu}^{I} \left(dx^{\mu} dx^{\nu} + dy^{\mu} dy^{\nu} \right) + 2 g_{\mu\nu}^{R} dx^{\mu} dy^{\nu} \right] \\ g_{\mu\nu}^{+} &= g_{\mu\nu}^{R} + g_{\mu\nu}^{I} \\ g_{\mu\nu}^{-} &= g_{\mu\nu}^{R} - g_{\mu\nu}^{I}, \end{split} \tag{3}$$

where we related the metric components to the pseudo-real and pseudo-imaginary part and we have used a symmetric metric.

As an additional requirement, we use a modified variational principle, as proposed in [20, 21]. The argument is, that when δS , with S being the action, is set to zero, then δS_{\pm} has also to be set to zero, due to the properties of the zero-divisor. As a consequence, we have formulated two independent GRs with no connection in between. In order to get something new, [20, 21] proposes (field theories were considered in these references, but it is a general argument) to require that the variation is within the zero divisor, i.e., the variation gives a *generalized zero*. Taking as an example a function proportional to σ_{-} (the same holds if it is proportional to σ_{+}) we have

$$\delta S = f(X_{-})\sigma_{-},\tag{4}$$

with the liberty to choose the function $f(X_-)$. Alternatively one can also propose to add to the Lagrangian in the σ_- component a contribution such that its variation gives $-f(X_-)$, in case someone prefers the old variational principle. In both views, there is an additional contribution, providing further liberty. Varying the action leads to the Einstein equations, which now read

$$\mathscr{R}_{\mu\nu} - \frac{1}{2} g_{\mu\nu} \mathscr{R} = -\frac{8\pi\kappa}{c^2} T^{\Lambda}_{\mu\nu} \sigma_-,\tag{5}$$

where $\mathcal{R}_{\mu\nu}$ is the pc-Ricci tensor, R the pc-curvature scalar and κ is the gravitational constant. The right hand side has been rewritten such that the identification of the additional contribution due to the modified variational procedure is clear, i.e., it represents an energy-momentum tensor.

The index Λ refers to the origin of this contribution, due to the appearance of a fluid which we call *dark energy*. One has to be careful to compare it with the dark energy on cosmological scale. Some idea how this contribution comes about can be found in [35, 36].

In [35] the coupling of a central mass to the vacuum fluctuations is considered. Semi-classical Quantum Mechanics is applied with the Schwarzschild metric as a background, thus, an event horizon still exists. The resulting density distribution of the dark energy is *negative* and the dominant term fall of as $1/r^6$. In [36] the authors also speculate about the effect of this additional contribution and design scenarios where the collapse of a star is halted before reaching the event horizon. It is important to note, that the vacuum fluctuation is a *local property* and can only be felt by a particle which is in a region where there is a non-zero contribution. For an observer at large distance, this contribution can be neglected and only the mass of the star is seen. Of course, the effects of the presence of the vacuum fluctuations can be observed due to the changes inflicted to the particle motion. Also the red-shift shows effects because the clock of the particle near the Schwarzschild radius runs differently when the vacuum fluctuations are included or not. The important point is that the dark energy does not act gravitationally to an observer very far away, such that he sees only the (baryonic) mass of the star. This is very different from the normal assumption of a fluid which acts gravitationally. The reason is that such a fluid consists of real particles while in our case they are virtual particles.

The projection to a real metric is defined also in [29]. In a first step, one has to write $g_{\mu\nu}^\pm(X_\pm)$ in the same functional form, introducing the same additional parameter dependent terms as in the σ_- component but with parameters set to zero. Then the variables and the parameters are mapped to their pseudo-real components. It is shown in [29] that for the case of the parameters this is in analogy on how to map the pc-Lorentz transformation, which contains acceleration, to the standard Lorentz transformation, which do not contain acceleration. Furthermore, substituting the pc-variables to their pseudo-real part corresponds to set the minimal length equal to zero. This implies that an important part of the complete pc-GR is neglected, namely the effects of the minimal length, which may play a role when for some other reasons a singularity appears or accelerations approach their maximal value, or when the quantization of the theory is considered.

In pc-GR we assume a model for $T_{\mu\nu}^{\Lambda}$ and calculate the effects of the fluid to the local properties of the metric, which can be deduced solving the Einstein equations. As a result [29] we obtain also a negative energy density but we assume a fall off as $-B/r^5$, with $B=bm^3$ (note, that B is mass dependent and represents how mass couples to the vacuum fluctuations), introducing the parameter B (or b). This is the minimal requirement which satisfies that in solar system experiments, or known systems of two neutron stars, no deviation is measured yet. The results computed in [29, 30] are based on this assumption but also changes are discussed as when the

P.O. Hess et al.

dependence in r is changed, with no important differences. The advantage of our procedure compared to [35, 36] is that we can calculate the effect of the vacuum fluctuations on the metric, but we cannot determine the energy-density by first principles. This can be done in [35, 36] but the disadvantage there is that they cannot determine the back coupling to the metric and thus still an event horizon appears. In pc-GR the metric component g_{00} acquires the form $\left(1-\frac{2m}{r}+\frac{B}{2r^3}\right)$ and we are allowed to choose the parameter B such that no event horizon appears $(g_{00}>0)$ everywhere), with $B>B_{\min}$. The square root of the g_{00} component is interpreted as the effective potential for zero angular momentum [37]. For the pc-Schwarzschild case [29] this produces a repulsive part in the potential such that the collapse of a very heavy star is halted at approximately 2/3 of the Schwarzschild radius. In other words, space is distorted by the mass and by the coupling of the mass to the quantum vacuum, such that space itself halts the collapse of a large mass. Thus, we predict that the observed size of the black hole should be smaller than in standard GR.

Now, we apply a simplification in order to show that the volume element, as proposed by Born, is contained within our theory. For that, we have to assume that the pseudo-imaginary component $y^{\mu} = \binom{l}{c} u^{\mu}$, with u^{μ} as the four velocity. This is a delicate assumption, because the four-velocity is in the tangent space of the manifold given by (x^{μ}) , thus, it transforms differently to x^{μ} in a curved space, a property which is not needed when we associate to y^{μ} just the pseudo-imaginary component of the coordinate X^{μ} . For more details we refer to the contribution of M. Schäfer [38]. As a further assumption, we use the same metric function in each zero-divisor component, i.e., $g^{\pm}_{\mu\nu} = g_{\mu\nu}(X_{\pm})$. This implies via (3) that the imaginary component of the metric vanishes. Next, we note that we can neglect the $(\frac{l}{c}) u^{\mu}$ dependence in the metric function, because $|u^{\mu}| \le c$ and $l \ll 1$, maybe of the order of the Planck length of 10^{-33} cm. With this, we can approximate the metric components by $g_{\mu\nu}(X_{\pm}) \approx g_{\mu\nu}(x)$. This cannot be applied for the differentials du^{μ} , because these are related to the acceleration and, for the moment, we still allow that it can reach its maximal value of 1/l. With this, the length element squared acquires the form

$$d\omega^2 \approx g_{\mu\nu}(x) \left(dx^{\mu} dx^{\nu} + \left(\frac{l}{c} \right)^2 du^{\mu} du^{\nu} \right) + 2I \left(\frac{l}{c} \right) g_{\mu\nu}(x) dx^{\mu} du^{\nu}. \quad (6)$$

We also demand that this length element square has to be real, when the motion of a particle is considered. Thus, the pseudo-imaginary part has to vanish, which is nothing but the *dispersion relation*, which therefore results automatically in our theory. Finally, the pseudo-real part is nothing but the length squared elements as proposed by Born and used by many others. We conclude that the pc-GR contains all theories related to Born's proposal, which treats a minimal length parameter.

When the acceleration is small, as we will assume from now on, then even the contribution due to the acceleration can be neglected and we arrive at the standard GR. The only property from pc-GR, which is left, comes from the modified variational principle which requires the appearance of an additional energy-momentum tensor on the right hand side of the Einstein equation.

For the experimental verifications of pc-GR we refer to the contribution of T. Boller [31].

We will directly go the the problem of neutron stars, which is the following: Outside the star we can estimate very well how the energy density is coupled to the mass (how it falls off as a function in the radial distance). There, an anisotropic fluid has to be assumed, which is due to the TOV equation for the dark energy fluid

$$\frac{dp_{\Lambda}r}{dr} = -\frac{(\varepsilon_{\Lambda}(r) + p_{\Lambda r}(r))}{r\left[r - 2m + 2m_{\Lambda}(r)\right]} \left[m - m_{\Lambda}(r) + \frac{4\pi k}{c^4}r^3p_{\Lambda r}(r)\right] + \frac{2(p_{\Lambda\theta} - p_{\Lambda r})}{r}.$$
(7)

The indexes r and θ referring to the radial and tangential pressure. For the equation of state we have to assume that $p_{\Lambda r} = -\epsilon_{\Lambda}$, because the energy density is negative and in order to fulfill the *Dominant Energy Condition* [39]. But with this equation of state, the first term in (7) vanishes. When an isotropic fluid is assumed, the radial derivative of the pressure is zero, therefore the pressure is constant and also the energy-density. Thus, in order to allow a fall-off of the energy density, an anisotropic fluid has to be assumed.

Nevertheless, for simplicity we use *inside* the star an isotropic fluid for both the baryonic and the dark energy density. For the baryonic equation of state we use the one as deduced in [40], within the hadronic chiral SU(3) model. The coupling between mass and the dark energy is not known, so we rely on models. We assume as in [34] that the coupling is linear, i.e., $\epsilon_{\Lambda} = \alpha \epsilon_{m}$, with a negative α . In Fig. 1 the total mass versus its radius is plotted. As one can see, a mass of up to six solar masses can

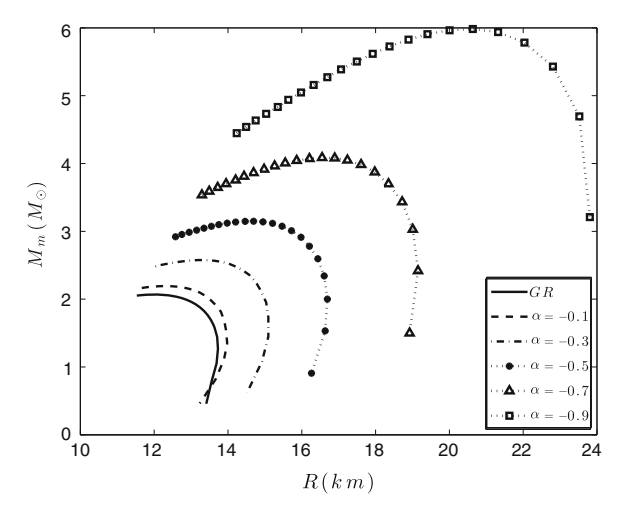


Fig. 1 The baryonic total mass versus total radius for different values of the coefficient α . The central Λ -term pressure $p_{\Lambda c}$ has been fixed to $1\varepsilon_0$, where ε_0 is the nuclear energy density

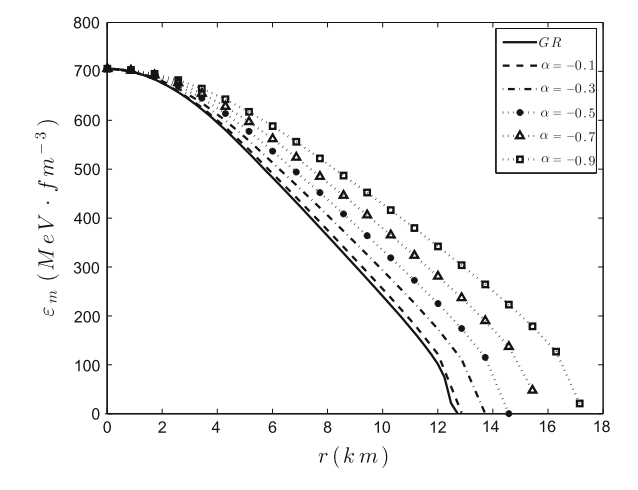


Fig. 2 The baryonic energy density profile for different values of the coefficient α . The central Λ -term pressure $p_{\Lambda c}$ has been fixed to $1\varepsilon_0$, where ε_0 is the nuclear energy density

easily be achieved. However for large masses the fall-off of the dark energy density with increasing r is not strong enough and it starts to evaporate outer layers. The problem lies clearly with the right equation of state, which we have to reconsider in future.

Another interesting observation is that for six solar masses the Schwarzschild radius of possible stars range from 14 to 24 km, i.e. of the same order as as the Schwarzschild radius. In Fig. 2 the density profile for a star with different values of α is shown. For the six solar masses ($\alpha = -0.9$) the radius is just above the Schwarzschild radius. Thus, it behaves in pc-GR as a near black hole (not really black, because it still may emit light) with a large red shift at the surface [30]. For the next lower value o $\alpha = -0.7$ the maximal mass is around four solar masses and the corresponding Schwarzschild radius is around 11.7 m, already well inside the star. Therefore, between 4 and 6 solar masses the neutron stars resembles more and more a classical black hole.

3 Conclusions

In this contribution a review on the pc-GR was given, philosophical aspects were discussed and also the basic assumptions. Definite prediction can be made on the differences to standard GR and we refer to the contribution of Boller [31].

One important message of pc-GR is that not only mass curves the space around it, but also changes the vacuum properties, which itself reacts back and provokes an additional curvature. The collapse of a star will be thus stopped by space itself.

We also discussed toward the end the inclusion of baryonic matter, with the uncertainty to pin down the coupling between the mass and the dark energy distribution inside the star. As a result we showed that stable stars with six solar masses can easily be obtained. With increasing mass, the calculated radius the star approaches quickly a state which is similar to a black hole (large red-shift), but also with a radius below the Schwarzschild radius.

Acknowledgments P.O.H. acknowledges financial support from DGAPA and CONACyT, and also from FIAS and GSI.

References

- 1. A. Einstein, Ann. Math. 46, 578 (1945)
- 2. A. Einstein, Rev. Mod. Phys. 20, 35 (1948)
- 3. M. Born, Proc. Roy. Soc. A 165, 291 (1938)
- 4. M. Born, Rev. Mod. Phys. 21, 463 (1949)
- 5. E.R. Caianiello, Nuovo Cim. Lett. 32, 65 (1981)
- 6. S.G. Low, J. Phys. A 35, 5711 (2002)
- 7. H.E. Brandt, Found. Phys. Lett. 2, 39 (1989)
- 8. H.E. Brandt, Found. Phys. Lett. 4, 523 (1989)
- 9. H.E. Brandt, Found. Phys. Lett. 6, 245 (1993)
- 10. R.G. Beil, Found. Phys. 33, 1107 (2003)
- 11. R.G. Beil, Int. J. Theor. Phys. **26**, 189 (1987)
- 12. R.G. Beil, Int. J. Theor. Phys. 28, 659 (1989)
- 13. R.G. Beil, Int. J. Theor. Phys. **31**, 1025 (1992)
- 14. J.W. Moffat, Phys. Rev. D **19**, 3554 (1979)
- 15. G. Kunstatter, J.W. Moffat, J. Malzan, J. Math. Phys. 24, 886 (1983)
- 16. G. Kunstatter, R. Yates, J. Phys. A 14, 847 (1981)
- 17. C. Mantz, T. Prokopec, arXiv:gr-qcl0804.0213v1, 2008
- 18. C. Mantz, T. Prokopec, Found. Phys. **41**, 1597 (2011)
- 19. P.F. Kelly, R.B. Mann, Class. Quant. Grav. 3, 705 (1986)
- F.P. Schuller, Dirac-Born-Infeld Kinematics, Maximal Acceleration and Almost Product Manifolds, Ph.D. Thesis, Cambridge, (2003)
- 21. F.P. Schuller, M.N.R. Wohlfarth, T.W. Grimm, Class. Quant. Grav. 20, 1 (2003)
- 22. P.O. Hess, W. Greiner, Int. J. Mod. Phys. E 16, 1643 (2007)
- 23. A. Crumeyrolle, Ann. de la Fac. des Sciences de Toulouse, 4e série, 26, 105 (1962)
- 24. A. Crumeyrolle, Riv. Mat. Univ. Parma (2) 5, 85 (1964)
- 25. R.-L. Clerc, Ann. de L'I.H.P. Section A 12(4), 343 (1970)
- 26. R.-L. Clerc, Ann. de L'I.H.P. Section A 17(3), 227 (1972)
- 27. P.O. Hess, W. Greiner, Int. J. Mod. Phys. E 18, 51 (2009)
- 28. P.O. Hess, L. Maghlaoui, W. Greiner, Int. J. Mod. Phys. E 19, 1315 (2010)
- 29. G. Caspar, T. Schönenbach, P. Hess, W. Greiner, Int. J. Mod. Phys. E 20(S1), 807 (2011)
- T. Schönenbach, G. Caspar, P.O. Hess, T. Boller, A. Müller, M. Schäfer, W. Greiner, Month. Notic. Roy. Astron. Soc. 430, 2999 (2013)
- 31. T. Boller, see contribution within this volume
- 32. F. Antonuccio, Semi-Complex Analysis and Mathematical Physics, gr-qc/9311032
- I.L. Kantor, A.S. Solodovnikov, Hypercomplex Numbers. An Elementary Introduction to Algebra (Springer, Heidelberg, 1989)
- C.R. Ghezzi, Astrophysics and space science (2011), http://link.springer.com/article/10.1007/ s10509-011-0663-4

P.O. Hess et al.

- 35. M. Visser, Phys. Rev. D 54, 5116 (1996)
- 36. C. Barceló, S. Liberati, S. Sonego, M. Visser, Phys. Rev. D 77, 044032 (2008)
- 37. C.W. Misner, K.S. Thorne, J.A. Wheeler, *Gravitation* (W. H. Freeman and Company, San Francisco, 1973)
- 38. M. Schäfer, see contribution within this volume
- 39. S.W. Hawking, G.F.R. Ellis, *The large scale structure of space-time* (Campridge University Press, Cambridge, 1973)
- 40. V. Dexheimer, S. Schramm, Astroph. J. 3, 943 (2008)

An Introduction to the Mathematics of Pseudo-complex General Relativity

M. Schäfer, Walter Greiner and P.O. Hess

Abstract This contribution gives an introduction to the mathematical background of the recently developed extension to the theory of *General Relativity*, called *pseudo-complex General relativity* (pc-GR). Apart from presenting the calculus of pseudo-complex (pc) numbers, the pc-GR is presented in more detail than in former publications.

1 Introduction

In this workshop two contributions were presented [1, 2], related to applications of the recently proposed pseudo-complex General Relativity [3–5]. This contribution we take as a chance to present the mathematical background of the pc-GR and also resume the foundations of the theory. In the second chapter we will introduce the mathematics of pc-variables, relating the methods as much as possible to the usual analysis of complex variables. In Sect. 3 some consequences of symmetry transformations in the pc-space are discussed and then the basis ingrediences of the pc-GR are given. Finally, in Sect. 4 conclusions are drawn.

2 Pseudo-Complex Mathematics

2.1 Definitions and Properties

Consider the following bases for the vector space of real-valued 2-tuples \mathbb{R}^2 :

$$\{1, I\}: 1 = (1, 0), I = (0, 1),$$

$$\{\sigma_{+}, \sigma_{-}\}: \sigma_{+} = \frac{1}{2}(1, 1), \sigma_{-} = \frac{1}{2}(1, -1).$$
 (1)

M. Schäfer (⋈). W. Greiner

FIAS, J.W.-Goethe University of Frankfurt, Ruth-Moufang-Str. 1,60438 Frankfurt, Germany e-mail: schaefer@fias.uni-frankfurt.de

P.O. Hess

Instituto de Ciencias Nucleares, UNAM, C.U., A.P. 70-543,04510 Mexico, Mexico e-mail: hess@nucleares.unam.mx

© Springer International Publishing Switzerland 2015 W. Greiner (ed.), *Nuclear Physics: Present and Future*, FIAS Interdisciplinary Science Series, DOI 10.1007/978-3-319-10199-6_25 266 M. Schäfer et al.

An element $x \in \mathbb{R}^2$ is written in terms of the respective bases as

$$x = x_{+}\sigma_{+} + x_{-}\sigma_{-} = x_{R}1 + x_{I}I. \tag{2}$$

It is straightforward to derive the following relations between the different basis vectors and the respective components:

$$\sigma_{\pm} = \frac{1}{2}(1 \pm I), \ x_{\pm} = x_R \pm x_I,$$

$$1 = \sigma_+ + \sigma_-, \ I = \sigma_+ - \sigma_-,$$

$$x_R = \frac{1}{2}(x_+ + x_-), \ x_I = \frac{1}{2}(x_+ - x_-).$$
(3)

We now construct the set of pseudo-complex numbers by endowing \mathbb{R}^2 with a multiplication rule. We define pseudo-complex multiplication as a linear product in terms of the basis $\{\sigma_{\pm}\}$ by

$$\sigma_{\pm} \cdot \sigma_{\pm} = \sigma_{\pm} , \ \sigma_{\pm} \cdot \sigma_{\mp} = 0.$$
 (4)

The algebra of 2-tuples together with the usual addition and this multiplication rule gives the pseudo-complex numbers \mathbb{P} . Addition of two elements $x, x' \in \mathbb{P}$ is given by the usual component wise addition in \mathbb{R}^2 , including the definition of inverse elements (x+(-x)=0) and the neutral element (x+0=0). Multiplication of two pseudo-complex numbers is defined as the component wise multiplication of its real-valued components with respect to the basis $\{\sigma_{\pm}\}$. We immediately observe that multiplication is associative and commutative, with the unity element $1=\sigma_++\sigma_-$. The inverse of a pseudo-complex number $x=x_+\sigma_++x_-\sigma_-$ is given by $x^{-1}=x_-^{-1}\sigma_++x_-^{-1}\sigma_-$. It follows directly that not all elements of \mathbb{P} have a multiplicative inverse. We define

$$\mathscr{P}_{+} = \{\lambda \sigma_{+} | \lambda \in \mathbb{R}\}. \tag{5}$$

The set $\mathscr{P} = \mathscr{P}_+ \cup \mathscr{P}_-$ is denoted as the set of zero-divisors, containing all elements which do not have a multiplicative inverse in \mathbb{P} . The pseudo-complex numbers thus do not represent a field (as for example the real numbers), but only a ring $(\mathbb{R}^2, +, \cdot)$. Recall that a ring is an algebraic structure with an addition and multiplication, where in general not every element has an a multiplicative inverse (as an example consider the ring of integer numbers, where for instance there is no integer n such that 2n = 1).

Up to now we have defined the pseudo-complex multiplication with respect to the basis $\{\sigma_{\pm}\}$. Using Eqs. (3), from the definition (4) we obtain

$$1 \cdot 1 = I \cdot I = 1, \ 1 \cdot I = I.$$
 (6)

It follows that the multiplication of two pseudo-complex numbers $x, x' \in \mathbb{P}$ is given by

$$x \cdot x' = (x_{+}\sigma_{+} + x_{-}\sigma_{-}) \cdot (x'_{+}\sigma_{+} + x'_{-}\sigma_{-}) = (x_{+}x'_{+})\sigma_{+} + (x_{-}x'_{-})\sigma_{-}$$

$$= (x_{R}1 + x_{I}I) \cdot (x'_{R}1 + x'_{I}I) = (x_{R}x'_{R} + x_{I}x'_{I})1 + (x_{R}x'_{I} + x_{R}x_{I})I. \quad (7)$$

In the following we will identify the set $\mathbb{P}_R = \{x \in \mathbb{P} | x_I = 0\}$ with the real numbers \mathbb{R} .

We conclude this section by determining the inverse of x in terms of the components x_R , x_I . Writing as usual $\frac{1}{x_+} = x_{\pm}^{-1}$, we get

$$x^{-1} = \frac{1}{x_{+}} \sigma_{+} + \frac{1}{x_{-}} \sigma_{-} = \frac{1}{2(x_{R} + x_{I})} (1 + I) + \frac{1}{2(x_{R} - x_{I})} (1 - I)$$

$$= \frac{x_{R}}{x_{R}^{2} - x_{I}^{2}} 1 - \frac{x_{I}}{x_{R}^{2} - x_{I}^{2}} I.$$
(8)

From this equation it becomes apparent that the set of zero divisors can also be written as

$$\mathscr{P} = \{ x = x_R 1 + x_I I | x_R^2 = x_I^2 \}. \tag{9}$$

2.2 Calculus

We write a function $f: \mathbb{P} \to \mathbb{P}$ as

$$f(x) = f(x_R + Ix_I) = f_R(x_R, x_I) + If_I(x_R, x_I)$$

= $f(x_+\sigma_+ + x_-\sigma_-) = f_+(x_+, x_-)\sigma_+ + f_-(x_+, x_-)\sigma_-,$ (10)

where f_R , f_I , f_+ , f_- are real valued functions $\mathbb{R}^2 \to \mathbb{R}$. We now give two different definitions for differentiability in \mathbb{P} [6, 7]. In order to obtain a positive definite norm, we will use the Euclidean norm in \mathbb{R}^2 for the pseudo-complex numbers:

$$||x|| = \sqrt{x_R^2 + x_I^2} = \sqrt{\frac{x_+^2 + x_-^2}{2}}.$$
 (11)

We always assume that $f_{R,I}$ and f_{\pm} are infinitely times differentiable for each of its components. Assume that for $x_0 \in \mathbb{P}$ there exists $f'(x_0) \in \mathbb{P}$ such that

$$\lim_{x \to x_0} \frac{||f(x) - f(x_0) - f'(x_0)(x - x_0)||}{||x - x_0||} = 0.$$
 (12)

268 M. Schäfer et al.

If this limit exists, we denote $f'(x_0)$ as the pseudo-complex derivative of f at $x = x_0$ [6]. It can be shown [7] that in general this definition of the derivative is equivalent to the more familiar limit

$$f'(x_0) = \lim_{\substack{x \to x_0 \\ x - x_0 \in \mathbb{P}^*}} \frac{f(x) - f(x_0)}{x - x_0},\tag{13}$$

where $\mathbb{P}^* = \mathbb{P}/\mathscr{P}$ is the group of invertible pseudo-complex numbers. If the derivative of a function f exists at each point in its domain, we call the function pseudo-holomorphic.

For complex numbers a necessary condition for holomorphy is that the function fulfills the Cauchy-Riemann equations. Analogously it can be shown [6, 7] that a function f is pseudo-complex differentiable at x_0 if and only if the following conditions are fulfilled:

$$\frac{\partial f_R(x_0)}{\partial x_R} = \frac{\partial f_I(x_0)}{\partial x_I} , \quad \frac{\partial f_R(x_0)}{\partial x_I} = \frac{\partial f_I(x_0)}{\partial x_R}, \tag{14}$$

where we have again assumed that all the partial derivatives exist.

Using the relations $f_{\pm} = f_R \pm f_I$ and the chain rule, it is straightforward to show that Eq. (14) is equivalent to the following property of pseudo-holomorphic functions:

$$\frac{\partial f_{-}}{\partial x_{+}} = \frac{\partial f_{+}}{\partial x_{-}} = 0. \tag{15}$$

It follows the important statement that a pseudo-holomorphic function f can be written as

$$f(x) = f_{+}(x_{+})\sigma_{+} + f_{-}(x_{-})\sigma_{-}.$$
 (16)

Since $\sigma_{\pm}\sigma_{\pm}=\sigma_{\pm}$, and $\sigma_{\pm}\sigma_{\mp}=0$, the product of two pseudo-holomorphic functions can be written as follows:

$$f(x)g(x) = \left(f_{+}(x_{+})\sigma_{+} + f_{-}(x_{-})\sigma_{-}\right) \cdot \left(g_{+}(x_{+})\sigma_{+} + g_{-}(x_{-})\sigma_{-}\right)$$
$$= f_{+}g_{+}\sigma_{+} + f_{-}g_{-}\sigma_{-}. \tag{17}$$

With Eq. (14) the derivative written explicitly in terms of components is given by

$$f'(x) = \frac{\partial f_R}{\partial x_R} + I \frac{\partial f_I}{\partial x_R} = \frac{f_I}{\partial x_I} + I \frac{\partial f_R}{\partial x_I},\tag{18}$$

or

$$f'(x) = \frac{\partial f_{+}}{\partial x_{+}} \sigma_{+} + \frac{\partial f_{-}}{\partial x_{-}} \sigma_{-}, \tag{19}$$

where we have used Eq. (16).

Similar to integration in \mathbb{R}^n or \mathbb{C} , for the integration of pseudo-complex functions f we have to provide a curve $\gamma:(a,b)\to\mathbb{P}$ to determine the path along we integrate in the pseudo-complex plane. We write

$$\gamma(t) = \gamma_R(t) + I\gamma_I(t), \tag{20}$$

where $t \in (a, b)$ is the real-valued parameter. We define pseudo-complex integration by

$$\int_{\gamma} f \, \mathrm{D}x = \int_{\gamma} (f_R \, \mathrm{d}x_R + f_I \, \mathrm{d}x_I) + I \int_{\gamma} (f_I \, \mathrm{d}x_R + f_R \, \mathrm{d}x_I) \,. \tag{21}$$

Written for components with respect to the basis $\{\sigma_+\}$ this can be recast into

$$\int_{\gamma} f \, \mathrm{D}x = \sigma_{+} \int_{\gamma} f_{+} \, \mathrm{d}x_{+} + \sigma_{-} \int_{\gamma} f_{-} \, \mathrm{d}x_{-}. \tag{22}$$

It is a well-known result of complex analysis, that a holomorphic function defined on a disk is entirely determined by its values on the boundary of this disk. For pseudo-holomorphic functions we can state a similar, but more general result. Consider a domain \mathcal{D} in the pseudo-complex plane, where the function f is pseudo-holomorph. We have shown that in this case the function f in this domain can be written as

$$f(x_+, x_-) = f_+(x_+)\sigma_+ + f_-(x_-)\sigma_-, \tag{23}$$

i.e. the function f_+ does not depend on x_- , and f_- does not depend on x_+ . It follows, that if we know the value of f_+ at some point $x_+^*\sigma_+ + x_-^*\sigma_-$, we know its value at all points $x_+^*\sigma_+ + x_-\sigma_-$ in its domain of pseudo-holomorphicity. The analogous result holds for f_- . This means that we only need to know the value of f_- at a rather small set of points in its domain of pseudo-holomorphicity.

2.3 Modules over the Pseudo-complex Numbers

The notion of a module is a generalization of the concept of a vector space. Recall that a vector space is a collection of elements (called vectors), which can be added, or multiplied by scalars, which are usually real numbers, but in general might be elements of any field $(\mathbb{R},\mathbb{C},\ldots)$. For a module, this scalar multiplication is allowed to take place with elements of a ring (the pseudo-complex numbers \mathbb{P} in our case) rather than a field (usually the real numbers). It follows that a vector field is always a module, but a module might lack some properties of a vector space. An important difference is, that not all modules have a basis. If a module has a basis, it is a called a free module [8].

270 M. Schäfer et al.

Consider an *n*-dimensional vector space V over the real numbers. The pseudocomplexification $V^{\mathbb{P}}$ of this vector space is defined as

$$V^{\mathbb{P}} = \{X + IY | X, Y \in V\}. \tag{24}$$

Let $\{e_1, e_2, \dots, e_n\}$ be a basis of V. Let $X = X^i e_i$ and $Y^i e_i$ be two vectors. Since the vector space is defined over the real numbers, it holds $X^i, Y^i \in \mathbb{R}$ for all i. The pseudo-complexified element is given by

$$X + IY = X^{i}e_{i} + IY^{i}e_{i} = \left(x_{R}^{i} + Ix_{I}^{i}\right)e_{i} = x^{i}e_{i}, \tag{25}$$

where we have identified the pseudo-complexified sum of the components of the vectors $X, Y \in V$ with the pseudo-complex components of the element $X + IY \in V^{\mathbb{P}}$. It directly follows, that a basis of V is also a basis of $V^{\mathbb{P}}$, which is thus a free module [8].

3 Pseudo-complex General Relativity

3.1 Pseudo-complex Lorentz Group

The pseudo-complex extension $SO_{\mathbb{P}}(1,3)$ of the proper part of the Lorenz group SO(1,3) is constructed by considering the finite transformations

$$SO_{\mathbb{P}}(1,3) = \left\{ \exp[\omega^{\mu\nu} L_{\mu\nu}] \right\}. \tag{26}$$

Here $\omega^{\mu\nu}$ are the pseudo-complex transformation parameters, and $L_{\mu\nu}$ are the generators of the real Lorentz algebra. Writing $\omega^{\mu\nu}$ in terms of the $\{\sigma_{\pm}\}$ basis, we obtain for $\Lambda \in SO_{\mathbb{P}}(1,3)$

$$\Lambda = \exp\left[\omega_R^{\mu\nu}L_{\mu\nu}\right] = \exp\left[(\omega_R^{\mu\nu} + I\omega_I^{\mu\nu})L_{\mu\nu}\right] = \exp\left[\omega_+^{\mu\nu}L_{\mu\nu}\sigma_+ + \omega_-^{\mu\nu}L_{\mu\nu}\sigma_-\right]$$
$$= \exp\left[\omega_+^{\mu\nu}L_{\mu\nu}\right]\sigma_+ + \exp\left[\omega_+^{\mu\nu}L_{\mu\nu}\right]\sigma_- = \Lambda_+\sigma_+ + \Lambda_-\sigma_-, \tag{27}$$

where Λ_{\pm} are real finite Lorentz transformation. It follows, that

$$SO_{\mathbb{P}}(1,3) = SO_{+}(1,3) \otimes SO_{-}(1,3),$$
 (28)

where $SO_{\pm}(1,3)$ is constructed from the real proper Lorentz group by multiplication with σ_{\pm} .

Using $\omega_{\pm}^{\mu\nu} = \omega_{R}^{\mu\nu} \pm \omega_{I}^{\mu\nu}$ we can rewrite $\Lambda \in SO_{\mathbb{P}}(1,3)$ as

$$\Lambda = \exp\left[(\omega_R^{\mu\nu} + \omega_I^{\mu\nu})L_{\mu\nu}\right]\sigma_+ + \exp\left[(\omega_R^{\mu\nu} - \omega_I^{\mu\nu})L_{\mu\nu}\right]\sigma_-$$
$$= \left(\exp\left[\omega_I^{\mu\nu}L_{\mu\nu}\right]\sigma_+ + \exp\left[-\omega_I^{\mu\nu}L_{\mu\nu}\right]\sigma_-\right)$$

$$\times \left(\exp \left[\omega_R^{\mu\nu} L_{\mu\nu} \right] \sigma_+ + \exp \left[+ \omega_R^{\mu\nu} L_{\mu\nu} \right] \sigma_- \right)$$

$$= \left(\Lambda_+^{(2)} \sigma_+ + \Lambda_-^{(2)} \sigma_- \right) \times \left(\Lambda_+^{(1)} \sigma_+ + \Lambda_-^{(1)} \sigma_- \right) = \Lambda^{(2)} \Lambda^{(1)}, \tag{29}$$

where $\Lambda_\pm^{(1)}$ and $\Lambda_\pm^{(2)}$ are again real proper Lorentz transformations, with $\Lambda_-^{(1)}=\Lambda_+^{(1)}$ and $\Lambda_-^{(2)}=(\Lambda_+^{(2)})^{-1}$.

Since

$$\Lambda^{(1)} = \exp\left[\omega_R^{\mu\nu} L_{\mu\nu} \sigma_+ + \omega_R^{\mu\nu} L_{\mu\nu} \sigma_-\right] = \exp\left[\omega_R^{\mu\nu} L_{\mu\nu}\right],$$

$$\Lambda^{(2)} = \exp\left[\omega_I^{\mu\nu} L_{\mu\nu} \sigma_+ - \omega_I^{\mu\nu} L_{\mu\nu} \sigma_-\right] = \exp\left[I\omega_I^{\mu\nu} L_{\mu\nu}\right],$$
(30)

it follows that every pseudo-complex Lorentz transformation Λ can be written as a product of a real Lorentz transformation $\Lambda^{(1)}$ and a pseudo-complex Lorentz transformation $\Lambda^{(2)}$ with purely pseudo-complex parameters [11]. It holds

$$\Lambda^{(2)} = \frac{1}{2} \left(\Lambda_{+}^{(2)} + (\Lambda_{+}^{(2)})^{-1} \right) + I \frac{1}{2} \left(\Lambda_{+}^{(2)} - (\Lambda_{+}^{(2)})^{-1} \right) = \Lambda_{R}^{(2)} + I \Lambda_{I}^{(2)}.$$
 (31)

Let us consider a set of real orthonormal frame vectors \mathbf{e}_a [10, 11]. As shown in the last paragraph, the application of a pseudo-complex Lorentz transformation can be split up into the application of first a real and second a pure pseudo-complex Lorentz transformation. We thus restrict our considerations to the latter case. By applying $\Lambda^{(2)}$ to the vectors \mathbf{e}_a we obtain the new, now pseudo-complex, frame vectors \mathbf{E}_a ,

$$\mathbf{E}_a = \Lambda^{(2)} \mathbf{e}_a = \left(\Lambda_R^{(2)} + I \Lambda_I^{(2)} \right) \mathbf{e}_a = \Lambda_R^{(2)} \left(\mathbb{I} + lI\theta \right) \mathbf{e}_a, \tag{32}$$

with

$$\theta = \frac{1}{l} (\Lambda_R^{(2)})^{-1} \Lambda_I^{(2)}. \tag{33}$$

Here l is a scalar parameter with the dimension of a length. Let now $\Lambda_+^{(2)}$ be a boost in the direction 1 with rapidity ϕ . From Eq. (31) it follows that $\theta^1_0 = \theta^0_1 = \frac{1}{l} \tanh[\phi]$, and all other components of θ vanish [11]. In [11] the tensor θ has been identified with the Frenet-Serret tensor of a co-moving system along the world line of an accelerated observer [9]. It follows that the form of θ implies a maximal value for the acceleration [10], which is, using the limit $\tanh[\phi] \to 1$ for $\phi \to \infty$,

$$\theta^{1}_{0} = \frac{1}{l} \tanh[\phi] \le \frac{1}{l}. \tag{34}$$

Following the arguments in [10, 11], we conclude that the pseudo-imaginary component of the group parameter $\omega_I^{\mu\nu}$ leads to the appearance of a maximal acceleration, and thus, the theory contains a minimal length scale.

272 M. Schäfer et al.

3.2 Mapping to the Real Part and Modification of the Variational Principle

In the last section we have shown that the pseudo-complex extension of the Lorentz group is given by the product structure

$$SO_{\mathbb{P}}(1,3) = SO_{+}(1,3) \otimes SO_{+}(1,3) \supset SO(1,3),$$
 (35)

which contains the real Lorentz group SO(1,3) as a subgroup. When acting on functions of pseudo-complex coordinates $x=x_R+Ix_I$, the representation of the generators of the Lorentz group is given by $\hat{L}_{\mu\nu}=\hat{x}_{\mu}\hat{p}_{\nu}-\hat{x}_{\nu}\hat{p}_{\mu}$ where $\hat{p}_{\mu}=\frac{\hbar}{i}\,\mathrm{D}_{\mu}$ is the pseudo-complex momentum operator. We can write both \hat{x}_{μ} and \hat{p}_{μ} using the $\{\sigma_{\pm}\}$ basis and obtain again a product structure as in Eq. (35). The mapping of this representation of the pseudo-complex Lorentz transformation to the representation of the real subgroup SO(1,3) is obtained by

$$\exp\left[\omega^{\mu\nu}\hat{L}_{\mu\nu}\right] \to \exp\left[\omega_R^{\mu\nu}\hat{L}_{\mu\nu}^R\right],\tag{36}$$

where $\hat{L}_{\mu\nu}^R$ is obtained from $\hat{L}_{\mu\nu}$ by replacing the pseudo-complex coordinate and momentum operators by their pseudo-real parts, that is $\hat{x}_{\mu} \to \hat{x}_{\mu}^R$, and $\hat{p}_{\mu} \to \hat{p}_{\mu}^R$ [4, 10].

In the following we will always adopt this mapping from a pseudo-complex to a real (physical) expression. As an example consider a pseudo-complex function f(x, A), which depends on a pseudo-complex coordinate x and parameter A. Extracting the real value of this function is then obtained by replacing $x \to x_R$, and $A \to A_R$ in f [4]. Using this approach we have already assumed, that the respective function maps a pseudo-complex number to a real number, or that it can be expressed as a real function with a pseudo-complex argument.

We have shown that the pseudo-complex numbers intrinsically display a product structure, which becomes apparent in terms of the $\{\sigma_{\pm}\}$ basis. In a pseudo-complex formulation of General Relativity this enables us to define two metric tensors, one in σ_+ , and the other one in the σ_- sector, and then to construct a standard General Relativity in each sector. In order to obtain more than two independent theories in the σ_+ and the σ_- sector, we have to add another ingredient. This ingredient is given by a modification of the variational principle. We demand that the variation of the action does not vanish, but lies in the zero divisor as a 'generalized zero', that is

$$\delta S \in \mathscr{P}.$$
 (37)

For a more detailed account of this modified variational principle consult [4, 10].

3.3 Formulation of Pseudo-complex General Relativity

In the pseudo-complex General Relativity, the space-time coordinates X^{μ} are pseudo-complex numbers [3, 4]. The pseudo-real components are identified with the real

space-time components $X_R^\mu = x^\mu$, while the pseudo-imaginary components are given by $(l/c)u^\mu$, proportional to the tangent vector at a given space-time point, which can be identified in case of a world line of a particle with its four-velocity. The parameter l is introduced for dimensional reasons and has the the units of a length. Note that the mapping from pseudo-complex numbers to real numbers as presented in the last section corresponds to setting l=0.

In the pseudo-complex General Relativity the metric has a pseudo-real and a pseudo-imaginary component, or the zero-divisor components,

$$g_{\mu\nu} = g_{\mu\nu}^R + Ig_{\mu\nu}^I = g_{\mu\nu}^+ \sigma_+ + g_{\mu\nu}^- \sigma_-.$$
 (38)

Here the metric is assumed to be symmetric. Due to the division into the σ_{\pm} -sectors we can define a standard General Relativity in both sectors, but with a different symmetric metric. Thus, parallel displacements, connections, four derivatives, etc., are defined in exactly the same way as in standard General Relativity. Also, the four-derivative of the metric is zero, permitting the definition of a universal pseudocomplex metric (for details, see [3]).

Due to the modified variational principle, the new Einstein equation is given by

$$\mathscr{R}^{\mu\nu} - \frac{1}{2}g^{\mu\nu}\mathscr{R} = -\frac{8\pi\kappa}{c^2}T_-^{\mu\nu}\sigma_-,\tag{39}$$

where we have chosen the right hand side to be proportional to σ_- . We choose the variation of the action proportional to σ_- and note that using σ_+ results in the same description, only with an exchange of the σ_+ and σ_- component. The notation on the right hand side is intentional, because the requirement that a function is within the zero-divisor introduces in the σ_- component a function, which can be associated to the energy of a yet to be determined field. As shown in [3] this term is responsible for the disappearance of the black hole (and the singularity), producing an antigravitational effect for high central mass density, which halts the collapse of the mass distribution.

As a mapping to physical real results, we use the procedure as introduced in the last section. Once a pseudo-complex function in terms of the coordinates and momenta is given, its mapping is obtained by substituting all pseudo-complex variables, momenta (velocities) and parameters of the theory by their pseudo-real parts. Also possibly appearing parameters in these functions, like the transformation parameters $\omega^{\mu\nu}$ in a finite Lorentz transformation, have to be substituted by their pseudo-real part.

In general, let us denote by G_{\pm} the geometrical space of the σ_{\pm} component. The zero-divisor metric components are given by $g_{\mu\nu}^{\pm}$. The two geometrical spaces commute due to the property of the σ_{\pm} operators. This we denote via $G_{+}\otimes G_{-}$ which is finally reduced by the mapping to the real geometrical space G, i.e.

$$G_+ \otimes G_- \supset G.$$
 (40)

Again, the mapping corresponds to set within the metric all contributions, which are proportional to powers in l, to zero.

274 M. Schäfer et al.

For the metric, the final mapping is achieved by

$$g_{\mu\nu}(X,A) \to g_{\mu\nu}(x,A_R),$$
 (41)

where X, x is a shorthand notation for X^{μ} , x^{μ} and A, A_R for a set of pseudo-complex A^{μ} and pseudo-real parameters A^{μ}_R respectively.

4 Conclusions

In this contribution we gave in length an introduction to the mathematical background of pseudo-complex General Relativity, which in this detail is usually not possible in a paper published in a regular journal. In one section we gave a detailed review on the pseudo-complex numbers/variables, with rules of calculations. As shown, these rules are very similar to standard complex analysis, with slight but important variations. In the following section the basis ingrediences of pc-GR were reviewed in detail and the mapping to the four-dimensional coordinate space was explained.

Acknowledgments Financial support from the Frankfurt Institute for Advanced Studies (FIAS), Stiftung Polytechnische Gesellschaft Frankfurt, DGAPA-UNAM (IN 103212) and from CONACyT are acknowledged.

References

- 1. P.O. Hess, I. Rodríguez, W. Greiner, consult contribution to this conference
- 2. T. Boller, consult contribution to this conference
- 3. P.O. Hess, W. Greiner, Int. J. Mod. Phys. E 18, 5 (2009)
- G. Caspar, T. Schönenbach, P.O. Hess, M. Schäfer, W. Greiner, Int. J. Mod. Phys. E 21, 1250015 (2012)
- T. Schönenbach, G. Caspar, P.O. Hess, T. Boller, A. Müller, M. Schäfer, W. Greiner, Mon. Not. R. Astron. Soc. 430, 2999 (2013)
- 6. F. Antonuccio, Semi-Complex Analysis and Mathematical Physics, gr-qc/9311032
- P.M. Gadea, J. Grifone, J. Muñoz Masqué, Manifolds modelled over free modules over the double numbers. Acta Mathematica Hungarica 100, 187–203 (2003)
- 8. P.M. Cohn, *Algebra*, 2nd edn. (Wiley, New York, 1982)
- 9. C.W. Misner, K.S. Thorne, J.A. Wheeler, *Gravitation* (W. H. Freeman Company, San Francisco, 1973)
- 10. P.O. Hess, W. Greiner, Int. J. Mod. Phys. E 16, 1643 (2007)
- F.P. Schuller, Dirac-Born-Infeld Kinematics, Maximal Acceleration and Almost Product Manifolds, Ph.D. Thesis, Cambridge, 2003

The Gauge Principle in Covariant Hamiltonian Field Theory

Hermine Reichau and Jürgen Struckmeier

Abstract In this contribution, a canonical transformation theory is presented that is worked out on the basis of the covariant Hamiltonian field theory in local coordinate description. To provide an unique covariant Hamilton approach in the realm of gauge theory, a method is shown, that makes it possible to render every globally gauge invariant Hamiltonian density into a locally gauge invariant Hamiltonian, and subsequently into a Lagrangian density. On the basis of the example of the globally gauge invariant Dirac Lagrangian density, the corresponding locally gauge invariant system is derived by means of the canonical transformation approach.

1 Introduction

Gauge theories are commonly formulated on the basis of a Lagrangian density [4, 5, 9]. Based on the pioneering work of De Donder and Weyl [1, 15], these theories also can be formulated as *canonical transformations* of a Hamiltonian density that is related to a corresponding Lagrangian density by a *covariant Legendre transformation*.

The covariant Hamiltonian density \mathscr{H} then is defined to depend on a set of conjugate 4-vector fields π_I^μ that represent the dual quantities of the four derivatives $\partial_\mu\phi_I$ of the Lagrangian density $\mathscr{L}(\phi_I,\partial_\mu\phi_I,x^\mu)$, such that $\mathscr{H}=\mathscr{H}(\phi_I,\pi_I^\mu,x^\mu)$. Corresponding to the Euler-Lagrange equations of field theory, the canonical field equations then take on a symmetric form with respect to the four independent variables of space-time. This approach is commonly referred to as *multisymplectic field theory*

Frankfurt Institute for Advanced Studies, Ruth-Moufang Str.1, 60438 Frankfurt, Germany e-mail: reichau@fias.uni-frankfurt.de

GSI Helmholtzzentrum für Schwerionenforschung, Planck Str. 1, 64291 Darmstadt, Germany e-mail: j.struckmeier@gsi.de

H. Reichau(⊠)

J. Struckmeier

[3, 7, 11]. Mathematically, multisymplectic Hamiltonian field theory is formulated in terms of modern differential geometry [6, 12]. This approach raises a couple of mathematical issues that are not yet clarified [2]. Therefore much of the discussion in covariant Hamiltonian field theory is shifted into the realm of mathematics. In this approach, the differential geometry path is not pursued. Instead a *local coordinate* treatise of De Donder's and Weyl's covariant Hamiltonian field theory is provided. The *local* description makes it possible to confine mathematical efforts to the level of tensor calculus. Nevertheless, the description is chart-independent and thus applies to *all* local coordinate systems. With this property, the description is sufficiently general from a physical point of view.

The standard model of particle physics is a quantum gauge field theory, which is currently seen as providing the description of the fundamental set of particles [10, 13]. This gauge theory is a physical field theory which complies with a local gauge symmetry, also called *gauge invariance* or *gauge principle* [14]. The interaction of particle fields in the standard model is described to emerge from gauge symmetries. As these symmetry transformations are supposed to map physical systems into physical systems, gauge theories can elegantly and most generally be formulated in terms of canonical transformations in the realm of covariant Hamiltonian field theory.

2 Local Coordinate Representation of Relativistic Field Theory

To obtain a covariant Hamiltonian density it is not sufficient to apply the conventional Legendre transformation with respect to the time derivative $\partial_t \phi$ of a field $\phi(t,x,y,z)$, since this will abandon the equal footing of space and time variables. Instead, the *covariant Legendre transformation*—first introduced by De Donder and Weyl [1, 15]—is applied, which retains the equal footing of space and time variables of the Lagrangian description. To this end, a four-vector of conjugate momentum fields must be defined such that π_I^μ establishes the dual quantity of the derivatives $\partial_\mu \phi_I$, hence

$$\pi_I^{\mu} = \frac{\partial \mathcal{L}}{\partial \left(\partial_{\mu} \phi_I\right)} \equiv \frac{\partial \mathcal{L}}{\partial \left(\frac{\partial \phi_I}{\partial x^{\mu}}\right)}.$$
 (1)

The covariant Hamiltonian as the covariant Legendre transform of $\mathcal{L}(\phi_I, \partial \phi_I, x)$ is then given by

$$\mathcal{H}(\phi_I, \pi_I, x) = \pi_J^{\alpha} \frac{\partial \phi_J}{\partial x^{\alpha}} - \mathcal{L}(\phi_I, \partial \phi_I, x)$$
 (2)

The covariant Hamiltonian density $\mathcal{H}(\phi_I, \pi_I, x)$ is also referred to as the *De Donder-Weyl Hamiltonian density*. From \mathcal{H} , the complete set of covariant canonical field equations is obtained as

$$\frac{\partial \mathcal{H}}{\partial \phi_I} = -\frac{\partial \mathcal{L}}{\partial \phi_I} = -\frac{\partial}{\partial x^{\alpha}} \frac{\partial \mathcal{L}}{\partial (\partial_{\alpha} \phi_I)} = -\frac{\partial \pi_I^{\alpha}}{\partial x^{\alpha}}
\frac{\partial \mathcal{H}}{\partial \pi_I^{\mu}} = \delta_{IJ} \delta_{\mu}^{\alpha} \frac{\partial \phi_J}{\partial x^{\alpha}} = \frac{\partial \phi_I}{\partial x^{\mu}} \iff \frac{\partial \mathcal{L}}{\partial (\partial_{\mu} \phi_I)} = \pi_J^{\alpha} \delta_{IJ} \delta_{\alpha}^{\mu} = \pi_I^{\mu}.$$
(3)

Provided that \mathscr{L} is a Lorentz scalar, which means that its form is invariant with respect to Lorentz transformations, this property is passed to the Hamiltonian by the covariant Legendre transformation.

Therefore, the covariant Legendre transformation allows to formulate a canonical transformation theory for fields. A transformation of fields $(\phi, \pi) \mapsto (\Phi, \Pi)$ is called *canonical* if the *variational principle* based on the action functional is maintained

$$\delta \int_{R} \left(\pi_{I}^{\alpha} \frac{\partial \phi_{I}}{\partial x^{\alpha}} - \mathcal{H}(\phi, \pi, x) \right) d^{4}x \stackrel{!}{=} \delta \int_{R} \left(\Pi_{I}^{\alpha} \frac{\partial \Phi_{I}}{\partial x^{\alpha}} - \mathcal{H}(\Phi, \Pi, x) \right) d^{4}x. \tag{4}$$

For this condition to hold, the integrands my differ by the divergence of a vector field F_1^{μ} , with

$$\delta \int_{R} \frac{\partial F_{1}^{\alpha}}{\partial x^{\alpha}} d^{4}x = \delta \oint_{R} F_{1}^{\alpha} dS_{\alpha} \stackrel{!}{=} 0$$
 (5)

This is called *integrand condition*, which means, that the variation of the divergence must vanish on the boundary ∂R of the integration region within space-time. As a consequence of the form invariance of the variational principle, the form of the covariant canonical field equations is maintained

$$\frac{\partial \mathcal{H}'}{\partial \Pi_I^{\mu}} = \frac{\partial \Phi_I}{\partial x^{\mu}}, \qquad \frac{\partial \mathcal{H}'}{\partial \Phi_I} = -\frac{\partial \Pi_I^{\alpha}}{\partial x^{\alpha}}.$$
 (6)

The condition for Lagrangian densities then is

$$\mathscr{L} = \mathscr{L}' + \frac{\partial F_1^{\alpha}}{\partial x^{\alpha}},\tag{7}$$

which means that any Lagrangian is defined up to the divergence of an arbitrary vector function, referred to as a *generating function*. In terms of a Hamiltonian density, the condition (4) is

$$\pi_I^{\alpha} \frac{\partial \phi_I}{\partial x^{\alpha}} - \mathcal{H}(\phi, \pi, x) = \Pi_I^{\alpha} \frac{\partial \Phi_I}{\partial x^{\alpha}} - \mathcal{H}'(\Phi, \Pi, x) + \frac{\partial F_1^{\alpha}}{\partial x^{\alpha}}$$
(8)

The local coordinate representation of the field transformation rules from a generating function $F_1^{\mu} = F_1^{\mu}(\phi, \Phi, x)$ is obtained by comparing the coefficients in Eq.(8)

$$\pi_I^{\mu} = \frac{\partial F_1^{\mu}}{\partial \phi_I}, \quad \Pi_I^{\mu} = -\frac{\partial F_1^{\mu}}{\partial \Phi_I}, \quad \mathcal{H}' = \mathcal{H} + \left. \frac{\partial F_1^{\mu}}{\partial x^{\alpha}} \right|_{\text{expl}}.$$
 (9)

The symmetry relations between the original and the transformed fields follow as

$$\frac{\partial \pi_I^{\mu}}{\partial \Phi_I} = \frac{\partial^2 F_1^{\mu}}{\partial \phi_I \partial \Phi_I} = -\frac{\partial \Pi_J^{\mu}}{\partial \phi_I}.$$
 (10)

Having set up one of the four possible generating functions, the remaining three can be attained by means of Legendre transformations. The complete set of all covariant canonical transformation rules can be summarized as

$$\pi_{I}^{\mu} = \frac{\partial F_{1}^{\mu}}{\partial \phi_{I}}, \qquad \Pi_{I}^{\mu} = -\frac{\partial F_{1}^{\mu}}{\partial \Phi_{I}}, \qquad \mathcal{H}' = \mathcal{H} + \frac{\partial F_{1}^{\alpha}}{\partial x^{\alpha}}\Big|_{\text{expl.}}$$

$$\pi_{I}^{\mu} = \frac{\partial F_{2}^{\mu}}{\partial \phi_{I}}, \quad \Phi_{I} \delta_{\nu}^{\mu} = \frac{\partial F_{2}^{\mu}}{\partial \Pi_{I}^{\nu}}, \quad \mathcal{H}' = \mathcal{H} + \frac{\partial F_{2}^{\alpha}}{\partial x^{\alpha}}\Big|_{\text{expl.}}$$

$$\Pi_{I}^{\mu} = -\frac{\partial F_{3}^{\mu}}{\partial \Phi_{I}}, \quad \phi_{I} \delta_{\nu}^{\mu} = -\frac{\partial F_{3}^{\mu}}{\partial \pi_{I}^{\nu}}, \quad \mathcal{H}' = \mathcal{H} + \frac{\partial F_{3}^{\alpha}}{\partial x^{\alpha}}\Big|_{\text{expl.}}$$

$$\Phi_{I} \delta_{\nu}^{\mu} = \frac{\partial F_{4}^{\mu}}{\partial \Pi_{I}^{\nu}}, \quad \phi_{I} \delta_{\nu}^{\mu} = -\frac{\partial F_{4}^{\mu}}{\partial \pi_{I}^{\nu}}, \quad \mathcal{H}' = \mathcal{H} + \frac{\partial F_{4}^{\alpha}}{\partial x^{\alpha}}\Big|_{\text{expl.}}. \tag{11}$$

The complete set of symmetry relations between original and transformed fields is then given by

$$\frac{\partial \pi_{I}^{\mu}}{\partial \Phi_{J}} = \frac{\partial^{2} F_{1}^{\mu}}{\partial \phi_{I} \partial \Phi_{J}} = -\frac{\partial \Pi_{J}^{\mu}}{\partial \phi_{I}}$$

$$\frac{\partial \pi_{I}^{\mu}}{\partial \Pi_{J}^{\nu}} = \frac{\partial^{2} F_{2}^{\mu}}{\partial \phi_{I} \partial \Pi_{J}^{\nu}} = \frac{\partial \Phi_{J}}{\partial \phi_{I}} \delta_{\nu}^{\mu}$$

$$\frac{\partial \Pi_{I}^{\mu}}{\partial \pi_{J}^{\nu}} = -\frac{\partial^{2} F_{3}^{\mu}}{\partial \Phi_{I} \partial \pi_{J}^{\nu}} = \frac{\partial \phi_{J}}{\partial \Phi_{I}} \delta_{\nu}^{\mu}$$

$$\frac{\partial \phi_{I}}{\partial \Pi_{I}^{\beta}} = -\frac{\partial^{2} F_{4}^{\mu}}{\partial \pi_{A}^{\mu} \partial \Pi_{I}^{\beta}} = -\frac{\partial \Phi_{J}}{\partial \pi_{A}^{\mu}} \delta_{\beta}^{\mu}.$$
(12)

3 Example Part I: Dirac Hamiltonian Density

As an example for the application of the covariant Hamilton formalism in local coordinate description consider the conventional Dirac Lagrangian density \mathcal{L}_D , given by

$$\mathcal{L}_D = i \,\overline{\psi} \gamma^\alpha \frac{\partial \psi}{\partial x^\alpha} - m \overline{\psi} \psi, \qquad \hbar = c = 1. \tag{13}$$

It is possible to render this Lagrangian symmetric in ψ , $\overline{\psi}$ by combining the adjoints

$$\mathcal{L}_D = \frac{i}{2} \left(\overline{\psi} \gamma^\alpha \frac{\partial \psi}{\partial x^\alpha} - \frac{\partial \overline{\psi}}{\partial x^\alpha} \gamma^\alpha \psi \right) - m \overline{\psi} \psi. \tag{14}$$

As a test, it can be seen that both Lagrangians, (13) and (14), yield the same Euler-Lagrange equations

$$i\gamma^{\alpha}\frac{\partial\psi}{\partial x^{\alpha}} - m\psi = 0, \quad i\frac{\partial\overline{\psi}}{\partial x^{\alpha}}\gamma^{\alpha} + m\overline{\psi} = 0.$$
 (15)

As the Lagrangians are linear in the derivatives of the fields, the Hessians of these Lagrangian densities are zero,

$$\det \left[\frac{\partial^2 \mathcal{L}_D}{\partial \left(\partial_\mu \psi \right) \partial \left(\partial_\nu \overline{\psi} \right)} \right] = 0. \tag{16}$$

Thus, the Hesse matrices are singular and, consequently, a Legendre transform does not exist. With Eq. (7), a Lagrangian density is determined up to the divergence of an arbitrary vector function. Thus, one can add to \mathcal{L}_D the divergence

$$\frac{\partial F^{\beta}}{\partial x^{\beta}} = \frac{\partial \overline{\psi}}{\partial x^{\alpha}} \frac{i\sigma^{\alpha\beta}}{3m} \frac{\partial \psi}{\partial x^{\beta}}, \qquad \sigma^{\alpha\beta} \equiv \frac{i}{2} \left(\gamma^{\alpha} \gamma^{\beta} - \gamma^{\beta} \gamma^{\alpha} \right), \tag{17}$$

which does not modify the subsequent Euler-Lagrange equations. Now, it is possible to create a *regularized* Dirac Lagrangian density $\mathcal{L}'_D = \mathcal{L}_D + \partial F^{\beta}/\partial x^{\beta}$. Making use of the algebra of the γ matrices, this yields

$$\mathscr{L}'_{D} = \left(\frac{\partial \overline{\psi}}{\partial x^{\alpha}} - \frac{im}{2}\overline{\psi}\gamma_{\alpha}\right) \frac{i\sigma^{\alpha\beta}}{3m} \left(\frac{\partial \psi}{\partial x^{\beta}} + \frac{im}{2}\gamma_{\beta}\psi\right). \tag{18}$$

Now

$$\det \left[\frac{\partial^2 \mathcal{L}'_D}{\partial \left(\partial_{\nu} \overline{\psi} \right) \partial \left(\partial_{\nu} \psi \right)} \right] = \det \left[\frac{i \sigma^{\mu \nu}}{3m} \right] \neq 0 \quad \text{since} \quad \det \sigma^{\mu \nu} = 1, \quad \nu \neq \mu \quad (19)$$

shows that the Hessian is no longer singular and thus the covariant Legendre transformation exists. Defining first the four-vector of conjugate momentum fields,

$$\overline{\pi}^{\mu} = \frac{\partial \mathcal{L}'_D}{\partial (\partial_{\mu} \psi)} = \frac{i}{2} \overline{\psi} \gamma^{\mu} + \frac{\partial \overline{\psi}}{\partial x^{\alpha}} \frac{i \sigma^{\alpha \mu}}{3m}
\pi^{\mu} = \frac{\partial \mathcal{L}'_D}{\partial (\partial_{\mu} \psi)} = -\frac{i}{2} \gamma^{\mu} \psi + \frac{i \sigma^{\mu \alpha}}{3m} \frac{\partial \psi}{\partial x^{\alpha}},$$
(20)

the covariant Dirac Hamiltonian density is finally obtained as

$$\mathcal{H}_D = \left(\overline{\pi}^{\alpha} - \frac{i}{2}\overline{\psi}\gamma^{\alpha}\right) \frac{3m\tau_{\alpha\beta}}{i} \left(\pi^{\beta} + \frac{i}{2}\gamma^{\beta}\psi\right) + m\overline{\psi}\psi, \tag{21}$$

where $\tau_{\mu\alpha}$ denotes the inverse of $\sigma^{\alpha\nu}$, $\tau_{\mu\alpha}\sigma^{\alpha\nu} = \delta^{\nu}_{\mu}\mathbb{1}$.

4 General U(N) Gauge Transformations

Given a Hamiltonian system \mathcal{H} that is form-invariant under a *global* gauge transformation, the covariant canonical transformation formalism is now applied to determine the corresponding Hamiltonian \mathcal{H}_3 that is form-invariant under U(N) *local* gauge transformations. This procedure will be worked out in the following in three steps.

Firstly, the canonical gauge transformation has to be defined by introducing a vector ϕ of N complex fields ϕ_I , I = 1, ..., N and $\overline{\phi}$ as its adjoined vector field

$$\boldsymbol{\phi} = \begin{pmatrix} \phi_1 \\ \vdots \\ \phi_N \end{pmatrix}, \quad \overline{\boldsymbol{\phi}} = (\overline{\phi}_1 \cdots \overline{\phi}_N). \tag{22}$$

A general local, linear transformation then can be expressed in terms of a dimensionless complex matrix $U(x) = (u_{IJ}(x))$ and its adjoint $U^{\dagger}(x) = (\overline{u}_{IJ}(x))$ that generally depend explicitly on the independent variables x^{μ} , as

$$\Phi = U\phi, \quad \overline{\Phi} = \overline{\phi}U^{\dagger}, \quad \Phi_I = u_{IJ}\phi_J, \quad \overline{\Phi}_I = \overline{\phi}_I\overline{u}_{II}.$$
 (23)

With this notation, ϕ stands for a set of $I=1,\ldots,N$ complex scalar fields ϕ_I or Dirac spinors. In other words, U is supposed to define an isomorphism within the space of the ϕ_I , hence to linearly map the ϕ_I into objects of the same type. The transformations will be restricted to those which preserve the norm $\overline{\phi}\phi$

$$\overline{\boldsymbol{\Phi}} \boldsymbol{\Phi} = \overline{\boldsymbol{\phi}} U^{\dagger} U \boldsymbol{\phi} = \overline{\boldsymbol{\phi}} \boldsymbol{\phi} \qquad \Longrightarrow \quad U^{\dagger} U = \mathbb{1} = U U^{\dagger}
\overline{\boldsymbol{\Phi}}_{I} \boldsymbol{\Phi}_{I} = \overline{\boldsymbol{\phi}}_{J} \overline{u}_{JI} u_{IK} \boldsymbol{\phi}_{K} = \overline{\boldsymbol{\phi}}_{K} \boldsymbol{\phi}_{K} \qquad \Longrightarrow \quad \overline{u}_{JI} u_{IK} = \delta_{JK} = u_{JI} \overline{u}_{IK}. \tag{24}$$

The transformation in Eq. (23) follows from a generating function that, corresponding to \mathcal{H} , must be a real-valued function of the generally complex fields ϕ_I and their canonical conjugates, π_I^{μ} ,

$$F_2^{\mu}(\boldsymbol{\phi}, \overline{\boldsymbol{\phi}}, \boldsymbol{\Pi}^{\mu}, \overline{\boldsymbol{\Pi}}^{\mu}, x) = \overline{\Pi}_K^{\mu} u_{KJ} \phi_J + \overline{\phi}_K \overline{u}_{KJ} \Pi_I^{\mu}. \tag{25}$$

The set of transformation rules follows as

$$\overline{\pi}_{I}^{\mu} = \frac{\partial F_{2}^{\mu}}{\partial \phi_{I}} = \overline{\Pi}_{K}^{\mu} u_{KJ} \delta_{JI}, \qquad \overline{\Phi}_{I} \delta_{\nu}^{\mu} = \frac{\partial F_{2}^{\mu}}{\partial \overline{\Pi}_{I}^{\nu}} = \overline{\phi}_{K} \overline{u}_{KJ} \delta_{\nu}^{\mu} \delta_{JI}$$

$$\pi_{I}^{\mu} = \frac{\partial F_{2}^{\mu}}{\partial \overline{\phi}_{I}} = \delta_{IK} \overline{u}_{KJ} \Pi_{J}^{\mu}, \qquad \Phi_{I} \delta_{\nu}^{\mu} = \frac{\partial F_{2}^{\mu}}{\partial \overline{\Pi}_{I}^{\nu}} = \delta_{\nu}^{\mu} \delta_{IK} u_{KJ} \phi_{J}. \tag{26}$$

The complete set of transformation rules and their inverses then read in component notation

$$\Phi_{I} = u_{IJ}\phi_{J}, \qquad \overline{\Phi}_{I} = \overline{\phi}_{J}\overline{u}_{JI}, \qquad \phi_{I} = \overline{u}_{IJ}\Phi_{J}, \qquad \overline{\phi}_{I} = \overline{\Phi}_{J}u_{JI},
\Pi_{I}^{\mu} = u_{IJ}\pi_{J}^{\mu}, \qquad \overline{\Pi}_{I}^{\mu} = \overline{\pi}_{J}^{\mu}\overline{u}_{JI}, \qquad \pi_{I}^{\mu} = \overline{u}_{IJ}\Pi_{J}^{\mu}, \qquad \overline{\pi}_{I}^{\mu} = \overline{\Pi}_{J}^{\mu}u_{JI}.$$
(27)

5 From Global to Local Gauge Invariance

The given covariant Hamiltonian density \mathscr{H} is supposed to be *form-invariant* under the *global* gauge transformation (27), which is given for U=const., hence for all u_{IJ} not depending on the independent variables x^{μ} . In contrast, if U=U(x), then the transformation in Eq. (27) is referred to as a *local* gauge transformation. The transformation rule for the Hamiltonian is then determined by the explicitly x^{μ} -dependent terms of the generating function F_2^{μ} from Eq. (25) according to

$$\mathcal{H}' - \mathcal{H} = \frac{\partial F_2^{\alpha}}{\partial x^{\alpha}} \bigg|_{\text{expl}} = \left(\overline{\pi}_K^{\alpha} \phi_J - \overline{\phi}_K \pi_J^{\alpha} \right) \overline{u}_{KI} \frac{\partial u_{IJ}}{\partial x^{\alpha}}. \tag{28}$$

To set up a Hamiltonian \mathcal{H}_1 that is *form-invariant* under *local*, hence x^{μ} -dependent transformations, the terms in Eq. (28) have to be compensated by the additional term

$$\mathcal{H}_a = ig \left(\overline{\pi}_K^{\alpha} \phi_J - \overline{\phi}_K \pi_J^{\alpha} \right) a_{KJ\alpha} \tag{29}$$

where g is a real valued coupling constant, which means that also the interaction Hamiltonian \mathcal{H}_a is real. The amended Hamiltonian then reads

$$\mathcal{H}_1 = \mathcal{H} + \mathcal{H}_a. \tag{30}$$

Submitting the amended Hamiltonian \mathcal{H}_1 to the canonical transformation generated by the generating function in (25), the new Hamiltonian \mathcal{H}_1' turns out to be

$$\mathcal{H}_{1}' = \mathcal{H}_{1} + \frac{\partial F_{2}^{\mu}}{\partial x^{\alpha}} \Big|_{\text{expl}} = \mathcal{H} + \mathcal{H}_{a} + \frac{\partial F_{2}^{\mu}}{\partial x^{\alpha}} \Big|_{\text{expl}} \\
= \mathcal{H} + \left(\overline{\pi}_{K}^{\alpha} \phi_{J} - \overline{\phi}_{K} \pi_{J}^{\alpha} \right) \left(i g a_{KJ\alpha} + \overline{u}_{KI} \frac{\partial u_{IJ}}{\partial x^{\alpha}} \right) \\
\stackrel{!}{=} \mathcal{H}' + \left(\overline{\Pi}_{K}^{\alpha} \Phi_{J} - \overline{\Phi}_{K} \Pi_{J}^{\alpha} \right) i g A_{KJ\alpha} \tag{31}$$

As the system Hamiltonian \mathcal{H} is supposed to be invariant under *global* gauge transformations, one has $\mathcal{H}' = \mathcal{H}$. Therefore, the gauge fields must satisfy the transformation rule

$$A_{KJ\mu} = u_{KL} a_{LI\mu} \overline{u}_{IJ} - \frac{i}{g} \frac{\partial u_{IK}}{\partial x^{\mu}} \overline{u}_{IJ}. \tag{32}$$

With the knowledge of the required transformation rule for the gauge fields, it is now possible to redefine the generating function from (25) to also describe the gauge field transformation. According to the general rules for canonical transformations generated by functions of type F_2^{μ} from Eq. (11), the transformation rules for the complex fields ϕ_I and their conjugates, π_I^{μ} in conjunction with the rule (32) for the gauge fields $a_{LI\mu}$ emerges from the *amended* generating function

$$\tilde{F}_{2}^{\mu} = \overline{\Pi}_{K}^{\mu} u_{KJ} \phi_{J} + \overline{\phi}_{K} \overline{u}_{KJ} \Pi_{J}^{\mu} + P_{JK}^{\alpha \mu} \left(u_{KL} a_{LI\alpha} \overline{u}_{IJ} - \frac{i}{g} \frac{\partial u_{KI}}{\partial x^{\alpha}} \overline{u}_{IJ} \right). \tag{33}$$

The transformation of the momentum fields $p_{IL}^{\alpha\mu}$ of the gauge fields $a_{LI\alpha}$ is obtained from this generating function as

$$p_{IL}^{\alpha\mu} = \frac{\partial \tilde{F}_2^{\mu}}{\partial a_{LI\alpha}} = \overline{u}_{IJ} P_{JK}^{\alpha\mu} u_{KL}. \tag{34}$$

Working out the difference of the Hamiltonians that are submitted to the canonical transformation generated by (33) means to calculate the divergence of the explicitly x^{μ} -dependent terms of \tilde{F}_{2}^{μ} .

$$\mathcal{H}_{2}' = \mathcal{H}_{2} + \frac{\partial \tilde{F}_{2}^{\mu}}{\partial x^{\alpha}} \bigg|_{\text{expl}}.$$
 (35)

All terms depending on the u_{IJ} and their derivatives must then be expressed through the physical fields ϕ_I , $\overline{\phi}_I$, $a_{IJ\mu}$ and their respective conjugates by means of the canonical transformation rules. In summary, the *form-invariant* amended Hamiltonian then follows as

$$\mathcal{H}_2 = \mathcal{H} + \mathcal{H}_a + \mathcal{H}_b. \tag{36}$$

with

$$\mathcal{H}_{b} = \frac{1}{2} p_{JK}^{\alpha\beta} \left[\frac{\partial a_{KJ\alpha}}{\partial x^{\beta}} + \frac{\partial a_{KJ\beta}}{\partial x^{\alpha}} - ig \left(a_{KI\alpha} a_{IJ\beta} - a_{KI\beta} a_{IJ\alpha} \right) \right]. \tag{37}$$

In the last step a kinetic term must be added to ensure the consistency of the canonical transformation rules with the subsequent field equations. This requirement uniquely determines the kinetic term as

$$\mathscr{H}_c = -\frac{1}{4} p_{JK}^{\alpha\beta} p_{KJ\alpha\beta}. \tag{38}$$

Concluding, any given Hamiltonian \mathcal{H} that is *globally* form-invariant under the SU(N) symmetry transformation (23) of the fields ϕ_I , $\overline{\phi}_I$ is *uniquely* converted into a corresponding *locally* form-invariant Hamiltonian \mathcal{H}_3 by amending \mathcal{H} with \mathcal{H}_g ,

$$\mathcal{H}_3 = \mathcal{H} + \mathcal{H}_g, \quad \mathcal{H}_g = \mathcal{H}_a + \mathcal{H}_b + \mathcal{H}_c,$$
 (39)

or, explicitly

$$\mathcal{H}_{3} = \mathcal{H} - \frac{1}{4} p_{JK}^{\alpha\beta} p_{KJ\alpha\beta} + ig \left(\overline{\pi}_{K}^{\alpha} \phi_{J} - \overline{\phi}_{K} \pi_{J}^{\alpha} \right) a_{KJ\alpha}$$

$$+ \frac{1}{2} p_{JK}^{\alpha\beta} \left[\frac{\partial a_{KJ\alpha}}{\partial x^{\beta}} + \frac{\partial a_{KJ\beta}}{\partial x^{\alpha}} - ig \left(a_{KI\alpha} a_{IJ\beta} - a_{KI\beta} a_{IJ\alpha} \right) \right]. \tag{40}$$

6 Locally Gauge-Invariant Lagrangian Density

A corresponding local gauge invariant Lagrangian density from a given globally gauge-invariant Hamiltonian $\mathcal{H}\left(\overline{\phi}_{I},\phi_{I},\overline{\pi}_{I},\pi_{I},x\right)$ can be obtained by the Legendre transformation

$$\mathcal{L}_{3} = \overline{\pi}_{K}^{\alpha} \frac{\partial \phi_{K}}{\partial x^{\alpha}} + \frac{\partial \overline{\phi}_{K}}{\partial x^{\alpha}} \pi_{K}^{\alpha} + p_{JK}^{\alpha\beta} \frac{\partial a_{KJ\alpha}}{\partial x^{\beta}} - \mathcal{H}_{3}, \quad \mathcal{H}_{3} = \mathcal{H} + \mathcal{H}_{g}, \quad (41)$$

where

$$p_{JK}^{\alpha\beta} \frac{\partial a_{KJ\alpha}}{\partial x^{\beta}} - \mathcal{H}_g = ig \left(\overline{\pi}_K^{\alpha} \phi_J - \overline{\phi}_K \pi_J^{\alpha} \right) a_{KJ\alpha} - \frac{1}{4} p_{JK}^{\alpha\beta} p_{KJ\alpha\beta}. \tag{42}$$

Therefore, the locally gauge-invariant Lagrangian for *any* given globally gauge-invariant Hamiltonian $\mathscr{H}\left(\overline{\phi}_{I},\phi_{I},\overline{\pi}_{I},\pi_{I},x\right)$ is given by

$$\mathcal{L}_{3} = -\frac{1}{4} p_{JK}^{\alpha\beta} p_{KJ\alpha\beta} + \overline{\pi}_{K}^{\alpha} \left(\frac{\partial \phi_{K}}{\partial x^{\alpha}} - i g a_{KJ\alpha} \phi_{J} \right) + \left(\frac{\partial \overline{\phi}_{K}}{\partial x^{\alpha}} + i g \overline{\phi}_{J} a_{JK\alpha} \right) \pi_{K}^{\alpha} - \mathcal{H}.$$

$$(43)$$

7 Example Part II: Dirac Hamiltonian Density

To show an application of this method, the globally form-invariant Dirac Hamiltonian density from Eq. (21) is rendered locally form-invariant by adding \mathcal{H}_g from Eq. (40), which yields

$$\mathcal{H}_{3,D} = \left(\overline{\pi}_{I}^{\alpha} - \frac{i}{2}\overline{\psi}_{I}\gamma^{\alpha}\right) \frac{3m\tau_{\alpha\beta}}{i} \left(\pi_{I}^{\beta} + \frac{i}{2}\gamma^{\beta}\psi_{I}\right) + m\overline{\psi}_{I}\psi_{I}$$
$$-\frac{1}{4}p_{JK}^{\alpha\beta}p_{KJ\alpha\beta} + ig\left(\overline{\pi}_{K}^{\alpha}\psi_{J} - \overline{\psi}_{K}\pi_{J}^{\alpha} + p_{JI}^{\alpha\beta}a_{IK\beta}\right)a_{KJ\alpha}. \tag{44}$$

By the Legendre transformation in Eq. (41), the related locally gauge-invariant Dirac Lagrangian Density is found to be

$$\mathcal{L}_{3,D} = \left(\frac{\partial \overline{\psi}_{I}}{\partial x^{\alpha}} + ig\overline{\psi}_{J}a_{JI\alpha} - \frac{im}{2}\overline{\psi}_{I}\gamma_{\alpha}\right)\frac{i\sigma^{\alpha\beta}}{3m}\left(\frac{\partial \psi_{I}}{\partial x^{\beta}} - iga_{IK\beta}\psi_{K} + \frac{im}{2}\gamma_{\beta}\psi_{I}\right) - \frac{1}{4}p_{JK}^{\alpha\beta}p_{KJ\alpha\beta},\tag{45}$$

wherein $p_{KJ\alpha\beta}$ no longer represents a canonical variable but abbreviates the Lagrangian quantity

$$p_{KJ\mu\nu} = \frac{\partial a_{KJ\nu}}{\partial x^{\mu}} - \frac{\partial a_{KJ\mu}}{\partial x^{\nu}} + ig \left(a_{KI\nu} a_{IJ\mu} - a_{KI\mu} a_{IJ\nu} \right). \tag{46}$$

From this locally form-invariant Lagrangian density the Euler-Lagrange equations are obtained as

$$i\gamma^{\alpha} \frac{\partial \psi_{I}}{\partial x^{\alpha}} + g\gamma^{\alpha} a_{IK\alpha} \psi_{K} - m\psi_{I} - \frac{g}{6m} p_{IK\alpha\beta} \sigma^{\alpha\beta} \psi_{K} = 0$$

$$i\frac{\partial \overline{\psi}_{I}}{\partial x^{\alpha}} \gamma^{\alpha} + g\overline{\psi}_{K} a_{KI\alpha} \gamma^{\alpha} - m\overline{\psi}_{I} - \frac{g}{6m} \overline{\psi}_{K} \sigma^{\alpha\beta} p_{KI\alpha\beta} = 0. \tag{47}$$

The gauge-invariant Dirac equation contains an additional term that is proportional to $p_{IK\alpha\beta}$, hence to the canonical momenta of the gauge fields $a_{IK\alpha}$. This term is separately gauge invariant. One thus encounters the description of the coupling of the anomalous magnetic moments of the fermions to the gauge bosons, i.e., a spin-gauge field coupling.

For the case of a system with a single spinor ψ representing a fermion of mass m_e , hence for the U(1) gauge group, the locally gauge-invariant Dirac equation reduces to

$$i\gamma^{\alpha}\frac{\partial\psi}{\partial x^{\alpha}} + g\gamma^{\alpha}a_{\alpha}\psi - m\psi + \frac{\mu_{B}}{3}\left(\frac{\partial a_{\beta}}{\partial x^{\alpha}} - \frac{\partial a_{\alpha}}{\partial x^{\beta}}\right)\sigma^{\alpha\beta}\psi = 0,\tag{48}$$

with $\mu_B = g/2m_e$ the Bohr magneton. This term is invariant under the combined gauge transformation of base and gauge fields

$$a_{\mu}(x) \mapsto A_{\mu}(x) = a_{\mu}(x) + \frac{1}{g} \frac{\partial \Lambda(x)}{\partial x^{\mu}}, \quad \psi(x) \mapsto \Psi(x) = \psi(x)e^{i\Lambda}(x) \quad (49)$$

with the spin-gauge field coupling term being separately gauge invariant. Here, the additional term corresponds to a coupling of the electromagnetic field with the spin-induced magnetic moment of the fermion represented by ψ , commonly referred to as *Pauli coupling* term. It is remarkable that Pauli interaction necessarily emerges in the context of the Hamiltonian formulation of gauge theory. In the Lagrangian description, this term is encountered if and only if the minimum coupling rule is applied to the *regularized* Lagrangian from Eq. (18).

In this context, it should be remarked that the Pauli-coupling terms in the field equations in Eq. (47) equally follow from the amended Dirac-Lagrangian

$$\mathcal{L}_{3,\text{Pauli}} = \frac{i}{2} \overline{\psi}_{I} \gamma^{\alpha} \left(\frac{\partial \psi_{I}}{\partial x^{\alpha}} - i g a_{IK\alpha} \psi_{K} \right) - \frac{i}{2} \left(\frac{\partial \overline{\psi}_{I}}{\partial x^{\alpha}} + i g \overline{\psi}_{J} a_{JI\alpha} \right) \gamma^{\alpha} \psi_{I} - m \overline{\psi}_{I} \psi_{I}$$

$$- \frac{1}{2} \ell \overline{\psi}_{J} p_{JK\alpha\beta} \sigma^{\alpha\beta} \psi_{K} - \frac{1}{4} p_{JK}^{\alpha\beta} p_{KJ\alpha\beta}$$

$$(50)$$

if the coupling constant $\ell[L]$ with $\ell=g/3m_e$. The addition of the term proportional to ℓ was proposed by Pauli [8]. It can be shown that the gauge-invariant Lagrangian from Eq. (45) and Pauli's amended Lagrangian from Eq. (50) yield the same classical field equations for the gauge fields $a_{JK\mu}$. But, the term inducing Pauli coupling in the Lagrangian of Eq. (50) is not consistent with the minimal coupling rule. In contrast, with the locally gauge-invariant Lagrangian $\mathcal{L}_{3,D}$ from Eq. (45) a description of Pauli coupling was derived that conforms with the minimal coupling rule. While both Lagrangians yield the same classical field equations, the QFT processes emerging from both Lagrangians are different. The Pauli-coupling term in the Lagrangian $\mathcal{L}_{3,D}$ was obtained from canonical gauge theory—rather than being postulated—and is consistent with the minimum coupling rule.

8 Conclusions

A consistent local coordinate description of the canonical formalism in covariant Hamiltonian field theory has been worked out. In this context a consistent formalism of canonical transformations was derived. On that basis, the procedure to amend a given *globally* gauge-invariant Hamiltonian \mathcal{H} in order to render the resulting system Hamiltonian \mathcal{H}_3 locally gauge invariant has been derived.

References

- 1. Th De Donder, *Théorie Invariantive Du Calcul des Variations* (Gaulthier-Villars and Cie, Paris, 1930)
- M. Forger, C. Paufler, H. Römer, The poisson bracket for poisson forms in multisymplectic field theory. Rev. Math. Phys. 15, 705 (2003)
- 3. M.J. Gotay, J. Isenberg, J.E. Marsden, R. Montgomery, Momentum maps and classical fields, part I, covariant field theory (2004), arXiv:physics/9801019
- W. Greiner, B. Müller, J. Rafelski, Quantum Electrodynamics of Strong Fields (Springer, New York, 1985)
- 5. D. Griffiths, Introduction to Elementary Particles (Wiley, New York, 1987)
- Ch. Günther, The polysymplectic Hamiltonian formalism in field theory and calculus of variations I: the local case. J. Differ. Geom. 25, 23 (1987)
- I.V. Kanatchikov, Canonical structure of classical field theory in the polymomentum phase space. Rep. Math. Phys. 41, 49 (1998)
- 8. W. Pauli, Rev. Mod. Phys. **13**, 203–232 (1941)
- 9. L.H. Ryder, *Quantum Field Theory* (Cambridge University Press, Cambridge, 2006)
- 10. J. Saletan, E.J.V. José, Classical Dynamics (Cambridge University Press, Cambridge, 1998)
- 11. G. Sardanashvily, *Generalized Hamiltonian Formalism for Field Theory* (World Scientific Publishing Co., Singapore, 1995)
- 12. D.J. Saunders, The Geometry of Jet Bundles (Cambridge University Press, Cambridge, 1989)
- S. Weinberg, The Quantum Theory of Fields, vol. I (Cambridge University Press, Cambridge, 1996)
- 14. H. Weyl, Eine neue Erweiterung der Relativitätstheorie. Ann. d. Physik 364, 101-131 (1919)
- H. Weyl, Geodesic fields in the calculus of variation for multiple integrals. Ann. Math. 36, 607 (1935)

Combining Quantum Electrodynamics and Electron Correlation

Ingvar Lindgren, Sten Salomonson, Daniel Hedendahl and Johan Holmberg

Abstract There is presently a large interest in studying highly charged ions in order to investigate the effects of quantum-electrodynamics (OED) at very strong fields. Such experiments can be performed at large accelerators, like that at GSI in Darmstadt, where the big FAIR facility is under construction. Accurate experiments on light and medium-heavy ions can also be performed by means of laser and X-ray spectroscopy. To obtain valuable information, accurate theoretical results are required to compare with. The most accurate procedures presently used for calculations on simple atomic systems are (i) all-order many-body perturbative expansion with added first-order analytical QED energy corrections, and (ii) two-photon QED calculations. These methods have the shortcoming that the *combination* of QED and correlational effects (beyond lowest order) is completely missing. We have developed a third procedure, which can remedy this shortcoming. Here, the energy-dependent QED effects are included directly into the atomic wave function, which is possible with the procedure that we have recently developed. The calculations are performed using the Coulomb gauge, which is most appropriate for the combined effect. Since QED effects, like the Lamb shift, have never been calculated in that gauge, this has required some development. This is now being implemented in our computational procedure, and some numerical results are presented.

1 Introduction

Highly charged ions are frequently used to investigate QED effects at strong fields, for instance at the GSI facility at Darmstadt, where H-, He-, Li-, and Be-like ions up to uranium can be produced.

If theory is trusted, comparison between theory and experiment can yield information about nuclear structure, fundamental constants, etc. One example is the proton radius, where the established value, 0.8775(51) fm, is obtained from electron-scattering data and by comparing theory and experiment for atomic hydrogen [1].

I. Lindgren(\boxtimes) · S. Salomonson · D. Hedendahl · J. Holmberg Department of Physics, University of Gothenburg, Gothenburg, Sweden e-mail: ingvar.lindgren@physics.gu.se

288 I. Lindgren et al.

Table 1 Theoretical value of the electronic g-factor of C^{5+}

Dirac theory	1.998 721 354 39(1)
QED	0.002 320 235 79(3)
Total theory	2.001 041 590 18(3)

Table 2 Transition $1s2s^1S_0 - 1s2p^3P_1$ in He-like Si (cm⁻¹) (1eV \simeq 8,000 cm⁻¹)

		References	
Expt'1 7230.585(6)		DeVore et al. [5]	
RMBPT	7231	Plante et al. [6]	
QED	7229(2)	Artemyev et al. [7]	

Table 3 Transition $1s^2 {}^1S_0 - 1s2p {}^1P_1$ in He-like ions (eV)

Z	Artemyev et al. [7]	Plante et al. [6]	Experimental
18	3139.582	3139.580	3139.553(38)
22	4749.644(1)	4749.639	4749.85(7)
36	13026.117(4)	13026.044	13026.8(3)

(Recently, new measurements on muonic hydrogen have yielded a significantly smaller value, 0.8409(4) fm [2], and the reason for this discrepancy is presently not understood.)

Another example is the measurement of the electronic g-factor of hydrogen-like ions (see Table 1), which can be determined with high precision by means of a single-ion trap [3]. From this comparison the value of the electron mass was deduced, 0.000 548 579 909 3(3) atomic mass units, which was four times more accurate than the previously accepted value [4].

One question that can be raised here is, of course, to what extent QED can be trusted? Is there a limit, and, if so, what is causing it? Accurate tests of QED can help answering these fundamental questions.

Besides heavy-ion experiments, interesting results can also be achieved by means of laser and X-ray spectroscopy. Some experimental data can be much more accurate than corresponding theoretical evaluations (see Table 2). Here, there is a great challenge to try to improve on the theoretical results.

In Table 3 we compare some X-ray data with accurate theoretical calculations for some medium-heavy helium like ions. The experimental values are taken from Ref. [7]. Here, we see that significant deviations can appear.

An interesting question is here how the accuracy of the theoretical calculations could be improved? For most atomic and molecular systems the electron correlation is the dominating perturbation. Therefore, a natural starting point is a procedure where this effect is treated to high order. The standard procedure is then to add first-order QED effects to the energy. In many cases this procedure yields sufficiently accurate results [6]. In order to reach beyond that level, however, it is necessary to include the QED perturbations into the wave function. Since most QED effects are time or energy dependent, this requires a time/energy-dependent perturbation procedure.

An alternative procedure that is also frequently used is the two-photon QED procedure, which in many cases leads to quite accurate results [7]. It has the disadvantage, however, that the electron correlation is included only to lowest order.

We have developed a procedure based upon a perturbation expansion, where the electron correlation is essentially carried to all orders and with QED corrections included in the wave function—a procedure that is presently being implemented. We believe this has the potential of yielding higher accuracy than methods presently employed. Before describing this procedure, we shall as a background review the standard time-independent methods.

2 Time-Independent Methods for Atomic Calculations

2.1 Non-QED Methods

2.1.1 Standard Many-Body Perturbation Theory (MBPT)

We consider a number of "target states", satisfying the Schrödinger equation [8]

$$H\Psi^{\alpha} = E^{\alpha}\Psi^{\alpha} \quad (\alpha = 1 \dots d). \tag{1}$$

For each target state there exists a *model state*, which in intermediate normalization is the projection on the model space

$$\Psi_0^{\alpha} = P\Psi^{\alpha} \quad (\alpha = 1 \dots d). \tag{2}$$

A wave operator transforms the model states to the full target states

$$\Psi^{\alpha} = \Omega \Psi_0^{\alpha} \quad (\alpha = 1 \dots d). \tag{3}$$

An *effective Hamiltonian* can be defined, so that it generates the exact energies, operating on the model functions

$$H_{\text{eff}}\Psi_0^{\alpha} = PH\Omega\Psi_0^{\alpha} = E^{\alpha}\Psi_0^{\alpha}. \tag{4}$$

The Hamiltonian is partitioned into a model Hamiltonian and a perturbation

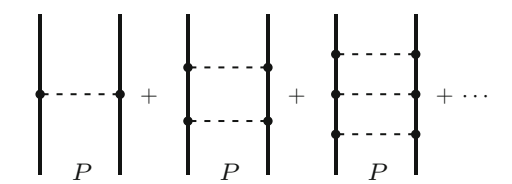
$$H = H_0 + V. (5)$$

The wave operator satisfies a *Bloch equation*

$$[\Omega, H_0]P = Q[V\Omega - \Omega W]_{\text{linked}}P, \tag{6}$$

290 I. Lindgren et al.

Fig. 1 Expanding the two-body part of the wave operator (without singles) leads to the pair function



where the subscript "linked" indicates that—under certain general conditions—only linked diagrams contribute (linked-diagram theorem). Here,

$$W = PV\Omega P \tag{7}$$

is the "effective interaction".

The last term of the Bloch equation represents the *model-space contribution*, which is the remainder after the singularities due to intermediate model-space states are eliminated. We shall see that this effect will play an important role in the generalization to energy-dependent formalism that we shall consider below.

2.1.2 All-Order Methods

In the perturbation expansion certain effects, such as the pair correlation, can be included iteratively to arbitrary order by separating the wave operator by means of second quantization into one-body, two-body, ... effects

$$\Omega = \Omega_1 + \Omega_2 + \cdots \tag{8}$$

This leads to the coupled equations

$$[\Omega_n, H_0]P = Q[V\Omega - \Omega W]_{\text{linked},n}P.$$
 (9)

Expanding the two-body part (without singles) leads to the pair function, illustrated in Fig. 1.

By means of the exponential Ansatz this leads to the Coupled-Cluster Approach [9].

2.1.3 Multi-Configuration Hartree/Dirac-Fock (MCHF/MCDF)

An alternative to the perturbation expansion is the *Multi-Configuration Hartree/Dirac-Fock Method*, where also electron correlation can be included essentially to all orders [10]. In neither scheme QED effects are included, but first-order QED effects can be added to the energy.

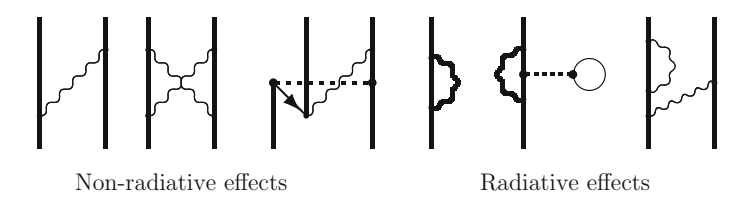


Fig. 2 Examples of QED effects

2.1.4 Relativistic MBPT

The standard relativistic MBPT is based upon the *Dirac-Coulomb-Breit Approxima*tion [11]

$$H = \Lambda_{+} \left[\sum_{i=1}^{N} h_{D}(i) + \sum_{i < j}^{N} \frac{e^{2}}{4\pi r_{ij}} + H_{B} \right] \Lambda_{+} , \qquad (10)$$

$$H_B = -\frac{e^2}{8\pi} \sum_{i < j}^{N} \left[\frac{\alpha_i \cdot \alpha_j}{r_{ij}} + \frac{(\alpha_i \cdot r_{ij})(\alpha_j \cdot r_{ij})}{r_{ij}^3} \right]$$
(11)

where the projection operators Λ_+ eliminate negative-energy states. This is known as the *No-(Virtual)-Pair Approximation (NVPA)*.

2.1.5 QED Effects

The effects beyond NVPA are defined as the QED corrections, which are of the order α^3 or higher. They can be separated into (see Fig. 2)

- Non-radiative effects (retardation, virtual pairs)
- Radiative effects (Lamb shift etc.).

2.2 QED Methods

There exist several standard methods for QED calculations, the most frequently used methods are

- *S-matrix formulation* [12],
- Two-times Green's function, developed by Shabaev et al. at St. Petersburg [13],
- *Covariant-evolution operator method*, developed by the Gothenburg group [14–16],

292 I. Lindgren et al.

All three methods are in practice limited to two-photon exchange, which implies that the electron correlation is treated only to lowest order.

3 Time-Dependent Perturbation Theory: Unification of QED and MBPT

We shall now see how we can go beyond the standard methods, described above, by means of time-dependent perturbation theory. This will be based upon the Covariant Evolution Operator (CEO) method mentioned above.

3.1 Covariant Evolution Operator (CEO)

The single-particle Green's function can be defined (in Heisenberg representation, T is the Wick time ordering)

$$G(t, t_0) = \frac{\langle 0_H | T[\hat{\psi}_H(x)\psi_H^{\dagger}(x_0)] | 0_H \rangle}{\langle 0_H | 0_H \rangle} . \tag{12}$$

The single-particle CEO can be defined analogously

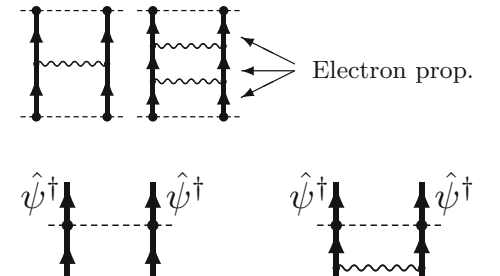
$$U_{\text{Cov}}(t, t_0) = \iint d^3x \, d^3x_0 \, \hat{\psi}^{\dagger}(x) \langle 0_H | T[\hat{\psi}_H(x) \hat{\psi}_H^{\dagger}(x_0)] | 0_H \rangle \hat{\psi}(x_0)$$
 (13)

The Green's function is a *function*, while the CEO is an *operator* (see Figs. 3 and 4). The covariant evolution operator represents the time evolution of the *relativistic* state vector,

$$\Psi_{\text{Rel}}(t) = U_{\text{Cov}}(t, t_0) \Psi_{\text{Rel}}(t_0). \tag{14}$$

Fig. 3 Graphical representation of the Green's function. The free ends are electron propagators

Fig. 4 Graphical representation of the covariant evolution operator. The free lines are electron-field operators



This is singular due to intermediate model-space states. The *regular* part is referred to as the *Green's operator*,

$$U_{\text{Cov}}(t, t_0)P = \mathcal{G}(t, t_0) \cdot PU_{\text{Cov}}(0, t_0)P. \tag{15}$$

The heavy dot on the right-hand side implies that operators to the left of the dot operate on the model-space state at the position of the dot. In contrast to the definition of the Green's function (Eq. 12), the Green's-operator definition (6) is valid also in the multi-reference case.

The Green's operator acts as a *time-dependent wave operator*

$$\Psi^{\alpha}(t) = \mathcal{G}(t, -\infty)\Psi_0^{\alpha} , \qquad (16)$$

which can be compared to the wave operator of standard MBPT (3).

The Green's operator satisfies the Bloch-type equation

$$[\mathcal{G}, H_0] = V\mathcal{G} - \mathcal{G}W + \left[\frac{\delta^*\mathcal{G}}{\delta\mathcal{E}}, H_0\right]W,$$
(17)

where the asterisk indicates that the derivation is restricted to the last interaction. The last two terms represent model-space contributions. This equation can be compared with the standard Bloch equation (6)

$$[\Omega, H_0] = V\Omega - \Omega W. \tag{18}$$

Here, we see that the only difference lies in the extra model-space term of Eq. (17), involving the energy derivative of the interactions. This demonstrates that the perturbation expansion based upon the Green's function is completely compatible with the standard procedure.

Using the Bloch equation (17) for the Green's operator, an iterative procedure can be constructed, where time-independent as well as time-dependent interactions can be arbitrarily mixed (see Fig. 5). This implies that also second- and higher-order QED effects can be included, provided that they are *reducible*, i.e., separable into lower-order effects. This is illustrated by the last diagram in Fig. 5. To include *irreducible* QED effects in the perturbation expansion is for the time being beyond reach. Such effects, however, can be expected to be extremely small.

4 Numerical Results

The combined effect of electron correlation and first-order QED beyond second order is compared with the two-photon retardation effect (Coulomb-Breit) for the ground states of some He-like ions in Table 4. We can see that the third- and higher-order

294 I. Lindgren et al.



Fig. 5 Iteration of the Bloch equation (17), can lead to a mixture of Coulomb and QED perturbations

Table 4 Combination of electron correlation and first-order QED beyond second order is compared with second-order QED for the ground states of He-like ions (in eV)

Z	Two-photon	MBPT-QED beyond two-photon				
	Retarded	Retardation	Virtual pairs	Self-energy	Vertex correction	
10	0.0033	-0.0011	0.0002			
14	0.0080	-0.0019	0.0004	0.0022		
18	0.0150	-0.0027	0.0006	0.0032		
24	0.0305	-0.0042	0.0009			
30	0.0519	-0.0057	0.0013	0.0086		
42	0.112	-0.0087	0.0019			
50		-0.011	0.002	0.017		

effects with first-order retardation, are quite significant, representing 10-30 of the corresponding second-order effect. These effects are out of reach for the standard procedure presently used.

The calculations are performed in the Coulomb gauge in order to be able to take full advantage of the development in MBPT. The renormalization in this gauge is more complicated than in the more frequently used Feynman gauge and has never been performed before. The procedure was recently developed by Holmberg and Hedendahl [17, 18], based upon the theoretical work of Adkins [19, 20]. The values of the self-energy contributions in the table are preliminary and do not include the model-space contribution. This will be evaluated together with the vertex correction, and such calculations are presently under way.

5 Summary and Conclusions

What has been presented here can be summarized in the following way:

- A procedure for time/energy-dependent perturbation theory has been developed and is now being implemented.
- Time/energy-dependent perturbations can be mixed into the many-body wave function, and the *combination* of electron correlation and QED can be evaluated.
- This has been applied to the ground states of He-like ions.

- This can lead to higher accuracy than the currently used methods for stationary problems, such as energy separations and atomic g-factors.
- The procedure can also be applied to dynamical processes.

References

- 1. P.J. Mohr, B.N. Taylor, D.B. Newell, Rev. Mod. Phys. 84, 1527 (2012). arXiv:1203.5425
- 2. A. Antognini et al., Science **339**, 417 (2013)
- H. Häffner, T. Beier, N. Hermanspahn, H.-J. Kluge, W. Quint, S. Stahl, J. Verdú, G. Werth, Phys. Rev. Lett. 85, 5308 (2000)
- T. Beier, H. Häffner, N. Hermanspahn, S.G. Karshenboim, H.-J. Kluge, Phys. Rev. Lett. 88, 011603 (2002)
- 5. T.R. DeVore, D.N. Crosby, E.G. Myers, Phys. Rev. Lett. 100, 243001 (2008)
- 6. D.R. Plante, W.R. Johnson, J. Sapirstein, Phys. Rev. A 49, 3519 (1994)
- A.N. Artemyev, V.M. Shabaev, V.A. Yerokhin, G. Plunien, G. Soff, Phys. Rev. A 71, 062104 (2005)
- 8. I. Lindgren, J. Morrison, *Atomic Many-Body Theory*, 2nd edn. (Springer, Berlin, 1986, reprinted 2009)
- 9. P. Čársky, J. Paldus, J. Pittner (eds.), Recent Progress in Coupled Cluster Methods: Theory and Applications (Springer, New York, 2009)
- 10. I.P. Grant, Relativistic Quantum Theory of Atoms and Molecules (Springer, Heidelberg, 2007)
- 11. J. Sucher, Phys. Rev. A 22, 348 (1980)
- 12. P.J. Mohr, G. Plunien, G. Soff, Phys. Rep. 293, 227 (1998)
- 13. V.M. Shabaev, Phys. Rep. 356, 119 (2002)
- 14. I. Lindgren, S. Salomonson, B. Åsén, Phys. Rep. **389**, 161 (2004)
- 15. I. Lindgren, S. Salomonson, D. Hedendahl, Phys. Rev. A 73, 062502 (2006)
- I. Lindgren, Relativistic Many-Body Theory: A New Field-Theoretical Approach (Springer, New York, 2011)
- 17. J. Holmberg, Phys. Rev. A 84, 062504 (2011)
- 18. D. Hedendahl, J. Holmberg, Phys. Rev. A 85, 012514 (2012)
- 19. G. Adkins, Phys. Rev. D 27, 1814 (1983)
- 20. G. Adkins, Phys. Rev. D 34, 2489 (1986)

Ultra High Energy Neutrons and Other Fermions

B.G. Sidharth

Abstract We revisit a formulation of relativistic Quantum Mechanical equations given by Feshbach and Villars to exhibit novel particle-antiparticle effects.

1 Introduction

It is well known that the KG (Klein-Gordon) relativistic equation displays the phenomenon of negative energies. The problems of the KG equation can be traced to the second time derivative. Thus if d/dt denotes the Quantum Mechanical energy E, then we have E^2 admitting, as we will see, both +E and -E. To avoid this Dirac considered a first-order equation, but here also there were negative energies and he had to further propose his Hole Theory to circumvent this. difficulty. Pauli and Weisskopf overcame the difficulties by treating the KG equation in a field theoretical sense, where the two degrees of freedom would represent distinctly charged particles. Subsequently, the first-order Dirac equation itself had to be interpreted in a field theoretic sense. In other words, there was no escape from an infinite particle theory [1]. We will now consider a formulation that retains the intended single-particle character of the original KG and Dirac equations.

2 The Feshbach Villars Formulation

We now come to an interesting formulation that has escaped much attention, but which nevertheless can lead to fruitful interpretations and insights as brought out by the author recently. Feshbach and Villars [2] interpreted the KG equation in a

B.G. Sidharth (⋈)

International Institute for Applicable Mathematics and Information Sciences, B.M. Birla Science Centre Complex, Adarsh Nagar, Hyderabad 500063, India e-mail: iiamisbgs@yahoo.co.in

B.G. Sidharth

Department of Mathematics and Informatics, University of Udine, Via Delle Scienze, Udine 33100, India

© Springer International Publishing Switzerland 2015 W. Greiner (ed.), *Nuclear Physics: Present and Future*, FIAS Interdisciplinary Science Series, DOI 10.1007/978-3-319-10199-6_28 298 B.G. Sidharth

single-particle rather than field-theoretic context. In fact they showed that this (F-V) formulation also applies to the Dirac equation. It is rather surprising that this study is hardly ever mentioned in textbooks, an exception being [3].

To see this, we can rewrite the K-G equation in the Schrödinger form, invoking a two-component wave function,

$$\Psi = \begin{pmatrix} \phi \\ \chi \end{pmatrix},\tag{1}$$

The KG equation then can be written as (cf. Ref. [2] for details)

$$i\hbar(\partial\phi/\partial t) = (1/2m)(\hbar/i\nabla - eA/c)^2(\phi + \chi) + (eA_0 + mc^2)\phi ,$$

$$i\hbar(\partial\chi/\partial t) = -(1/2m)(\hbar/i\nabla - eA/c)^2(\phi + \chi) + (eA_0 - mc^2)\chi .$$
 (2)

It will be seen that the components ϕ and χ are coupled in (2). In fact we can analyse this matter further, considering free-particle solutions for simplicity. We write,

$$\Psi = \begin{pmatrix} \phi_0(p) \\ \chi_0(p) \end{pmatrix} e^{i/\hbar(p \cdot x - Et)}$$

$$\Psi = \Psi_0(p) e^{i/\hbar(p \cdot x - Et)}$$
(3)

Introducing (3) into (2) we obtain, two possible values for the energy E, viz.,

$$E = \pm E_p; \quad E_p = [(cp)^2 + (mc^2)^2]^{\frac{1}{2}}$$
 (4)

The associated solutions are

$$E = E_{p} \quad \phi_{0}^{(+)} = \frac{E_{p} + mc^{2}}{2(mc^{2}E_{p})^{\frac{1}{2}}}$$

$$\psi_{0}^{(+)}(p): \quad \chi_{0}^{(+)} = \frac{mc^{2} - E_{p}}{2(mc^{2}E_{p})^{\frac{1}{2}}}$$

$$E = -E_{p} \quad \phi_{0}^{(-)} = \frac{mc^{2} - E_{p}}{2(mc^{2}E_{p})^{\frac{1}{2}}}$$

$$\psi_{0}^{(-)}(p): \quad \chi_{0}^{(-)} = \frac{E_{p} + mc^{2}}{2(mc^{2}E_{p})^{\frac{1}{2}}}$$

$$\phi_{0}^{2} - \chi_{0}^{2} = -1$$

$$(5)$$

It can be seen from this that even if we take the positive sign for the energy in (4), the ϕ and χ components get interchanged with a sign change for the energy. Furthermore we can easily show from this that in the non relativistic limit, the χ component is suppressed by order $(p/mc)^2$ compared to the ϕ component exactly as in the case of the Dirac equation [4]. Let us investigate this circumstance further [5, 6].

It can be seen that (2) are Schrödinger equations and so solvable. However they are coupled. We have from them,

$$i\hbar(\dot{\phi} + \dot{\chi}) = (eA_0 + mc^2)(\phi + \chi) - 2mc^2\chi$$
 (6)

In the case if

$$mc^2 \gg eA_0 \quad \text{(or } A_0 = 0) \tag{7}$$

that is we are dealing with energies or interactions much greater than the electromagnetic (or in the absence of an external field) we can easily verify that

$$\phi = e^{i/\hbar(px - Et)}$$
 and $\chi = e^{i/\hbar(px + Et)}$ (8)

is a solution.

That is ϕ and χ belong to opposite signs of $E(m \neq 0)$ (cf. Eq. 5). The above shows that the K-G equation mixes the positive and negative energy solutions.

If on the other hand $m \approx 0$, then (6) shows that χ and ϕ are effectively uncoupled and are of same energy. This shows that if ϕ and χ both have the same sign for E, that is there is no mixing of positive and negative energy, then the rest mass m vanishes. A non vanishing rest mass requires the mixing of both signs of energy. Indeed it is a well known fact that for solutions which are localized, both signs of the energy solutions are required to be superposed [1, 4]. This is because only positive energy solutions or only negative energy solutions do not form a complete set.

Interestingly the same is true for localization about a time instant t_0 . That is physically, only the interval $(t_0 - \Delta t, t_0 + \Delta t)$ is meaningful. This was noticed by Dirac himself when he deduced his equation of the electron [7]. He pointed out that averages over intervals at the Compton scale need to be taken. Strictly speaking, the electron would have the velocity of light, if we work with spacetime points.

In any case both the positive and negative energy solutions are required to form a complete set and to describe a point particle at x_0 in the delta function sense. The narrowest width of a wave packet containing both positive and negative energy solutions, which describes the spacetime development of a particle in the familiar non-relativistic sense, as is well known is described by the Compton wavelength. As long as the energy domain is such that the Compton wavelength is negligible then our usual classical type description is valid. However as the energy approaches levels where the Compton wavelength can no longer be neglected, then new effects involving the negative energies and antiparticles begin to appear (cf. Ref. [2]). It must be stressed that these considerations are valid for the Dirac equation as well except that ϕ and χ above are themselves two component spinors.

Further, we observe that from (8)

$$t \to -t \Rightarrow E \to -E, \quad \phi \leftrightarrow \chi$$
 (9)

(Moreover in the charged case $e \to -e$). It can be shown that the Schrödinger equation goes over to the Klein-Gordon equation if we allow t to move forward and also backward in $(t_0 - \Delta t, t_0 + \Delta t)$ (cf. Ref. [6]). Here we have done the reverse of getting the Klein-Gordon equation into two Schrödinger equations. This is expressed by (2).

300 B.G. Sidharth

In any case we would like to reiterate that the two degrees of freedom associated with the second time derivative can be interpreted, following Pauli and Weisskopf as positive and negatively charged particles or particles and antiparticles.

3 Remarks and Discussion

We summarize the following:

- (i) From the above analysis it is clear that a localized particle requires both signs of energy. At relatively low energies, the positive energy solutions predominate and we have the usual classical type particle behaviour. On the other hand at very high energies it is the negative energy solutions that predominate as for the negatively charged counterpart or the antiparticles. More quantitatively, well outside the Compton wavelength the former behaviour holds. But as we approach the Compton wavelength we have to deal with the new effects.
- (ii) To reiterate if we consider the positive and negative energy solutions given by $\pm E_p$, as in (5), then we saw that for low energies, the positive solution ϕ_0 predominates, while the negative solution χ_0 is $\sim (\frac{v}{c})^2$ compared to the positive solution. On the other hand at very high energies the negative solutions begin to play a role and in fact the situation is reversed with ϕ_0 being suppressed in comparison to χ_0 . This can be seen from (5).
- (iii) We could now express the foregoing in the following terms: It is well known that we get meaningful probability currents and subluminal classical type situations using positive energy solutions alone as long as we are at energies low enough such that we are well outside the Compton scale. As we near the Compton scale however, we begin to encounter negative energy solutions or these antiparticles.
 - From this point of view, we can mathematically dub the solutions according to the sign of energy $(p_0/|p_0|)$ of these states: +1 and -1. This operator commutes with all observables and yet is not a multiple of unity as would be required by Schur's lemma, as it has two distinct eigen values. This is a superselection principle or a superspin with two states and can be denoted by the Pauli matrices. The two states would refer to the positive energy solutions and the negative energy solutions (cf. Refs. [5, 6]).
- (iv) We now observe that in the above formulation for the wave function

$$\Psi = \begin{pmatrix} \phi \\ \chi \end{pmatrix}, \tag{10}$$

where, as noted, ϕ and χ are, for the Dirac equation, each two spinors. ϕ (or more correctly ϕ_0) represents a particle while χ represents an antiparticle. So, effectively for one observer we have

$$\Psi \sim \begin{pmatrix} \phi \\ 0 \end{pmatrix} \tag{11}$$

and for another observer we can have

$$\Psi \sim \begin{pmatrix} 0 \\ \chi \end{pmatrix}$$
 (12)

that is the two observers would see respectively a particle and an antiparticle. This would be the same for a single observer, if for example the particle's velocity got a boost so that (12) rather than (11) would dominate after some time. However it must be borne in mind that, this idealization apart, the localized particle has to include solutions of both signs of energy.

Interestingly, just after the Big Bang, due to the high energy, we would expect, first (12), that is antiparticles to dominate, then as the universe rapidly cools, particles and antiparticles would be in the same or similar numbers as in the Standard Model, and finally on further cooling (11) that is particles or matter would dominate.

(v) We now make two brief observations, relevant to the above considerations. Latest results in proton-antiproton collisions at Fermi Lab have thrown up the B_s mesons which in turn have decayed exhibiting CP violations in excess of the predictions of the Standard Model, and moreover this seems to hint at a new rapidly decaying particle. Furthermore, in these high energy collisions particle to antiparticle and vice versa transformations have been detected.

Acknowledgments I am grateful to Prof. Walter Greiner of FIAS for useful discussions.

References

- S.S. Schweber, An Introduction to Relativistic Quantum Field Theory (Harper and Row, New York, 1961)
- 2. H. Feshbach, F. Villars, Rev. Mod. Phys. 30, 24–45 (1958)
- 3. W. Greiner, B. Müller, J. Rafelski, *Quantum Electrodynamics of Strong Fields* (Springer, Berlin, 1985)
- J.D. Bjorken, S.D. Drell, Relativistic Quantum Mechanics (Mc-Graw Hill, New York, 1964), p. 39
- B.G. Sidharth, Ultra High Energy Behaviour in New Advances in Physics 5(2), 55-66, arXiv:1103.1496.v3 (2011)
- 6. B.G. Sidharth, Int. J. Mod. Phys. **E20**, 2177–2188. arXiv:1104.011.v1 (2011)
- P.A.M. Dirac, The Principles of Quantum Mechanics (Clarendon Press, Oxford, 1958), pp. 4ff, 253ff



Hotel Jakobsberg



View of the Rhine valley



In the lecture hall



Making a point



That was interesting ...



The help desk



Mikhail Itkis



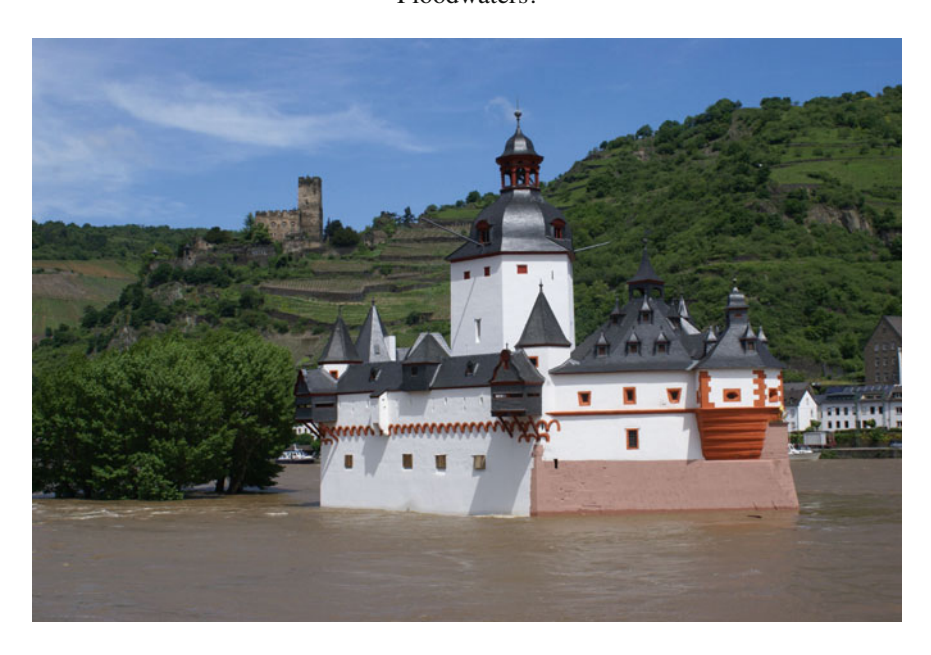
Enjoying the coffee break



Cruising on the river Rhine



Floodwaters!



Pfalzgrafenstein Castle—collecting toll since 1327



Katz Castle near St. Goar

Credits for all pictures: Andrej Popeko